

Collisions during planetary systems formation

Inauguraldissertation
der Philosophisch-naturwissenschaftlichen Fakultät
der Universität Bern

vorgelegt von
Alexandre Emsenhuber
von Schüpfen BE

Leiter der Arbeit
Prof. Dr. Willy Benz
Physikalisches Institut der Universität Bern

Collisions during planetary systems formation

Inauguraldissertation
der Philosophisch-naturwissenschaftlichen Fakultät
der Universität Bern

vorgelegt von
Alexandre Emsenhuber
von Schüpfen BE

Leiter der Arbeit
Prof. Dr. Willy Benz
Physikalisches Institut der Universität Bern

Von der Philosophisch-naturwissenschaftlichen Fakultät angenommen.
Bern, den 28. November 2017

Der Dekan
Prof. Dr. Gilberto Colangelo

Contents

1	Introduction	1
1.1	Solar system	2
1.2	Extrasolar systems	3
1.3	Collision outcomes	5
1.4	Thesis overview	7
2	Formation of planetary systems	9
2.1	Gas disc	9
2.2	Solid disc	11
2.3	Planetary embryos	12
2.4	Giant planets	13
2.5	Terrestrial planets	15
2.6	Interactions	15
	2.6.1 With the disc	15
	2.6.2 Between planets	16
3	The <i>Bern</i> model of planetary system formation	17
3.1	Disc	17
3.2	Planets	18
3.3	Migration	23
3.4	Population synthesis	26
4	N-body and migration problem	29
4.1	N-body	29
	4.1.1 Collisions	30
4.2	Migration	31
4.3	The problem of distant giant planets	32
	4.3.1 Comparison with hydrodynamical simulation	35
	4.3.2 Cause of outward migration	36
4.4	Modification of damping timescales	39
4.5	Alternative migration schemes	45
	4.5.1 Reference frame	46
	4.5.2 Correction method	50
	4.5.3 Application to the formation model	54

4.5.4	Application to whole populations	58
5	Collisions during planetary formation	61
5.1	Demographics	62
5.1.1	With damping prescription from Cresswell and Nelson (2008)	68
5.1.2	Dependence on the number of embryos	71
5.1.3	Influence of radius used for collision detection	72
5.2	In the context of planetary formation	81
5.3	From a planet point of view	84
5.4	Effect on whole population	86
5.5	New model for collisions between terrestrial planets	89
5.5.1	Re-analyse of the previous collisions	96
5.5.2	Population with new model	99
5.6	Other possible improvements	103
5.7	Summary	106
6	Modelling of collisions	109
6.1	Basic equations	109
6.2	SPH formalism	111
6.2.1	Smoothing	111
6.2.2	Particles	113
6.2.3	Hydrodynamics	113
6.2.4	Artificial viscosity	115
6.2.5	Solid-state	116
6.2.6	Angular momentum conservation with solid strength	119
6.2.7	Time and location dependent smoothing length	121
6.2.8	Time integration	122
6.2.9	Density computation at interfaces	124
6.3	Equation of state	125
6.3.1	Coupling with solid model	128
6.4	Implementation	132
6.4.1	Tree	132
6.4.2	Computer code	133
6.4.3	Optimisations	137
6.5	Verification of the solid model	139
6.6	Performing collision simulations	140
6.6.1	1D radial profile	141
6.6.2	SPH body	141
6.6.3	Orbit setup	142
6.6.4	Analysis	146
6.7	Test of miscible SPH	147
6.7.1	Alternative set up procedure	149
7	Application: Moon-forming giant impact	155

8	Application: Mars-scale collisions	183
A	Equations for the disc's vertical structure	237
	Bibliography	239

Chapter 1

Introduction

Collisions are an integral part of the formation of planetary systems and are involved at every step of the process. They lead to the growth of objects whose sizes span over many orders of magnitude. The formation of planets takes place in an accretion disc, which results from the formation of the central star. The disc has initially the same properties as the interstellar medium. It is mainly constituted of gas, with a small fraction of solids in the form of particles with sizes of micrometre. Collisions lead to the coagulation of these dust particles, and to the formation of planetary embryos. If the objects reach a sufficient mass (typically in the range of a few Earth masses) while the gas disc is still present, they will bind a certain amount of gas and possibly become gas giants. On the other hand, the formation of the terrestrial planets can occur on time scales which are longer than the life of the gas disc. At the end of the formation stages, giant impacts take place between planets, which have sizes of thousands of kilometres.

A collision occurs when at least two bodies are close together so that they are in physical contact. In the general case, the bodies are not identical, and the most massive is called the *target* while the smaller one is referred to as the *impactor* or *projectile*. The properties of the bodies, as well as their relative velocity (which relates to the energy) and geometry characterise the collision.

The governing physics of collisions greatly varies with the objects' size. For the dust grains, surface forces will cause them to stick together and grow (Güttler et al. 2010). The relative importance of surface forces decreases as grains grow, and when sizes of centimetre to metre are reached, material strength becomes predominant. The exact mechanism that leads to further growth are yet unknown, as the expected collision velocity distribution results in erosion rather than growth, an issue which is called the *metre-size barrier*. For the larger bodies, with sizes above tens to hundreds of kilometres, gravity becomes dominant. The knowledge of the outcomes of collisions is important in the field of planet formation, as this determines the evolution of the bodies, and the rate of growth. Collisions between similar sized bodies can lead to rapid and significant changes of the overall properties.

Remnants of collisions are observable on Earth in the form of numerous craters visible on the surface. However, geological processes and weathering permit craters to survive only for periods of time which are considerably shorter than the age of the planet. The

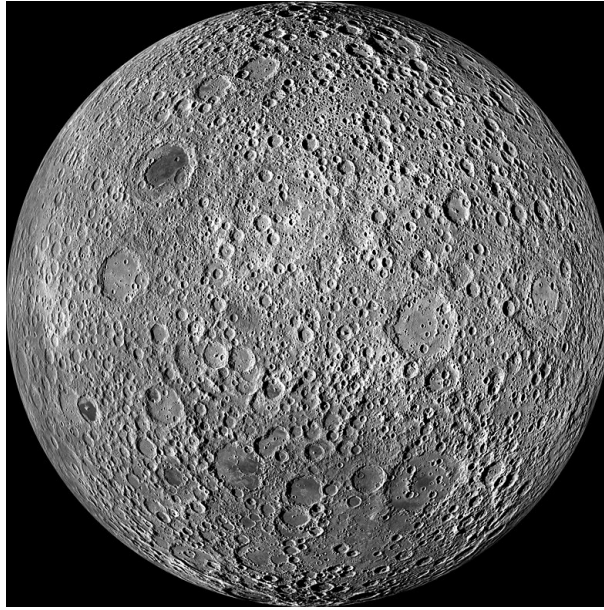


Figure 1.1: Far side of the Moon showing impact craters, as viewed by Lunar Reconnaissance Orbiter's Wide Angle Camera (WAC). Image credit: NASA/GSFC/Arizona State University.

far side of the Moon on the other hand shows a multitude of impact craters that occurred since its formation (figure 1.1); the limiting factor for the age of the craters being more the impact activity with newer crater hiding older ones. Evidences of more ancient collisions, for instances the ones that occurred during the formation stages, are not directly visible. However, geochemists are able to date for instance different events that occurred during the formation of the Earth (see next section).

1.1 Solar system

The formation of the solar system is a long-standing subject of research. The general idea (*nebular hypothesis*) was already proposed by Kant and Laplace in the XVIIIth century, but the refinements came with the availability of precise measurements from either the ground or space probes. For instance, we know that the four giant planets are enhanced in heavy elements compared to the sun, and the enhancement lowers with increasing planet mass. This lead to models for the formation of giant planets involving the differential accretion of solids and gas (e.g. Pollack et al. 1996). For the terrestrial planets, dynamical constraints and mass distribution lead to the creation of, for instance, the *Nice model* (e.g. Tsiganis et al. 2005) or *Grand Tack* (Walsh et al. 2011). Chemical evidences (e.g. König et al. 2011) constrain the duration of the terrestrial planets' formation phase to about 50 – 100 Myr, or close to an order of magnitude more than the expected life time of the gas disc. These planets form then out of the left over from the phase where the gas

disc was present and under the influence of gas giants, which had to have formed earlier.

Giant impacts are likely to occur at the end of the formation of the terrestrial planets (e.g. Raymond et al. 2014, for a review of the different models to form the terrestrial planets). They are invoked to explain different features observed on the terrestrial planets, such as the martian surface dichotomy (Wilhelms and Squyres 1984; Marinova et al. 2008) or the stripping of Mercury’s mantle, which may explain its anomalously high bulk density (Benz et al. 2007; Asphaug and Reufer 2014).

The formation of the terrestrial planets’ satellites (as well as Pluto’s) is also supposed to be the results of giant impacts: our Moon (Hartmann and Davis 1975), Mars’ moons Phobos and Deimos (Citron et al. 2015; Rosenblatt et al. 2016) or the Pluto-Charon system (Canup 2005). The giant impact scenario is often invoked to explain the formation of planet-moon systems because an impact can easily leave material on a bound orbit around the planet.

For the case of the Earth-Moon system, extensive isotopic measurements are available and show that both objects are identical in terms of their main elements (for oxygen e.g. Wiechert et al. 2001; Herwartz et al. 2014; Young et al. 2016) while the Moon is depleted in volatiles elements. In the canonical Moon formation models, the Moon accretes from materials originating from the impactor. Efficient mixing is not a natural result of giant impacts; models that achieve sufficient mixing require specific initial conditions. The following possibilities can explain the observed similarities:

- Both the Earth and the impactor had a similar isotopic composition. This possibility is supported by recent work (Dauphas 2017) that show that material accreted in the late part of Earth formation (i.e. the impactor) has the same chemical composition as material accreted previously.
- The collision properties were such that the material that formed the Moon mostly originates from the proto-Earth. Extensive work has been performed to find alternative impact scenario where most of the Moon-forming material originates from the proto-Earth. Different alternative scenarios are described in the introduction section of the manuscript presented in chapter 7.
- The Earth and the proto-Moon mixed in the aftermath of the giant impact (Pahlavan and Stevenson 2007), although this possibility is debated as the required time scale is longer than the one for the agglomeration of the disc into a single body (Zindler and Jacobsen 2009).

For the case of Mars’s moons Phobos and Deimos, we don’t have the same quality of data yet, but there a few missions being proposed to perform a sample return, such as JAXA’s Martian Moons eXploration (MMX).

1.2 Extrasolar systems

With the detection of the first extrasolar planet around a main sequence star (*51 Pegasi b*, Mayor and Queloz 1995) the field of planetary science has been significantly broadened.

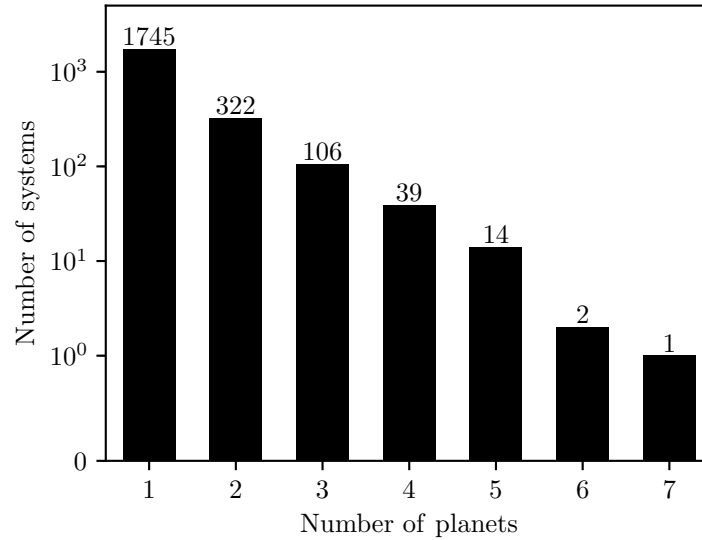


Figure 1.2: Histogram of the multiplicity of observed exoplanetary systems.

Since then, 2951 exoplanets have been discovered¹, most of them by the *Kepler* space telescope. Planets are common, as results from the *Kepler* mission (Fressin et al. 2013) indicate that more than the half of stars ($52.3 \pm 4.2\%$) have a planet whose orbital period is between 0.8 and 85 days.

Observational biases favour the detection of close-in, massive planets. Indeed the first discovered planet falls into this category, as it is Jupiter-like ($M \geq 0.47 M_J$), but on a very close-in orbit ($a \approx 0.05$ AU). With the refinement of the techniques, a broader range of planets are accessible, with sizes down to terrestrial planets. Direct imaging permits observation of massive planets at large separation, like β Pictoris b (Lagrange et al. 2009). The discoveries of extrasolar planets challenged the view that we had on planetary systems. Up to that point, we had only our own solar system, which is divided into two parts: the inner one with the terrestrial planets and the outer part with the gas and ice giants.

Extrasolar planetary systems are very diverse. There is a non-negligible fraction of systems with multiple planets; the number of detected planets per system is shown in figure 1.2. The fraction of systems with multiple planets can be higher, as it is probable that only some components have been detected. It can also be that more planetary embryos existed during the formation stages of those systems, which later on have been removed by close encounters or collisions.

The vast number of discovered planetary systems and their diversity challenged our understanding of the mechanisms that lead to their formation. Different models have been proposed to combine various aspects of planet formation: e.g. Ida and Lin (2004); Alibert et al. (2004). The goal of these models is not to reproduce the formation of a particular

¹<http://exoplanets.org/>; retrieved 20th September 2017.

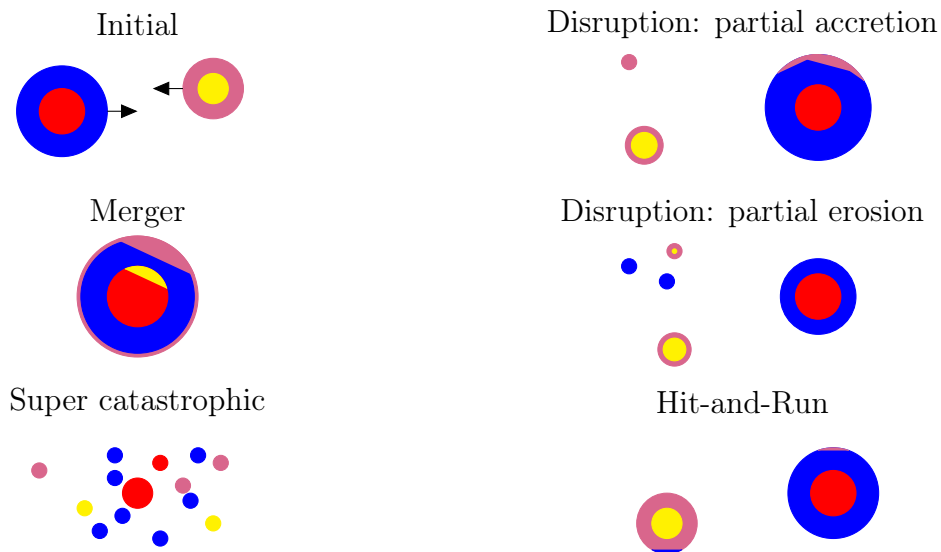


Figure 1.3: Possible outcomes in the different regimes for similar-sized collisions. Differentiated bodies are pictured.

system. There are more parameters in these formation models than constraints that can be derived for a single system. The aim is rather to understand the overall process of planetary formation, and the interactions between the different mechanisms that occur (disc evolution, growth of the proto-planets and their migration for example). The results of these models can then be statistically compared to the population of observed planets.

1.3 Collision outcomes

The regime in which a collision occurs determines the properties of the resulting bodies. A sketch of the different possible outcomes is shown in figure 1.3. It shows the most common cases that occur in the gravity regime; for a similar sketch applied to the smaller scales, the reader is referred to the figure 1 of Güttler et al. (2010).

The different collision outcomes are as follows: for the low energy and velocity (i.e. up to the escape velocity), the objects stick together and the collision ends up in *merger*. In this regime, a lower number of more massive objects remains. On the other hand, very energetic events lead to erosion or fragmentation, and so the objects are dispersed in a number of smaller ones. When the mass of the largest remnant body is less than the half of the initial one, the collision is called *catastrophic* and *super catastrophic* when its mass fraction is lower than 10%. In the latter case, a high number of smaller objects results. In between is the regime where one body retains the majority of material, but mass transfer occurs. In the case the projectile is very small compared to the target, the usual result is a crater, and the mass loss or gain remains small compared to the total mass. For similar sized collisions, a moderate offset is sufficient so that part of the projectile misses the target (Asphaug et al. 2006). In the case the majority of the smaller body "misses" the

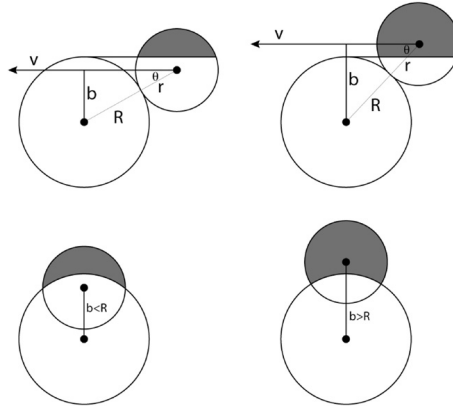


Figure 1.4: Impact geometry of similar-sized collisions at initial contact in side view (top) and front view (bottom). Left column is for an impact angle $\theta = 30^\circ$, with the majority of the smaller body interacting with the larger one. In the right column $\theta = 45^\circ$, and the majority of the impactor "misses" the target. From Asphaug (2010).

target (figure 1.4, right column), then these events are referred to as *hit-and-run* because a substantial part of the impactor will remain intact.

Despite the diversity of collision outcomes, models that follow growth of bodies still mainly rely on simple collisions models. The wide range of initial conditions, body sizes that span over several orders of magnitude, impact angle and velocity leads to an extremely large parameter space. At the smaller scales, laboratory experiments can be performed, possibly under microgravity. At larger scales however this method is not applicable and therefore we must rely on numerical simulations. From the aggregate of the experimental and numerical results, theoretical relationships can be derived for common outcomes (principally the mass of the resulting bodies), known as *scaling laws*. These laws are based on dimensionless quantities and should therefore apply over a wide range of input parameters. This procedure has long been used for the small bodies, for instance to determine the collisional evolution of a population of asteroids in the main belt (e.g. Davis et al. 2002, for a review). More recently, it has been performed for planetary scale objects, e.g. Reufer (2011); Leinhardt and Stewart (2012). Those results can be implemented in N-body algorithms so that they can predict (with their limits) the variety of outcomes from the impact conditions (mass of the involved bodies, their relative velocity and angle) without the need a complex underlying model.

While in this section the focus has been on the resulting masses, it should be emphasised that collisions have diverse implications. Composition can change if two objects of different kind collide, or when a differentiated body is eroded, losing preferentially the upper layers (as shown in the *partial erosion* case in figure 1.3). In the presence of porosity, collisions can trigger compaction and affect the bulk density. A part of the kinetic energy is transformed into heat, increasing the temperature, and can cause the loss of volatile elements. Finally, angular momentum transfer will affect the object's rotation rate.

1.4 Thesis overview

The subject of this thesis is the study of collisions between relatively massive objects (greater than our Moon's mass) during the formation of planetary systems. The next chapter is thus devoted to the overall description of the formation process while chapter 3 describes the planet formation model that is used in this work. In chapter 4, the N-body method used to model gravitational interactions between the forming planets is described, and a problem of spurious outward migration when multiple massive planets are being formed in one system is investigated. Collisions detected by this N-body code are analysed in chapter 5. The effects of eccentricity and inclination damping as well as the method to determine the radius used for collision detection are investigated. Mass accretion from giant collisions is then analysed. The existing collision model is expanded by using the scaling-law approach of Leinhardt and Stewart (2012) for collisions between terrestrial planets. The consequences on the formation of planets are analysed.

On a second part, specific events are studied in more details. Chapter 6 introduces the physical background for the *Smoothed Particle Hydrodynamics* (SPH) technique with which we model the physics of collisions. The aim is to add a subset of the solid forces model (Benz and Asphaug 1994, 1995) to the code developed by Reufer (2011). Two components of the model (equation of state, density computation) are also discussed in more depth.

This method is applied to two specific events: a potential Moon-forming impact involving icy impactors (chapter 7) and a Moon-sized impactor colliding with a Mars-like object (chapter 8). The latter is part of a collaboration in order to couple the SPH impact model with a thermochemical model that can follow the long term effects on the planet's internal structure. We will show that the solid forces model is important even at this scale.

Chapter 2

Formation of planetary systems

Planets are thought to form inside proto-planetary disc, which forms along with the central star. The star and disc form from the collapse of a molecular cloud. Angular momentum conservation prevents the concentration of all material onto a single location (the one of the star), hence the presence of a disc. Star formation is a complicated process which has been subject to extensive research. The interested reader is referred to reviews about different aspects of star formation (Dobbs et al. 2014). For the following discussion, we assume that the star is already formed, and that a proto-planetary disc is present.

The occurrence rates of discs around young stellar objects (Mamajek 2009; Li and Xiao 2016) give two important information. The first is that most of young stars have a disc around them. The second comes the rate as function of the object's age, and relates to the lifetime of these disc, which has characteristic value of $\tau_{\text{disc}} \approx 2.7 - 3.3$ Myr. Only a small fraction of stars aged more than 10 Myr have been observed with a proto-planetary disc. This give a limit on the duration of the formation phase of giant, which cannot extend past the dispersal of the gaseous disc. Other key disc characteristics are the disc-to-star mass ratio ($\sim 0.5 - 1\%$) and the dust-to-gas ratio with the disc ($\sim 1\%$) (Andrews and Williams 2005, 2007).

As the star and the disc form out of the same material, they should have the same elemental abundances. However, the gas giants in the solar system show an enhanced fraction of heavy elements compared to the Sun, from a factor 5 for Jupiter to a few hundred for the ice giants. This implies that the planets accreted preferentially heavy elements compared to H-He, which lead to the *core accretion* (or *core instability*) paradigm, where first a core composed of heavy elements is built and, when a sufficient mass is reached, start to bind a gaseous envelope.

The following discussion is mainly based on Armitage (2009) and Benz et al. (2014).

2.1 Gas disc

Disc height is normally small compared to its radial extend, so the description of the disc is easiest in cylindrical coordinates (r, ϕ, z) . $z = 0$ refers to the disc midplane, and disc's behaviour is symmetric with respect to the latter. The vertical structure of the disc is

given by hydrostatic equilibrium

$$\frac{\partial p}{\partial z} = -\rho g_z \quad (2.1)$$

with p being the gas pressure, ρ its density and g_z the acceleration in the vertical direction. The acceleration is due to gravitation forces with the central star and the inner disc. As usually disc masses are small compared to the one of the central star, the former may be neglected for this purpose and we obtain

$$g_z = \frac{GM_\star}{(r^2 + z^2)^{3/2}} z \approx \Omega_k^2 z \quad (2.2)$$

with $\Omega_k = \sqrt{GM_\star/r^3}$ the Keplerian frequency. The approximation result from neglecting the z in the denominator as for thin discs $z \ll r$. In order to solve the hydrostatic equilibrium, an equation of state is required to relate p and ρ . A simple choice would be a locally-isothermal equation of state (i.e. the temperature does not depend on z), which despite not being entirely correct, permits to have a simple relation $p = \rho c_s^2$ and easily derive other quantities, with c_s the sound speed. In this case, equation (2.1) reduces to

$$\frac{1}{\rho} \frac{\partial \rho}{\partial z} = -\frac{\Omega_k^2}{c_s^2} z \quad (2.3)$$

whose solution is

$$\rho(z) = \rho_0 e^{-\frac{z^2}{2H^2}} \quad (2.4)$$

with $H = c_s/\Omega_k$ is the scale height of the disc. Constant temperature along the vertical direction is not generally correct, however this simple method permits to retrieve useful properties such as the vertical scale height H . In the general case, the disc is not isothermal in the vertical component, and a more sophisticated described must be used.

We now come to the radial description of the disc. The radial force balance is given by gravity a pressure gradient

$$\frac{v^2}{r} - \frac{GM_\star}{r^2} - \frac{1}{\rho} \frac{\partial p}{\partial r} = 0. \quad (2.5)$$

This implies that in the presence of a such gradient, the orbital and Keplerian velocities are not equal. If pressure decreases with distance then the contribution is directed outwards and thus a lower orbital velocity is needed, the gas will be *sub-Keplerian*, which is the most common case (except close to the inner boundary of the disc). The difference in orbital velocity due to the pressure gradient is small, so the general picture of a disc orbiting roughly at the keplerian velocity holds. This deviation will nevertheless be important for the solid component.

Different methods have been postulated for angular momentum transport. In the case of a Keplerian motion, the specific angular momentum

$$l = rv = \sqrt{GM_\star r} \quad (2.6)$$

increases with radius, which stabilises the disc. Angular momentum must therefore be transported outwards in order for material to flow inward.

In order to avoid a too great complexity, we will remove the dependency on the azimuthal and vertical coordinates. Averaged or integrated quantities will be defined. The principal one is the *surface density* defined as

$$\Sigma_g(r, \phi) = \int \rho(r, \phi, z) dz \quad (2.7)$$

then averaged over ϕ .

Inward material flow with outward angular momentum transport can be achieved with shear forces (Lynden-Bell and Pringle 1974). They derived the equation for radial gas flow

$$\frac{\partial \Sigma_g}{\partial t} = \frac{3}{r} \frac{\partial}{\partial r} \left(r^{1/2} \frac{\partial}{\partial r} (\tilde{\nu} \Sigma_g r^{1/2}) \right) \quad (2.8)$$

and $\tilde{\nu} = \int_{-\infty}^{\infty} \nu \rho dz / \Sigma_g$ is the vertically averaged (or effective) viscosity.

The steady state radial mass flow can be easily derived from this equation, assuming that both $\tilde{\nu}$ and Σ_g are independent of r . In this case the above equation reduces to

$$\frac{\partial \Sigma_g}{\partial t} = -\frac{3}{2r} \tilde{\nu} \Sigma_g \quad ; \quad \dot{M}_* = -2\pi r \frac{\partial \Sigma_g}{\partial t} = 3\pi \tilde{\nu} \Sigma_g \quad (2.9)$$

Taking the molecular viscosity $\nu \sim \lambda c_s$ (λ being the mean free path) fails to explain the observed disc evolution time scales by several orders of magnitude. Another source of viscosity must then be the source of angular momentum transport inside the disc. Following Shakura and Sunyaev (1973), a turbulent viscosity is postulated. It is parametrised as

$$\nu = \alpha_{\text{vis}} c_s H = \alpha_{\text{vis}} c_s^2 / \Omega_k \quad (2.10)$$

following that H is the smallest distance scale of the system (as $h \ll 1$) and that any velocity larger than c_s would be dissipated with shocks. α_{vis} is a non-dimension parameter with usual values in the range 10^{-5} to 10^{-2} . It has neither to be constant in space or in time, but for simplicity it usual is. The second equality holds in the case of an isothermal disc.

2.2 Solid disc

In addition to the gas, giant molecular clouds also contain dust particles, initially with sizes on the order of μm . Due to aerodynamic drag, these particles quickly settle to the disc's mid-plane and at the same time grow due to coagulation (Dullemond and Dominik 2005). For the next steps, there are concurrent effects on the dust particles: The aerodynamic drag, but now acting radially rather than vertically. From the gas disc discussion, we remember that the gas does not orbit exactly at the Keplerian velocity as a result of the presence of a pressure gradient. The solids, on the other side are not sustained by the pressure gradient and thus have to orbit at the Keplerian velocity. Hence, solids feel a head-wind as they orbit the star faster than the gas. A drag will result, and in the case the pressure diminishes with the radius (which is the case in most locations),

will drift inward. The drag regime depends on the particle size and the Reynold's number (Rafikov 2004). The stokes number

$$St = t_s \Omega_k \quad (2.11)$$

describes the coupling between the dust particles and the gas, with $t_s = mv_{\text{rel}}/|F_D|$ the stopping time due to the drag force F_D and m the mass of the particle and v_{rel} its relative velocity to the gas. When $St \ll 1$, particles are strongly coupled to the gas and when $St \gg 1$, they are almost not coupled to the gas. The maximum radial drift velocity is for $St \approx 1$. The corresponding sizes are in the range of centimetre to metre. Those particles have a drift time scale ($\tau_{\text{drift}} = r/v_r$) that can be as short as ~ 1000 yr and will then be rapidly accreted onto the star. Furthermore, the high radial velocities v_r of particles of these sizes, and the relative velocities between different sizes, the collisions lead to disruption rather than accretion (Dominik et al. 2007). The growth beyond the size of the metre becomes a challenge, as they rapidly drift inward and at the same time are prevented to grow further.

Scenarios have been proposed to overcome this *metre size barrier*; such as the direct formation of planetesimals from millimetre particles (e.g. Meheut et al. 2012) or the formation of fluffy planetesimals (Kataoka et al. 2013). Planets could also form directly from centimetre-sized objects (*pebbles*) that quickly drift inward (Bitsch et al. 2015).

2.3 Planetary embryos

The further growth into planetesimals and planetary embryos is easier to understand. Gravity plays an important role starting with sizes a few hundred metres, necessitating higher impact specific energies in order to disrupt them (e.g. Benz and Asphaug 1999) and enhancing the interactions with the other bodies (the central star, planets, other planetesimals). On the other hand, the gas drag is less important so the planetesimals do not rapidly drift inward.

The mass growth rate, assuming that collisions result in accretion, can be estimated as

$$\frac{dm}{dt} = \pi r^2 F_g \rho_s \sigma. \quad (2.12)$$

The first part of the right-hand side, πr^2 , is the geometrical cross section of the planetesimal assuming a spherical shape. In a constant density case, $r \propto m^{1/3}$. The next factor, F_g , is the enhancement of the capture cross-section due to gravitational perturbation that will attract other passing-by bodies, known as gravitational focusing. It is given as

$$F_g = 1 + \frac{v_{\text{esc}}^2}{\sigma^2} \quad (2.13)$$

with $v_{\text{esc}} \propto \sqrt{m/r} \propto m^{1/3}$ the escape velocity (see equation (5.3) for a correct definition) and σ the velocity dispersion. The last two factors give the mass flux of solids per unit surface that goes through the planetesimal. Assuming a constant velocity dispersion σ

results in the mass accretion rate being proportional to $m^{4/3}$, i.e. the accretion rate increases with time. This phase is called *runaway* growth.

As objects grow, the gravitational stirring of eccentricities and inclinations increases. When the proto-planet reaches a critical mass (Ida and Makino 1993), the runaway growth slows down. The most massive proto-planets will then grow slower, but nevertheless, proto-planets grow faster than planetesimals (Kokubo and Ida 1998). This is called the *oligarchic* growth. They deplete the surrounding planetesimals disc, stopping their accretion. The maximum mass than an object can attain is called the *isolation mass*, given as

$$m_{\text{iso}} = \frac{3}{\sqrt{3}} \pi^{3/2} C^{3/2} M_{\star}^{-1/2} \Sigma_s^{3/2} a^3 \quad (2.14)$$

with $C = 2\sqrt{3}$ the ratio between the planetesimals feeding zone and the Hill's radius (Lissauer 1993). The oligarchs are separated by $\sim 10r_{\text{H}}$ from each other (Kokubo and Ida 2002). The Hill's radius r_{H} is an important quantity which roughly gives is the distance from the planet until which it produces a bigger gravitational influence that the central star. It is defined as

$$r_{\text{H}} = a \sqrt[3]{\frac{m}{3M_{\star}}} \quad (2.15)$$

with a the semi-major axis of the body and m its mass.

2.4 Giant planets

Terrestrial planets are formed from embryos that were not massive enough to accrete gas while the gaseous disc was still present. For the giant planets, two main paradigms exist

- *Core accretion* or *Core instability* (Mizuno 1980), where first a solid core is formed as for the terrestrial planets, but on a shorter time scale. When the core attains a sufficient mass (typically a few Earth masses), then the planet starts to accrete a substantial amount of gas.
- *Disk instability* or *Gravitational instability* (Boss 2003), where a part of a massive disc is unstable against its own self-gravity and collapses to directly form a planet.

In the core accretion paradigm, the giant planets form initially in the same way as terrestrial ones. There are then three stages:

- The planet accretes mostly solids. The low mass does not permit to gravitationally bind a surrounding gaseous envelope. This is the continuation of the oligarchic growth that forms terrestrial planets. It ends when the supply of solids has been exhausted.
- If the planet could reach a mass of $\sim M_{\oplus}$ during the first stage, it is able to start gravitationally binding gas. The gaseous envelope enhances the capture radius, as friction reduces the relative velocities between the planet and the surrounding planetesimals. The planet thus has access to larger supply of material than if

didn't have an envelope. The presence of an envelope permits the planet to grow further. Solids and gas are concurrently accreted. Their in fall leads to the release of gravitational energy, which has to be removed from the planet by radiation. The energy flux increases the gas temperature relative to the surrounding disc and thus expand it. The accretion of gas is thus governed by the ability of the planet to remove the gravitational energy. The boundary between the envelope and the disc is continuous, which

- The runaway gas accretion phase. The accretion rate of solids drops again, decreasing the energy flux from the core. The gas accretion rate eventually gets limited by the disc. When the planet accretes gas faster than the gas disc can supply, then there is no longer a continuity between the disc and the envelope. This is the *detached* phase.

The change to the *detached* phase may also occur at the end of the formation process when the gas disc vanishes.

When the envelope is in equilibrium with the disc, we need to set the transition between the two. Two criterion can be given to asses the extend where the gas is affected by the presence of the planet: the Hill's equation (2.15) and the *Bondi* radius

$$r_{\text{acc}} = \frac{Gm_t}{c_s^2} \quad (2.16)$$

which defines the distance at which gas molecules will escape the gravitational potential of the planet due to only their thermal velocity $v_{\text{th}} = \sqrt{2k_bT/(\mu m_H)}$. Thus the gas orbiting further than either of these two limits is not bound to the planet. The outer radius may then be retrieved by taking the minimum of the two quantities

$$r_{\text{out}} = \min(r_H, r_{\text{acc}}). \quad (2.17)$$

In order to compute the gas mass present in the envelope, the following differential equations for its internal structure are solved, assuming spherical symmetry (e.g. Bodenheimer and Pollack 1986)

$$\frac{\partial m}{\partial r} = 4\pi r^2 \rho \quad (2.18)$$

$$\frac{\partial p}{\partial r} = -\frac{Gm(r)\rho}{r^2} \quad (2.19)$$

$$\frac{\partial T}{\partial p} = \max(\nabla_{\text{ad}}, \nabla_{\text{rad}}) \quad (2.20)$$

$$\frac{\partial L}{\partial m} = \varepsilon - T \frac{\partial S}{\partial t} \quad (2.21)$$

The first equation is simply mass conservation. Here $m(r)$ denotes all the mass enclosed within a radius r . The second one the hydrostatic equilibrium rewritten to replace g by its direct expression. The third one gives the temperature gradient due to energy transport. The Schwarzschild criterion is used to determine whether it occurs due

to radiative transport or convection. For an ideal gas, we have $\nabla_{\text{ad}} = (1 - \gamma)/\gamma$ and $\nabla_{\text{rad}} = (\partial T/\partial r)_{\text{rad}} (\partial r/\partial p)$ with the first partial derivative can easily be deduced from equation (A.2) and the second one is the inverse of equation (2.19). The last equation gives energy conservation; ε is a source term due to energy deposition by accretion of solids. The second terms accounts for the energy released by the contraction of the envelope. This is more clearly understandable if this term is rewritten following the first law of thermodynamics

$$dU = TdS - pdV \quad \rightarrow \quad T \frac{\partial S}{\partial t} = \frac{\partial U}{\partial t} + p \frac{\partial V}{\partial t}. \quad (2.22)$$

Boundary conditions are given at the interface with the disc for the pressure and temperature. Mass is known at the core-envelope boundary $m(r_c) = m_c$ as for the luminosity due to the accretion of solids

$$L_{\text{acc}} = \frac{Gm_c \dot{m}_c}{r_c}. \quad (2.23)$$

2.5 Terrestrial planets

The formation of terrestrial planets follows the same principle as the core of the gas giants. They are bodies that did not grow to a sufficient mass in order to bind some gas while the gaseous disc is still present. In the inner part of the disc, the accretion is fast but limited by the isolation mass, unless migration occurs. This result in a population of small bodies in the range of lunar to Mars size. In the outer part of the disc, the time scale for the accretion of solid is long, and proto-planets cannot reach a sufficient mass before the disc's dispersal. In the contrary to gas giants, the formation of terrestrial planets can continue after the dispersal of the gas disc. Their eccentricities and inclinations are no longer being damped, and will be pumped by self-stirring and interaction with the giant planets. Planetesimal-driven migration (e.g. Fernandez and Ip 1984; Minton and Levison 2014) can still change planets' orbit at those times.

2.6 Interactions

2.6.1 With the disc

The presence of a planet inside the gaseous disc will alter its structure. The perturbation will create dynamical features that will spread along the disc, and these features in turn will have a feedback onto the planet. This leads to energy and angular momentum exchange between the planet and the disc, which affects the planet by making it migrate (change of semi-major axis) as well as damp its eccentricity and inclination relative to the disc.

There are observational evidences in favour of migration; two of them will be mentioned here. First, giant planets found close to their star (hot Jupiters) cannot form from only the surrounding disc material, as there only a tiny fraction of the disc mass located

so close to the star. These planets must therefore have access to material coming from further away from the star, implying that either

- form where they are currently but from material that drifts inwards, or
- form further away in the disc, typically just beyond the ice line, and then migrate inwards to the location where they are observed.

The second evidence is that for various multi-planetary systems, the period ratio of consecutive planets is close to the ratio of two small integer number (e.g. Fabrycky et al. 2014, for results from *Kepler* space observatory). These are called *mean-motion resonances* (MMR) and are mostly believed to be the remnant of convergent migration between planets.

For the planets not massive enough to significantly alter the local disc structure, migration speed is roughly proportional to its mass (Ward 1997). This is called *Type I* migration. As the planet grows, its perturbation on the surrounding disc increases and the planet gives angular momentum to the gas outside while taking some from the inside disc, which has the effect of opening a gap (Lin and Papaloizou 1979; Goldreich and Tremaine 1980). The further migration is linked to the viscous evolution of the disc (Lin and Papaloizou 1986a,b), which is called *Type II*.

2.6.2 Between planets

There are various effects of having multiple planets forming concurrently in the same system (Alibert et al. 2013, and references therein). They include the concurrent accretion of solids and gas for planets that have their feeding zone touching each other. The perturbations produced by the presence of a planet inside the disc will affect the other ones. Gravitational interactions between the forming planet increase along with their mass, and work in the same way as between the planetesimals. They include

- Mutual excitation of eccentricity and inclination. These are damped while the gas disc is present, but can affect the shape of the system after the formation phase.
- Convergent migration lead to trapping planets mean-motion resonances. This forces planets to migrate together, possibly avoiding collision.
- Close encounters, which depending on the distance at closest approach may end in collisions or scattering events.

Chapter 3

The *Bern* model of planetary system formation

To model the formation of planetary systems, we will use the *Bern* model (Alibert et al. 2004, 2005), which is discussed in this chapter, except for the part about gravitational interactions between the planets (N-body) which takes place in the next chapter. This model will be used for the study of collisions in forming planetary systems (chapter 5).

All the sections except the last one describe the methods to model the formation of a single system. To statistically compare it with the observed exoplanets, the model is used to generate a population synthesis of planets. The parameters are determined using a Monte Carlo approach depicted in section 3.4, which are used to set the initial disc profile and embryos location.

The *Bern* formation model is based on the core accretion paradigm, where planet can accrete simultaneously solids and gas (Pollack et al. 1996). A fixed number of planetary embryos roughly of the Moon's mass $M_{\text{emb}} = 0.0123 M_{\oplus}$ consisting only of solids are randomly placed in the innermost 20 AU of the disc (with an equivalent probability in log of the distance). The growth of the embryos is modelled self-consistently with the evolution of the gas and solid discs. Interactions with the gas disc cause exchange of angular momentum and energy, which leads to migration.

3.1 Disc

The model assumes an axisymmetric disc and so the angular component ϕ will be neglected. The equations governing the vertical disc structure of the gas disc are provided in appendix A. In our model, we do not solve them; instead the relevant quantities are interpolated in a table in function of r and Σ_g , and the surface density evolution is computed according to equation (2.8) with additional term for the accretion onto the planets (see next section) and for photo-evaporation.

The initial surface density profile is given by a power law with exponential cut-off

$$\Sigma_g(r, t = 0) = \Sigma_0 \left(\frac{r}{r_0} \right)^{-\beta} e^{-(r/r_{\text{cutoff}})^{2-\beta}} \quad (3.1)$$

with Σ_0 the gas surface density at the reference location $r_0 = 5.2$ AU, β the power law index, and r_{cutoff} the cut-off radius. The relation between Σ_0 and the total disc mass is given by

$$M_{\text{disc}} = \frac{2\pi\Sigma_0}{2-\beta} \left(\frac{1}{r_0}\right)^{-\beta} \left(\frac{1}{r_{\text{cutoff}}}\right)^{\beta-2} \quad (3.2)$$

For the solids disc, planetesimals are not directly simulated; instead a statistical approach is adopted. The used quantities are Σ_s , the surface density of solids, e_p and i_p , the RMS of their eccentricity and inclinations. As for the gas disc, the quantities depend only on the radius. All the planetesimals are assumed to have a radius $r_p = 300$ m; no fragmentation or growth of the planetesimals occur. The initial surface density of solids is taken as

$$\Sigma_s(r, t = 0) = \Sigma_g(r, t = 0) f_{D/G} f_{R/I}(r) \quad (3.3)$$

with $f_{D/G}$ the dust to gas ratio and $f_{R/I}(r)$ is the rock to ice mass ratio, which we take as a step function

$$f_{R/I}(r) = \begin{cases} 1 & r < a_{\text{ice}} \\ 4 & r > a_{\text{ice}} \end{cases} \quad (3.4)$$

following Hayashi (1981). a_{ice} is the location of the water ice line and computed as the location where the disc mid-plane conditions cross the condensation line (approximately 160 K for the pressures found in protoplanetary discs). Only water ice is considered in our model, there are however various volatile specific with different condensation temperature. Each compound will condense at a different location, and the surface density will therefore be more complex.

The radial drift is not included in model, so the time evolution of the surface density is only given by the accretion onto the planet (and the related ejection) for region located inside the feeding zones (see next section). On the other hand, the distributions of planetesimals' eccentricity and inclination are evolved following the model of Fortier et al. (2013) with

$$\frac{\partial e_p^2}{\partial t} = \frac{\partial e_p^2}{\partial t} \Big|_{\text{drag}} + \frac{\partial e_p^2}{\partial t} \Big|_{\text{VS,e}} + \frac{\partial e_p^2}{\partial t} \Big|_{\text{VS,p}} \quad (3.5)$$

$$\frac{\partial i_p^2}{\partial t} = \frac{\partial i_p^2}{\partial t} \Big|_{\text{drag}} + \frac{\partial i_p^2}{\partial t} \Big|_{\text{VS,e}} + \frac{\partial i_p^2}{\partial t} \Big|_{\text{VS,p}}. \quad (3.6)$$

The first term is the drag from the gas disc which damps both the eccentricities and inclinations as described above; the two others are the viscous stirring terms for planetary embryos-planetesimals and planetesimal-planetesimals interactions.

3.2 Planets

The model assumes that the forming proto-planets have a solid core at the centre surrounded by an envelope made purely of hydrogen and helium. In reality, solid material from the accreted planetesimals would also be deposited in the envelope due to ablation.

This have mainly two consequences: the mean molecular weight of the atmosphere would be higher, thus reducing its scale height and the opacity would also change due to the higher content of dust. This was studied by Venturini (2016), but not applied to the formation model.

The solids are accreted by either collision with the core's surface (when no or only a small envelope is present) or by friction while going through the envelope (Mordasini 2004). The cross section is then set by the capture radius r_C . Its physical representation is that any planetesimal located closer to the planet than this value will be accreted by the planet. According to Inaba et al. (2001), the solid accretion rate is given by

$$\dot{m}_c = \left(\frac{2\pi\Sigma_s r_H^2}{P} \right) P_{\text{coll}} \quad (3.7)$$

with $P = 2\pi/\Omega_k$ the orbital period of the planet and P_{coll} the collision probability with planetesimals. The latter depend on the collision radius between the planet and a planetesimal ($r_C + r_p$) with r_p the radius of the planetesimal, the Hill's sphere radius as well as $\tilde{e}_p = ae_p/r_H$ and $\tilde{i}_p = a_p/r_H$, the reduced eccentricity and inclination of the planetesimals.

Here Σ_s is the mean surface density of solids within the planet's feeding zone. To determine it, we must first calculate radial extend of the feeding zone, which is given in addition to the Hill's radius, by the eccentricities of both the planet itself and of the planetesimals. The width of the planetesimals feeding zone is affected by their eccentricity and so is modified to

$$r_F = r_H \sqrt{C^2 + \tilde{e}_p} \quad (3.8)$$

Given the planet's eccentricity e , the distance from the star varies from $r_- = a(1 - e)$ to $r_+ = a(1 + e)$ during one period. Combining the two, the feeding extend radially between $(r_- - r_F)$ and $(r_+ + r_F)$. The planet's eccentricity, in our model does not increase the accretion rate (at least initially), but rather allows it to cover a larger radial extend of the disc. The result is that with a greater eccentricity, the feeding zone will be depleted at a slower rate, the enabling the planet to obtain a more massive core on the long term.

Core radius is given following Valencia et al. (2010)

$$r_c = 9800 \text{ km} \left(\frac{m_c}{5 M_\oplus} \right)^{(0.28+0.02\sqrt{m_c/5 M_\oplus})} 10^{(-\log_{10}(1+p_c\sqrt{m_c/5 M_\oplus}))^3} \quad (3.9)$$

with p_c is the envelope pressure at the core-envelope boundary.

Envelope structure Now we come the envelope structure. In contrary of the solid part, the planet's eccentricity is neglected, and all the disc properties are taken at the planet's semi-major axis. Also they are the ones of the midplane.

The outer planet radius is computed with

$$r_{\text{out}} = \frac{1}{\frac{1}{k_1 r_{\text{acc}}} + \frac{1}{k_2 r_H}} \quad (3.10)$$

with $k_1 = 1$ and $k_2 = 1/4$ following Lissauer et al. (2009) who found that gas parcels further away than $\sim r_H/4$ to $\sim r_H/3$ are not bound to the planet and will eventually return to the gas disc. To determine the envelope mass, the structure equations are solved with the simplification that equation (2.21) is left out and instead constant luminosity throughout the envelope is assumed. The equation of state $\rho(p, T)$ is taken from Saumon et al. (1995). Boundary condition and the range of integration are as follow: core's mass m_c and radius r_c are known. In the attached phase, we know the outer radius r_{out} but not the total mass m_t . Pressure and luminosity are derived from disc's values with

$$p_{\text{out}} = p_{\text{disc}}(a), \quad (3.11)$$

$$T_{\text{out}} = \sqrt[4]{T_{\text{disc}}^4(a) + \frac{3\tau_{\text{out}}L_{\text{out}}}{8\pi\sigma r_{\text{out}}^2}}. \quad (3.12)$$

The independent variable is thus selected as the radius as this is the only one known on both ends. Then, two quantities are known at the outer edge (p and T) while the mass is at the inner edge. The wanted result is the total mass. Its value will be determined using a shooting method: its value will be guessed, which incidentally allows to compute the total luminosity L_{out} , then the set of differential equation integrated from r_{out} to r_c which will give m_c' . This result is compared to the true core mass m_c ; when the two match, then the correct value of m_t has been found. To be able to solve the equations, we must still give the luminosity, which is basically the time derivative of the energy $L = -\partial E/\partial t$, or since we have a discrete model we will compute as the variation of energy across one time step using

$$L_{\text{out}} = -\frac{E'_{\text{tot}}(t + \Delta t) - E_{\text{tot}}(t)}{\Delta t} \quad (3.13)$$

with Δt the time step and where the time $t + \Delta t$ is the epoch of the new structure being computed. The total energy can be calculated from the internal structure with

$$E_{\text{tot}} = -\frac{3}{5}\frac{Gm_c^2}{r_c} + \frac{1}{2}\sum_{i=1}^{n-1}(m_{i+1} - m_i)\left(u_i + u_{i+1} - G\left(\frac{m_{i+1}}{r_{i+1}} + \frac{m_i}{r_i}\right)\right) \quad (3.14)$$

where the first term is gravitational binding energy of the core and the sum iterate over all shells of the envelope for both the internal and gravitation binding energies. The different indexed quantities are the value at each location r_n and the first index is located at the core-envelope boundary, i.e. $m_1 = m_c$ and $r_1 = r_c$ whereas the last ones are at the outer edge so $m_n = m_t$ and $r_n = r_{\text{out}}$. One can see that a difficulty arises here: the total energy depends on the envelope structure, but at the same time the luminosity is required to compute the structure. This implies that the new energy has to be guessed. We here follow the simplified method introduced by Mordasini et al. (2012) with some adjustments. The real total energy is linked to the gravitational binding energy of the whole planet (assuming a constant density) so that the factor between the two is

$$\xi(t) = \frac{E_{\text{tot}}(t)}{\frac{Gm_t^2(t)}{r_{\text{out}}(t)}} \quad (3.15)$$

which can be computed at time t since the structure is known (note that the factor $-3/5$ has been left out) and then used to estimate the new total energy

$$E'_{\text{tot}}(t + \Delta t) = \xi(t) \frac{Gm_t^2(t + \Delta t)}{r_{\text{out}}(t + \Delta t)}. \quad (3.16)$$

This neglect the change of ξ during the time step. This change is small compared to the ones of mass and radius but nevertheless there are a couple of issues here. First, the luminosity is computed from the change rate of energy, so even if the error in the energy is small, it can induce a big one in the luminosity. Energy must be retrieved with a sensible accuracy. A couple of method are available to solve this issue: one could iterate over ξ to find the correct value as once the structure has been computed, the corresponding ξ is available. This add an additional convergence loop and so does the difficulty of the problem to solve. The second method is to obtain the true total energy once the structure is found, which enables the retrieve the *true* luminosity of the planet a posteriori, and thus to determine the correction factor that should be applied to the guessed luminosity. This method is similar that to apply a first order correction on the change of ξ over time. The second big issue here is the value of $r_{\text{out}}(t + \Delta t)$. This is more a numerical problem: the point is when the planet's semi-major axis varies so does the outer radius. For instance, it is linked to the sound speed in the gas disc. To mitigate these variations that are not linked to the mass growth, one can estimate the new outer radius from the old one, taking only into account the increase of the Hill's sphere due to the accretion of material

$$r'_{\text{out}}(t + \Delta t) = r_{\text{out}}(t) \sqrt[3]{\frac{m_t(t + \Delta t)}{m_t(t)}} \quad (3.17)$$

which is used for the purpose of computation of equation (3.16). The model assume that the luminosity is constant throughout the envelope. This is of course not correct, as the energy is deposited all along the envelope. The energy transport at every layer is then equal to the one of the energy deposited deeper. An easy way to determine a luminosity profile, is to compute the luminosity at the core-envelope boundary, and then to assume a linear relationship between the luminosity and the envelope mass. The core energy a a few contributions, first due to the accretion of solids onto the core (equation (2.23)) and second from its contraction. As we can see with its equation of state (equation (3.9)), it will contract with increasing envelope pressure which release energy into the core

$$L_{\text{cont,core}} = -\frac{3}{5} Gm_c^2 \left(\frac{1}{r_c^2} - \frac{1}{(r'_c)^2} \right) \quad (3.18)$$

with r_c the current core radius, consistent with the equation of state and $r'_c(t + \Delta t) = m_c(t) \sqrt[3]{m_c(t + \Delta t)/m_c(t)}$ is the radius the core would have with the new mass, the density from the previous step. The core luminosity is the $L_{\text{core}} = L_{\text{acc}} + L_{\text{cont,core}}$. Note that with these method, both core accretion and core contraction energy term are already taken into account in L_{out} , so the considerations here do not affect the calculation of the

total energy. There are however other sources of luminosity which are not included in either of the two quantities here: the radiogenic luminosity, coming from the decay of radioactive isotopes, such as ^{26}Al and the deuterium fusion (Mollière and Mordasini 2012) that happen in the envelope for sufficiently massive planets.

Maximum gas accretion rate With the new envelope structure, it is now possible to compute the gas accretion rate $\dot{m}_e = (m_e(t + \Delta t) - m_e(t))/\Delta t$ with $m_e(t) = m_t(t) - m_c(t)$ the mass of the envelope. The supply from the disc is limited by a few conditions. However, when the disc is depleted, the accretion rate should equilibrate with the radial mass flow of the disc. The equilibrium flow is given by equation (2.9), but the presence of a planet disturbs the radial disc profile and so the non-equilibrium rate

$$\dot{M}_{\text{disc}} = 3\pi\tilde{\nu}\Sigma_g + 6\pi r \frac{\partial\tilde{\nu}\Sigma_g}{\partial r} \quad (3.19)$$

has to be taken into account. The second term in the equation is the first order correction in case ($\tilde{\nu}\Sigma_g$) varies with radius. This value is evaluated both $r_{\pm} = a \pm 1/2r_{\text{H}}$ to account for the flow geometry (gas flows inwards in the inner part of the disc and outwards in the outer part), so the maximum gas accretion rate is

$$\dot{M}_{e,\text{Flow}} = \left| \min\left(\dot{M}_{\text{disc}}(r_-), 0\right) + \max\left(\dot{M}_{\text{disc}}(r_+), 0\right) \right| \quad (3.20)$$

which takes into account the outward flow inside the planet and the inward flow outside it. It should be noted that the fact the planet migrates (see next section) has not been considered here. In the case of the old model for type II migration, where the planet follows the gas, then actually no gas at all should be accreted by the planet. Another limit is set by the Bondi rate

$$\dot{M}_{e,\text{Bondi}} = \pi r_{\text{out}}^2 \rho_{\text{disc}} v_{\text{rel}} \quad (3.21)$$

which gives the mass flux of gas going through the planet. The v_{rel} term is the relative velocity between the gas and the planet. The final maximum gas accretion rate is then set by

$$\dot{m}_{e,\text{max}} = k_{\text{lub}} \max\left(\dot{M}_{e,\text{Bondi}}, \dot{M}_{e,\text{Flow}}\right) \quad (3.22)$$

with $k_{\text{lub}} = 0.9$ is a factor that takes into account that part of the gas flows past the planet (Lubow and D'Angelo 2006).

Once the required gas accretion needed to maintain the hydrostatic equilibrium throughout the envelope until the outer radius is greater than what the disc can supply, the outer region of the envelope will be depleted in gas and thus begins to contract. The gas accretion rate is now set by the disc properties rather by the planet itself. As consequence for the structure model of the envelope, the unknown quantity changes. Before, the radius was known and the mass was searched for, now the mass is known and the radius is searched for. The general idea to determine the radius remains the same, except for the

swap in the quantity used for the iteration. The boundary conditions are also slightly modified

$$p_{\text{out}} = p_{\text{disc}}(a) + \frac{\dot{m}_e v_{\text{ff}}}{4\pi r_{\text{out}}^2} + \frac{2g}{3\kappa} \quad (3.23)$$

$$T_{\text{out}} = \sqrt[4]{(1-A)T_{\text{disc}}^4(a) + \frac{3\tau_{\text{out}}L_{\text{out}}}{8\pi\sigma r_{\text{out}}^2}}. \quad (3.24)$$

The middle term of the pressure is the pressure generated by the gas free falling from the disc onto the planet surface, with $v_{\text{ff}} = \sqrt{Gm_t(1/r_{\text{out}} - 1/r_{\text{H}})}$ the gas velocity when it reaches the planet's surface. The last one is the photospheric pressure with g the acceleration due to gravity on the planet surface. The boundary conditions for the temperature only changes slightly, with now the albedo A being effective.

3.3 Migration

Migration is due to angular momentum exchange with the gas disc. The force acting on the planet is the result of the gravitational attraction with every gas parcel of the disc. As our model contains only a one dimensional description of the gas disc, it is impossible to compute self-consistently the disc-planet interaction. Instead, the migration rates are computed from laws derived from numerical hydrodynamical simulations. The migration rates are then converted into time scales, which are provided to the N-body (see chapter 4) in which they will be used to set the additional forces acting onto the planet. They are defined as

$$\tau_{\text{mig}} = -\frac{a}{\dot{a}}, \quad \tau_e = -\frac{e}{\dot{e}} \quad \text{and} \quad \tau_i = -\frac{i}{\dot{i}}. \quad (3.25)$$

Type I migration For small mass planets, up to about $10 M_{\oplus}$ (though this depends also on disc parameters, such as the turbulent viscosity factor α_{vis}), the planet is embedded in the disc. This is the so-called *type I* migration. In this regime, the torques are usually expressed in units of a reference torque given by

$$\Gamma_0 = \left(\frac{q}{h}\right)^2 \Sigma_g a^4 \Omega_k^2 \quad (3.26)$$

with $q = m_t/M_{\star}$ the mass ratio between the planet and the central star and $h = H/r$ the disc aspect ratio. This torque can then be converted into a migration time scale with the relation

$$\tau_{\text{mig},0} = -\frac{1}{2} \frac{h^2}{q} \frac{M_{\star}}{\Sigma a^2} \Omega_k^{-1} \quad ; \quad \tau_{\text{mig},1} = \tau_{\text{mig},0} \left(\frac{\Gamma_0}{\Gamma}\right). \quad (3.27)$$

As a note, the migration time scale depends on the planet's mass through the q parameter. So, for a constant Γ/Γ_0 factor, the migration velocity increases linearly with the planet's mass.

The following results are taken from Paardekooper et al. (2010, and references therein). They use discs with profiles for surface density and temperature given as power laws. For the purpose of the following formula, these indices are retrieved from the actual profiles of our disc by numerically evaluating the following derivatives at the planet's location

$$\alpha = -\frac{\partial \ln \Sigma_g}{\partial \ln r} \quad ; \quad \beta = -\frac{\partial \ln T}{\partial \ln r}. \quad (3.28)$$

In type I migration, the planet generates two main perturbations onto the disc: wakes which are spiral waves and in the co-rotation region. The wakes are positive density perturbation which propagate radially. Their angular frequency is given by the local gas, so the inner arm is leading the planet and the outer one trailing. Along the path of the wake, the density increases, and thus they exert a greater gravitational force than the remaining of the gas disc, with the inner part giving a positive torque (favouring outward migration) and the outer part a negative torque (favouring inward migration). The total net torque due to wakes is the sum of the two components. It turns out that the two wakes are not symmetric, neither in the amount of the density perturbation nor in the location where they exert the strongest influence. The outer wake produces a stronger torque and the migration due to wakes is normally inwards. In our model, its contribution is given by (Paardekooper et al. 2010)

$$\gamma \frac{\Gamma_L}{\Gamma_0} = -2.5 - 1.7\beta + 0.1\alpha, \quad (3.29)$$

with the subscript L standing for Linblad torque.

Another contribution of the disc on small mass planets is the co-rotation torque. It is due to angular momentum exchange with gas parcels that travel on a horseshoe orbit (as seen from a frame co-rotating with the planet). As for the wakes, the behaviour is not symmetric with respect to the planet's location, and thus a net torque is created. However, there are different regimes depending on the predominant time scales acting in the co-rotation region. The co-rotation torque acts due to entropy and potential vorticity gradients in the region and works while redistributing them. The time scale for this process is given by the time needed for a libration of a gas parcel inside the co-rotation region, that we note τ_{lib} . On the other hand, there are mechanisms that still try to restore the entropy and potential vorticity gradients, such as viscous diffusion which acts on a time scale τ_{visc} . If viscous diffusion acts faster than the equalisation mechanism, then the gradients remain and the co-rotation torque is not reduced. However, when the opposite holds, then the gradients within the co-rotation region are reduced and so is the co-rotation torque. In the latter case, the reduction of the co-rotation component is according to Dittkrist et al. (2014) using

$$\Gamma_{\text{sat}} = \frac{\Gamma_{\text{unsat}} - \Gamma_L}{s_2} + \Gamma_L \quad (3.30)$$

with $s_2 = \tau_{\text{visc}}/\tau_{\text{lib}}$. Γ_{unsat} is the total torque of the type I migration without saturation, so the factor s_2 only affects the component not in Γ_L .

For the angular momentum transfer while a gas parcel is performing the U-turn close to the planet, there are again two different regimes. In the case the time required to perform the U-turn, τ_{turn} , is small compared to the time required for the cooling of the air parcel, τ_{cool} , then the process is adiabatic as the entropy remains constant. Opposite to this, when cooling is more rapid than the U-turn time, then the temperature of the gas parcel equilibrates with the surrounding disc and the process is isothermal. The transition between the two regimes is modelled using

$$\Gamma_{\text{unsat}} = z\Gamma_{\text{isoth}} + (1 - z)\Gamma_{\text{adia}} \quad (3.31)$$

$$z = 1 - \frac{s_1^4}{1 + s_1^4} \quad (3.32)$$

with $s_1 = \tau_{\text{cool}}/\tau_{\text{turn}}$. When $\tau_{\text{cool}} \ll \tau_{\text{turn}}$, the torque is essentially given by Γ_{isoth} , the isothermal case. On the contrary, when $\tau_{\text{cool}} \gg \tau_{\text{turn}}$, the torque is now given by Γ_{adia} . These two torques are now given by

$$\frac{\Gamma_{\text{isoth}}}{\Gamma_0} = -2.5 + 0.5\beta + 0.1\alpha - 1.4\beta + 1.1 \left(\frac{3}{2} - \alpha \right) \quad (3.33)$$

$$\gamma \frac{\Gamma_{\text{adia}}}{\Gamma_0} = -2.5 - 1.7\beta + 0.1\alpha + 1.1 \left(\frac{3}{2} - \alpha \right) + 7.9 \frac{\xi}{\gamma} \quad (3.34)$$

with $\xi = \beta - (\gamma - 1)\alpha$ the radial entropy gradient. The time scales τ_{visc} , τ_{lib} , τ_{cool} and τ_{turn} according to Dittkrist et al. (2014, and references therein).

Gap formation and type II migration As the planet grows, the wakes eventually become shocks. They will damp the wakes and transfer energy and angular momentum to the disc. This will also cause material to be transferred away from the planet. Crida et al. (2006) developed a criterion to determine when the gas surface density drops to 10% of its initial value,

$$\frac{h}{\sqrt[3]{q}} + \frac{50\alpha_{\text{vis}}h^2}{q} < 1. \quad (3.35)$$

Once this criterion is fulfilled, it is assumed that the migration changes to type II. The original approach was that the planet's radial velocity is equal to the one of the gas due to viscosity

$$v_r = -\frac{3\nu}{2r} \quad ; \quad \tau_{\text{mig},2} = -\frac{r}{v_r} = \frac{2r^2}{3\nu} \quad (3.36)$$

When the planet mass is higher than the mass of the disc inside the location of the planet, then the contribution of the planet on the mass of the outer disc is no longer negligible (Hasegawa and Ida 2013). In this case, the radial velocity is limited by the mass of the planet compared to the approximate inner disc mass derived from the local gas surface density with

$$v_r = -\frac{3\nu}{2r} \min \left(1, \frac{2\pi r^2 \Sigma_g}{m_t} \right). \quad (3.37)$$

Note that the approach here is not consistent with the latest results. Dürmann and Kley (2015) found that the type II migration does not depend on the viscous inflow velocity, and the migration rate may be faster and the viscous one depending on disc conditions. Also, the general picture that gas cannot cross the gap has been found to be erroneous. The formula used here should therefore be corrected to reflect these new results.

Eccentricity and inclination damping As already stated above, the presence of a disc also leads to damping of eccentricity and inclination. For the type I migration, the original model is using the formula from Fogg and Nelson (2007),

$$\tau_e = \tau_i = \frac{Q_e}{0.78} \frac{M_\star}{m_t} \frac{M_\star}{\Sigma_g a^2} h^4 \left(1 + \frac{1}{4} \left(\frac{e}{h} \right)^3 \right) \Omega_k^{-1} = -\frac{Q_e}{0.39} \left(h^2 + \frac{1}{4} \frac{e^3}{h} \right) \tau_{\text{mig},0} \quad (3.38)$$

with $Q_e = 0.1$ an efficiency factor. A slightly more elaborate method to determine the damping time scales is to use the fits from Cresswell and Nelson (2008). Their results are given in terms of the damping time scale from Tanaka and Ward (2004)

$$t_{\text{wave}} = \frac{M_\star}{m_t} \frac{M_\star}{\Sigma_g a^2} h^4 \Omega_k^{-1} = -2h^2 \tau_{\text{mig},0} \quad (3.39)$$

and their fits are then

$$\tau_e = \frac{t_{\text{wave}}}{0.780} (1 - 0.14\tilde{e}^2 + 0.06\tilde{e}^3 + 0.18\tilde{e}\tilde{i}^2) \quad (3.40)$$

$$\tau_i = \frac{t_{\text{wave}}}{0.544} (1 - 0.30\tilde{i}^2 + 0.24\tilde{i}^3 + 0.14\tilde{i}\tilde{e}^2) \quad (3.41)$$

with $\tilde{e} = e/h$ and $\tilde{i} = i/h$ the scaled planet's eccentricity and inclination. One can note that the behaviour between damping and migration time scales is of $\mathcal{O}(h^2)$ and $h \approx 0.05$. This implies that the eccentricity and inclination damping occur on shorter time scales than migration. In the case of type II migration, this is not well constrained. The previous argument that damping is more efficient than migration and that they are related is kept. We adopt in this case

$$\tau_e = \tau_i = \frac{|\tau_{\text{mig}}|}{10}. \quad (3.42)$$

3.4 Population synthesis

The purpose of our formation is not to reproduce single systems. Instead, the idea is to model the formation of a large set (a few hundreds) of systems and then to perform statistical analysis. Initial conditions for the different systems are chosen using a Monte Carlo method. We will here just give a brief overview of the method, as it will be used in this thesis to simulate different sets of planetary systems. A detailed description of the technique is provided in Mordasini et al. (2009).

The following variables are selected with the Monte Carlo method:

- The dust-to-gas ratio $f_{\text{D/G}}$.

- Initial gas disc properties: the reference surface density of gas Σ_0 , the power law index of β the inner radius and the exponential cutoff radius r_{cutoff} . Those values are selected from one of the twelve systems observed by Andrews et al. (2010). The disc mass is converted into reference density using equation (3.2).
- The external photo-evaporation rate $\dot{\Sigma}_{\text{wind}}$, calculated so that the modelled systems have roughly the same life time as observation (with a maximum of 15 Myr).
- The starting location of the embryos. In the nominal model, there are initially 10 of them, with the semi-major axis equally distributed in log between 0.2 and 20 AU. It is also checked that the local isolation mass m_{iso} is greater than the initial mass of the embryo m_{emb} and two embryos within a single system may be closer than $10r_{\text{H}}$.

There are other model parameters which are kept constant within a population:

- The turbulent viscosity parameter α_{vis} . In all the populations presented in this thesis, we set $\alpha_{\text{vis}} = 2 \cdot 10^{-3}$.
- The mass of the central star. As we aim to model planetary formation around Sun-like star, we use $M_{\star} = 1 \text{ M}$.

Chapter 4

N-body and migration problem

Planets gravitationally interact with the disc and between themselves; this has been described in section 2.6. Planet-planet interactions lead to pumping of eccentricities and trapping into mean-motion resonances. At the same time, the presence of a gas disc will damp the eccentricities and inclinations. The N-body part of the formation model permits the correct modelling of gravitational interactions between the planets in a single system and the detection of collisions. Effects of the gas disc onto the planets (migration, eccentricity and inclination damping) are modelled by means of external forces. These forces can produce unphysical results (spurious outward migration) when multiple planets are being formed in the same system. The cause of those results is investigated and improvement to the migration scheme proposed.

The analyse of collisions detected by the N-body and the improvement of the collision model (detection and outcome) will be the topic of the next chapter.

4.1 N-body

The N-body code employed in the formation model is called *EMPS* and was developed by Carron (2013). It uses a Bulirsch-Stoer algorithm in order to integrate the differential equation

$$\ddot{\mathbf{x}}_i = G \sum_{j=0, j \neq i}^n \frac{m_j}{x_{ij}^3} \mathbf{x}_{ij} \quad (4.1)$$

with m_i the mass of body i and $\mathbf{x}_{ij} = \mathbf{x}_i - \mathbf{x}_j$ the relative position of the bodies i and j . The index 0 is for the central star, the others for the n forming planets; so $m_0 = M_*$ and $m_i = m_{t_i}, i \geq 1$.

The full system is then a set of $3(n+1)$ coupled second order differential equations. At the same time, the choice of the reference frame is arbitrary, as long it is Galilean. To reduce the complexity of the system, one can select specific frames that allow to reduce the number of differential equations to $3n$. Two examples provided here are the heliocentric and barycentric frames. Let us now denote the heliocentric coordinates by a superscript h and barycentric ones by a b . The former is defined by $\mathbf{x}_0^h = \mathbf{0}$ and is therefore not

Gallilean, and so an additional term is needed to compensate. The equation of motion is then written as (Beutler 2005)

$$\ddot{\mathbf{x}}_i^h = -G \left((m_0 + m_i) \frac{\mathbf{x}_i^h}{(x_i^h)^3} + \sum_{j=1, j \neq i}^n m_j \left(\frac{\mathbf{x}_{ij}^h}{(\mathbf{x}_{ij}^h)^3} + \frac{\mathbf{x}_j^h}{(\mathbf{x}_j^h)^3} \right) \right). \quad (4.2)$$

On the other hand, the barycentric frame fulfills the condition

$$\sum_{i=0}^n m_i \mathbf{x}_i^b = \mathbf{0} \quad (4.3)$$

and so the movement of one body is fully described by the other ones. Usually, the central star is left out. The advantage is that no correction term is needed while computing the accelerations, however its position and velocity must be retrieved using the above equation each time the accelerations are needed. The change from one to the other is quite easy, as the location of the barycentre or the one of star are readily available.

Integrating systems with either frame give the same result (besides numerical effects). However, when additional forces are included, results can differ if care is not taken.

Another popular scheme for N-body is symplectic integrator. It solves Hamilton's equation $\dot{p} = -\partial H/\partial q$ and $\dot{q} = \partial H/\partial p$. Among others, the symplectic has the advantages of computational efficiency and bounded errors, whereas with the direct schemes presented above errors accumulate. The choice of a direct scheme over a symplectic one is due to the way it is used in the overall formation model and efficiency. The formation code performs time steps which are typically 10^1 to 10^4 years. At each of these steps, planet structures are computed. Disc evolution uses a sub-stepping method. N-body integration is performed with the current planet masses for the duration of the formation model step. That duration is short compared to evolution models that can last for millions of years; the drift of total energy caused by direct scheme is thus not important, and the fact that masses changes at every step of the formation model would anyway break conservation with a symplectic scheme. Initial comparison with symplectic schemes did not show significant variations in computational requirements. These have been carried out again recently using the Mercury program (Chambers 1999) and have shown that this method used in this work is up to two orders of magnitude slower. This comparison has unfortunately been carried out too late, and therefore the following results are based on the conventional scheme that has just been discussed.

4.1.1 Collisions

The method to detect and handle them was described in Carron (2013). Collisions are detected when the relative distance between two objects is smaller than the sum of their radii and they are treated as perfect merging.

The simple collision treatment has strong implications. The underlying assumption is that a collision will always result in a single body containing most of the mass. However, if the radius is defined by the Hill's radius of the planet, as it is the case in the initial

phase of planetary formation when the planet envelope is still in equilibrium with the disc, the assumption is incorrect. In the outer part of the envelope gas density is close to the one of the disc, and a body going through only the upper planet's atmosphere will not suffer a sufficient drag that would make it gravitationally bound with the other planet. A way to avoid modelling such events as mergers is to assign a different radius to the planet for the purpose of collision detection. Hence, the previous case will not be treated as a collision. In our case, we define the radius used for collision detection as if the envelope had the same density as the core, i.e.

$$R_{\text{tot}} = \sqrt[3]{\frac{3m_t}{4\pi\rho_c}} = r_c \sqrt[3]{\frac{m_t}{m_c}} \quad (4.4)$$

The assumption of perfect merging may also be wrong for certain collisions between terrestrial bodies: in the *Hit-and-Run* regime, the target remains almost intact while some part of the projectile may be transferred or ejected, but a significant fraction will remain.

Another point to mention, is that the treatment of collisions occurs in two parts. The first happen within the N-body at the moment it is detected: position and velocity of the resulting body are computed assuming a purely inelastic collision. It is however assumed that the planet only retains the solids, and so the masses of both envelopes are removed. This planet is then further evolved in this state for the remaining of the formation step. The second part of the collision treatment occurs after the N-body completed. Its purpose is to determine whether the planet actually retains an envelope following the collision. The envelope of the smallest planet is always removed, and the fate of the envelope of the bigger one is determined by the comparison between its gravitational binding energy and the impact energy. The binding energy is given by

$$E_{\text{bind}} = -G \sum_{i=1}^n \frac{(M_{i-1} + \Delta M_i/2)\Delta M_i}{R_i} \quad (4.5)$$

with ΔM_i is the mass of the mass layer, $M_i = \sum_{j=0}^i \Delta M_j$, $M_0 = m_c$ and R_i the corresponding radius. The impact energy is determined by assuming that the core of the smallest body reaches the core of the bigger object and that there is no relative velocity at infinity (i.e. the impact velocity is the same as the escape velocity). The formula is then

$$E_{\text{coll}} = \frac{Gm_{t,\text{small}}m_{c,\text{big}}}{r_{c,\text{big}}}. \quad (4.6)$$

So if the impact energy exceeds the binding energy (i.e. $|E_{\text{coll}}| > |E_{\text{bind}}|$), the envelope is deemed to be lost following the collision. There is a caveat when computing the impact energy with equation (4.6): it is not self-consistent as the impact condition that were found by the N-body are disregarded, and mutual escape velocity is always implied.

4.2 Migration

As discussed in section 3.3, the presence of a gas disc leads to migration as well as the damping of eccentricity and inclination relative to the disc. A self-consistent model,

where a 3D disc is present and its interaction with planets is directly computed may only be performed for a small period of time (compared to the several million years required to form a planetary system) and number of systems due to extensive computational requirements. To be able to model the formation of various planetary systems in a timely manner, as simplified approach is used. The N-body itself does not have a gas disc; the effects of the latter are modelled by the addition of external forces. These forces are parametrised by three time scales given in equation (3.25), namely τ_{mig} for migration, τ_e and τ_i for eccentricity and inclination damping. The former may take either a positive or negative value for inward or outward migration respectively; the other two may only have positive values. Their values are computed according to the procedure shown in section 3.3 and remain constant for the duration of a time step of the overall formation model. They are converted into external forces following Papaloizou and Larwood (2000):

$$\ddot{x}_j^{\text{mig}} = -\frac{\dot{\mathbf{x}}_j}{2\tau_{\text{mig}j}} \quad (4.7)$$

$$\ddot{x}_j^e = -2\frac{(\mathbf{x}_j \cdot \dot{\mathbf{x}}_j)\mathbf{x}_j}{x_j^2\tau_{e,j}} \quad (4.8)$$

$$\ddot{x}_j^i = -2\frac{(\mathbf{z} \cdot \dot{\mathbf{x}}_j)\mathbf{z}}{\tau_{i,j}} \quad (4.9)$$

with \mathbf{z} a unit vector perpendicular to the disc plane. As a result, the acceleration is modified to include the additional terms in the following manner

$$\ddot{x}_j \rightarrow \ddot{x}_j + \ddot{x}_j^{\text{mig}} + \ddot{x}_j^e + \ddot{x}_j^i. \quad (4.10)$$

As we shall see, the presence of these external forces may lead to unexpected results. We discuss these result in the next section, and argue that they are certainly unphysical. We will then follow two different paths to mitigate the problem, firstly by modifying the method that computes the time scales and secondly by investigating alternate schemes for the external forces.

4.3 The problem of distant giant planets

The formation of distant giant planets is thought to not be possible with the core accretion paradigm. This is the result of the long dynamical time scale at large separation that prevent from forming a core of a few Earth masses before the dispersal of the gas disc. In some population synthesis generated with the Bern model, giant planets were found at large separation from central star (figure 4.1; the upper right part). They are also further away than the upper limit of where planetary embryos are placed initially (20 AU; the dashed vertical line in that figure), meaning that migration occurred to move them out. The presence of such planets warrants further investigations to understand the processes that lead to their formation.

By looking at the formation tracks of such planets (black lines on the figure), we find that it is a rather steady process and not the result specific events, such as scattering following a close encounter with another forming planet. We also note that all planets have

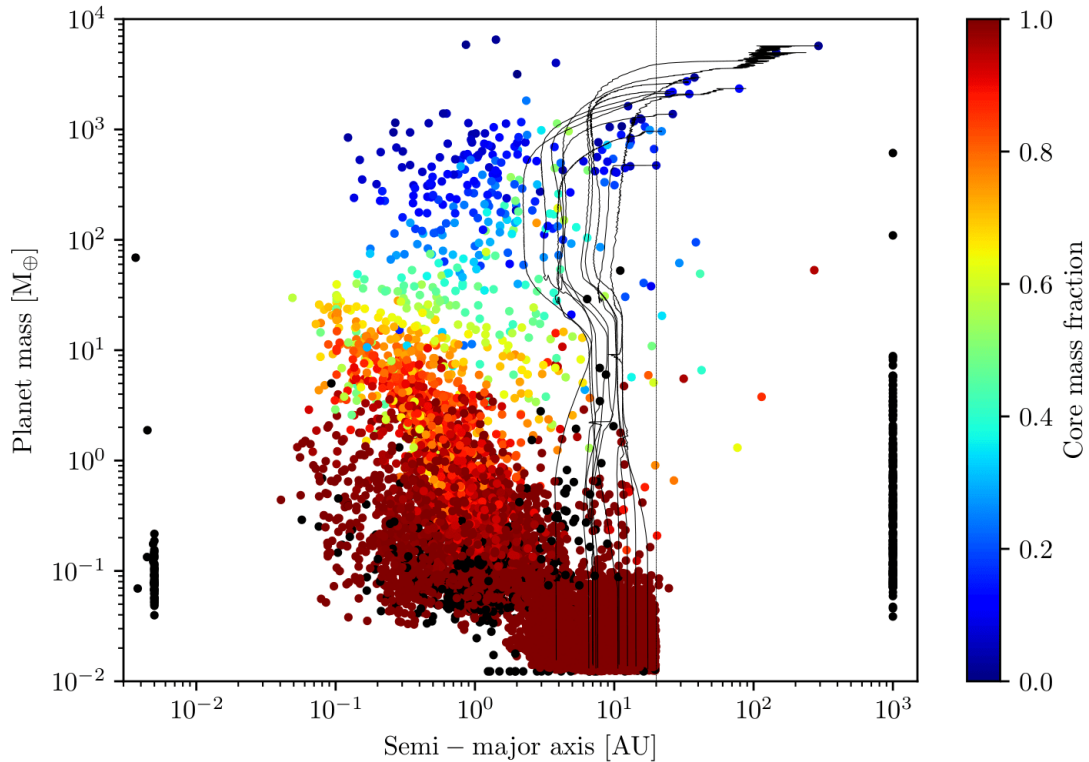


Figure 4.1: Mass-distance plot showing the results of a population with numerous distant giant planets. The colour gives the envelope mass fraction, from purely rocky (dark red) to purely gaseous (dark blue). Planets in black were lost during their formation, due either to ejection (the vertical line at 1000 AU), collision with the star (the one at $5 \cdot 10^{-3}$ AU) or another planet. The formation tracks for planets more massive than $100 M_{\oplus}$ and further away than 20 AU are shown as thin black lines. Data courtesy of D. Swoboda.

at some point been inside around 10 AU and subsequently migrated outward. Interestingly, the outward migration happens while $\tau_{\text{mig}} > 0$, indicating that inward migration is expected. To understand this possible contradiction and whether the outward migration is physical, we will restrict ourselves to a specific system where this phenomenon has been observed. Only the N-body part of the formation model is necessary. This will allow us to study specific situations and to modify parameters to know which part of the model is responsible for the deviation.

The initial conditions for the N-body are provided in table 4.1, and its behaviour over one million year is shown in figure 4.2. The scatter in both semi-major axis and eccentricity is due to the fact that the system as a whole is a 3-body problem, whereas the orbital elements are computed in the usual way, assuming separate 2-body problems. Several things can be learned from these two plots. The first is that the inner planet follows the expected path; semi-major axis decreases at the correct rate and eccentricity is damped. The change rate of the latter is not comparable with the prescribed time scale,

	Star	Inner planet	Outer planet
Mass	$1 M_{\odot}$	$1 \cdot 10^{-3} M_{\odot}$	$1.2 \cdot 10^{-3} M_{\odot}$
a	–	2 AU	8 AU
e	–	$1 \cdot 10^{-4}$	$5 \cdot 10^{-3}$
i	–	$1 \cdot 10^{-3}$	$3 \cdot 10^{-4}$
τ_{mig}	–	$2.5 \cdot 10^6$ yr	$2 \cdot 10^6$ yr
τ_e	–	2 yr	0.8 yr
τ_i	–	3 yr	1 yr

Table 4.1: Initial conditions of a system that showed outward migration. The other orbital elements are random.

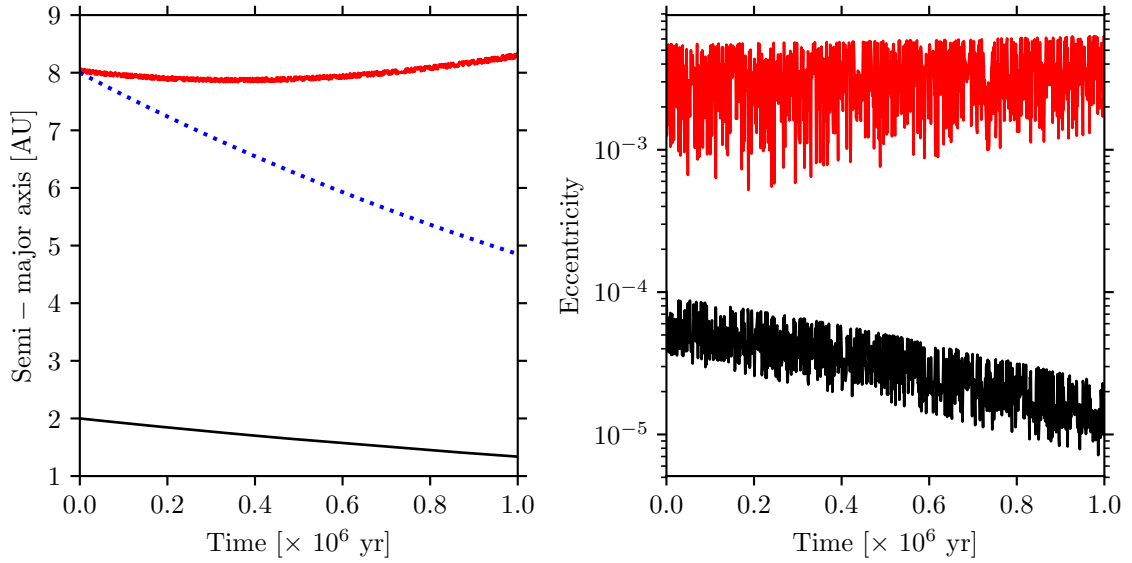


Figure 4.2: Semi-major axis and eccentricity as function of time for the two planets (black line for the inner one and red for the outer one) using the initial conditions provided in table 4.1. The blue dots show the expected semi-major axes due to migration.

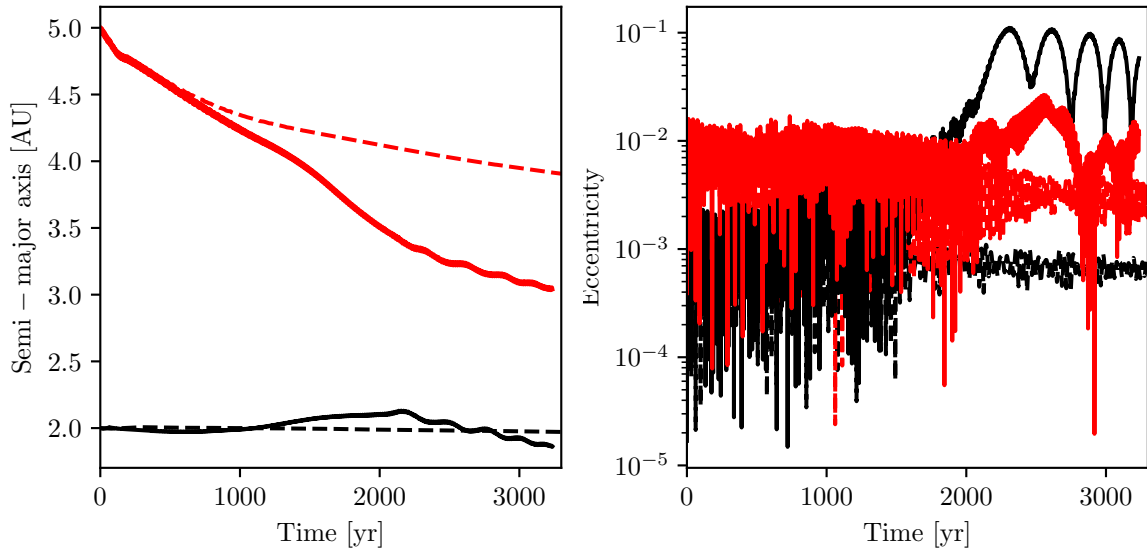


Figure 4.3: A similar kind of system simulated by a full disc hydrodynamics code. The location of the outer planet is initially at 5 AU rather than 8 AU so to restrict the physical extend of the disc to be simulated. Solid lines show results when both planets are in the same disc while dashed lines are for results when the planets are in two distinct discs. Data courtesy of S. Ataiee.

as the interaction with the outer planet will tend to excite the orbit. The behaviour of the outer planet is on the other hand surprising; its semi-major axis does not follow at all the expected migration. Also, the eccentricity remains higher than for the inner planet despite having a shorter damping time scale.

4.3.1 Comparison with hydrodynamical simulation

In order to determine whether the outward migration is physical in the presence of two massive planets, a comparison has been performed a full hydrodynamical simulation with first each planet taken separately and second when they are inside the same disc. All these results are shown in figure 4.3. The migration of the outer planet is initially unaffected the presence of the inner one, but as they approach each other, they start to feel the perturbation of the gas disc caused by the other planet and convergent migration occurs. Slightly after 2000 yr they get trapped inside the same gap and continue to migrate together. The time scale of this simulation compared to the pure N-body case is different by more than two orders of magnitude. We observe here that the planet migrated from 5 to 3 AU in period of about 3000 yr while for the latter this should take a few hundred thousands years. The eccentricities are slightly higher in the hydrodynamical simulations compared to the N-body. For the outer planet, it is on the order of 10^{-2} in the hydrodynamics simulation and $3 \cdot 10^{-3}$ with the N-body. The inner planet show an eccentricity close to 10^{-3} initially and increases while the two planets come closer,

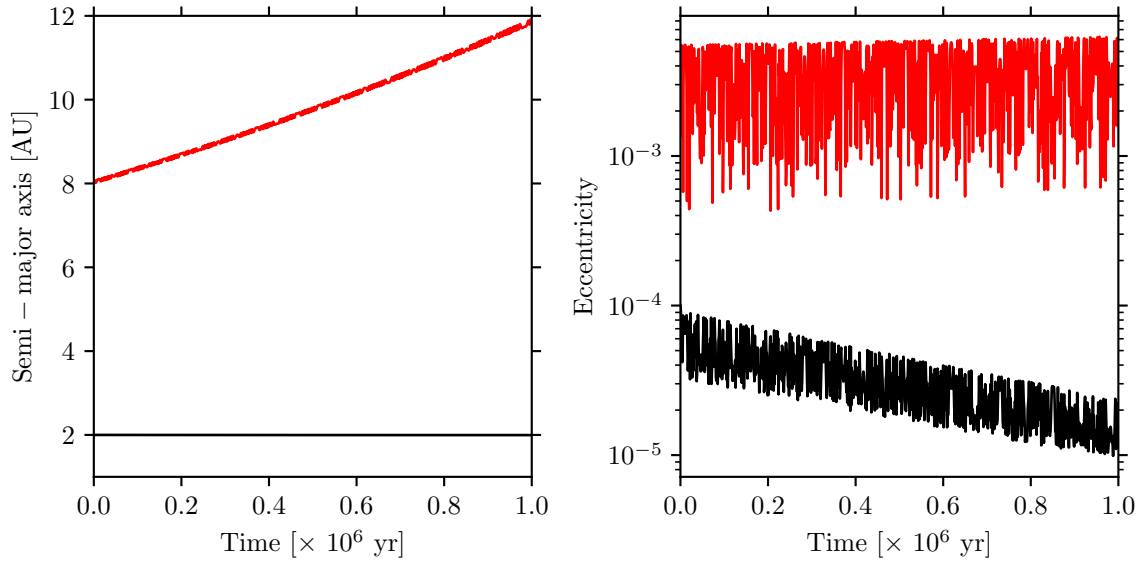


Figure 4.4: Same as in figure 4.2, but with eccentricity damping only (migration and inclination damping are removed).

oscillating in the range of 10^{-2} to 10^{-1} .

So to summarise the findings with hydrodynamical simulations, we find that when two massive planets are in the same disc, the outer one does not migrate outwards. The migration rate is the same whether or not a second planet is present, as long as the planets remain distant from each other. This implies that the outward migration observed with the N-body simulation is spurious. Also, the damping of eccentricity is too strong with our N-body case. For the latter we can suppose that the damping time scales are too short, as they are even shorter than the orbital period for the outer planet.

4.3.2 Cause of outward migration

Now that we found that the outward migration is spurious, we investigate its precise cause. We proceed by taking away the different external forces in turn. This leads to the discovery that the outward migration is caused by the eccentricity damping term of the outer planet. For comparison, figure 4.4 show the results of the same system with migration and inclination damping terms removed. The difference between the theoretical (assuming the semi-major axis only changes due to migration) and final locations is of a similar value as before – about four astronomical units. The eccentricities follow the same patten as in the previous run, this is to be expected as identical damping is used in both cases. It remains to understand why the eccentricity damping term causes the unexpected outward migration. The presence of a third planet lead to the scatter in eccentricity and may thus play a role in the problem. The perturbation is linear with the mass of the third body. On order to reduce the perturbation, we perform the same simulation, but with the planet masses reduced by a factor ten. The corresponding results are provided

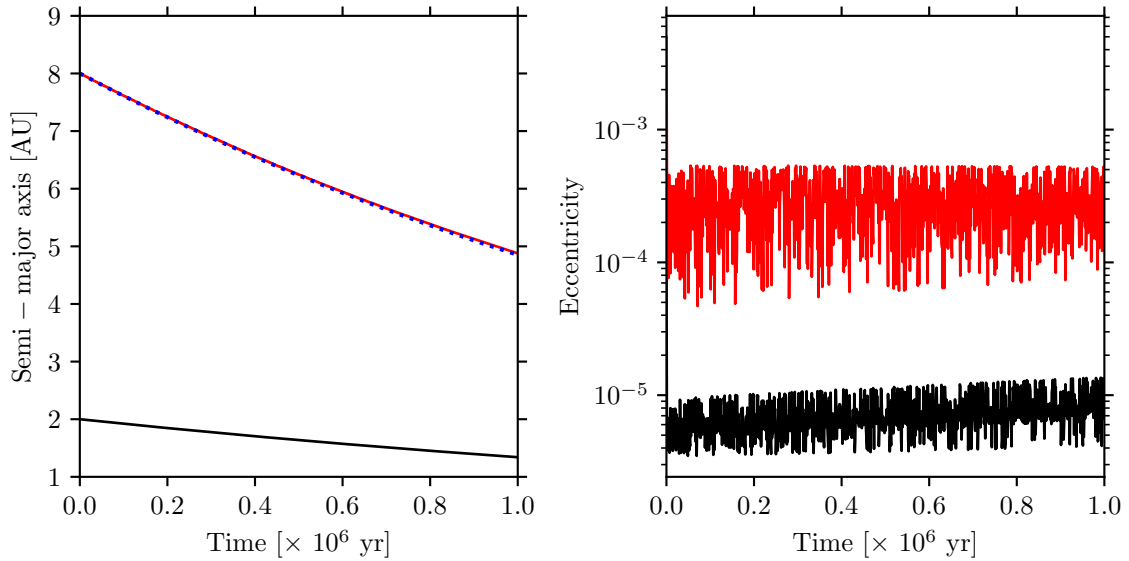


Figure 4.5: Same as in figure 4.2, but with planet masses reduced by a factor ten.

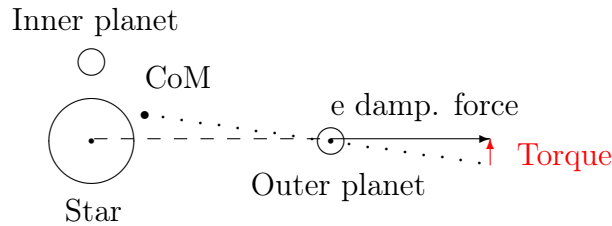


Figure 4.6: Sketch of a system with a massive inner planet present (not to scale). Eccentricity damping force is applied radially from the star. With another massive planet, the centre of mass is not aligned with the star, so the damping force produces a torque.

in figure 4.5. The change is dramatic, in the sense that the outer planet follows almost perfectly the expected behaviour in semi-major axis. A slight deviation is still observed, though. Eccentricities are more strongly damped, and show an order decrease from the original case. We can thus say that the planet masses play an important role. The location of both planets also has an effect: we see in figure 4.2 that the outer planet gets an higher outward migration time as time passes. The presence of another massive planet closer to the star can also be deduced from the formation tracks shown in figure 4.1 as we see the same perturbation in semi-major axis as the one depicted here.

The underlying issue is the form of the external forces. We note that the eccentricity damping force – eq. (4.8) – is directed towards the central star. In the case of a two body problem, the centre of mass is on the line that joins the centre of the two objects. The force is then radial and hence the planet does not feel any torque. When the number of bodies is higher, this is generally not the case and so the eccentricity damping force may lead to a torque on the planet. As planets grow, the centre of mass of the whole

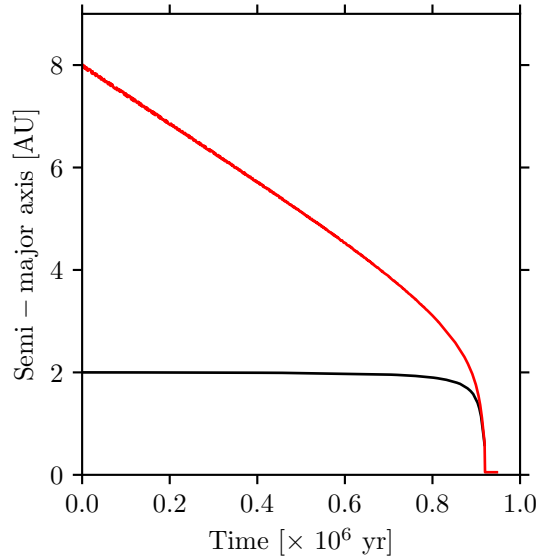


Figure 4.7: The same initial conditions as for figure 4.4, but the motion of the inner planet has been reversed.

moves slightly away from the central star, and thus the damping force is not radial with respect of the barycentre, so a torque appears (see figure 4.6). An other massive body (in this case the inner planet) is required for a torque to appear, and so our test case does not show outward migration when the planets are taken separately. A first guess would be that on average the planet should not gain angular momentum as the inner is sometimes be "in front" of the outer one leading to gain of angular momentum (as in figure 4.6) and otherwise "behind" it which would result in angular momentum loss. These two situations should happen roughly for the same duration as the motion of the two planets is not linked. The fact that the outer planet gains angular momentum means that there is an asymmetry between the two cases. An interesting result is obtained when the motion of one of the two planets is reversed, which is shown in figure 4.7. In that case, the outer planet is migrating inward due to the eccentricity damping force. Also, the rate is faster than in the other case and the outer planet even pushes the inner one into the star. The geometry is thus affected by the relative directions.

We also checked to see whether the time scale itself is a problem. For this various simulation were performed with the eccentricity damping time scale multiplied by arbitrary factors. The integration time was also multiplied by the same factor, so that all systems were integrated for the same amount of damping time scales. The corresponding results are shown in figure 4.8. We observe that the original case has the smallest outward migration after being integrated for a given amount of damping time scales. Actually, it seems that the rate of migration saturates when the eccentricity damping time scale is about twice the original one; the two first cases have almost the same rate when the comparison is made in terms of physical time. On the other side, the outward migration rate per time scale converges when the time scale is big enough (around ten times the original value

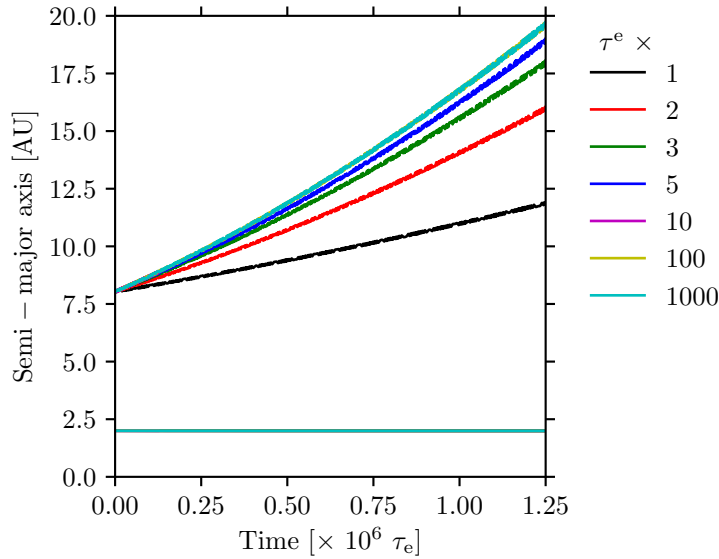


Figure 4.8: Influence of different values of eccentricity damping. The case with factor 1 is the same as in figure 4.4. For the other ones, both the eccentricity damping time scale and integration time were multiplied by the given factor.

is our case). We can say that this phenomenon is always present when massive planets are involved, but it was made visible by the very short value of the eccentricity damping time scale in specific situations.

We did see that the spurious outward migration only happens when the two conditions are met: the presence of massive third body, and short damping time scales. So, one solution to the problem would be to ensure that the time scale is always big compared to both the orbital period and the migration time scale, as eccentricity damping by the gas disc is stronger than obtained with the full hydrodynamics simulation. One could also try to find a relation of the outward migration rate as function of at least the planet masses, their relative distance and the eccentricity damping time scale so that an additional term could be added in the migration time scale to compensate the drift. However, as we have seen in this section, it depend on multiple parameters with no straightforward relationship, so the actual formula would end up being quite complicated and it would be difficult to cover the whole parameter space. The last alternative is to investigate other migration scheme that would have such problem.

4.4 Modification of damping timescales

The initial attempt to avoid the spurious outward migration is to correct the damping time scales. As we saw in figure 4.8, a longer damping time scale does not prevent outward migration, but rather it results in eccentricity damping a less visible cause of spurious migration. Also recalling from the previous section, it was discussed that the spurious

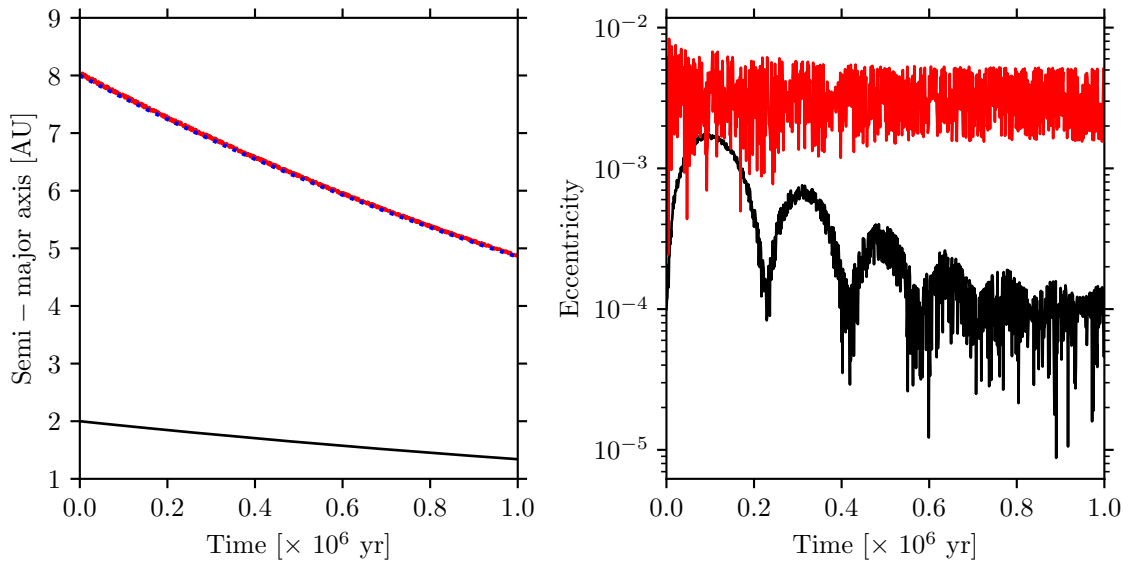


Figure 4.9: As figure 4.2, but the damping time scales have been set according to equation (3.42).

outward migration happens quite late in the formation, principally when planet masses are above a couple hundred Earth masses. In this regime, the planets are in the process of opening a gap in the proto-planetary disc and thus the migration change to type II. This is the same situation for the specific system presented in table 4.1. Damping time scales for the population shown in figure 4.1 were computed using the formula by Cresswell and Nelson (2008) during the whole process. This problem is not encountered (or at least not as this pronounced) when using the approach by Fogg and Nelson (2007). This may imply that applying damping time scales following Cresswell and Nelson (2008) when planets are migrating in type II leads to spurious outward migration. It was further confirmed by Gavin Coleman (priv. comm.) that these formulae are not intended to be used in case of type II migration. We thus follow the same approach as when damping time scales are computed according to Fogg and Nelson (2007): in case of type II migration, damping time scales are set following equation (3.42). This should have as consequence to diminish damping, as migration is rather slow in type II.

The results with this modified approach for the test system investigated in the previous section are shown in figure 4.9. Spurious outward migration is not perceptible, as the semi-major axis of the outer planet closely follows the theoretical expectation. Eccentricities are not that different from the original case though. For the outer planet, it remains in the range 10^{-3} to $5 \cdot 10^{-3}$ whereas the outer planet shows initially a behaviour that resembles the hydrodynamical simulation (though not on the same time scale), ending close to 10^{-4} . The eccentricity damping of the inner planet might too strong when related to the hydrodynamical simulation, as there the obtained eccentricity is about an order of magnitude higher (with a single planet in the disc). Hence, the use of equation (3.42) to compute the damping time scales does actually result in similar eccentricities while the

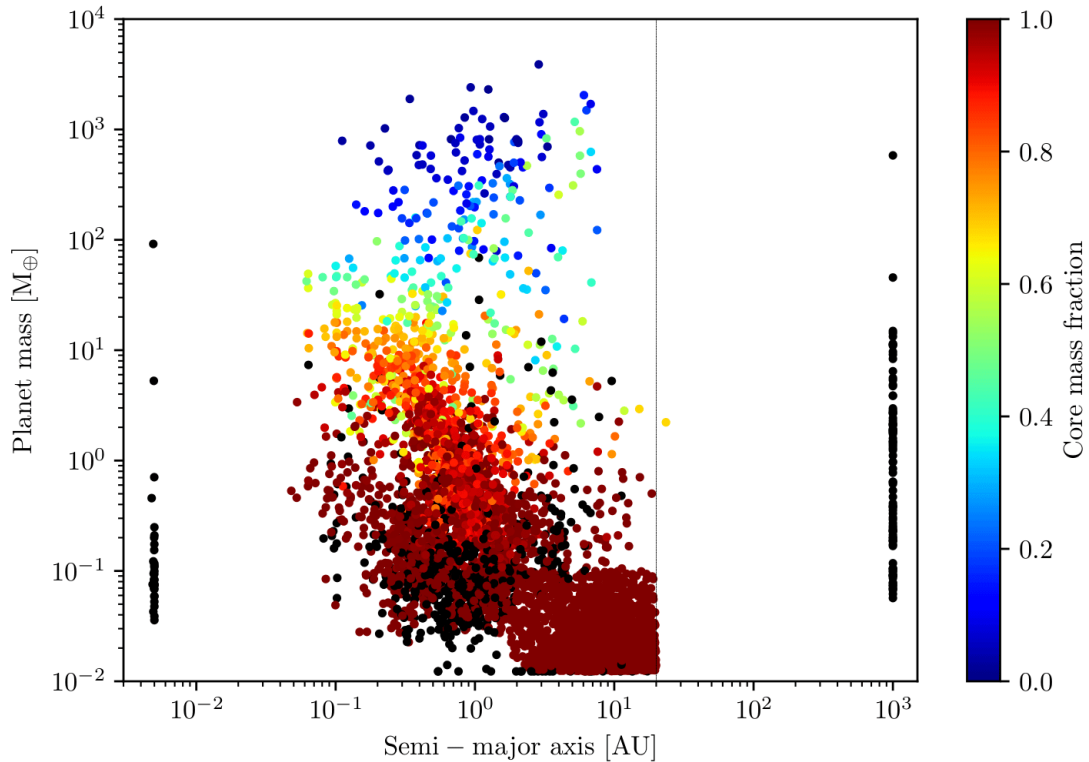


Figure 4.10: Same as figure 4.1, but the computation of damping timescales has been changed to use eq. (3.42) when migration is in type II. Data courtesy of D. Swoboda.

spurious outward migration is strongly reduced. It therefore seems to better reproduce the results obtained with the hydrodynamical simulation.

We now apply the modified approach to an entire population. The corresponding results are shown in figure 4.10. We don't obtain giant planets with a semi-major axis greater than 10 AU. This is consistent with the observation that was made on the previous population that all giant planets first migrated within that distance. Note that the number of planets in the two populations cannot be used to determine if this modification also changes the masses, as the two populations do not have the same number of systems.

It is also interesting to see what this modification imply for a specific system. This is shown in figure 4.11. This system was not chosen randomly; it perhaps one where the biggest differences are found. The reason is that there are three giant planets formed (light blue, light and middle grey) and thus the outward migration is more pronounced when the non-modified scheme is used. The formation model is relatively chaotic, especially the N-body part; so the slight modification performed here has other consequences which in turn may affect the overall results. For instance, the fate of the shown by the red line is the same – the planet collides both times – but the moment of the event changes from late (a few million years) and with a planet that has previously been scattered by another one to quite early on ($1.5 \cdot 10^5$ years). The main differences are however due to the change of damping time scale computation: the end location of the two outer giant planets.

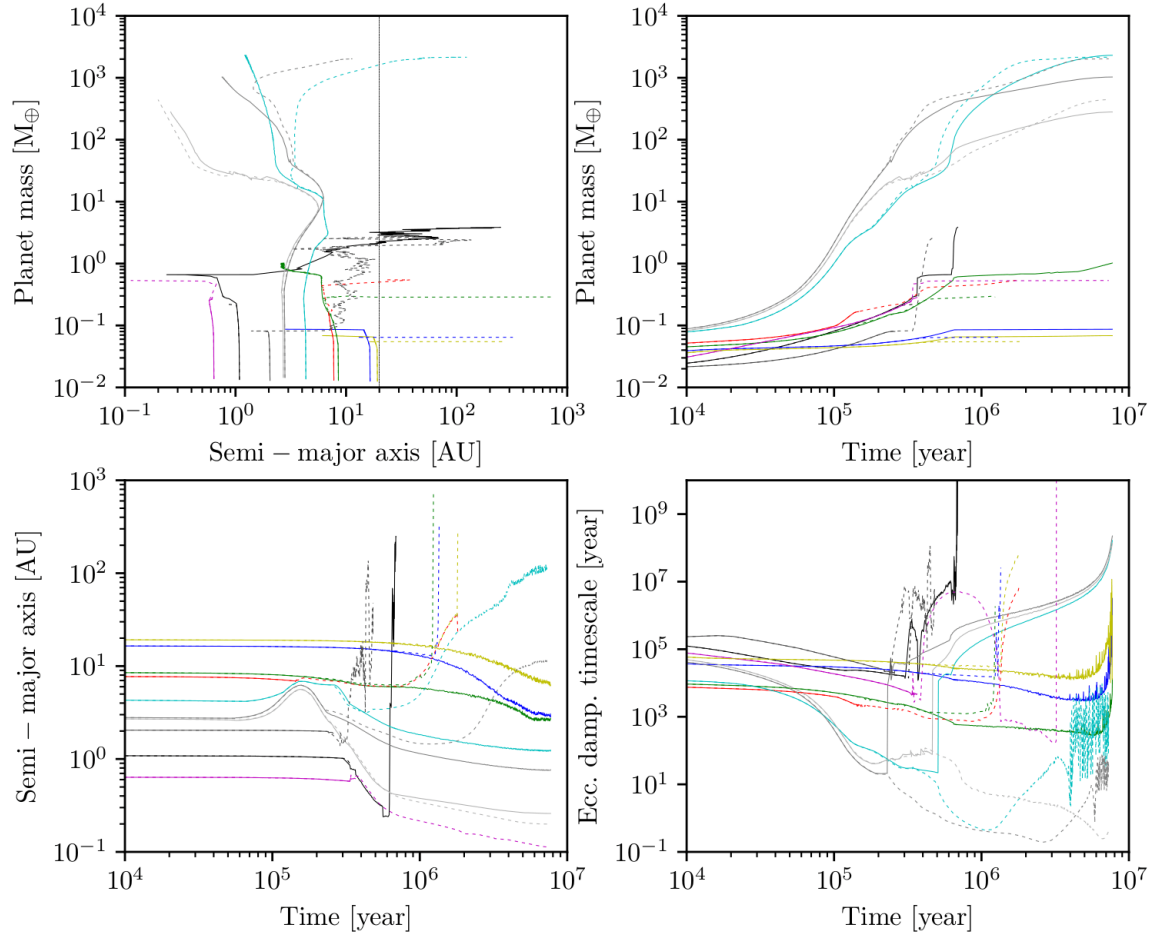


Figure 4.11: Comparison of formation tracks for one specific system, but with the two prescriptions for eccentricity and inclination damping when in type II migration. Each colour is one planet. Plain lines are for the modified model where eq. (3.42) is used; dashed line is for the old model where the values come from the formula in Cresswell and Nelson (2008). Data courtesy of D. Swoboda.

The innermost one is slightly shifted outwards. The middle one end just within one AU, compared to roughly ten otherwise. The biggest change is for the outermost planet, where the ratio between the two end locations is of the order of hundred (just further away than 1 AU, compared to 100 AU). The hierarchy of the changes is consistent with the observation of the previous section, namely that a giant planet affects the migration of other planets further away. The inner giant planet is thus not affected by this phenomenon, the middle one by the inner planet and the outermost one by the two inner planets. Indeed, the eccentricity damping time scale (lower right panel of figure 4.11) looks totally different for the planet that changed their migration to type II. When using Cresswell and Nelson (2008) all the time, we see that the damping time scale is very low (a few years, down to a fraction of a year) for the massive planets. The switch from type I to type II is easily distinguishable for the modified version, as a jump of a few orders of magnitude happens at that moment. In the latter case, the time spent by giant planets with a damping time scale lower than say, a thousand years is heavily reduced. Also in this case the minimal value is increased to around a hundred years compared to the fraction of a year previously. This change thus avoids remaining for too long in the situation that lead to spurious outward migration. As stated above, there are other changes induced, one example is the number of close encounters that lead to either collisions or scattering and thus the number of planets at the end of the formation phase. The number of collision is increased from one to four, but in the same time, the number of ejections is decreased from five to a single event; the end number of planets is thus increased from four to six. The case of collisions will be discussed in more details in chapter 5. The ejection events are related to be the outward migration of the giant planets; as the outer planet drifts, it catches multiple planets in mean-motion resonances which leads to dynamical effects. The smaller planets are not affected by outward migration themselves as their value for eccentricity damping is much higher than for the giant planets that already switched to type II migration.

Since we modified the way damping time scales are computed, we may compare the new results with the original scheme. This is done in figure 4.12. The same system as in figure 4.11 is shown, but the case with dashed lines has been replaced by the one where damping time scales are computed following Fogg and Nelson (2007). At first, we see that the values of damping time scales following Cresswell and Nelson (2008) are an order of magnitude higher than the one following Fogg and Nelson (2007) (lower right panel). This means that eccentricities and inclinations are less strongly damped with the newer approach. Similar observation as for the previous case can be done, such as the fact that only this change has other effects that make the comparison somewhat harder. There is a higher discrepancy later on, but it could be also linked to the fact that positions and masses are no longer the same. In the original case, one of the three giant planets (in light blue) does not reach the end of the simulation. Nevertheless, the location of the three outermost planets is interesting:

The two innermost planets have a different fate in the two simulations. With the older damping time scales, these two planets reach the end, whereas for the new one they first collide together and then the resulting body is ejected.

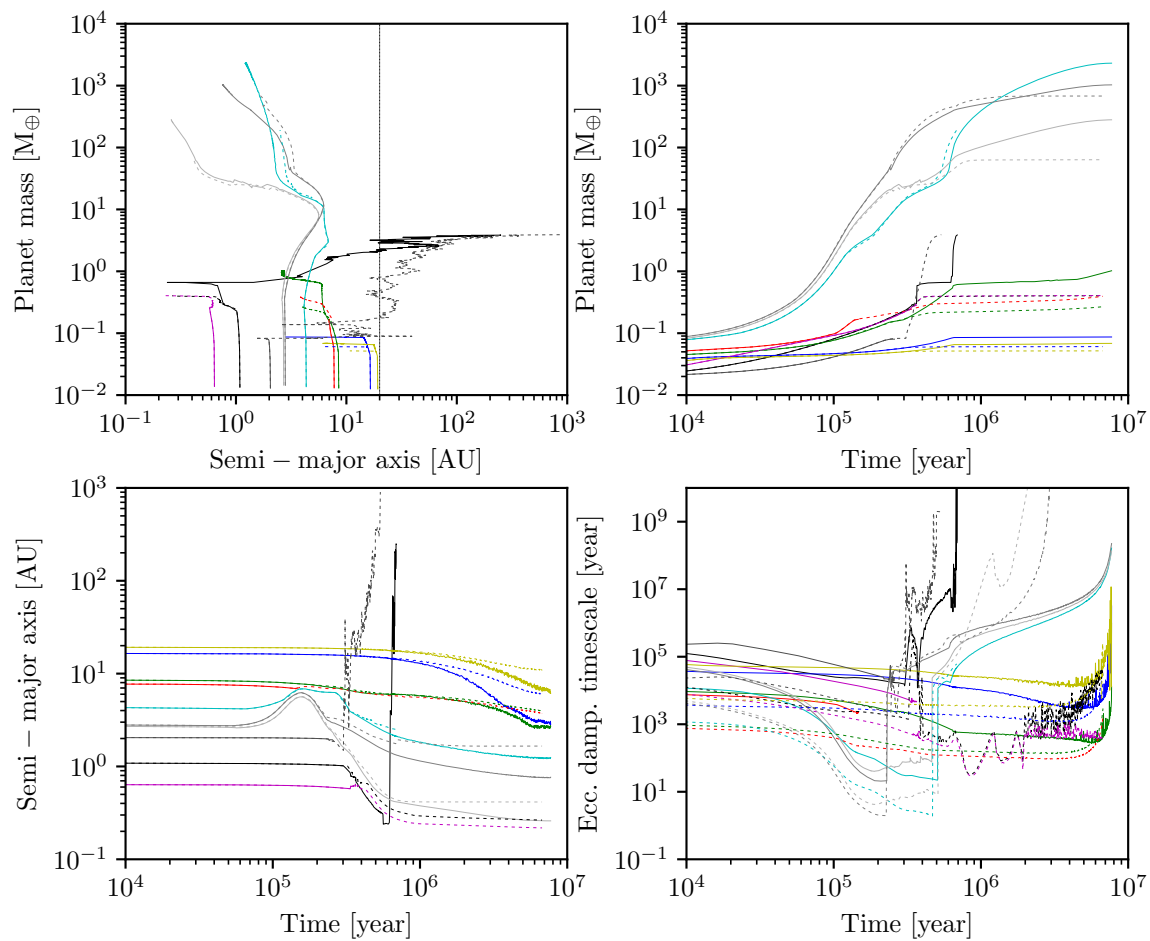


Figure 4.12: Same as the two lower panels of figure 4.11, but comparing the damping time scale from Cresswell and Nelson (2008) (solid lines) with the from Fogg and Nelson (2007) (dashed lines). Data courtesy of D. Swoboda.

4.5 Alternative migration schemes

We did see in the previous section that the original migration scheme does not work well when the planet masses are not small compared to the central star. In particular, the outer planets were found to spuriously migrate outwards. Here, we investigate alternative schemes for the external forces. We will first focus on eccentricity damping, as it is the major cause of trouble. One of the inherent caveat here is that we cannot find a reference quantity that would tell us if the scheme is working properly. The issue is that we are not modelling a closed system, as the gas disc itself is not present in the N-body. Also, eccentricity damping cannot conserve both energy and angular momentum. We can see this by remembering that the energy of a two-body problem is linked only to the semi-major axis with

$$\epsilon = -\frac{\mu}{2a} \quad (4.11)$$

(μ the standard gravitational parameter) whereas the angular momentum is linked to both semi-major axis and eccentricity with

$$L \propto \sqrt{a(1 - e^2)}. \quad (4.12)$$

Thus a scheme that only damps the eccentricity without changing the semi-major axis would conserve the energy but not the angular momentum. It is possible also to correct the semi-major axis along with eccentricity damping in order to conserve angular momentum using

$$0 = (dL)^2 = (1 - e^2)da - 2ae de \quad (4.13)$$

so

$$\frac{1}{a}da = \frac{2e}{1 - e^2}de. \quad (4.14)$$

The original migration scheme should conserve angular momentum as the additional force used to perform eccentricity damping – eq. (4.8) – is radial so its torque is null. As we don't have a closed system (the gas disc is not directly modelled in the N-body) it is not possible to check for angular momentum or energy conservation. The different schemes are nevertheless usually designed to conserve either of these two quantities.

Investigations for other migration schemes were conducted in the following directions: alternative reference frames or correction methods. As planet masses increase, the reference frame becomes of greater importance. When the central star has essentially all the mass then barycentric and heliocentric frames nearly coincide, but this no longer holds as planets grow in mass. The frame appears on two occasions: as general frame with which the evolution is computed (section 4.1) and when computing the correction terms for migration and damping. The two are not necessarily the same. Second, the exact way disc interact with the planet is not precisely known and the formulae from Papaloizou and Larwood (2000) are only one mean to perform migration and damping. There are other ways given in the literature, such as in the annex of Lee and Peale (2002). It has also been suggested to entirely de-couple these external terms from the N-body, by directly modifying the orbital elements between each integration step. The two additional methods directly involve the orbital elements, so variants that conserve angular momentum rather than energy were also used.

4.5.1 Reference frame

The idea is that the additional forces mimicking migration might be better computed and added in a different reference frame. This modified frame will also be used for the computation of the orbital elements for the new correction methods. In the latter case, the choice of the frame will also affect the mass used to compute the standard gravitation parameter μ . In addition to the already used heliocentric frame, two new ones are investigated: barycentric and Jacobian.

The conversion between barycentric and heliocentric frames is straightforward. Let us now write \mathbf{x}_j^b and $\dot{\mathbf{x}}_j^b$ the barycentric coordinates of the central star and the planets. The location and velocity of the central star in the barycentric frame is

$$\mathbf{x}_0^b = -\frac{1}{m_s} \sum_{i=1}^n m_i \mathbf{x}_i \quad (4.15)$$

$$\dot{\mathbf{x}}_0^b = -\frac{1}{m_s} \sum_{i=1}^n m_i \dot{\mathbf{x}}_i \quad (4.16)$$

with $m_s = \sum_{i=0}^n m_i$ the total mass of the system. The summation starts with index one, as the position and velocity of central star (index 0) in the heliocentric frame are null per definition. The position and velocity the planets are then simply given by a translation

$$\mathbf{x}_j^b = \mathbf{x}_0^b + \mathbf{x}_j \quad (4.17)$$

$$\dot{\mathbf{x}}_j^b = \dot{\mathbf{x}}_0^b + \dot{\mathbf{x}}_j. \quad (4.18)$$

The Jacobian coordinates are defined with references to the centre of mass of the bodies located inside the one being considered. Before computing these coordinates, the planets have to be sorted according to their separation from the central star. For the following discussion, let us assume that the indexes i are ordered with increasing separation so that the planet with $i = 1$ is the closest to the star and the one with $i = n$ is the furthest away. For the innermost planet, the Jacobian coordinates are the same as the heliocentric ones. For the remaining planets the same method as for the barycentric coordinates but iteratively where the upper boundary in equations (4.15) and (4.16) is changed from n to $i - 1$ for the computation of the planet i .

The comparison of these three frame for the original migration scheme is show in figure 4.13. These simulations were performed used only the eccentricity damping, so they should theoretically remain on a constant semi-major axis. The behaviour of the planets using the barycentric frame is dramatic, both migrate rapidly in a opposite direction, and the inner planet is rapidly accreted by the central star (in less than 10^5 years). Once the inner planet is lost, the outer one does not migrate any more. The results obtained with the Jacobian frame are encouraging; the semi-major axis remains constant, as for and the original heliocentric case and furthermore the outer planet now also conserves its semi-major axis.

This peculiar behaviour of the barycentric case warrants further investigation. Three other additional calculations were performed, and their results are shown in figure 4.14.

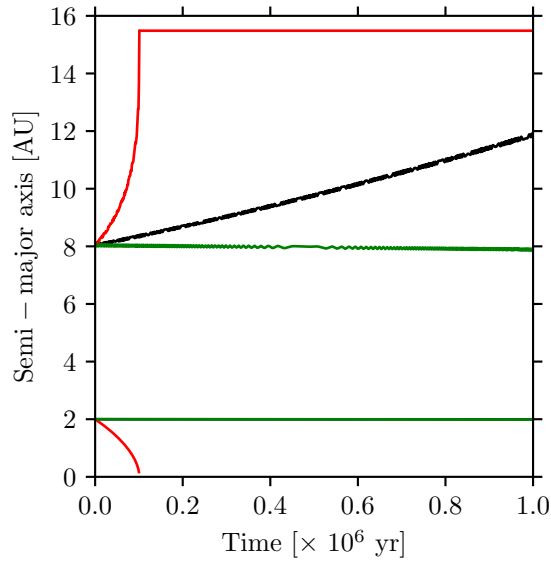


Figure 4.13: Semi-major axis as function of time for the two planets using the initial conditions provided in table 4.1 (only with eccentricity damping), with three different references frames used to compute the additional forces: black for the heliocentric, red for the barycentric and green for the Jacobian. The curves of the inner planet for the heliocentric and Jacobian frame overlap.

The first case, shown in red involves a complete modification of the whole N-body scheme: everything is now computed in the barycentric frame. The position of the star is now computed and equation (4.1) is used to compute the interaction instead of (4.2). The implication is that the additional forces are computed in the same frame as for the other acceleration terms. In this case, we observe that the second planet remains with a constant semi-major axis while the inner planet migrates inwards, with a similar behaviour as the previous model. This result can be seen with analogy with the original problematic case: when the heliocentric frame is in use for all the calculations, then the outer planet drifts outward while the inner one keeps its semi-major axis; when the barycentric frame is in use also for all the calculations, then the inner planet drifts inward while the outer one remains at the same distance. The barycentric frame then does not provide an advantage over the heliocentric one. The implications of the change in reference frame are not only numerical; the additional forces also have an indirect influence on the other objects. Newton's law of motion is not fulfilled as the gas disc not being present to account for the back reaction. The consequences depend on the reference. When the system is computed in the heliocentric frame, the location of the barycentre drifts with a factor m_i/m_s with respect to the additional motion induced onto the planet while the central star and the other planet remain at the same position. Conversely, when the barycentric frame is used, this affects the position and velocity of the central star. Meanwhile the other planet remains at the same position with respect to the barycentre.

The two remaining modifications are much simpler: the eccentricity damping term has

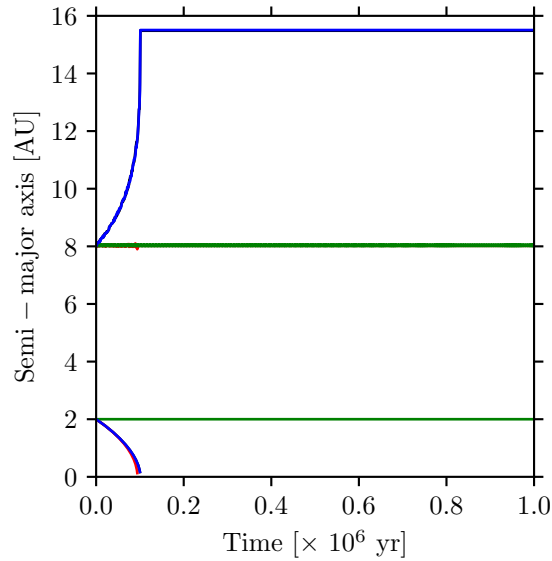


Figure 4.14: Further variations of the barycentric case shown in figure 4.13; black: the problematic case show previously, red: with the whole N-body computed in a barycentric frame, green: only the outer planet has eccentricity damping, blue: only the inner planet has eccentricity dampig.

been removed from one planet in each case. When the outer does not have eccentricity damping (blue lines in figure 4.14), then the results are very similar to the previous case. On the contrary, when the inner planet does not have eccentricity damping the outer planet does not drift, so it caused by the inward drift on the inner planet.

The corresponding angular momentum and total energy for these cases are shown in figure 4.15. These values help to understand the reason for these different behaviours. First, we note that energy is only conserved in the case when the inner planet has no eccentricity damping, i.e. when the damping force produces no contribution. This could be expected, as the additional force that model the eccentricity damping is not made to conserve energy. Secondly, the jump for the three other cases around 10^5 years is linked to the removal of the inner planet as it is accreted by the central star. At that moment, the potential energy of the inner planet is no longer considered, and since it is close to the central star is actually make a major contribution to the total energy. After the removal, only the contribution of the outer planet remains (and the kinetic energy of the central star).

The angular momentum results are much more interesting. Again, the case where the inner planet does not have eccentricity damping has angular momentum conserved as the damping force produces almost no contribution. In the two other cases where the main reference frame is heliocentric (black and blue lines in figures 4.14 and 4.15) the total angular momentum is conserved until again the inner planet is accreted by the central star. It can be noted that at the moment the inner planet is lost, its contribution to the total angular momentum is very low, a couple of percent.

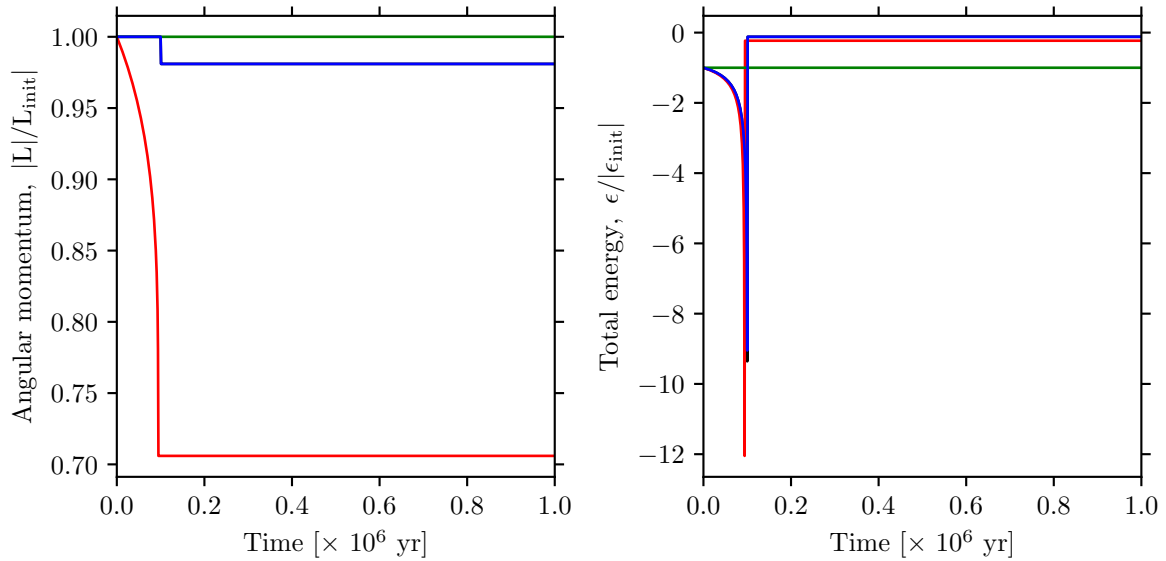


Figure 4.15: Total angular momentum (left) and energy (right) for the cases shown in figure 4.14.

For the case where the whole computation is made with the barycentric frame, the angular momentum is not conserved and a greater component is removed until the inner planet is lost. There is no angular transfer between the planets, or between a planet and the central star.

We thus can conclude that performing the whole computation in barycentric frame does not lead to angular momentum exchange due to damping whereas with the heliocentric frame and additional forces computed with reference to the barycentre conserves the total angular momentum.

These findings, that heliocentric frame is more suitable for migration and damping of the inner planet and barycentric is more suitable for the outer one did result in the development of the Jacobian frame that would so suit these different cases together. There are nonetheless several practical difficulties with this frame:

- The case of planets with similar semi-major axis or significant eccentricity are to be treated carefully. The simulation shown here has the two planets well separated and do not migrate, so this is practically not a problem. The model shown here compares the distance to the central star, and in the case planet would cross their orbit, a jump occurs in the Jacobian coordinates. Also, co-orbital planet could show a complex situation as their semi-major axis is similar, but either one can be closer to the star depending on their position on the orbit. A smoothing would a candidate solution.
- Its computation is expensive in terms of operations to perform. This is not a physical reason, but the N-body is already the part of the model which requires the

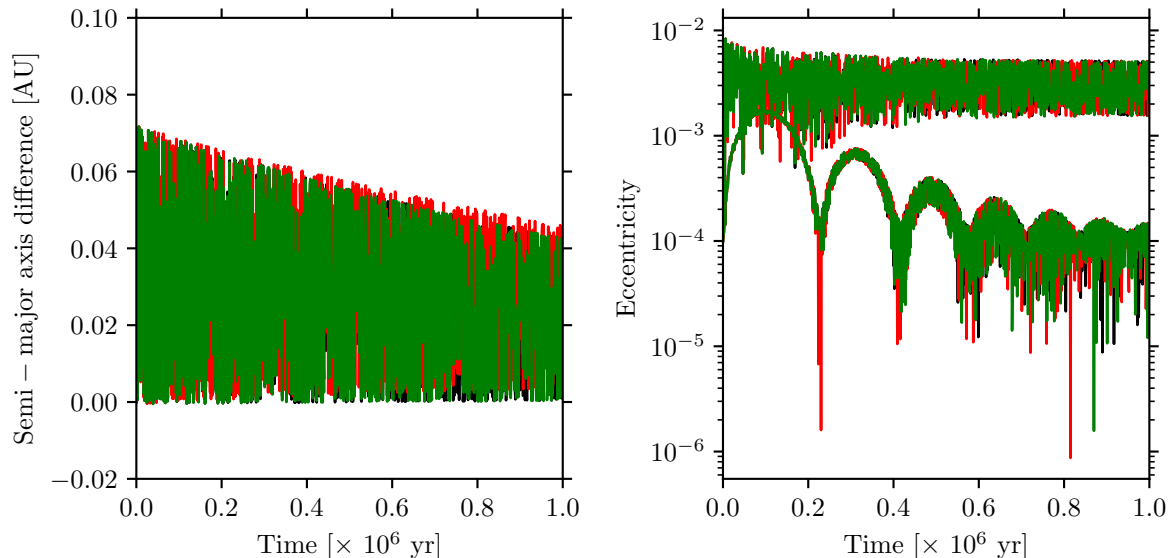


Figure 4.16: Difference between observed and expected semi-major axis of the outer planet and eccentricities for the system described in table 4.1 but where the damping time scales have been set according to equation (3.42). Colours are the same as in figure 4.13.

most computational resources; so adding the computation of the frame results in a doubling of the computational time.

It can be observed though that the obtained results are encouraging (green lines in figure 4.13): the outer planet shows not spurious outward migration while the behaviour of the inner planet is similar than in the original heliocentric frame.

To assess the consequences of the change of the reference frame on a more realistic system, we apply we perform the same simulation as shown in figure 4.13 but with the damping time scales computed with the new approach discussed in the previous section. As we saw that the spurious outward migration is small compared to the expected one, we show the difference between the two in figure 4.16. We observe that the barycentric frame (red line) shows an higher spurious outward migration than with the two other frames, but small compared the actual migration (slightly more than 3 AU). The eccentricities have the same behaviour with all the three frames. So, the modification of the reference frame does not play an important role with the new approach to compute the damping time scales.

4.5.2 Correction method

In this section, we investigate two additional approaches to implement the additional forces that model the disc interaction:

- Following Lee and Peale (2002), where both position and velocities are modified to

model the change of orbital elements.

- A decoupled method, where migration and damping are modelled by evolving the orbital elements separately from the N-body.

The original model of Lee and Peale (2002) is only made for migration and eccentricity damping. In our model, we additionally need inclination damping. In order to derive it, the same principle was applied for inclination. The additional terms are (using their notation)

$$\left. \frac{dx}{dt} \right|_i = r \sin \iota \sin \Omega \sin (\omega + f) i \quad (4.19)$$

$$\left. \frac{dy}{dt} \right|_i = -r \sin \iota \cos \Omega \sin (\omega + f) i \quad (4.20)$$

$$\left. \frac{dz}{dt} \right|_i = r \cos \iota \sin (\omega + f) i \quad (4.21)$$

for the position, and

$$\left. \frac{d\dot{x}}{dt} \right|_i = \sin \iota \sin \Omega (\dot{r} \sin (\omega + f) + r \dot{f} \cos (\omega + f)) i \quad (4.22)$$

$$\left. \frac{d\dot{y}}{dt} \right|_i = -\sin \iota \cos \Omega (\dot{r} \sin (\omega + f) + r \dot{f} \cos (\omega + f)) i \quad (4.23)$$

$$\left. \frac{d\dot{z}}{dt} \right|_i = \cos \iota (\dot{r} \sin (\omega + f) + r \dot{f} \cos (\omega + f)) i \quad (4.24)$$

for the velocity. This method is computationally intensive as the orbital elements are needed each time the acceleration (and the velocity) are computed. Some optimisation can be performed however. For instance, the longitude of the ascending node Ω needs not to be known, only its sine and cosine are needed. These are easier to compute than the angle itself. Similarly, $\omega + f$ is a direct result of the algorithm, so there is no need to retrieve the argument of periapsis. This means that out of six orbital elements, the exact value is only needed for three of them (a , e and ι).

The algorithm for the decoupled method is as follows: first a Bulirsch-Stoer step is performed without external force, then the orbital elements are computed, evolved and finally the position and velocity are computed back from the modified elements. The advantage is that the N-body part is left intact, and thus contributions of the two different parts can be retrieved separately.

The decoupled method has three items that are worth mentioning: first the choice of the anomaly to use is free. In our case we keep the true anomaly constant, but either the eccentric or the mean anomaly could be used as well. The second is that the time interval between two corrections is also a model parameter. Here we selected to not constrain it, and to simply perform the correction after each N-body step, without putting any constraint of its size. Thus it could happen that the correction is applied preferentially at specific moment during the orbit. The last item is that there is a discontinuity between

two consecutive N-body steps. For instance, the actual distance to the star depends on both semi-major axis and eccentricity with

$$r = a \frac{1 - e^2}{1 + e \cos f}. \quad (4.25)$$

Also the inclination defines in which plane the planet orbits the star. Modifying any of them causes the planet to perform a jump in both position and velocity. This makes for instance collision detection and their outcome more difficult to predict, as the exact shape of the orbit is not exactly known.

In addition, these new schemes have both a few caveats:

- They have a strong dependence on the orbital elements. Therefore, not only their position and velocity are required, but also the mass used to compute the standard gravitational parameter. This is accounted for with the different reference frames that were just shown; for the heliocentric frame, only the masses of the central star and of the concerned planet are considered; for the barycentric one, the entire mass of the system is used and for the Jacobian frame, the central star and the planets up to the one concerned.
- Close encounters between planets may cause problems. The perturbation created by the presence of close-by body will affect the computation of the orbital elements. It can happen that semi-major axis and eccentricity reach extreme values during a short period of time (e.g. $e > 1$ or $a > 200$ AU). When this occurs, then it may happen that the Bulirsch-Stoer method does not converge (in the case of of the scheme following Lee and Peale 2002) or that the correction would bring the planet on a completely unrelated orbit. To mitigate this problem, criteria were introduced to not apply migration and damping in case unusual values for the eccentricity are found.

The comparison between these different schemes is presented in figure 4.17. We observe that the inner planet does not migrate for any scheme, which is the expected result. For the outer planet though, the results are completely different. To prevent the planet from migrating too rapidly with the new schemes, the eccentricity damping time scales were multiplied by a factor ten. The original scheme causes the smallest spurious migration, the planet drifting outwards by about 1 AU. The other two schemes produce the same results, in their original version, where the eccentricity damping only changes the eccentricity itself, then both planets are ejected in $6 \cdot 10^5$ years (equivalent to $7.5 \cdot 10^4$ eccentricity damping time scales). However, when the damping should conserve angular momentum, then there is an inward drift, which has a higher magnitude than the original scheme. We thus note that both new schemes and their variation lead to a greater spurious migration and thus bring no advantage compared to the current scheme.

The same comparison, but when using the barycentric frame as reference for the migration and damping schemes is shown in figure 4.18. The behaviour of the original scheme has already been discussed, but there is nevertheless an interesting result: the inner planet is now accreted by the central star after about $2 \cdot 10^5$ years. In the last part

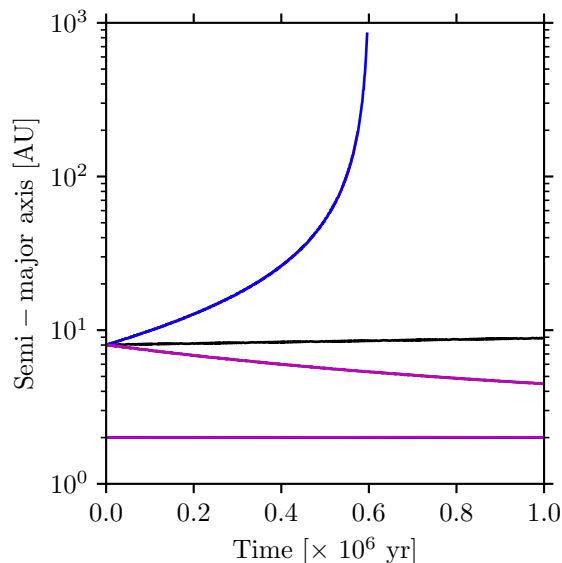


Figure 4.17: Semi-major axis as function of time for the two planets using the initial conditions provided in table 4.1 (no migration and inclination damping; eccentricity damping time scale multiplied by ten) with different migration schemes. *black*: original version from Papaloizou and Larwood (2000), *red*: according to Lee and Peale (2002), *green*: the same, but eccentricity damping conserves angular momentum, *blue*: migration separated from the N-body, *purple*: the same, but eccentricity damping conserves angular momentum. *Note*: red and blue curves overlap, as for green and purple ones. All the five curves of the inner planet overlap as well.

discussing the reference frame, we did see that it was so in about half of the time, but with a damping time scale ten times smaller. So it seems that the relationship between these two times is not linear, as we saw in figure 4.8. For the two new schemes, we can make the same observation that both lead to a similar result, the difference being with whether eccentricity damping conserves angular momentum or not. The original schemes (red and blue curves) lead to a strong outward migration of both planets; the inner planet has its semi-major axis multiplied by a factor of ten during the simulation. With the modified schemes, spurious migration is reduced, but still present. The inner planet drifts outwards by the same rate both times; for the outer planet, in the case of the separated method it remains at the same location whereas for the scheme following Lee and Peale (2002) it slightly drifts inwards. This different can be explained by the fact that for the latter scheme, angular momentum of the system is conserved: since the inner planet drifts outward, the other one must drift inward to compensate. The situation with the most favourable case (either of the new scheme, but with eccentricity damping conserving angular momentum) is reversed from the original problem: the outer planet now remains quite at the same location, but on the other hand the inner one now drifts outward.

The Jacobian frame is not shown here, but the results are that all planets remain at

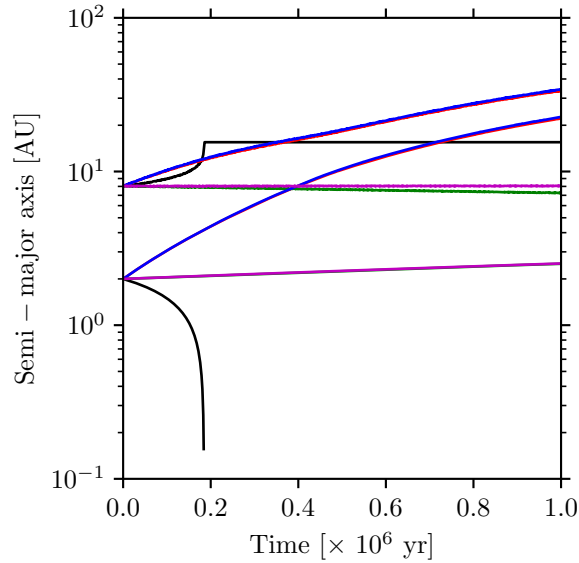


Figure 4.18: Same as figure 4.17, but with barycentric frame to compute migration.

the same location, with a drift up to 0.002 AU for the inner planet and 0.05 AU for the outer one. We thus conclude that changing the migration scheme brings no advantage. The frame used to compute migration is certainly the root of the problem with the observed outward migration. Also, the strong dependency on the orbital elements also cause trouble since the correct mass is now required.

4.5.3 Application to the formation model

To determine whether migration with the Jacobian frame is suitable for planetary system formation simulations, the modified N-body is combined with the whole formation model. The first step is the analysis of a specific system. For this purpose, we go back to the one shown in the previous section about the modification of damping time scales (figures 4.11 and 4.12). The different schemes will induce variations early in the results, such as close encounters which are stochastic by nature, but the comparison is not made on them. The interesting results are actually the behaviours of the outer planets, i.e. the ones that are subject of spurious outward migration. Following the previous results, all systems have their damping time scales computed with the formula of Cresswell and Nelson (2008) while in type I migration and using equation (3.42) while in type II. Three versions of the specific are compared:

- The original scheme, where all reference frames are heliocentric.
- With additional forces computed in the Jacobian reference frame, as a discussed in the relevant part.
- As the last one, but with the orbital elements provided to the remaining part of

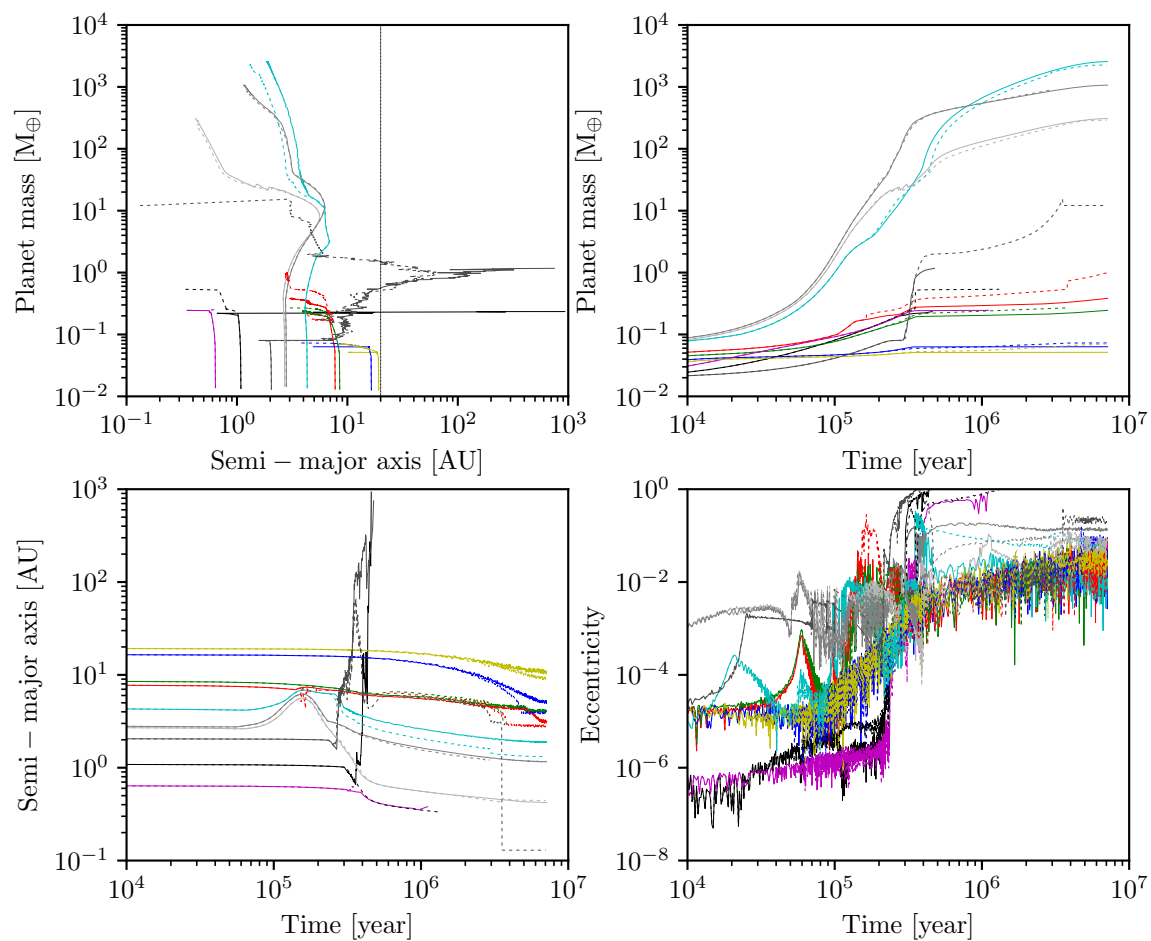


Figure 4.19: Similar to figures 4.11 and 4.12, but for the comparison of reference frames to apply additional forces: Jacobian (solid lines) and heliocentric (dashed lines).

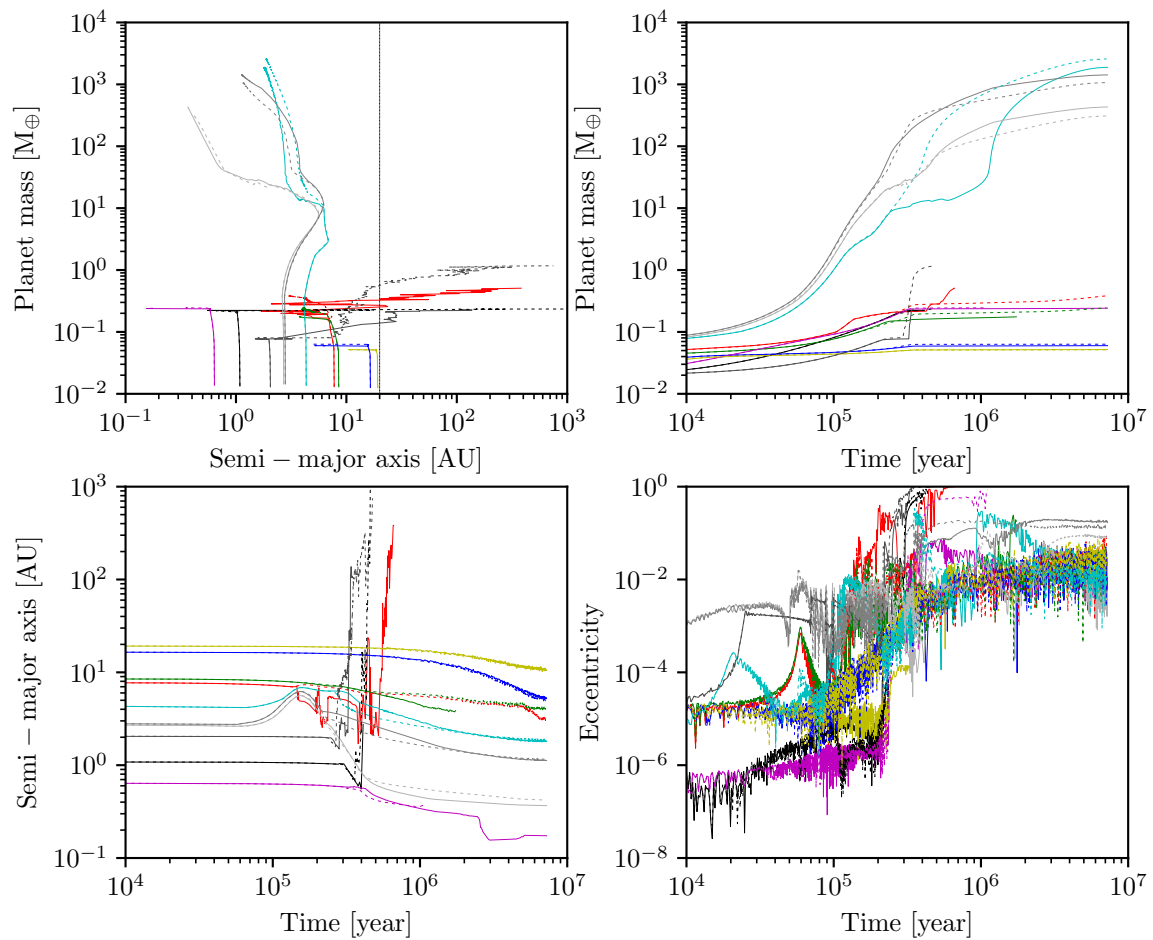


Figure 4.20: Same as figure 4.19, but the additional forces are always computed in the Jacobian frame; the difference is which coordinates are used to compute the orbital elements seen by the remaining of the formation model: Jacobian (solid lines) and heliocentric (dashed lines).

the formation model also computed from the Jacobian coordinates (and with a modified mass for the standard gravitation parameter, as discussed in the part about reference frame).

For the two cases with Jacobian coordinates involved, a smoothing has been introduced when planets have similar distances to the central star in order to avoid a sharp transition when their orbits cross.

The comparison of the first two items is shown in figure 4.19 and between the second and the third appears in figure 4.20. The general picture of all variants is the same, with three massive planets being formed. The Jacobian frame would affect the motion of the outer planets only. In the first comparison, the farthest massive planet (light blue) has a slightly different motion after $3 \cdot 10^5$ yr and remains at an higher semi-major axis in the case with the Jacobian frame while its mass history remains similar in both cases. The different position of the outer planets is explained by this change, as the location of the resonances are shifted. The most important point is that no outer migration is observed with the heliocentric frame. Actually, we do note that the system computed with the original scheme shows outer planets further in than the one using the Jacobian frame.

The purpose of the second comparison is to observe the eccentricity that is effectively being damped. With the original scheme, the target is to lower the usual eccentricity so that the planet follows a circular motion around the central star only. However due to the change of the reference frame that is analysed here, this is no longer the case for the modified scheme. The eccentricity shown from the third case is now computed consistently with the one that is being damped. The results show not significant change on the oscillation of the orbital elements, which are still present. The values of eccentricities are roughly similar in both cases at the end, and increase along with the planet masses. There seem thus not to have any benefit from this change in the present case, though it has been observed that for another system where a single massive planet is formed (not shown here), that the retrieved orbital elements are steadier. The fact that multiple massive planets are formed here and the perturbations they put on the other planets makes the problem more complicated. As a side note, the modification of orbital element computation changes the formation track of the giant planets; their location is different from about $2 \cdot 10^5$ yr until during the second million year. Also, the mass of the furthest of the three remains low and constant up to the first million year.

The inner planets suffer close encounter with the giants, and, expect for one planet in the third case (purple line in figure 4.20) the planets are lost (mostly ejections, few collisions with the central star). The moment when the event occurs and the behaviour are chaotic, so the difference in the outcomes is not important. It can be noted though than for one planet with the heliocentric frame (middle grey, third from the inside) the events do not lead to an ejection; the planet is sent to an orbit further away and is then scattered back on a close-in orbit after a few million years.

So overall, the original scheme with modified damping time scales seems not to show spurious outward migration for the outer planets.

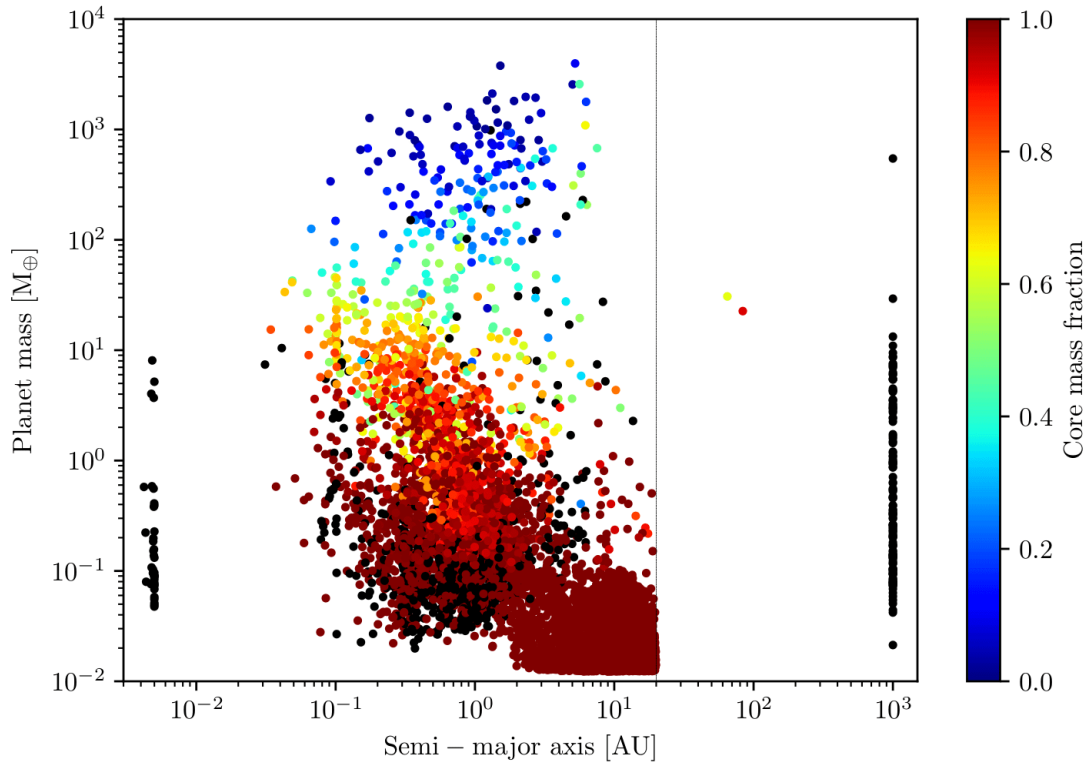


Figure 4.21: Mass versus semi-major axis of formed planets from a population generated with the original migration scheme.

4.5.4 Application to whole populations

As a last check, we apply the same modification to a complete population of formed planets. The results are shown in figures 4.21 and 4.22. The former has the same properties as the for the results shown in figure 4.10, but it is nevertheless shown here as the base model itself has been modified quite a bit in order to accommodate the part to enable reference frame conversion. We see here that the reference population has not much changed compared to the previous one.

The same general outcome as in the comparison of a single system applies here as well, i.e. that no strong effect is found. The number of planets with masses greater than about $100 M_{\oplus}$ is similar as are their locations. In both cases there are no massive planets further away than 13 AU. The implication is that eccentricity damping produces almost no spurious outward migration in the reference population. We thus confirm the previous results from the former part that with the modified migration and damping time scales, the change of reference frame is of small importance.

The moderate and relatively high eccentricities ($e > 0.01$) are slightly shifted downwards by about 10% when using the Jacobian coordinates, so the difference is not important. It is useful to remember however that these eccentricities are still computed in the heliocentric frame and so they don't correspond exactly to the values. To be rep-

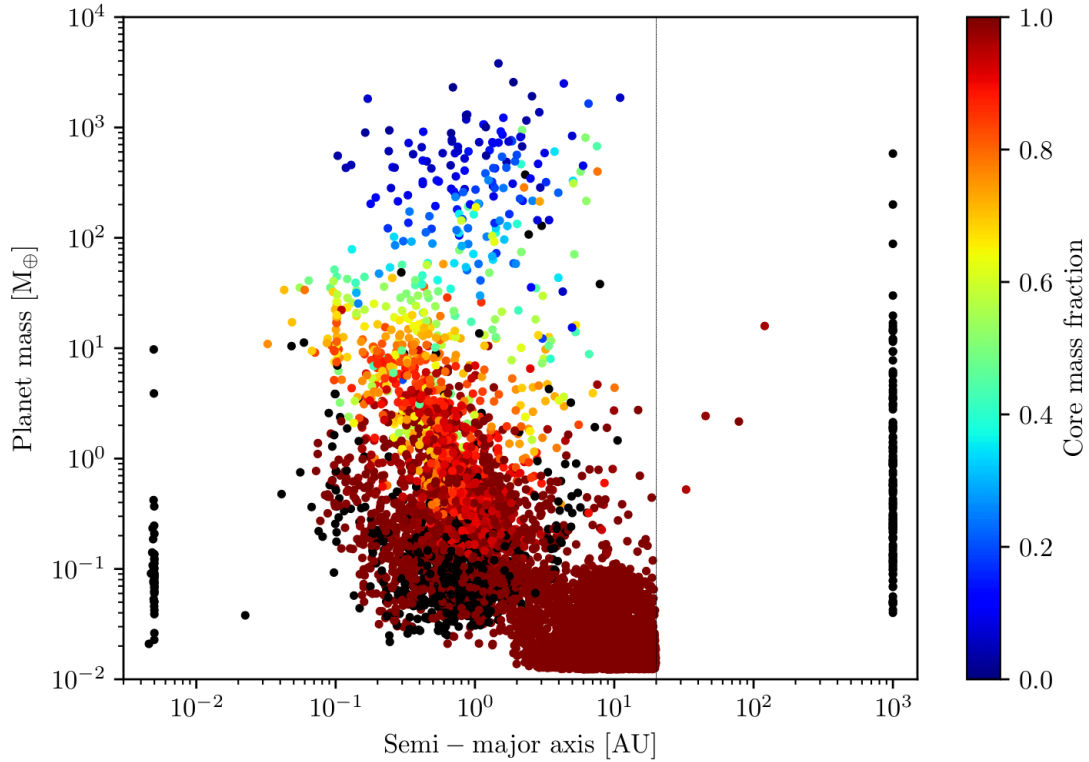


Figure 4.22: Same as figure 4.21, but with Jacobian frame to compute migration.

representative, the orbital elements given to the remainder of the formation ought to be computed with the same frame as for migration. This has been attempted, but raised further problems that have not been addressed yet; those results are unfortunately not available to present in this work.

As a conclusion to this chapter, the modification of the damping time scales has been sufficient in order to prevent the strong spurious outward migration. The underlying problem is still present, though, but the rate of artificial migration induced by the eccentricity damping is low enough to not be significant. Also, the uncertainties on the migration rates make the change unnecessary, as the shift would be on the same order (or even smaller).

Chapter 5

Collisions during planetary formation

Collisions between similar size object are important, as single events may lead to substantial changes in body properties, for instance mass, internal structure and trajectory. During planetary systems formation, the most massive objects are the planets themselves. The presence of multiple forming planets in a single system will stir eccentricities, potentially bringing the planets onto crossing orbits. Interactions with the gas disc leads to migration, which may also bring planets closer together, as well as damping of eccentricities and inclinations.

The work presented in this chapter is related to collisions between planets during their formation stages. We use the formation model described in chapter 3. Collisions are detected in the N-body (section 4.1.1). We start with the demographics of the collisions, to understand which cases are the most likely and to select which regime of collisions should be improved. We also study the effects of two parameters: the approach used to compute and eccentricity and inclination damping time scales, and the radius used for collision detection. The effects of collisions onto planetary formation are studied in section 5.3 for single planets and section 5.4 for whole populations. On a further step, the current simple collision model will be improved to reproduce the diversity of outcomes.

We shall first discuss the parameters that characterise a collision event, which will be used throughout this chapter. Firstly, there are the two involved bodies, the most massive is called the *target* and the other one the *impactor* (or sometimes *projectile*). Each body has its properties such as mass, bulk density, internal structure or rotation. Here we restrict to the case of spherical, no rotating, homogeneous bodies. They are described thus by two parameters: mass (m_{tar} and m_{imp} respectively) and radius (r_{tar} and r_{imp}). The mass ratio between the two objects is given by

$$\gamma = \frac{m_{\text{imp}}}{m_{\text{tar}}}. \quad (5.1)$$

Secondly there are two parameters are needed to describe the event, normally the impact velocity and geometry. A collision occurs when the objects touch each other, i.e. when their relative distance is

$$r_{\text{coll}} = r_{\text{tar}} + r_{\text{imp}}, \quad (5.2)$$

which enables us to retrieve the mutual escape velocity

$$v_{\text{esc}} = \sqrt{\frac{2\mu}{r_{\text{coll}}}} \quad (5.3)$$

where μ is the standard gravitational parameter

$$\mu = G(m_{\text{tar}} + m_{\text{imp}}) \quad (5.4)$$

and G the gravitational constant. The impact velocity v_{coll} is often expressed in terms of escape velocity. Impact geometry is given either by the impact angle θ_{coll} or the impact parameter b . The relation between the two is given by

$$b = \sin \theta_{\text{coll}}. \quad (5.5)$$

Here we use the definition that $\theta_{\text{coll}} = 0$ indicates a head-on collision while $\theta_{\text{coll}} = \pi/2$ denotes a grazing event, when the two bodies barely interact with each other. More on the subject of celestial mechanics related to collisions will be treated in section 6.6.3.

5.1 Demographics

To improve the treatment of collisions, we must first know what kind events are observed. This will help us determine which are the most frequent cases and focus ourselves to improve the treatment on those. The knowledge of the nature of giant collisions is also interesting by itself.

This section is divided in sub parts, where different aspects of the formation are modified. We begin with the standard parameters, then change the approach to compute the eccentricity and inclination damping time scales to follow Cresswell and Nelson (2008) when in type I migration, which is the approach described in section 4.4.

The analysis will first be performed on a planet population that has been modelled with the standard parameters of the formation model. As such, the approach to compute the damping time scales is to follow Fogg and Nelson (2007) when the planet is in type I migration and to use equation (3.42) while in type II. We will change to use approach discussed in the previous chapter further on.

The starting point is the occurrence rate of collisions. Figure 5.1 shows a histogram of the number of collisions per planetary system among the population. Note that planets may also be lost due to a collision with the central star or being ejected from the system, so the numbers presented here do not reflect the number of planets that reached the end of the formation stage. The planet population is based on 920 systems. With 924 collision events in total, there is on average, one collision between planetary embryos per system during the formation stage. There are 524 systems, or about 57%, which have no collisions at all. Then we observe 128 systems which have a single collision, and this values steadily decreases down to a single system having 8 collisions.

We continue with the relation between the number of collisions and the mass of the planets formed. Cumulative distributions of both the number of systems and of collisions

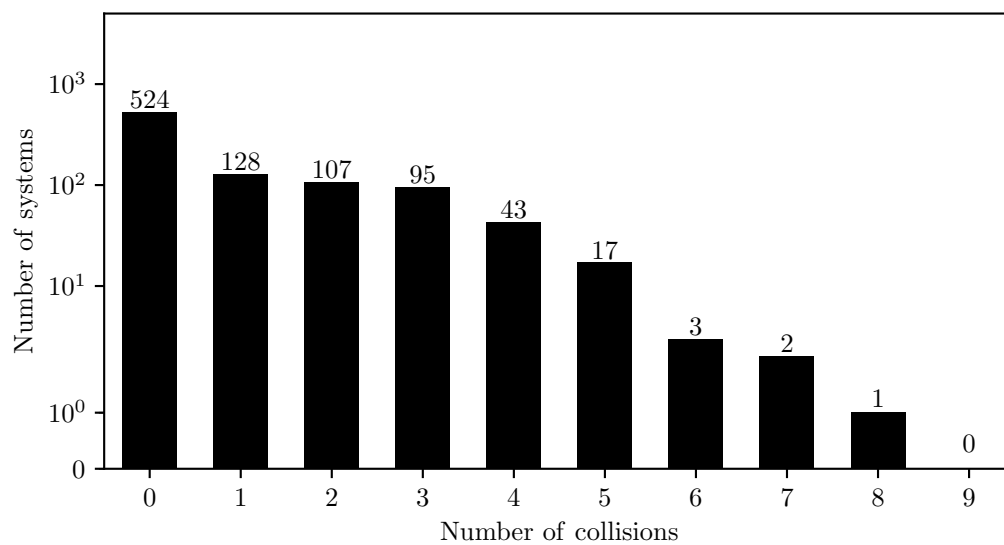


Figure 5.1: Histogram of the number of collisions per forming system. There are 920 systems and each one has initially ten embryos, so at most nine collisions may occur.

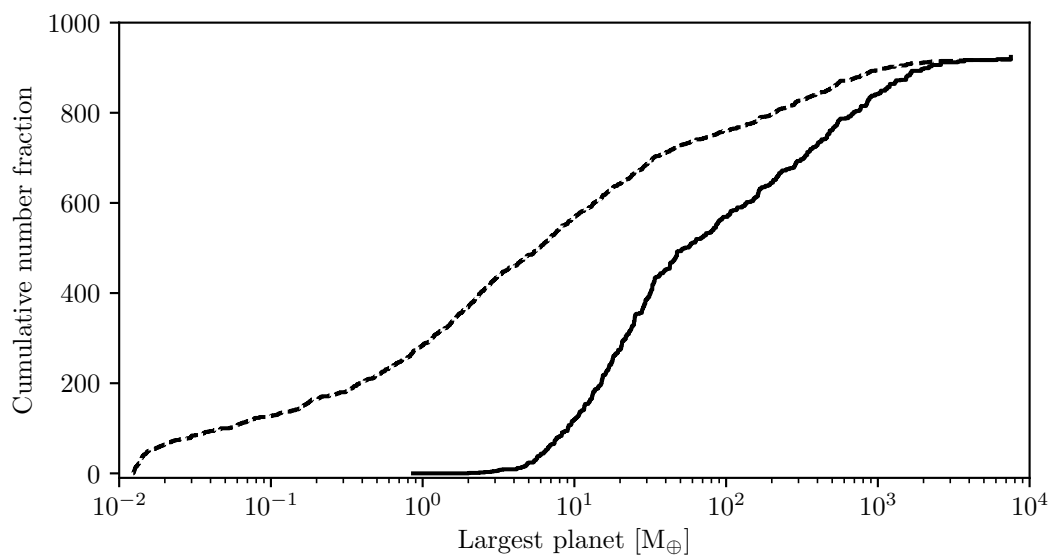


Figure 5.2: Cumulative distribution of the number of collision (solid line) and planetary systems (dashed line) versus the mass of the biggest planet at the end of formation.

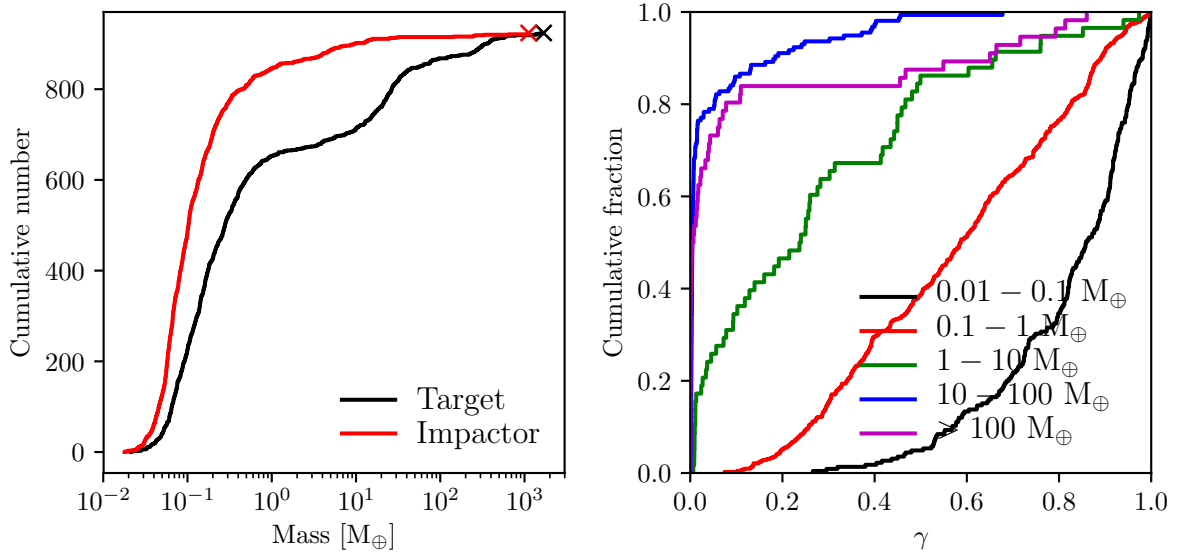


Figure 5.3: *Left*: cumulative mass distribution of planets that collide. The crosses denote the end of each distribution. *Right*: cumulative distributions of the mass ratio γ , for different mass ranges of the target body.

against the mass of the heaviest planet formed in the system are shown in figure 5.2. A direct result is that no collisions occur in systems where all planet remains below $0.8 M_{\oplus}$ despite the fact that they represent about one third of the systems. The number of collisions then increases slowly for systems with planets up to $4 - 5 M_{\oplus}$; most of the collisions taking place in systems with planets more massive than $5 M_{\oplus}$. Both distribution are similar for masses above about $10 M_{\oplus}$. This indicates that there is no, or only a small, influence of more massive planets on the likelihood of collisions. There are a few reasons why there are no or few collisions for system with small mass planets. It might be related to the fact that these systems are rather short-lived and with light discs. Also low mass planets do not induce strong dynamical interactions between the planet, and the radial velocity induced by migration goes linearly with the planet mass in type I migration (see chapter 3.3 and specifically equation (3.27)). So, if the systems where no planet is more massive than the Earth are taken out, then there are 285 systems less. There is the single collision event in them. This implies that the rate of collisions jumps to about 1.56 per system.

We now come to the collision parameters, and start with the masses. The left panel of figure 5.3 show the cumulative mass distribution for both the target and impactor. The horizontal distance between the two curves gives an estimate of the mass ratio of collision: the closer the two curves are, the more the average γ approaches unity. As the minimum mass of the embryos is slightly more than $10^{-2} M_{\oplus}$, there is a lower boundary for γ in the mass range below $\sim 10^{-1} M_{\oplus}$. A high proportion of collision events happen for target masses lower than $\sim 1 M_{\oplus}$: 652 events out of 920 or 71 %. A plateau is then reached, and only 58 targets have a mass between 1 and $10 M_{\oplus}$, whereas this value goes up to 157

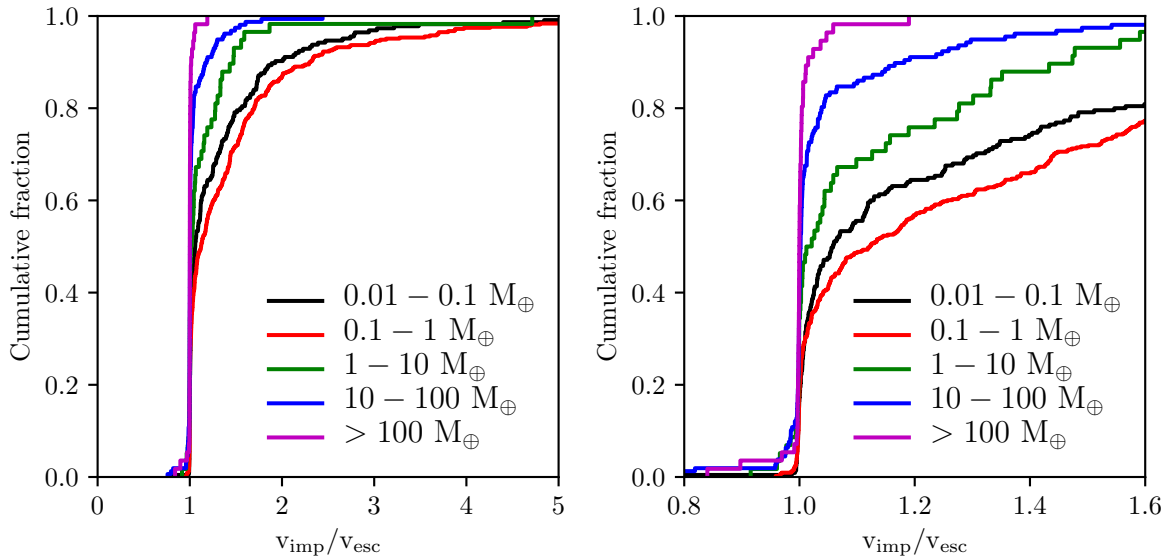


Figure 5.4: *Left*: cumulative distribution of the impact velocity in term of escape velocity for various mass ranges of target body. *Right*: the same but zoomed on the region $0.8 < v_{\text{imp}}/v_{\text{esc}} < 1.6$.

for target masses between 10 and $100 M_{\oplus}$. Finally, there are 56 events remaining that have a target mass bigger than $100 M_{\oplus}$. In contrast, the number of projectiles shows no such plateau, the number steadily decreases. The deduction is that events where the target is between 10 and $100 M_{\oplus}$ have the lowest mass ratio. Interestingly, the two curves re-approaches for massive objects, and there are a few events with a massive impactor. This is verified by plotting γ for different mass ranges of the target, as on the right panel of figure 5.3. We find that this value is globally lower (indicated by a curve rising for γ values close to zero in the cumulative plot) as the target's mass increases, except for the most massive bin ($m_{\text{tar}} > 100 M_{\oplus}$) that lies somewhere between the two previous bins.

The impact velocity is related to the specific kinetic energy involved in the collision, which provides information on the outcome. It is usually given in terms of the escape velocity, as this allows to get an idea of the relative velocity at large separation.

Figure 5.4 shows its distribution. The higher spread for the low target mass bins is more due to the lower mutual escape velocity rather than different distribution of relative velocities. Following energy conservation, the relation between impact, escape and relative velocity at infinity is given by

$$v_{\text{coll}}^2 = v_{\text{esc}}^2 + v_{\infty}^2. \quad (5.6)$$

This relation is only valid for $v_{\text{coll}} > v_{\text{esc}}$. The opposite case should not be common as it requires the objects to be bound prior to the impact (the additional acceleration terms that model the effects of the gas disc might be the cause). To determine what constraints such velocities imply on pre-impact orbit, we can make a simple theoretical calculation of the maximum distance between the two objects, i.e. the distance at which the relative

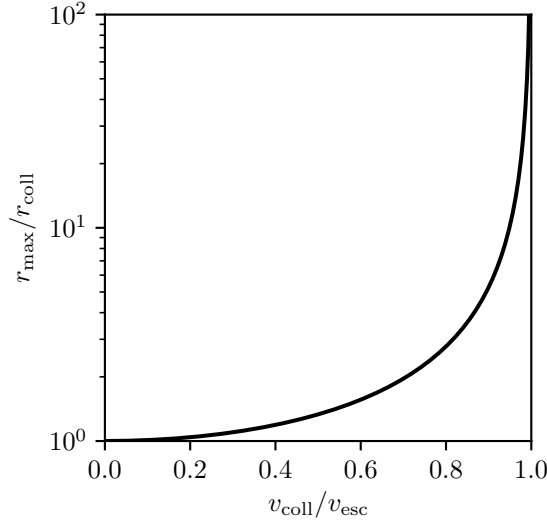


Figure 5.5: Maximum separation between two objects in the impact velocity is a given fraction of the escape velocity.

velocity is zero. We will use orbital energy defined by equation (6.80) and assume that the impact velocity is a fraction of the escape velocity $v_{\text{coll}} = t \cdot v_{\text{esc}}$. We want to obtain r_{max} , the distance at which $v = 0$. We thus use energy conservation and write

$$\epsilon = \frac{v_{\text{coll}}^2}{2} - \frac{\mu}{r_{\text{coll}}} = -\frac{\mu}{r_{\text{max}}}. \quad (5.7)$$

Let's now divide the whole equation by μ and substitute v_{coll} by its expression, so we obtain

$$\frac{t^2 \left(\frac{2\mu}{r_{\text{coll}}} \right)}{2\mu} - \frac{1}{r_{\text{coll}}} = -\frac{1}{r_{\text{max}}} \quad (5.8)$$

which after simplification becomes

$$\frac{t^2 - 1}{r_{\text{coll}}} = -\frac{1}{r_{\text{max}}}; \quad \frac{r_{\text{max}}}{r_{\text{coll}}} = \frac{1}{1 - t^2}. \quad (5.9)$$

The only dependence on the body properties is in r_{coll} , the sum of their radii. The corresponding relation is shown in figure 5.5. For instance, to obtain $v_{\text{coll}}/v_{\text{esc}} = 0.95$ the bodies should have no relative velocity at a distance which is about ten times r_{coll} . This ratio decreases to about five if $v_{\text{coll}}/v_{\text{esc}} = 0.9$. However, it is practically impossible to find a situation where such bodies have no relative velocity so close together; this means that collisions where $v_{\text{coll}}/v_{\text{esc}} \lesssim 0.95$ need some mechanism to reduce the relative velocity as the bodies approach. If we look back at the distribution (figure 5.4), we find 13 such events. Of those, 10 have a ratio lower than 0.9. They warrant further investigations to determine the mechanism that can produce such low impact velocities. For each, we find

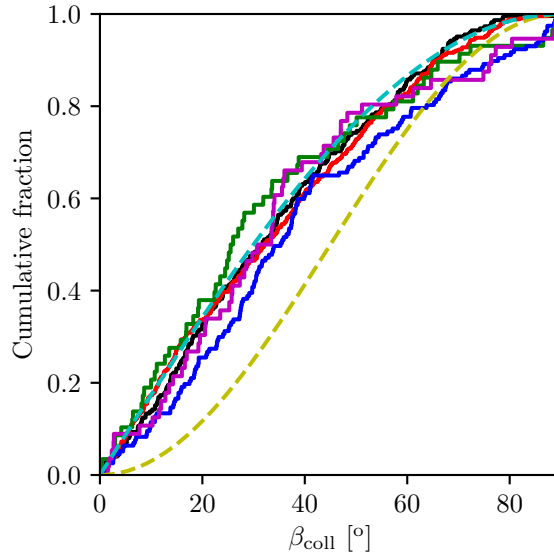


Figure 5.6: Cumulative distribution of the impact angle. The different ranges of target mass are the same as in the previous figure. In addition, a theoretical distribution from Shoemaker (1962) (dashed yellow) and a modified one for 2D systems (dashed light blue, see text) are displayed.

that the damping time scales of at least one of the involved body is comparable or shorter than the orbital period, which is not consistent with the formalism as the latter is based on an orbit averaged description. During the approach the velocity vector can slightly differ from the one of a circular orbit due to the mutual interaction. The damping terms (either for eccentricity or inclination) will thus try to re-circularise the orbit, by adding a force which is directed against the relative motion. This effect induces a reduction of the relative velocity all along the path, and thus leads to the observed distribution of impact velocities. *Note:* the damping force is not in the opposite direction of the velocity, but in the direction of the radial vector and pointing against the velocity vector; equations (4.8) and (4.9). We may thus say that the migration can influence the collision parameters, and a correct migration and damping scheme is also important for collisions. The problem is however different from the one seen in the previous chapter. The model at base for this analysis is based on the original one for the population synthesis, that is with the damping time scales computed according to Fogg and Nelson (2007) for the type I migration. The comparison with the scheme proposed in the previous chapter (i.e. computing the damping time scales according to Cresswell and Nelson 2008 when in type I) will be performed in section 5.1.1.

The last collision parameter is describing the geometry. There are various possibilities to express it, such as angular momentum, impact parameter or angle. Here the choice is to use the impact angle. The distribution is shown in figure 5.6. In addition, a theoretical distribution can be computed according to Shoemaker (1962). It assumes that the probability of the impactor being located at any point within the capture cross-

section is the same (at large separation), and thus the differential probability is

$$dP = 2 \sin \beta_{\text{coll}} \cos \beta_{\text{coll}} d\beta_{\text{coll}} \quad (5.10)$$

where β_{coll} is the impact angle. In our convention, 0 denotes an head-on collision and 90° a grazing one. The above relation implies that the most likely collision, as well as the mean and median of the distribution are located at 45° . For our simulations however, the mutual inclinations are low, and thus there is an higher probability that the objects will both have a trajectory in the plane of the proto-planetary disc. The limiting case is then a 2D system where all orbits are on a single plane. In this case, the theoretical distribution is modified, and the probability that the impactor will pass at a distance x from the capture cross-section R is now

$$dP \propto dx \quad ; \quad P(R) = 1 \quad (5.11)$$

(compared to $dP \propto x dx$ in the original case). The derivative of the impact angle with x remains the same, so that we easily obtain

$$dP = \cos \beta_{\text{coll}} d\beta_{\text{coll}}. \quad (5.12)$$

This modified distribution favours head-on collisions compared to the true 3D one. For instance the median is now at 30° and the probability to find head-on events is non-zero. Both theoretical distributions are shown in figure 5.6, with dashed yellow line for the 3D probability (the one from Shoemaker 1962) and dashed light blue for the modified one derived here.

The obtained distributions follow more the modified distribution than the original one. This indicates that it is likely that the collisions happen on a plane rather than randomly in space. Indeed, the two small mass bins barely differ from the 2D distribution. For the larger ones, they are further away, but we may note that there are fewer events there and so it is possible that this come from the statistics. We also observe quite a few events that happen with an almost grazing angle, whereas both distribution indicate that only few events shall take place at such angles. We might recall what has been discussed in the previous paragraph about the modification in the trajectory induces by the damping forces which also affect the impact angle in addition to the impact velocity, as we shall see in the next section.

5.1.1 With damping prescription from Cresswell and Nelson (2008)

In the previous section, we saw that there are quite some collisions with low impact velocities $v_{\text{imp}}/v_{\text{esc}} < 0.9$ and that the distribution of impact angles relates more to a 2D system rather than a 3D one. It is possible that these outcomes are related to the external forces that model eccentricity and inclination damping. The magnitude of those forces has been computed following the approach of Fogg and Nelson (2007). It has been observed in section 4.4 that during type I migration, the time scales obtained while following the approach by Cresswell and Nelson (2008) are roughly one order of

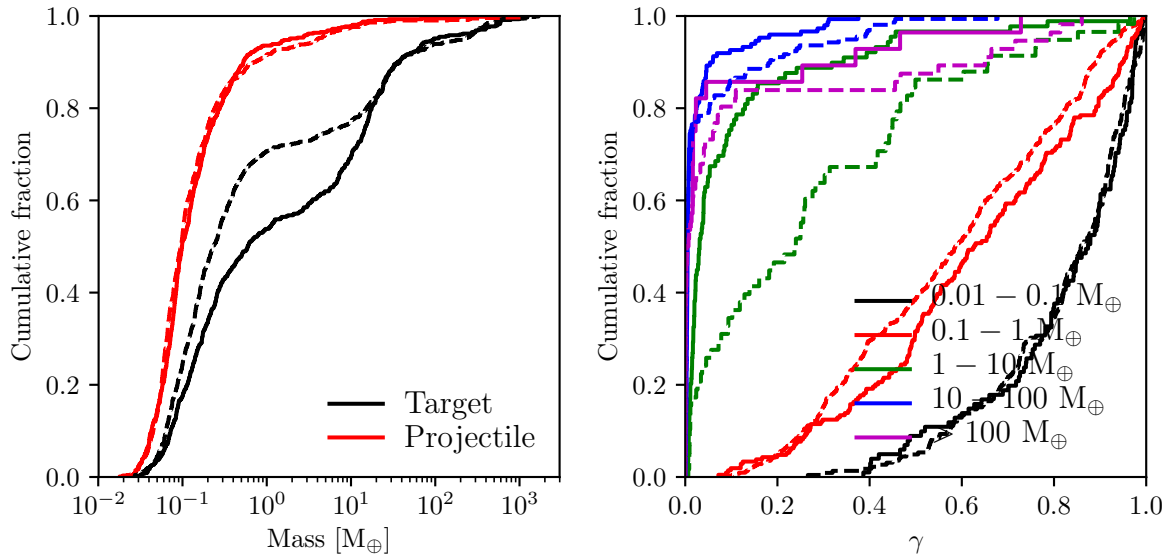


Figure 5.7: Same as figure 5.3, but the damping time scales for type I migration have been computed following Cresswell and Nelson (2008). The dashed curves represent the cases shown in the referenced figure to ease comparison. The left panel is now normalised as the total amount of collisions is different.

magnitude larger, hence the force weaker. We thus change the approach to compute the damping of eccentricity and inclination time scales to the one proposed in the previous chapter: following Cresswell and Nelson (2008) when the planet is migrating in type I. This should lower the effects of the damping scheme on the collision parameters. When the value of the damping time scale is comparable with the orbital period, then force may act on the same scale as the one needed for the bodies to approach and thus affect the final trajectory just prior impact. These forces should not act on such small time scale, and so the purpose of the change is to prevent this situation from happening.

A new population with the modified model has been generated. To determine whether short damping time scales are the cause of these surprisingly small impact velocity, we will compare the collision properties of the new population with the one analysed in the previous section. The number of systems is not the same, however.

On average, a slightly lower amount of collisions is found per system: 1.41 when taking only the ones that have a planet that reached $1 M_{\oplus}$ (9-10% less than previously). The distribution of number of collisions per system changes slightly: while the proportion of systems without collisions remains the same, there are more systems with one or two collisions and less with a higher number. For the distribution of target masses, a higher proportion is found in the $10^1 - 10^2 M_{\oplus}$ mass range while the plateau between 1 and $10 M_{\oplus}$ remains. On the other hand, the impactor masses remain similar (figure 5.7; left panel). The γ values are thus modified accordingly, as the values are only slightly shifted towards unity for the $10^{-1} - 1 M_{\oplus}$ bin, and the two next bins (right panel of the same figure).

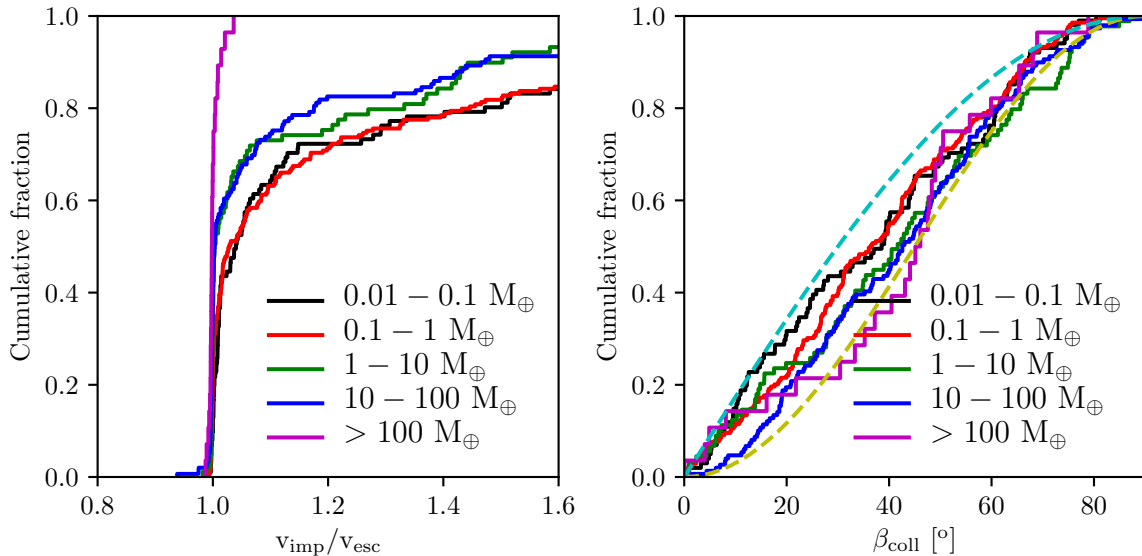


Figure 5.8: *Left*: same as right panel of figure 5.4, but the damping time scales for type I migration have been computed following Cresswell and Nelson (2008). *Right*: same as figure 5.6, with the same modification.

We find that modifying the damping time scales also affects the distributions of the other two collision parameters. For the impact velocity (figure 5.8; left panel), the relative number of events with $v_{\text{coll}} < v_{\text{esc}}$ slightly increased from 27% to 30%. However, the numerical integration may produce an error in the actual impact velocity. Thus, if we use the condition $v_{\text{coll}}/v_{\text{esc}} < 0.99$, then we find the opposite situation where the relative number of collision matching this criterion reduces from 4.7% to 1.7%, almost a factor three. Additionally, the lowest relative collision velocity found is 0.94, whereas before it went down to 0.75. We thus encounter less and not such extreme values for this parameter. There are also changes on the other side of the curve: except for one bin ($10 - 100 M_{\oplus}$; in blue on the figure), there are relatively more collisions with velocity close to the escape one.

The distributions of impact angles (figure 5.8; right panel) are now in between the theoretical curves for 2D and 3D systems. While for the low angles ($\beta_{\text{coll}} \lesssim 10^{\circ}$) the distributions are more consistent with the 2D case, while they get closer to the 3D one for grazing angles.

The computation of the damping time scales following the Fogg and Nelson (2007) approach in type I migration migration is responsible for a good part of the low impact velocity cases as well as for the impact angle distribution which relates to theoretical expectation of 2D systems. Changing to the approach by Cresswell and Nelson (2008) leads to a reduction by a factor of about three of the number of events that have $v_{\text{coll}}/v_{\text{esc}} < 0.99$ and the lowest impact-to-escape velocity ration is 0.94 compared to 0.75 previously. The distribution of impact angles also follows the expected one more closely. The modification of the approach to compute the damping time scales results in a reduction of unrealistic

collision events. For the remaining of this chapter, we will use this modified approach to obtain more realistic impact properties.

5.1.2 Dependence on the number of embryos

The standard case for planetary formation simulations is to start with 10 embryos. The choice of this number is a result of a trade-off between physical correctness and time required to perform the simulations themselves (the most resources consuming part of the code is the N-body which has complexity of $\mathcal{O}(N^2)$). It was shown (Swoboda in prep.) that the number of formed giant planets converges when there are at least ten embryos per system. We did observe however that most of the collisions happen with small bodies, whose number does not converge with this number of embryos. So, we will now check the dependence of the previous collisions analysis with the initial number of embryos per system. For comparison, a population with twenty embryos per system has been generated.

We first analyse the general outcome. The standard mass-distance plot is shown in figure 5.9. The difference in the number of embryos implies that there are less planets with the ten embryos case (5416 versus 8080) whereas the number of systems is higher (615 versus 472). For comparison, the influence of the initial location of the embryos is shown in figure 5.10. The original planet population in black is the same as the one with ten embryos shown in figure 5.9, while the one with modified initial placement of the embryos is shown in red. With twenty embryos, the maximum mass is $1739 M_{\oplus}$ whereas this value goes up to $2306 M_{\oplus}$ with ten embryos. In the remaining of the mass distribution, there are slightly more planets per system with masses above $10 M_{\oplus}$ with ten embryos, an equivalent number in the $1 - 10 M_{\oplus}$ range; the over number of planets remains in the mass range below $1 M_{\oplus}$. This confirms the previous results (e.g. Swoboda in prep.).

As expected, where there are twenty embryos per system, the number of collisions increases. Across the 472 systems that were formed, 1245 collisions were detected. This results in a mean of 2.6 events per system. The same behaviour as for the relation between the number of events and the mass of the biggest planet is observed, as only 111 collisions occur in the 200 systems where no planet reach the Earth mass. For the other systems (the ones where one planet reaches at least one Earth mass), 28 of them do not experience a collision at all.

The change of the mass distribution found in the general outcome should also be reflected in the collision properties. The distribution of γ does not change for target masses lower than $1 M_{\oplus}$; but for higher ones, then its values moves towards zero. This means that for massive targets, impacts with small bodies are more frequent. One should also remember that there are more collisions in total, and on an absolute scale, there are more events with γ close to unity. The impact velocity shows a similar pattern. The impact angle distribution is not significantly affected.

The increase of the initial number of embryos induces a higher rate of collisions with the small bodies. The number of collisions with planets more massive than $10 M_{\oplus}$ is not affected by the number of embryos per system. Thus the number of embryos per system

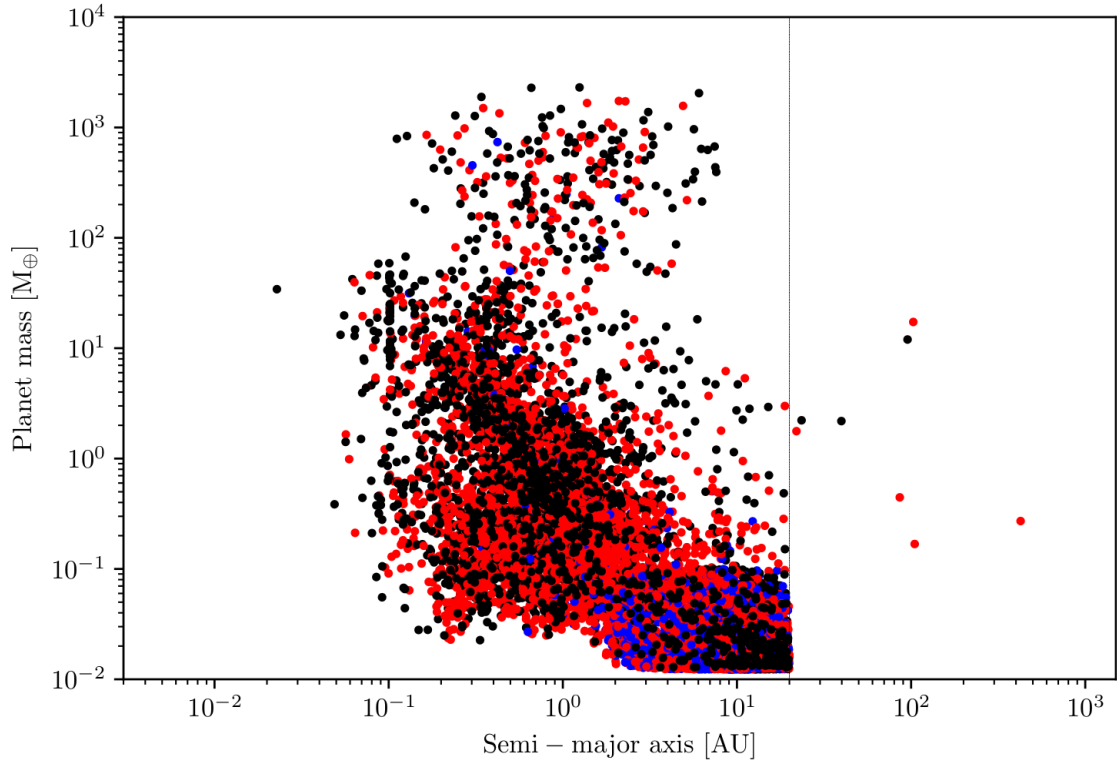


Figure 5.9: Comparison of two populations generated with the same parameters, except for the initial number of planetary embryos. The one in black has 10 embryos per system whereas the one in red has 20. Planets shown in blue have the same characteristics in both populations (within a tolerance of 10 % in both mass and distance). For simplicity, all bodies that were lost during the formation phase (due to either collisions, accretion by the central star or ejection) are removed from the plot. The number of planets are 5416 and 8080 respectively.

does not affect significantly the collisions with giant planets. It may at most play a role during the early stages when the solid core is being built as the number of collisions is higher for such bodies. As there is no significant influence of the initial number of embryos on the formation giant planets due to collisions, we will stick to the usual value of 10 embryos per system.

5.1.3 Influence of radius used for collision detection

As discussed in section 4.1.1, the radius set for purpose of collision detection is different from the one found by internal structure model. The procedure to treat collisions is simple, i.e. the cores are merged and the fate of the envelope depends on the collision energy. So, to be consistent with this procedure, we only want take into account collisions that will end up with the solid cores interacting with each other, either directly or following aerodynamic due to the traversal of the gaseous envelopes. For the planets without

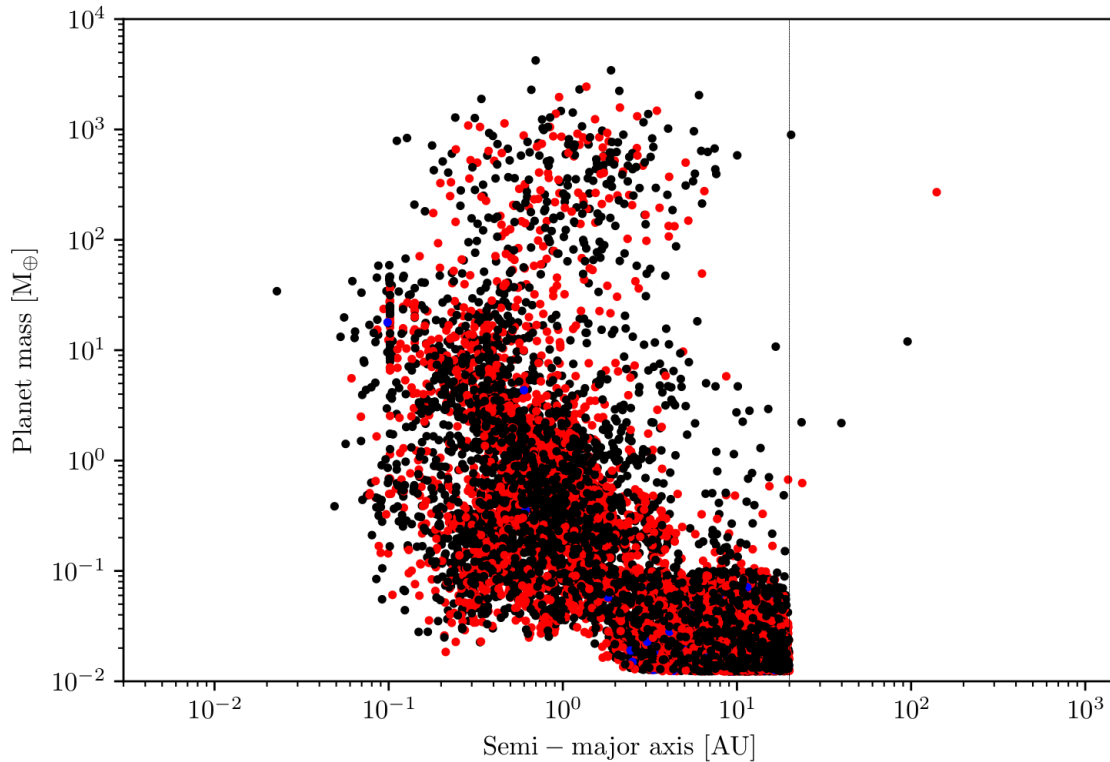


Figure 5.10: Comparison of two populations generated with the same parameters, except for the initial location of planetary embryos. The original one is in black while the one with modified initial location is in red.

no significant envelope there is no problem as the core radius is readily available to serve this purpose, but once the planet has accreted a significant amount of gas, the problem becomes more complicated. In the latter case, a lower limit for the separation at which the drag is almost certain to be sufficient to bring both cores together can be estimated in the following way: calculating the total radius assuming that the envelope has the same density as the core. This approach is however not accurate for gas giants where the core represents a small fraction of the total mass. After the change of accretion regime and the contraction of the envelope, its scale height becomes small compared to the radius. Thus, an object going through the atmosphere will most often suffer a strong aerodynamic drag. In this regime, the assumption that a body going through the envelope of the planet will get gravitationally bound and the event ending up in a merger is relatively accurate. In this section, we investigate the influence of the successive improvements of the criterion to set the radius used for collision detection.

To compute the radius for the purpose of collision detection, the core radius is required. In our formation model, the embryos start with roughly the mass of the Moon and the corresponding radius is thus similar to the Moon radius

$$r_{c,ini} \approx 1763 \text{ km.} \quad (5.13)$$

In the old model, it was assumed to remain constant during the formation phase for the purpose of computing the resulting radius using equation (4.4). The results presented in this chapter are already computed with a core radius consistent with the remaining of the formation model. It is however interesting to use this opportunity to see the influence of the collision radius on the number of collisions.

The different possibilities for the collision detection algorithm that will be investigated in this section are:

- No detection at all; which is equivalent to setting the radius to zero for the purpose of collision detection.
- The old, incorrect method, described in the previous paragraph.
- The current method, where the radius is computed according to equation (4.4).
- The current method in the planet-dominated accretion regime (*attached* phase), and the planetesimals' capture radius in the disc-dominated accretion regime (*detached* phase).

Note that neither of the first three methods produces a radius which is consistent with the envelope structure calculation, and the fourth one only does so in the later phase of growth of massive planets. In the *attached* case, when the envelope is in equilibrium with the proto-planetary disc, the outer radius is defined by equation (3.10). The boundary conditions require that the envelope's pressure is equivalent to proto-planetary disc. It is therefore not realistic to treat all the cases where bodies go through the envelope as mergers. The consistent way would be to compute the trajectory inside this radius and determine whether the two would become gravitationally bound due to the drag produced by the encountered mass of gas. For the *detached* case, the boundary conditions change and the radius is determined in function of the envelope's mass. The scale height is also smaller so that the encountered mass of gas become rapidly big when a body crosses the outer radius. This implies that a body going through the envelope of the planet will suffer from substantial aerodynamic drag, even in the upper layers. The initial contraction phase is more delicate, as for a short period of time (of the order of a few thousand years) the outer radius is similar to the Hill's radius, like in the attached phase. To avoid accretion of large bodies going through the other region, the capture radius of planetesimals can be used as a compromise.

As an example, the radii given by the different methods mentioned above are shown in figure 5.11. This shows the formation phase of a single planet for an in-situ case at 5.2 AU. The black lines show the different planet radii or methods to determine the collision radius. The long dashed line represents the outer planetary radius, which is computed according to equation (3.10) in the attached phase. The short dash-dotted line shows the planetesimal's capture radius, which is initially equal to the core's radius and gets larger when envelope structure calculation is enabled once the core reaches $0.1 M_{\oplus}$. The short dashed line shows the old, inconsistent method for comparison. As long as the envelope mass is small in front of core mass (until about $4 \cdot 10^5$ yr), the radius remains constant. Only when a massive envelope has been accreted is this value changing. This

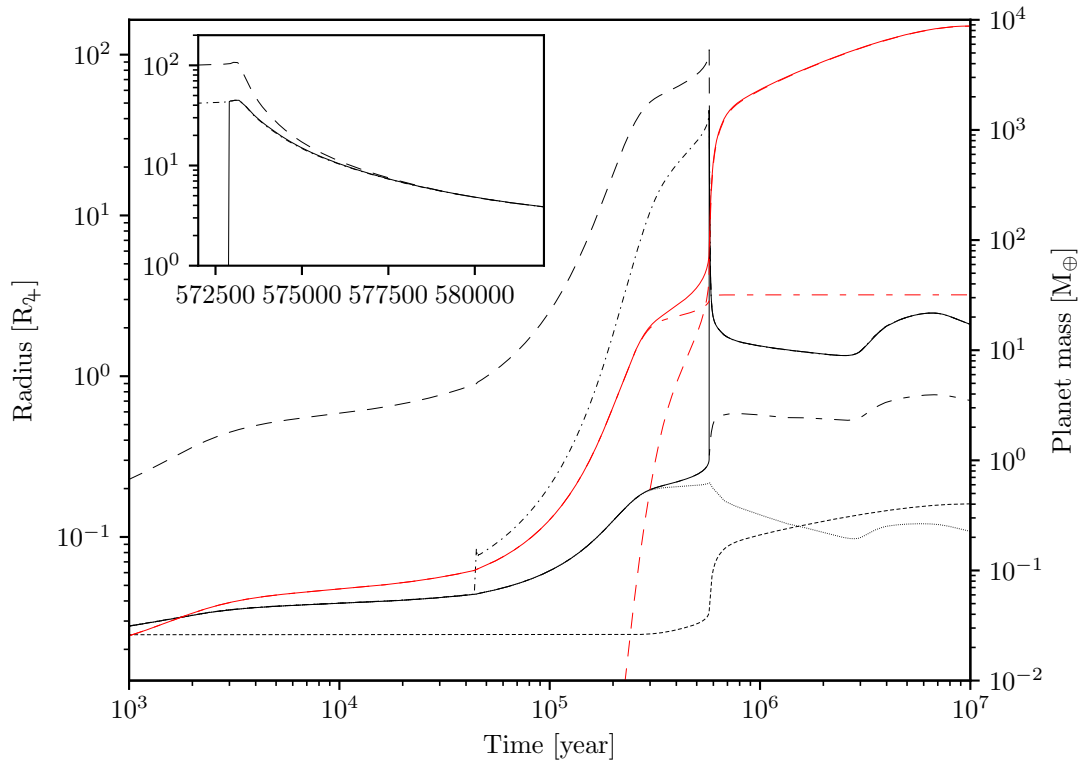


Figure 5.11: Comparison of the radii that given by the different method used for collision detection. Black lines: radii (left scale); solid: the new model; long dashed: outer radius, long dash-dotted: assuming core density across the whole planet; short dashed: the previous, incorrect method, short dash-dotted: planetesimals' capture radius; dotted: core radius. Red lines: masses (right scale); solid: total, dashed: envelope, dash-dotted: core. Top left: Radii as function of time close to the change of accretion regime; the time span is 10^4 years.

happens only shortly before the accretion regime changes. The long dash-dotted line is the radius computed assuming core density across the whole planet. Early on, this is equivalent to the core radius itself, but we note that this value is a factor of two higher than the one obtained by the previous method. Finally, the solid line shows the radius computed with the new method, where the collision radius is consistent with the outer radius in the disc-dominated regime. In this case, we observe that there is about a factor two between this and the previous method, indicating that the mean envelope density is lower than the core one. The contraction of the core following the change of accretion regime is due to the increase of the pressure at the core-envelope boundary. The increase of radii starting at 3 Myr is due to increase of luminosity resulting from deuterium fusion. Core radius increases following the decrease of pressure at the core-envelope boundary resulting from the envelope expansion. In the insert on the top left of figure 5.11, the behaviour of the outer and planetesimals' capture radii during the initial contraction phase can be observed. During a small period, the two radii remain large and then contraction takes place. The planetesimal's capture radius is initially about the half of the outer radius, but converges with the latter within a few thousand years.

We now compare the effect of the collision detection radius on planet populations. The populations have the same initial conditions, and only the systems that finished to compute in all of them are accounted for. This is slightly different for the last approach with the consistent radius in the detached phase: an enhanced formation model need to be used to obtain this value, as the original model does not compute the structure in the detached phase. The results are then separated according to the formation model to disentangle the effects due to the method used to retrieve the radius for collision detection from the change of formation model. The nominal formation model is used to compute the first three cases and the enhanced one for the last method. The current approach to determine the radius has been used twice, one per for each of the two formation models.

To get a rough idea on how the radius affects the number of collisions, we first show the average rate across the different populations for the different kind of events that lead to a loss of planet: collisions between planets, collisions with the central star and ejections. We also show the number of planets that are still present at the end of the formation process. These rates are given in number of planets per system, and all populations have initially ten.

Results from the three different populations computed with the original formation model are shown in table 5.1. Each of these populations has been computed with a different method to determine the radius used for collision detection. We first note that for all of them, more than 90% of the embryos reach the end of the formation process. The number of collisions cannot be compared with the first population, as they have been purposely disabled. Between the two other populations, the average number of collisions increases by about 60%, from 0.433 to 0.708 per system. This increase is compensated in two other categories: the planets still present and the ejected ones. The average number of ejections steadily decreases as the number of collisions increases, implying a reduction of the amount of scattering events. This part is easy to understand: the closest the bodies get, the stronger their mutual interaction. So as the approach used to determine the collision radius evolves and the radius increases, the most likely cases leading to ejections

Average number of planets per system	No planet-planet collisions	Old method (fixed core radius)	Current method (consistent core radius)
in the disc	9.588	9.230	9.004
close-in (inside the disc)	0.092	0.092	0.097
collided with another planet	–	0.433	0.708
collided with star	0.069	0.049	0.054
ejected	0.251	0.156	0.137

Table 5.1: Average number of planets per system per status at the end of the formation phase; the first two categories denote planets that are still present whereas the three last are for embryos that did not reach the end of the formation phase. There are three populations, each one with a different method used to determine collision detection radii (nominal formation model).

	Current method (consistent core radius)	New method (planetesimals' capture radius in disc-dominated accretion)
Rate of planets in the disc	8.560	8.481
Rate of close-in planets	0.157	0.145
Rate of collisions	0.800	1.042
Rate of collisions with star	0.114	0.093
Rate of ejections	0.359	0.238

Table 5.2: Average number of planets per system per status at the end of the formation phase; the first two categories denote planets that are still present whereas the three last are for embryos that did not reach the end of the formation phase. There are two populations, each one with a different method used to determine collision detection radii (enhanced formation model).

Average number of planets per system	Usual initial location	Modified initial location
in the disc	8.884	8.852
close-in (inside the disc)	0.092	0.114
collided with another planet	0.790	0.782
collided with star	0.070	0.062
ejected	0.164	0.190

Table 5.3: Average number of planets per system per status at the end of the formation phase; the first two categories denote planets that are still present whereas the three last are for embryos that did not reach the end of the formation phase. There are two populations, computed with the same formation model but with different initial locations of the embryos (nominal formation model).

are prevented. However, the collision rate with the central star is mostly independent of the approach. We thus have a discrepancy between the two cases, as the only possibility of a planet being accreted by the central star is following a scattering event with another planet. Accretion by the central star is not possible only with migration, as it only works when the planet is in the gas disc and could at most bring planets to its inner boundary.

We also compare the variations observed following the modification of the radius with the ones that can be expected by varying the initial conditions. For this purpose, we consider another planet population where the only difference is the initial locations of the embryos (it is the same population as the second one show in figure 5.10). These results are provided in table 5.3. The left column is based on the same population as the right column of table 5.1, but the underlying systems are not the same, hence the fluctuations of the numbers. The variations between the two populations are in the range of 0.02 to 0.03 per system on average for every category. The variations in the number of planet in the disc, that collided with another planet and ejected following the change of radius are significant in comparison with the ones following the change of initial conditions. For the two other categories, (inside the disc and collision with the central star), the changes are not significant.

The same comparison for the new formation model is shown in table 5.2. First, we compare the results of the populations that have the same method to determine the collision radius, but using different formation models. The rate of collisions increases by around 6% for the enhanced model compared to the nominal one, whereas the number of planets that end in the central star and the one that are ejected do more than double. The small increase in the collisions fraction is not really significant and is dependent on the underlying set of simulations that are compared. Next, between the different methods to set the collision radius, we note quite a strong increase in the number of collision, of about 30%, from 0.800 to 1.042. This increase is large compared to the amount of planets that change the accretion regime, on average 0.7 per system, i.e. 7%. It indicates that there should be an increased number of collisions that occur with massive planets. We will discuss this shortly. We arrive at a somewhat different conclusion than before for the

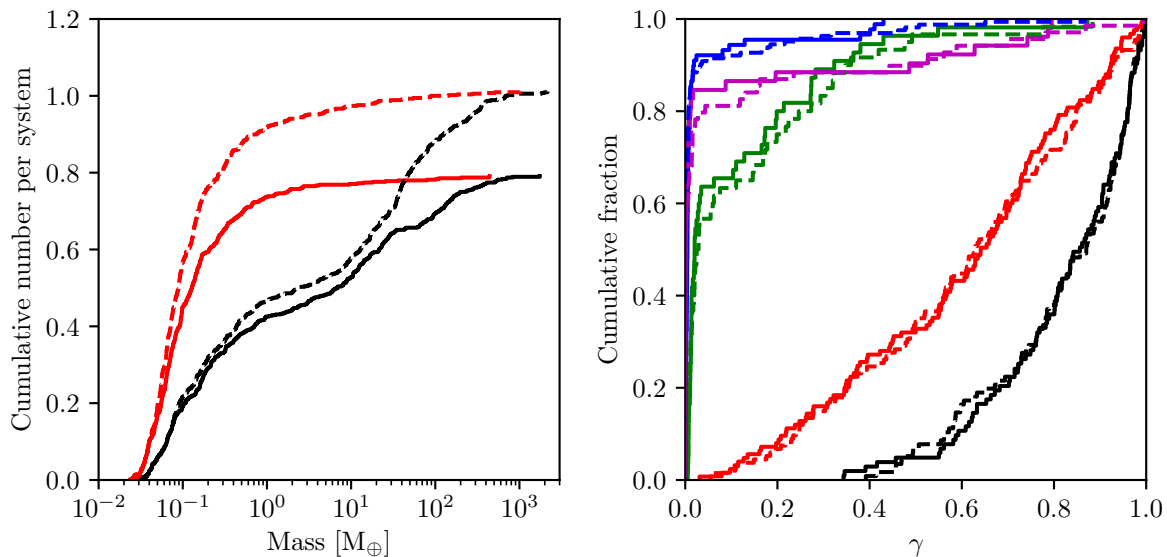


Figure 5.12: *Left*: mass distribution of the colliding bodies for the enhanced formation model with the two methods to determine the collision radius: always assuming core density (solid line) and planetesimal’s capture radius in the disc-dominated accretion (dashed line). *Right*: mass ratio distribution (colours are the same as in the previous figures).

consequence of the increasing rate of collision: it leads to a reduction principally on the number ejections, by about a factor two. The other categories decrease by a lower extend. It is however difficult to draw a conclusion on the number of planets being accreted by the central star, as the statistics are already on small numbers. Also, one can note that biggest change in this number is due to the modification of the formation model and not in the radii.

For reference, a population where the collision radius is set to the outer radius in the detached phase has also been computed. With that one, the average number of collisions per system is 1.007. Compared to the current model, the increase is about 43%, the double as when the collision detection radius has been changed to the planetesimal’s capture radius. As these are significantly different only during a short period of time after the change of the accretion regime, this indicates that quite a fraction of the additional collisions is detected during the initial contraction phase. There can still be over-detection of collisions that lead to accretion as the capture radius for planet is lower than the one for planetesimals during the initial contraction stage. However, most of those cases should be prevented by using the capture radius rather than the outer one.

Now we come to the effect on other impact properties. We will here compare the two populations generated with the new formation model. The mass distributions and the mass ratios are shown in figure 5.12. The number of events that occur for the small masses remains similar; the number of collisions increases slightly for targets masses above $0.1 M_{\oplus}$, and further above $30 M_{\oplus}$. This behaviour was expected as the radius

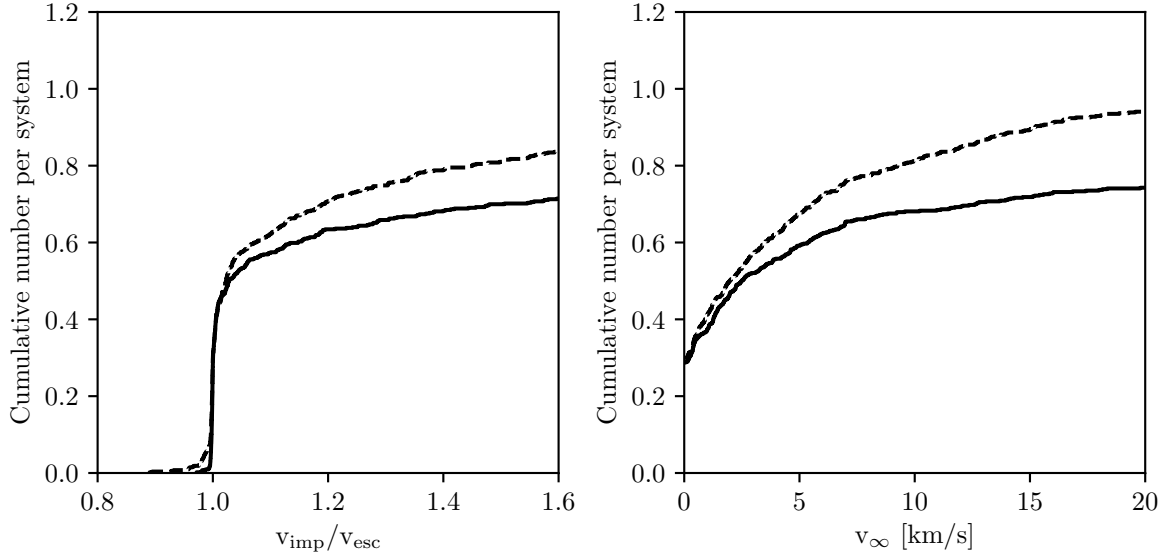


Figure 5.13: *Left*: distribution of impact-to-escape velocities for the new formation model with the two methods to determine the collision radius: always assuming core density (solid line) and planetesimal's capture radius in the disc-dominated accretion (dashed line). *Right*: as left panel, but with the relative velocity at infinity on the horizontal axis.

have only been modified for objects that went to the detached phase. Also, we note that some "features" are modified or disappear: we now find quite a few collisions with target masses between 30 and $70 M_{\oplus}$ whereas previously the cumulative distribution was showing a plateau in that range, indicating that only few events were found there. Note that in the right panel of figure 5.12, all curves are normalised to unity, therefore the relative increase of events for the higher mass bins is not directly observable. The gamma distributions retain the same overall shape, with the average value decreasing as the target's mass increase, except for the highest mass bin. Most of the differences are not significant when compared to the changes obtained by varying the initial conditions (not shown in a figure, data come from the same populations that are compared in table 5.3). The most significant change is the distribution of the $0.1 M_{\oplus} < M_{\text{tar}} < 1 M_{\oplus}$ (in red in the figure), even though the consequences are small.

The distribution of impact velocities is affected by the approach to determine the radius. The comparison for the new formation model is shown in figure 5.13. A higher spread in the collision velocity is observed with the new approach. We note quite an increase in the number of events happening with objects which are gravitationally bound prior to the impact, and we find again events with $v_{\text{imp}}/v_{\text{esc}} < 0.95$. As though not shown here, these events happen for a great majority when $m_{\text{tar}} > 10 M_{\oplus}$. On the other side, we also observe more collisions with $v_{\text{imp}}/v_{\text{esc}} > 1.1$. The change of approach affects the value of the mutual escape through r_{coll} . As the radii are now larger, the escape velocity diminishes, so for a given v_{∞} , the ratio $v_{\text{coll}}/v_{\text{esc}}$ increases. The values of v_{∞} have been retrieved using equation (5.6) and provided on the right panel of figure 5.13 (all the events

where $v_{\text{imp}} < v_{\text{esc}}$ have been gathered at $v_{\infty} = 0$). We do observe a similar behaviour for the v_{∞} distribution, meaning that the number of events where for instance $v_{\infty} > 5$ km/s increases more than the remaining, which implies that we newly detected events have higher relative velocity at large separation. As previously, this increase is mostly due to events where $m_{\text{tar}} > 10 M_{\oplus}$. The distribution of impact angle, in the contrary, shows a similar shape for both approaches.

The change of approach to determine the collision radius has been carried to make it more consistent with the remaining of the formation model. For terrestrial planets, this was not a problem, as the surface can be clearly defined and the radius is readily available. For planets with significant envelopes, the result of the drag due to the traversal of the envelope depend on, for instance, the orbital energy of these two objects. Envelope traversals must be followed individually to determine whether they will lead to collisions between the cores. For simplicity, we nevertheless assume that this only depends on whether bodies get closer than pre-defined radius, as for terrestrial planets.

5.2 In the context of planetary formation

In the previous section, we investigated the properties of collisions needed to determine their immediate outcome, with the addition of the link between the number of collisions related to the most massive planet formed in each system. In this section, we investigate further in that direction, with the moment and the location within the proto-planetary disc where these collisions occur.

Let us start with the moment at which a collision takes place. Three populations from the previous sections are shown in figure 5.14. In the context of our formation model, time zero is the moment the embryos are placed in the proto-planetary disc and start to grow. The general outcome is that most of the collisions happen between $3 \cdot 10^5$ and 10^6 yr and very few before $2 - 3 \cdot 10^5$ yr; this is the time needed for the initial growth of the embryos. In the early stages, they are not massive, which has two consequences: there are no (or very small) dynamical interactions between them and migration happens only on very large time scales (migration rate goes with the planetary mass to first order; see section 3.3). There must be thus some growth happening before collisions between embryos can occur. We see that starting with a million years, the number of forming systems decrease. The formation model follows the systems until the gas disc's mass goes below $10^{-6} M_{\odot}$. The distribution of times where this limit is crossed is shown with dashed lines on the same figure. As only a smaller amount of systems are followed after 1 Myr, this reduces the possibilities for collisions to take place. The distributions of disc life times are not identical as the underlying sets of systems are not the same.

It should not be forgotten that we only model systems that are still being formed, hence the necessity of the presence of the gas disc (for the giant planets; terrestrial planets may take a longer time). The dispersal of the gas disc removes its contribution to the damping of eccentricities and inclinations, but long-term evolution study shows that eccentricity remains mostly unchanged (Pfyffer 2015). It is nevertheless possible (and probable) that further collision will take place during the evolution phase, which may

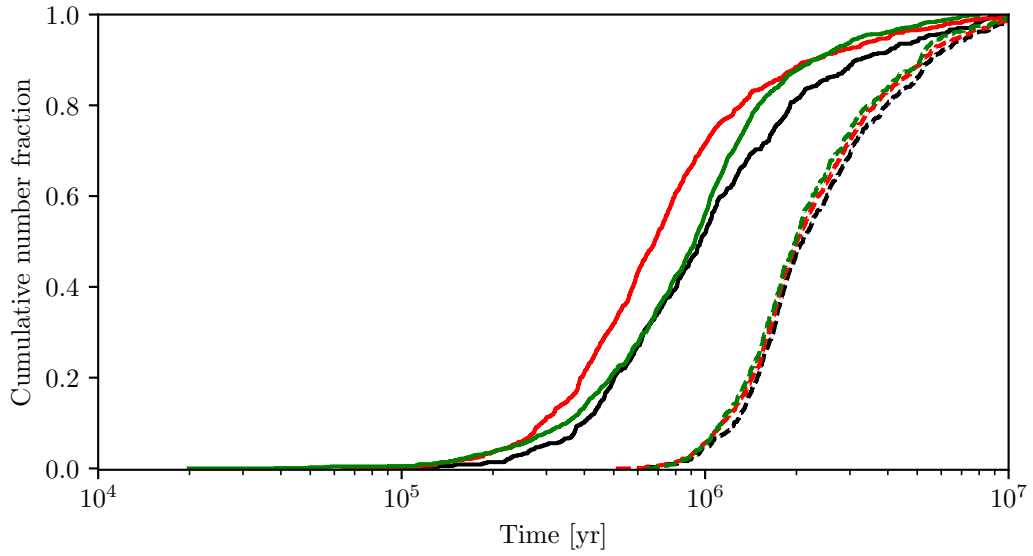


Figure 5.14: Cumulative distribution of the times at which collision happen (solid lines) and gas disc life time (dashed lines) for three populations: damping time scales according to Cresswell and Nelson (2008) (black), Fogg and Nelson (2007) (red) and Cresswell and Nelson (2008) with 20 embryos (green).

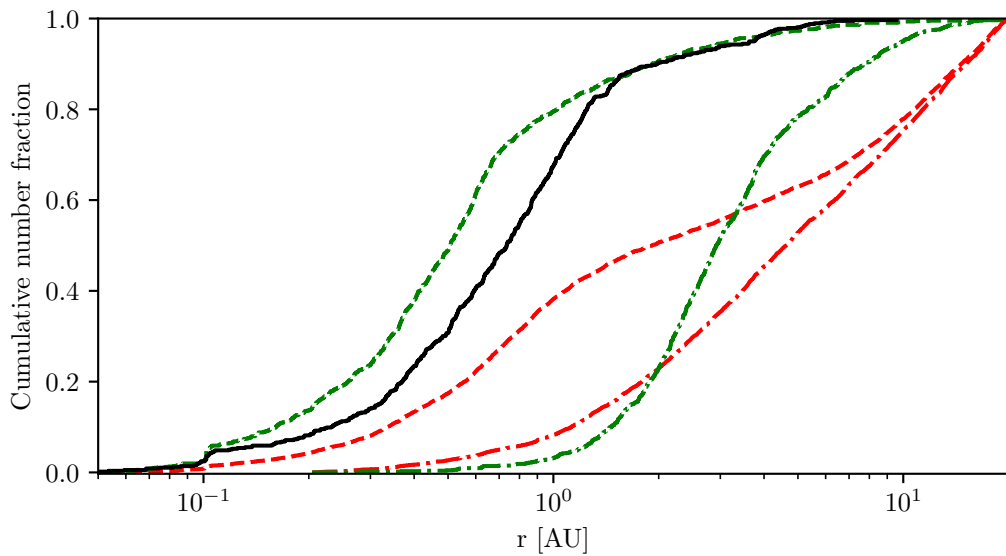


Figure 5.15: Cumulative distribution of the location where collisions took place (black) as well as the initial (dash-dotted) and final (dotted) locations of planets for all masses (red) and only above $1 M_{\oplus}$ (green) for the population with damping time scales computed according to Cresswell and Nelson (2008) and 10 embryos.

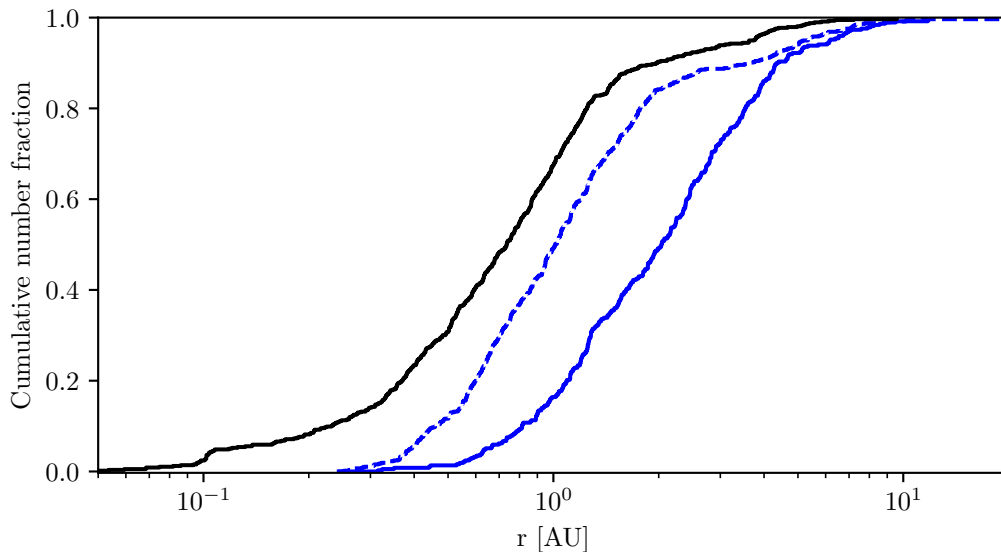


Figure 5.16: Cumulative distribution of the location where collisions took place (black; same as in figure 5.15) as well as the initial location of bodies that have been involved in at least one collision (blue lines): target (solid) and impactor (dashed).

as well the composition of the planets as there is no longer a gas disc that will serve as reservoir to replenish the envelope.

Next, we will investigate the locations where collisions take place, which is shown in figure 5.15. A majority of them occurs within 1 AU, where there is initially only a small number of embryos. It implies that this relates more to the end location of the planets (the dotted lines), rather than the initial one (the dash-dotted lines).

The small jump at 0.1 AU is due to this being the inner edge of the disc. Planets inside this limit do not migrate as there is no gas; this leads to trapping of a few planets at that location and an enhancement of the collision probability. We may as well look at the distribution of starting location of the embryos. The model is designed to place them with equal probability in log between twice the inner edge of the disc (in our case 0.2 AU) and 20 AU. The red dash-dotted curve should then be a straight line in the plot between these two points, but this is obviously not the case as at deficit of planets within a couple of AUs is observed. This results from the fact that when placing an embryo at a given location, the local isolation mass is computed first. If it does not exceed the embryo's mass, a new location is drawn. The inner part of the disc is more prone to show an insufficient local isolation mass, hence the lower fraction of embryos placed there initially.

The bodies involved in collisions also come predominantly from specific regions of the disc. This is shown in figure 5.16. We observe that the initial location of the impactors is quite close to where the collisions happen. Since most of them don't grow beyond 0.1 to 1 M_{\oplus} , they don't migrate much and hence the two distribution match quite well. This also indicates that collisions are not efficient in mixing material coming from different regions

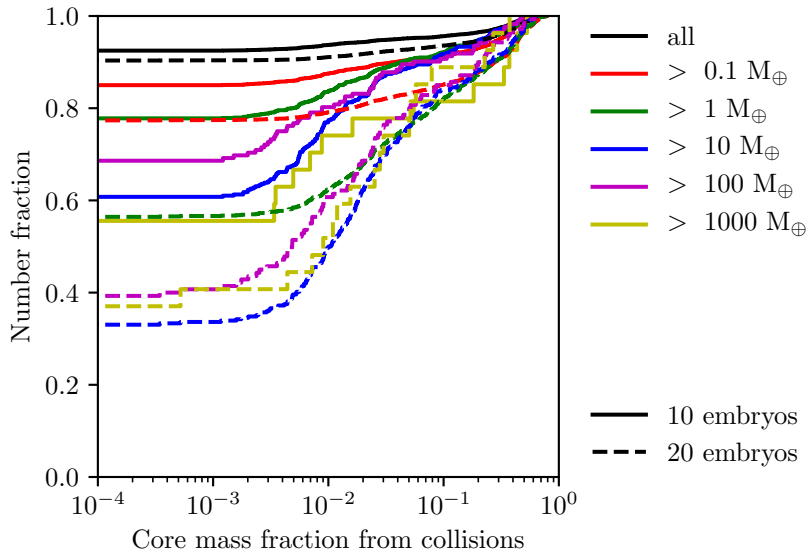


Figure 5.17: Cumulative distribution of the mass fraction that has been accreted from collision with other forming planets for two populations generated with the nominal formation model.

of the disc. About the half of all the impactors are initially located within 1 AU; this is much greater fraction that the overall distribution, where is account for only around 10%. Thus, embryos initially located in the have an enhanced collision probability. The initial location of targets are further beyond, and do relate with the location where massive planets originate (dash-dotted green curve on figure 5.15).

5.3 From a planet point of view

Collisions with other massive object can bring a significant amount of mass to a planet on a short time period (compared to the whole formation process which takes places over $10^6 - 10^7$ years.) Also, a small number of such events can be responsible for a substantial fraction of the total mass. In this section, we investigate the implications of these collisions on the forming planets. For instance, we will look at the proportion of such planet that suffer impacts by massive objects. In our case, massive objects would other forming planets.

The plots in this section show the cumulative core mass fraction that has been accreted due to collisions with other forming planets. The initial value of the curves (i.e. the one at 10^{-4}) is the fraction of planets that did not suffer a collision at all with another forming planets. Note that the bins are also now only providing a lower limit on the final mass, i.e. the black curve represents now all the planets that have been formed in a given population and that a new bin for masses above $1000 M_{\oplus}$ has been added. Also, there is no indication as when the collisions did occur during the formation process.

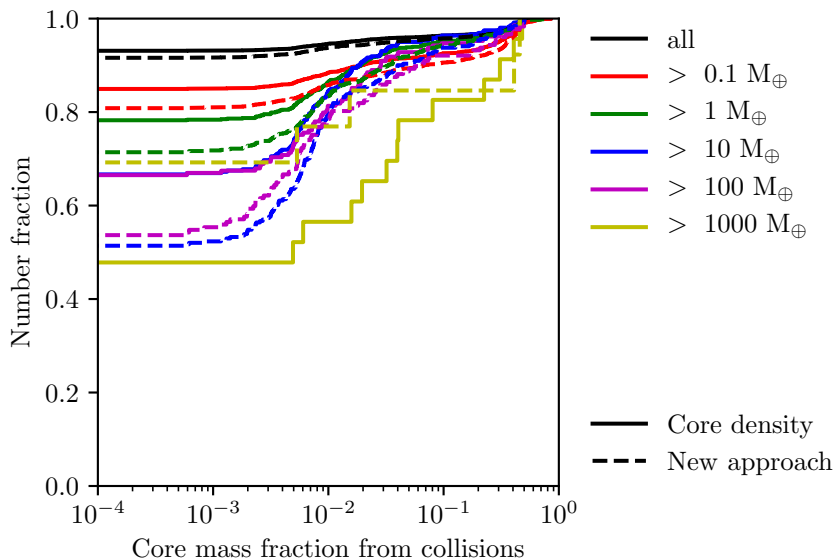


Figure 5.18: Cumulative distribution of the mass fraction that has been accreted from collision with other forming planets.

The results for the nominal formation model are shown in figure 5.17. The populations with initially ten and twenty embryos per system are compared. We note that the tendency is that bigger planets are more likely to suffer a collision during their formation. Across the entire populations, less than 10% of the planets did have at least one event, while this number increases to 45% for the biggest planets (with 10 embryos).

The highest fraction of accreted mass due to collisions is found for planets between 10 and 100 M_{\oplus} . This is related to both the number of collision event per planet and the mass of the impactor. As we did see in the previous sections, the mass ratio between colliding bodies (γ) lowers as the target mass increases. There is thus an optimum mass which can accrete the highest mass fraction for such source.

As we have already seen, the number of collisions increase with the number of embryos per system. In figure 5.17 we observe that this leads in an increase of the fraction of planets that did encounter a collision during their formation. On the other hand, the mass fractions gained through collisions with other forming planets remains similar. Thus, the increase of the number of collisions that has been described in the previous sections results in an increase of fraction of embryos that gained mass from collisions with the massive bodies rather than an increase of the mass delivered to a fixed set of bodies; increasing the number of embryos further will not increase the core mass of the giant planets. The exception is the highest mass bin, where we observe that a higher proportion of planets have accreted a greater mass fraction than 0.07 when there are 10 embryos per system.

The difference between the results considering the whole collision history or only the most massive impactor are not very much different; at most a factor two. We thus note that the single most massive event is the major contributor to the accreted mass due to

collisions rather than the possibly more numerous smaller events.

The same results for the new formation model are presented in figure 5.18, for two approaches used to determine the collision detection radius. The "Core density" case is equivalent to the 10 embryos case from figure 5.17. Except for the largest mass bin, we arrive at the same observation that with the old formation model: the increase in the number of collisions affects more planets while the mass accretion rate retains a similar shape. For the largest mass bin however, there is a net decrease of the fraction of planets that did undergo a collision event, from 53% to 32%. However, the small number of planets with such high masses does not permit to draw a strong conclusion. The distributions show a more bi-modal shape than for the nominal formation model; in this figure we see an increase between $4 \cdot 10^{-3}$ and $4 \cdot 10^{-2}$, followed by a plateau until 10^{-1} , and then a second increase. There are then only few planets that a core mass fraction between 4% and 15%.

Collisions with other forming planets is a source of solid material. In this section, we did observe that more than the half of the planets that reach at least $10 M_{\oplus}$ did undergo at least one collision event during their formation. Accretion from such collisions contribute to a fraction usually between 1% and 30% of the core's mass, and thus plays a minor role on the overall contents of solids within giant planets. These collisions are not efficient in mixing material between the different regions of the disc.

5.4 Effect on whole population

This part is devoted to study the effects of collisions between forming planets on whole populations. In the previous section, we did look at the effects of collisions on single planets, but did not observe their effects on planet populations as a whole or looked at other properties such as the location of the planets. As we did see in the part about the number of events in function of the radius used for collision detection, the number of planets only changes slightly as the number of collision is low compared to the number of planets.

The current collision model principally affects the core mass. Envelope ejection depends on the impact energy and the following consequences: if the planet is still in the attached phase then the envelope will likely be re-accreted shortly after the collision (consistent with results from Broeg and Benz 2012) if it has been lost or otherwise will adapt its mass to accommodate the new solid component coming from the impactor. If the planet is in the detached phase, the envelope is usually massive so its binding energy is normally higher than the typical impact energies, so envelope loss is minimal. We thus compare the core masses first; they are shown for two populations in figures 5.19 and 5.20. On the overall, there are not much differences between the two populations, we observe some smaller changes though. The few planets with core masses around $10 M_{\oplus}$ are not present in the second population, but we have some with smaller core masses. The main difference might be the mass of the most massive cores. For the reference population, the maximum core mass increases along with distance up to around 2 AU and then reaches a plateau. The shape is different for the population with the consistent collision radius

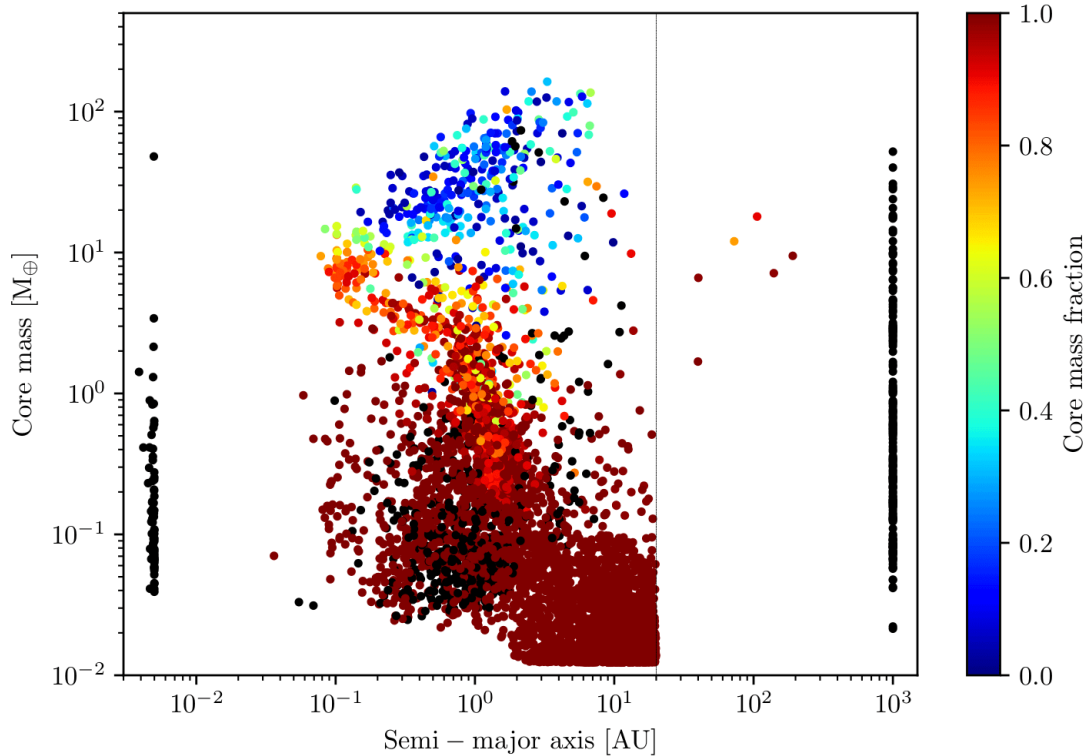


Figure 5.19: Core mass versus semi-major axis for a population generated with the new formation model and with collision radius computed assuming always core density.

in the detached phase.

A common pattern for these high mass cores is the collision with another massive planet during the late stages of formation, i.e. after the change of the gas accretion regime. In these cases, the total mass remains similar, as the envelope is unaffected by the collision but the core mass still increases, leading to a somewhat higher core mass fraction for those planets. On average for planets more massive than $1000 M_{\oplus}$, the core mass fraction increases from 5.5% to 6.1%. For the slightly less massive planets, more than $100 M_{\oplus}$, the fraction remains constant. The number of those planets decreases by about 4% with the new method to determine the collision radius.

The location where planets that undergo collisions are in the mass-distance diagram is shown in figure 5.21. The data come from the same population already shown in figure 5.20. We learned that most of the collisions happen within 1 AU as well as that the probability that a planet undergo a collision correlates with its mass. Both observations appear in this figure. We indeed notice that the topmost part of the plot, most planets did have a collision during their formation, and for a few of them even multiple such events. Even if the remaining did not have a collision itself, they are only a small fraction of giant planets that form in systems that do not see a collision between embryos. In that part of the figure, collisions are not limited to the inner region of the disc; the latter is for the low mass planets with a core mass lower than $1 M_{\oplus}$. Planets that have been lost during

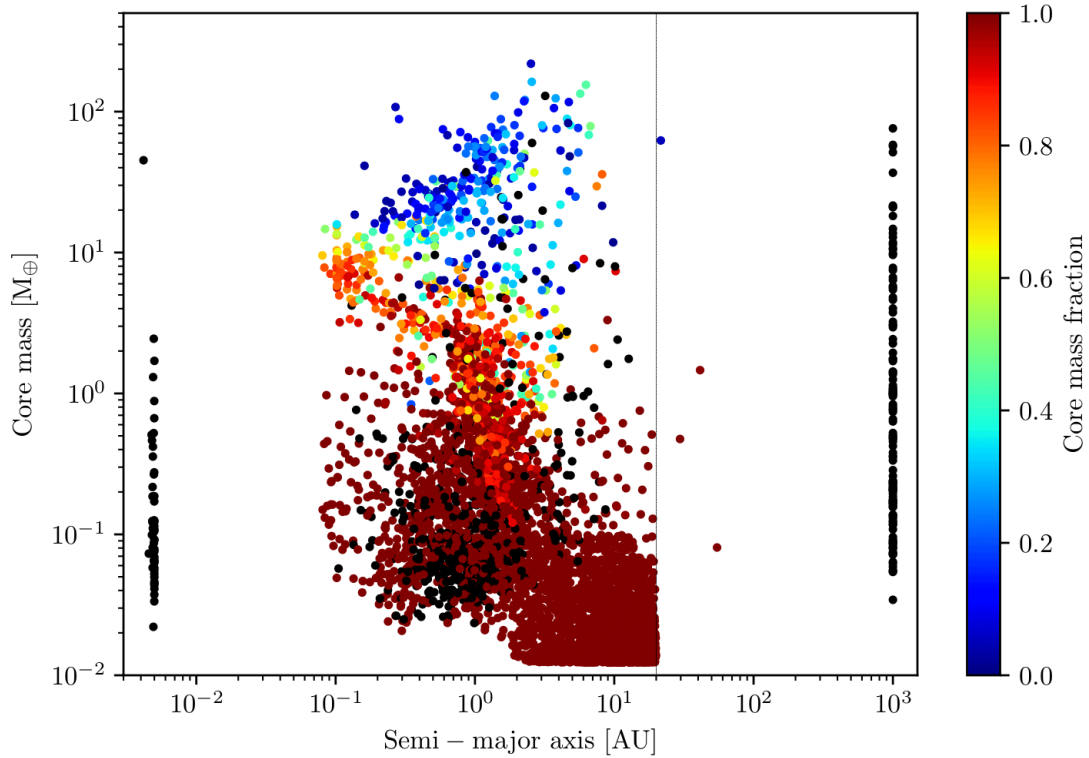


Figure 5.20: Similar to figure 5.19, but for the population with collision radius computed consistently in the detached phase.

their formation are not shown in this figure, for it would be hard to distinguish them. An implication is then that only the remnant objects from collisions are shown there; thus, planets with relatively low mass and still happen to have a collision during their formation had one other small forming planet. The corresponding mass of the largest impactor is shown in figure 5.22. We do note that that collisions with the most massive impactor are almost restricted to planets which are found beyond 1 AU. The giant branch within that, though having numerous collisions, only shows events with small bodies. There are even some events with moderately massive impactor on light cores, which implies more similar sized collisions again only beyond 1 AU.

In this section, we looked at the effects of collisions between forming planets on planet populations. As observed in the previous section, the likelihood of a planet to undergo a collision during the formation stages increase with its mass. While the mass fraction of solids accreted following such kind of collisions is important for some planets, particularly the most massive ones, it does not affect significantly the overall results at the level of planet populations. The observations made in the previous section, about most of collisions happening with 1 AU are consistent with the results shown here.

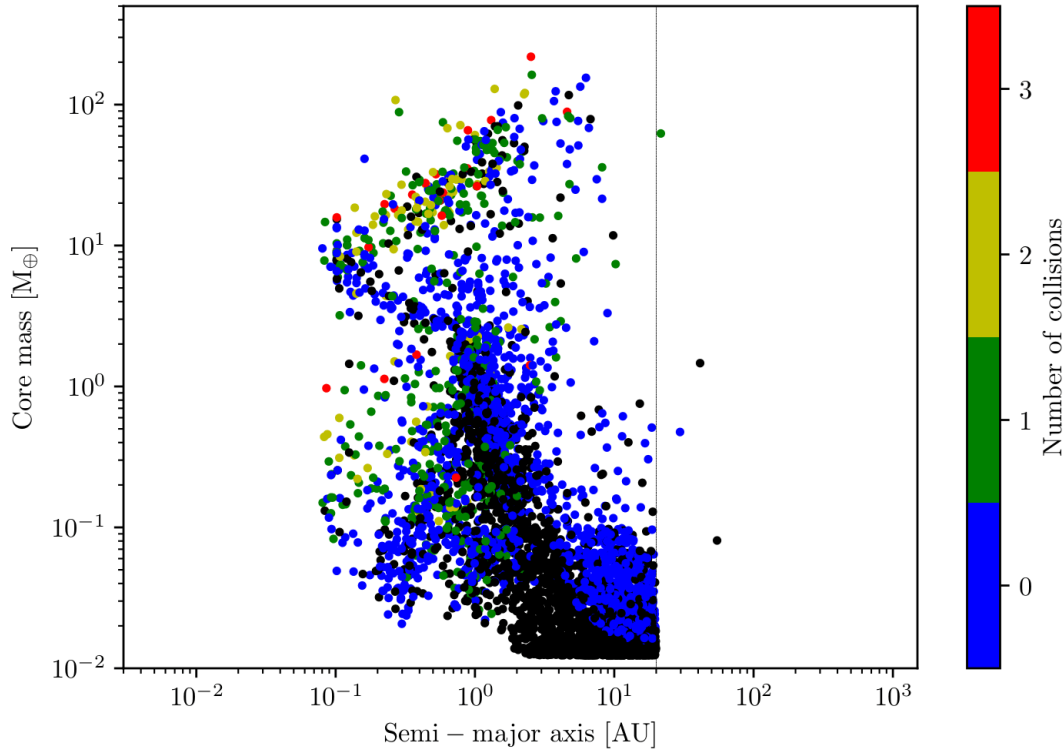


Figure 5.21: Same as figure 5.20, but the colour is now representing the number of collisions encountered by the planets. Black indicates planets in systems where no collisions occurred, whereas blue is for planets that did not undergo a collision while in a system where other planets did. Planets that have been lost following a collision are not shown.

5.5 New model for collisions between terrestrial planets

The current collision model present in the planetary formation model is quite simple, and it was highlighted that it is not self-consistent. The model is designed for giant planets with massive envelopes rather than for purely rocky ones; in the case where two rocky planets collide, only one outcome is possible: perfect merging. The number of small planets is however more important than for gas giants and so one might expect that such collisions are more frequent. The model has other smaller problems. For instance, the impact energy is also computed assuming that the collision happens exactly at escape velocity, thus discarding the results of the N-body.

Finding general laws that predict outcome of collisions from a simple set of parameters has been a vast subject of study; first for the smaller, strength-dominated bodies (e.g. Housen and Holsapple 1990), more recently for larger, gravity-dominated objects. In the formation model that is used, only a given number, usually 10, planetary embryos are directly modelled. Their initial mass is $0.0123 M_{\oplus}$, or roughly a Moon's mass, with a

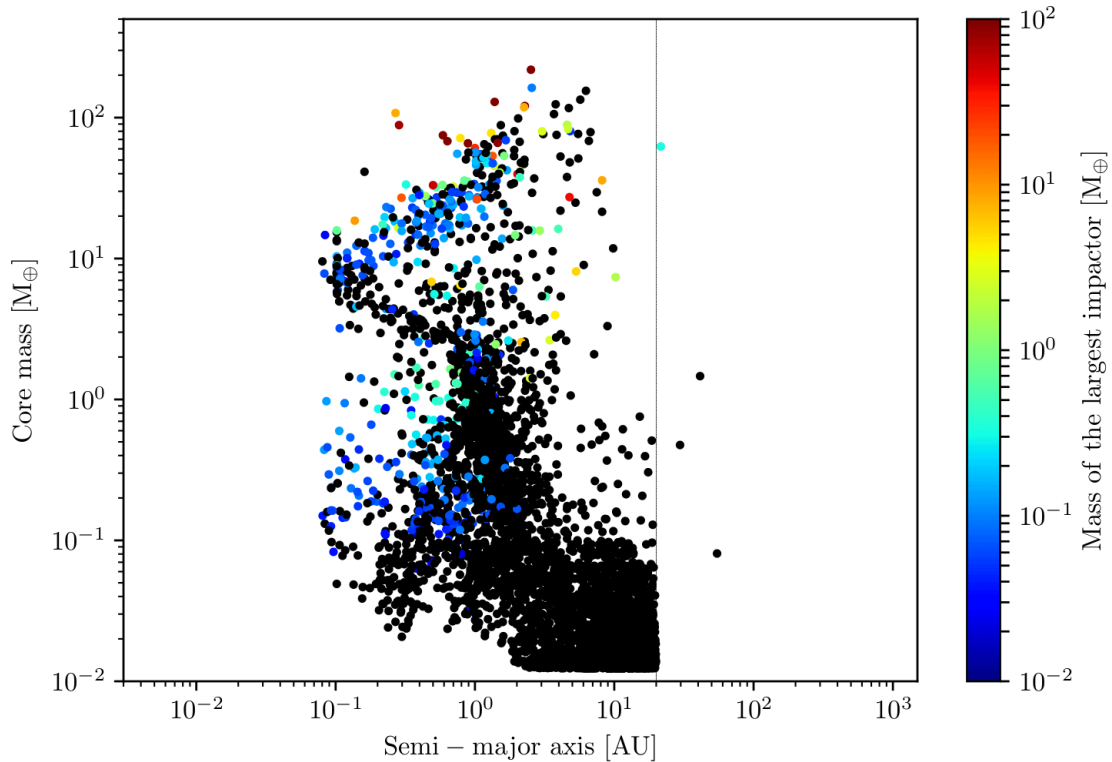


Figure 5.22: Same as figure 5.20, but the colour is now with the mass of the largest impactor.

corresponding radius of ~ 1700 km. We can then assume that all these collision events will be in the gravity-dominated regime (Benz and Asphaug 1999; Leinhardt and Stewart 2009). We will thus neglect the effects of the strength-dominated regime as well as the transition.

As we did see on the previous sections, most of the collisions involve bodies that have a mass lower than a few Earth masses. These objects don't have a large enough mass to bind an important mass of gas and therefore do not have massive envelopes. The physics of such collisions is then like the ones of purely solid bodies. This regime has been extensively studied, and a few scaling laws are available to determine the outcome without having to run an hydrocode for every event. The modified collision model will thus work as follows:

- First the fraction of mass being in the envelope is checked for both objects. If for either of them, this value is higher than 1%, the old model will be used (see hereafter for the adaptations to it).
- Otherwise, the collision result is estimated using the scaling laws derived by Leinhardt and Stewart (2012), using the total mass and assuming a constant density which is provided by the core's equation of state from the general formation model.

Only the first two resulting bodies are computed. Due the formation's model inherent structure, it is difficult to add a new forming planet during the process.

- The masses of the resulting objects are checked. If for either object it is lower than the initial mass (one Moon's mass), then the body is discarded.
- The largest remnant, provided it fulfils the conditions mentioned above, is set in lieu of the most massive of the colliding bodies. The second largest remnant will take the place of the other colliding body, provided it also fulfils the conditions.

The reasons for using the old model in the presence of significant envelope is that the dynamics of such event is different than for collision between purely solid bodies. The envelope will cause a drag, possibly stripping of some part of them. As seen in the previous section, the mass ratio between the two colliding (γ) objects lowers on average as the target's mass increases. This means that in this regime, most of the events occur between one massive object with a significant envelope and a smaller one, possibly without envelope at all. This case can be considered in a similar manner as the accretion of a planetesimal, but of a much bigger size. In this case, we could even consider using the algorithm used to determine the capture radius of planetesimals (Mordasini 2004), but with the parameters of the impactor. It should be noted than in this case, the collision radius is not at a fixed value, but depends of the different impact properties: for instance, the relative velocity plays an important role. If this value is close to the mutual escape velocity, then only a slight drag might be sufficient to dissipate enough energy that will lead the bodies to be gravitationally bound together. It will follow that the body will be accreted. On the other hand, a body with a higher relative velocity can go through deeper in the envelope without being ultimately accreted. The outcome thus depends on velocity, geometry and internal structure rather than on a fixed separation.

The original model, which is still used when at least one of the planet has a significant amount of mass in the envelope has been corrected for a few problems. First, the impact energy is now computed consistently with the results from the N-body, i.e. the real impact velocity is used. The second, is that in case a planet is in the disc-dominated accretion regime and its envelope is lost, then it is set back to the planet-dominated regime where its envelope is in equilibrium with the surrounding disc. Since the core's mass remains, it is entirely possible that it will go to the disc-dominated regime at the first time step after the collision, but it is never known in advance.

We start by looking at the distribution of envelope mass fraction among the detected collision events with the enhanced formation model, which will serve as the base of the enhanced model presented here. Results are shown in figure 5.23. The envelope fraction shown here is actually the maximum of both objects in each collision event. Note that it is mainly determined by the value of the largest body, as the envelope fraction normally increases with mass. For the same reason, the horizontal axis is also a measure of the planet masses. The value of 10^{-2} roughly corresponds to planets with a few Earth masses. This criterion matches about 53% of the collisions occurring in the population where the collision detection radius is determined assuming core density and 44% with the modified one that uses the planetesimal's capture radius in the *detached* phase. This decrease

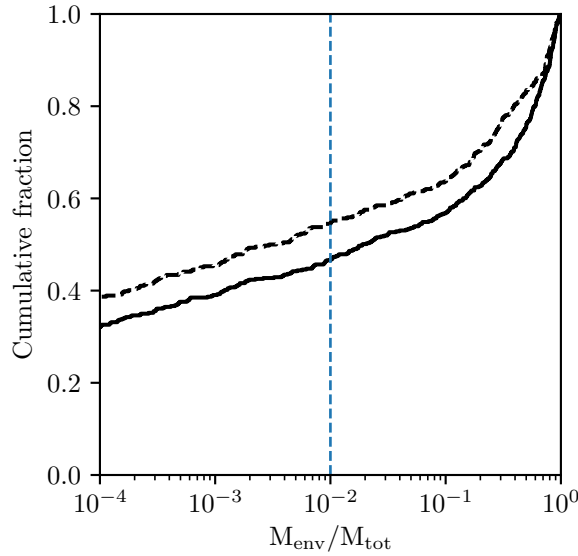


Figure 5.23: Cumulative distributions of envelope mass fraction, for the two populations generated with the enhanced formation model and discussed in section 5.1.3: always assuming core density (dashed line) and otherwise using the planetesimal’s capture radius in the *detached* phase (solid line). The vertical line at 10^{-2} shows the limit of the new collision model.

in ratio is actually due to the relative increase of events involving massive planets with the modified radius; the absolute number of events is actually slightly larger. Also, it is to note that these results were obtained using the current collision model for all events, it does not represent the actual number of collisions that will be handled by the new model. The fact is that the new model may give zero to two objects as remnants from the collision whereas this number is always one for the current model.

The scaling laws from Leinhardt and Stewart (2012) will be now be discussed with the adaptations that were made. In the following, masses are the total ones and radii the ones used for the purpose of collision detection, so the resulting average density is the one of the core. As reminder, the impact velocity and specific energy are linked with

$$Q_R = \frac{1}{2} \frac{m_r v_{\text{coll}}^2}{m_{\text{tar}} + m_{\text{imp}}} \quad (5.14)$$

and can be exchanged using that relation. The subscript R denotes the use of the reduced mass (or the energy measured from the barycentre). It was introduced to correctly handle events where the impactor mass is not negligible compared to the target (Stewart and Leinhardt 2009); as we did see, this is the case for this study. Here $m_r = m_{\text{tar}} m_{\text{imp}} / (m_{\text{tar}} + m_{\text{imp}})$ is the reduced mass. However, the derivation of the scaling laws is, for some extend, based not on the actual impactor mass, but only considering the part which interacts with the target, $m'_{\text{imp}} = \alpha m_{\text{imp}}$. In Leinhardt and Stewart (2012), the factor α is derived from the impact angle (or parameter) as well as the bodies’ radii assuming a constant density.

This assumption is also sufficient in our case since the envelope mass is small compared to the total mass and the radius has already been computed assuming core density, with

$$\alpha = \frac{r_{\text{coll}}^2(1-b)^2(3r_{\text{imp}} - r_{\text{coll}}(1-b))}{4r_{\text{imp}}^3}, \quad (5.15)$$

and $b = \sin \phi_{\text{coll}}$ the impact parameter. In the case of low impact angles, when

$$b < \frac{r_{\text{tar}} - r_{\text{imp}}}{r_{\text{tar}} + r_{\text{imp}}}, \quad (5.16)$$

then the impactor interacts entirely with the target and $m'_{\text{imp}} = m_{\text{imp}}$, i.e. $\alpha = 1$. In the following, quantities denoted with a prime are computed using the interacting impactor's mass m'_{imp} rather than its total mass m_{imp} . With the value of α , one can compute the modified reduced mass m'_r and escape velocity v'_{esc} . The latter is lower than the actual mutual escape velocity in the case when not the entire impactor interacts. Note that the following criterion for the collision regime is based on this modified velocity, and so it cannot be assumed that it is always identical to the value shown in the previous sections.

Another useful quantity for impact geometry is set by the critical impact parameter

$$b_{\text{crit}} = \frac{r_{\text{tar}}}{r_{\text{coll}}}. \quad (5.17)$$

This value corresponds to impact parameter where roughly half of the impactor interacts with the target (Asphaug 2010). If $b > b_{\text{crit}}$ then the impact is called *grazing*. Other transitions are set by impact energies. A standard value is the one where the mass of the largest has half of the target's mass, referred as catastrophic disruption threshold. The first step is to compute its value, but in the case of a head-on, equal mass collision ($\gamma = 1$),

$$Q_{\text{RD},\gamma=1}^* = \frac{4}{5}c^*\rho_1GR_{\text{C1}}^2, \quad (5.18)$$

with $c^* = 1.9$ a dimensionless material parameter obtained from numerical simulations for planet-size bodies (Leinhardt and Stewart 2012), $\rho_1 = 1000 \text{ kg/m}^3$, and R_{C1} is the radius of a sphere holding the total mass with a density of ρ_1 . This critical specific impact energy for an arbitrary value of γ is then (Leinhardt and Stewart 2012)

$$Q_{\text{RD}}^* = Q_{\text{RD},\gamma=1}^* \left(\frac{1}{4} \frac{(\gamma+1)^2}{\gamma} \right)^{\frac{2}{3\bar{\mu}}-1} \quad (5.19)$$

with $\bar{\mu} = 1/3$ so that the exponent is actually unity. Finally, we can derive the specific critical energy for an arbitrary impact angle:

$$Q_{\text{RD}}^{*\prime} = Q_{\text{RD}}^* \left(\frac{m_r}{m'_r} \right)^{2-\frac{3\bar{\mu}}{2}}. \quad (5.20)$$

From this value, it is possible to determine the mass of the largest remnant in the disruption regime using a linear relation

$$\frac{m_{\text{lr}}}{m_{\text{coll}}} = -s \left(\frac{Q_{\text{R}}}{Q_{\text{RD}}^{*\prime}} - 1 \right) + \frac{1}{2}, \quad (5.21)$$

with $s = 1/2$. The value for which the mass of the largest remnant is equal to the mass of the target is

$$\frac{Q_{\text{RE}}}{Q_{\text{RD}}^{\star\prime}} = \frac{2\gamma}{\gamma + 1}. \quad (5.22)$$

For high impact energies, the linear relation breaks down (it would otherwise return negative masses). Another transition is then set for *super catastrophic disruptions*, when the mass of the largest remnant is 10% of the total mass, so we obtain $Q_{\text{RS}}/Q_{\text{RD}}^{\star\prime} = 1.8$ again from equation (5.21). In this regime, the relationship for the mass of the largest remnant becomes a power law (e.g. Takagi et al. 1984).

These different quantities allow us determining the regime in which the collision occurs. They can be summarised as follows:

- If the impact velocity is lower than the mutual escape velocity, $v_{\text{coll}} < v'_{\text{esc}}$, then the case is treated as a perfect merger. In this case, the result is similar than from the previous model; the mass of the envelope being small compared to the one of solids.
- If the impact energy is greater than the limit for a super catastrophic event, $Q_{\text{RD}} > Q_{\text{RS}}$, then the event falls in that category and a single body will emerge from the collision. Its mass is computed from the law for super catastrophic events; position and velocity are computed as in the perfect merger case.
- If the impact energy is smaller than the erosion threshold, $Q_{\text{RD}} < Q_{\text{RE}}$, and the impact is *grazing* then the event is in the *hit-and-run* regime. The target is taken as the largest remnant; the mass of the second largest remnant is computed following the procedure described in Leinhardt and Stewart (2012) about the reverse collision of the interacting impactor mass onto the impactor itself. The position and velocity of the largest remnant remain the same for the target; for the second largest remnant a two-body problem is assumed, the result is thus similar than if this was a scattering event. Reufer (2011) did find that for grazing collisions, $\beta_{\text{imp}} \approx 90^\circ$, the velocity and angle differ only slightly from a pure two bodies problem; in our case we assume this for all impact angles.
- Otherwise the impact is in the disruptive regime (or partial accretion). The mass of the largest remnant is computed from equation (5.21); its position and velocity are determined according to the method proposed with the laws, i.e. for $b = 0$ it is the value of the centre of mass, for $b > 0.7$ it keeps the values of the target and in between it is a linear relation between the two. The mass of secondary largest remnant is calculated using

$$\frac{m_{\text{srlr}}}{m_{\text{coll}}} = \frac{(3 - \beta) \left(1 - N_{\text{lr}} \frac{m_{\text{lr}}}{m_{\text{coll}}}\right)}{N_{\text{srlr}} \beta} \quad (5.23)$$

with $N_{\text{lr}} = 1$, $N_{\text{srlr}} = 2$ and $\beta = 2.85$ (Leinhardt and Stewart 2012). The limit $m_{\text{lr}} + m_{\text{srlr}} \leq m_{\text{coll}}$ is furthermore enforced. In the case all the mass is present in the

largest and second largest remnants, then the position and velocity of the secondary are determined assuming momentum conservation. Otherwise the position and velocity of the secondary largest remnant are computed in the same way that for *hit-and-run* regime by solving a two-bodies problem.

To avoid further detection of the same collision event, these resulting bodies are placed a distance slightly larger than at contact and on diverging trajectories. The impactor is immediately moved to its post-impact location. This implies that time is not entirely conserved, but the error is actually small compared to an orbital period. The method to solve the two-bodies problem is simplified, as its only usage is to determine the position and velocity in a point further in time at a given separation. The first step is to determine the angular momentum vector

$$\mathbf{h} = \mathbf{r} \times \mathbf{v} \quad (5.24)$$

which defines the orbital plane, thus replacing both the inclination and the longitude of the ascending node. Here \mathbf{r} and \mathbf{v} are the relative position and velocity at the time of collision detection. Next the eccentricity vector

$$\mathbf{e} = \frac{\mathbf{r} \times \mathbf{h}}{\mu} - \frac{\mathbf{r}}{r} \quad (5.25)$$

gives the eccentricity ($e = |\mathbf{e}|$) and the direction of the periapsis, thus replacing the argument of the pericentre. μ is the standard gravitational parameter (equation 5.4). The semi-major axis now follows from the ellipse parameter

$$p = \frac{\mathbf{h}^2}{\mu} \quad ; \quad a = \frac{p}{1 - e^2} \quad (5.26)$$

The true anomaly θ_0 at the new location is obtained following equation (6.93) for $r_0 = 1.01r_{\text{coll}}$. The direction of the major axis, pointing towards the pericentre is given by \mathbf{e} ; the one of the minor axis, pointing in the direction of motion of the impactor at pericentre is $\mathbf{q} = \mathbf{h} \times \mathbf{e}$. Let us now denote $\hat{\mathbf{e}}$ and $\hat{\mathbf{q}}$ the unit vectors pointing along \mathbf{e} and \mathbf{q} respectively and $v_0 = \sqrt{\mu/p}$ the reference velocity; the new relative position and velocity are

$$\mathbf{r}' = r_0 (\hat{\mathbf{e}} \cos \theta_0 + \hat{\mathbf{q}} \sin \theta_0) \quad (5.27)$$

$$\mathbf{v}' = v_0 (\hat{\mathbf{e}}(-\sin \theta_0) + \hat{\mathbf{q}}(e + \cos \theta_0)), \quad (5.28)$$

which enables determining the location and velocity of the second largest remnant since these are already fixed by the largest one. This implies that the impactor is small compared to the target, since it is assumed that the trajectory of the latter is unperturbed by the passage of the other body. A better solution would be to assume that the location and momentum of the centre of mass are conserved.

This new model is developed as a separate software library written in C which can be embedded directly into computer programs written in multiple languages (C, C++ and Fortran with some adaptation). Language binding for Python¹ are also provided, which is a common language for the analysis tools. Its design is based on the following goals:

¹<https://www.python.org/>

Target mass [M_{\oplus}]	Old model	Perfect merging	Super cata- strophic	Disruption	Hit-and- run
<0.1	0	4	5	43	64
0.1–1	20	1	0	58	55
1–10	39	4	0	8	5
10–100	162	0	0	2	0
>100	69	0	0	0	0

Table 5.4: Breakdown of the number of collisions by type and target mass for the previously generated population.

- The target users of this library are N-body scheme, and so the bodies involved in the collision are treated as *objects* with the following properties: mass, radius position and velocity. Collision velocity and angle are determined from their relative positions and velocities. They also do not need to be placed at initial contact; in case their relative distance is not the sum of their radii, a two-body problem is calculated to retrieve the collision parameters. Likewise, the resulting bodies are returned as the same kind of objects with updated properties following the collision; so they can directly be given back to the N-body code.
- The underlying model can easily be modified or extended. At the moment, only perfect merging and this new model are included but the inclusion of additional models can be done in a straightforward way.

There are a few helper functions included in the library, such as to set the position and velocity of the initial object if only the magnitude of the velocity and the angle are known. Some others give the impact quantities which are consistent with the ones used by the scaling laws, i.e. correcting if there is a mismatch between their current separation and the sum of their radii. These functions have already been used throughout this chapter to retrieve the different impact quantities.

5.5.1 Re-analyse of the previous collisions

For the first application of this new collision model, we come back at the previous results (new formation model, with consistent radius in the *detached* phase) and re-analyse them. There is no feedback of the outcome of the new collision model onto the formation scheme yet.

A breakdown of the regime type is shown in table 5.4. The column "Old model" show collisions that did not match criterion to use the new collision model, i.e. they have an envelope mass fraction greater than 1%. We see that there are no cases for target masses below $0.1 M_{\oplus}$ and about 15% when the mass is between 0.1 and $1 M_{\oplus}$. This indicates that there are a few planets that have a mass below the Earth mass and already a significant envelope mass fraction. These events happen late (after roughly 1 Myr) with planets

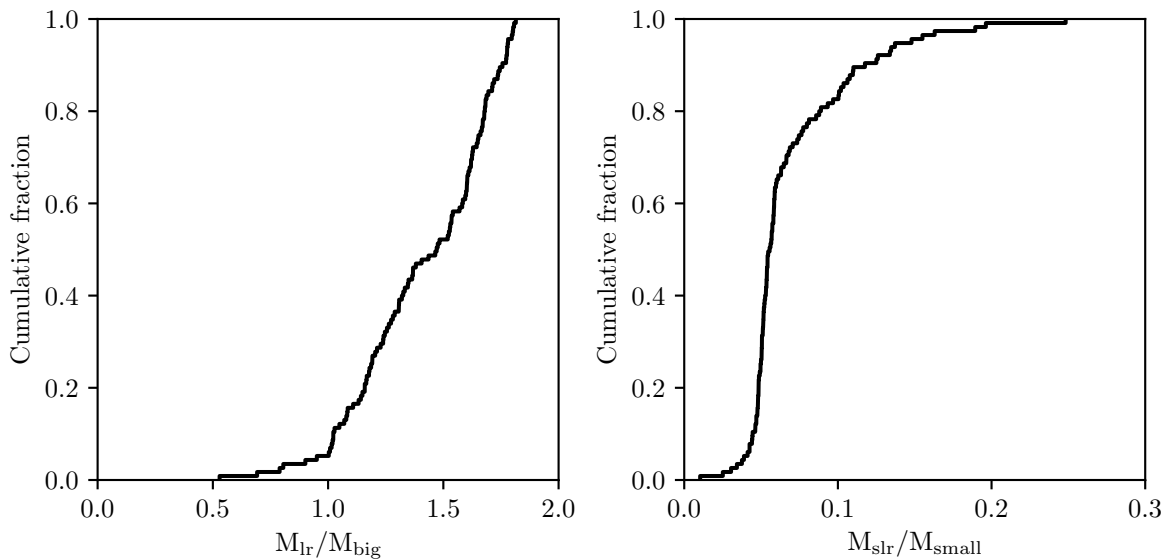


Figure 5.24: Cumulative distributions of masses for the largest remnant compared to the target, and second largest remnant compared to the impactor for cases in the disruption regime.

whose core no longer grow, hence having a small luminosity. For the higher masses, as expected, most of the event do not fulfil the criterion. The "Perfect merging" is the first of the cases listed above; only a small fraction of the events falls in this category. It should be noted that the fraction of events increases with the target's mass, as for the first three mass bins the count remains almost the same whereas the number of events that are computed with the new model decreases. Super catastrophic events only involve low mass planets. They have common characteristics, such as $v_{\text{coll}}/v_{\text{esc}} > 3$ and $\gamma \gtrsim 0.4$, although they are not exclusive to this category. We did observe that the lower mass bins have a tendency to have an higher fraction of similar sized collisions and $v_{\text{coll}}/v_{\text{esc}} > 3$, so there is an enhanced likelihood for collisions to take place in the super catastrophic regime. As these always happen in the lowest mass bin, and the implication of this category is that the mass of the largest remnant is at most 10% of the total mass involved in the collision, the resulting mass is always lower than the limit set to retain the bodies. They are thus destroyed. "Disruption" and "Hit-and-run" are the most common regimes for collisions treated with the new model, with 111 and 124 events respectively out of 249. For the former, the mass distribution of the resulting bodies is shown in figure 5.24. We see that most cases are actually in the *partial accretion* regime, as the mass of the largest remnant is larger than the target in 105 cases (95%) and only 6 of them are in the *partial erosion* regime. In contrast, the mass of the second largest remnant, is always much smaller than the impactor mass, and there are no cases where $m_{\text{slr}}/m_{\text{imp}} > 0.3$. Thus, in only 26 cases the mass of the second largest remnant is greater than the minimum mass ($0.0123 M_{\oplus}$), implying that this body will be retained. In the "Hit-and-run" regime, the mass of the largest remnant is always kept equal to the one of the target and the second

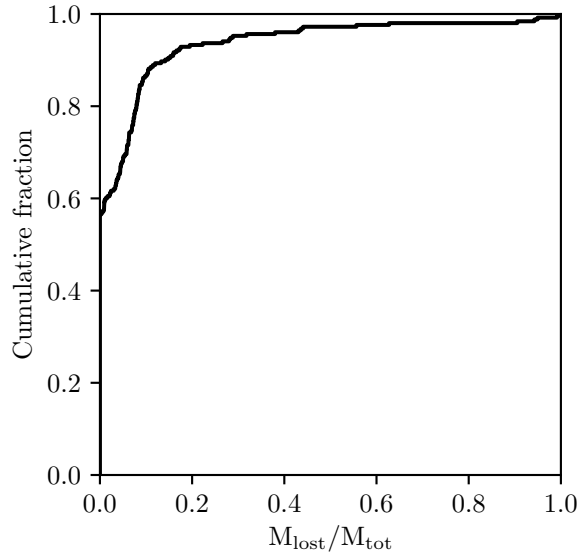


Figure 5.25: Cumulative distributions of mass loss (i.e. neither in the two largest remnants) for the collision events using the new model.

largest remnant mass is calculated with the *reverse collision* procedure (Leinhardt and Stewart 2012). After analysis of the results, it has been observed that the latter is, except in one case, the same as the impactor's mass. There is thus almost no mass loss in this regime.

The number of resulting bodies with the new collision model would be as follows: 9 perfect merging events that return one body each by definition, 5 super catastrophic where no object is left, all partial disruption events return a largest remnant as well as for 26 of them, a second object, and all hit-and-run events return two bodies. The total gives 394 bodies from 244 collision events, that is 150 more than with the old model. The great majority of these additional bodies come from the hit-and-run events, which were not handled properly with the previous approach. In contrast, the object masses are slightly slower than previously. The older model was always the equivalent of perfect merging in this range, and so there was no to little mass loss (only the envelopes). There are two consequences: as the number of resulting bodies increases, their mass lowers and secondly solid mass loss may occur. The mass loss fraction is shown in figure 5.25. The 60% of collisions that have no mass loss are the perfect merger and hit-and-run cases. The super catastrophic events are the few one that make the contributions above 0.9, as expected. The remaining ones are in the disruption regime. Most of those have a small mass loss fraction, so that overall, 81% of the cases have a mass loss ratio of less than 10%.

The outcome of the new collision model is quite different from the original one. Applying the new model, we observe that most of the collisions happen in the "disruption" and "hit-and-run" regimes, while only a small fraction is found in the "Perfect merging" and "Super catastrophic" regimes. The original collision model was treating all events as

Target mass [M_{\oplus}]	Old model	Perfect merging	Super cata- strophic	Disruption	Hit-and- run
<0.1	0	2	8	51	55
0.1–1	14	3	0	42	64
1–10	68	10	0	14	0
10–100	213	0	0	2	1
>100	85	0	0	0	0

Table 5.5: Breakdown of the number of collisions by type and target mass for the population generated with the new collision model.

	Old collision model	New collision model
Rate of planets in the disc	8.533	8.607
Rate of close-in planets	0.139	0.111
Rate of collisions	1.020	0.928
Rate of collisions with star	0.096	0.086
Rate of ejections	0.213	0.268

Table 5.6: Average number of planets per system per status at the end of the formation phase; the first two categories denote planets that are still present whereas the three last are for embryos that did not reach the end of the formation phase. The results of population with the old collision model only and with the new one are compared.

perfect merging. The main effect is a strong reduction of mass accretion from collisions between massive bodies, and an increase of the number of bodies that result from those collisions. In particular, collisions in the "hit-and-run" regime result in almost no mass transfer between bodies.

5.5.2 Population with new model

We now come to the analysis of a population where the new collision model is used directly in the formation model. There is now a feedback of the new collision model on the forming systems. As expected, we observe that the number of collisions increases in comparison to the old collision model, as there are now 641 collisions, compared to 543 previously. The breakdown by collision type and target mass is shown in table 5.5. Quite surprisingly, the increase is mostly due to events in the "Old model" case. We do observe an increase in the collisions in the mass range of 10 – 100 M_{\oplus} , where almost all collisions are handled by the old model as they have a significant envelope fraction.

For the fate of the planets, there are interesting outcomes. Results are provided in table 5.6. The number of planets which are lost following a collision is, as expected, reduced by a value close to 9%, when comparing the common subset of systems in both

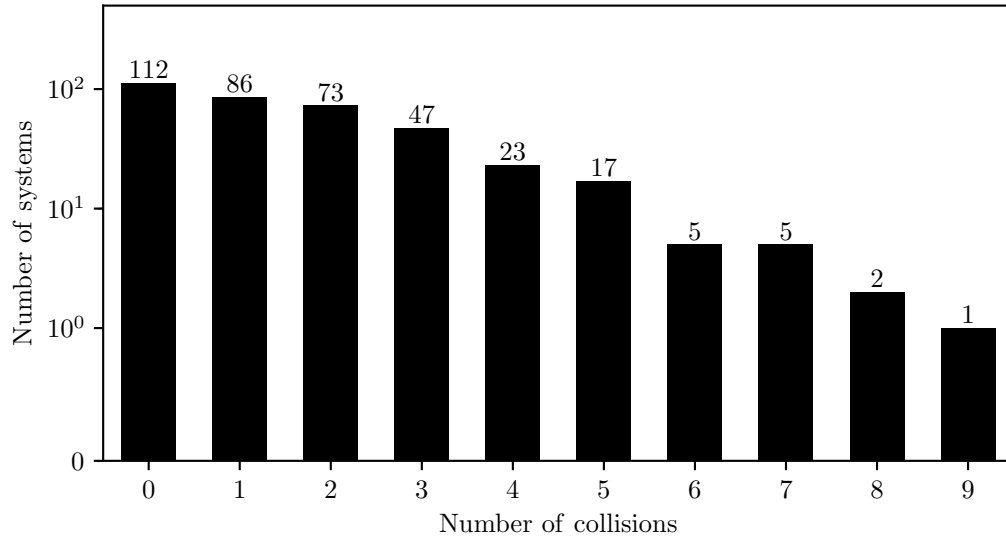


Figure 5.26: Histogram of the number of collisions per forming system. This is for the new formation model with the new collision model. Only systems that have a planet which attained $1 M_{\oplus}$ are counted (which discards a single collision).

population. An also interesting result concerns the number planets that end up being ejected, which increases by 25%. It was found that as the method to determine the radius for the purpose of collision detection evolved, the number of ejections decreases. The increase following the change of model for collision treatment can be due to presence of second largest remnants, which can have eccentric orbits, potentially leading to ejections.

The histogram of the number of collisions per system is shown in figure 5.26. The difference with figure 5.1, which shown the same histogram but for the original case, is pronounced. Note that the total number of systems formed has decreased and that systems which have no planet more massive than $1 M_{\oplus}$ have been left out. The latter point is responsible for the fact that there is only a small decrease between the number of systems that show no collisions and a single one. The decrease of the number of system that have higher collisions count is lower. On the overall population, we observe that there are 73 collision events that involve the second largest remnant of a previous collision across 57 different systems. This number is roughly 60% of the number of hit-and-run events shown in table 5.5, so the scenario where a hit-and-run collision leads to another one is common. We will now analyse a bit further these second largest remnants that collide again and determine whether the new collision happens with the same body again, meaning that the same pair of objects collide multiple times or not. The further analysis is based on 136 collisions, including the 73 ones involving a second largest remnant, as well as the ones that initially produced the second largest remnants. In them, 9 cases accounting for 23 events involve series of collisions between the same bodies. This means that there 113 events that involve different bodies. The most likely scenario is thus that the second largest remnant, when it collides again does so with another body. We may

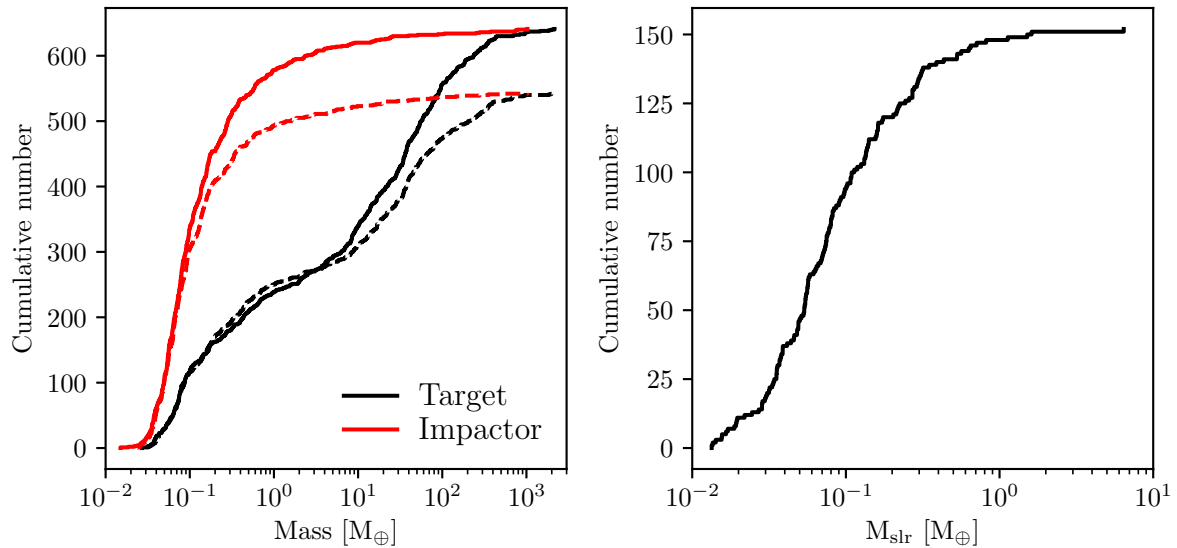


Figure 5.27: *Left*: cumulative distributions of target and impactor masses for collision events found with the new collision model (solid line) compared to the old one (dashed lines). *Right*: Cumulative mass distribution of the second largest remnants.

provide a plausible reason that reduces the number of further collision between the same objects: the presence of external forces, with migration and damping will slightly modify the orbits.

The cumulative mass distributions of the colliding bodies are shown on the left panel of figure 5.27. The new results (solid lines) are compared to the ones obtained with the old collision model (dashed lines). The expectation was that the number of collisions would increase for the lower masses, as the modified collision model should increase the number of planets with low masses. This is not what is obtained, instead we do observe an increase in the collisions where the mass of target is between 10 and 100 M_{\oplus} . Furthermore, the lower frequency of events in the 0.1 – 1 M_{\oplus} and the increase for the more massive planets smooth the mass distribution of targets so that the plateau between 1 and 5 M_{\oplus} is less pronounced. For the impactors however, the increase is for masses between 0.1 and 1 M_{\oplus} . This increase is consistent with the masses of the second largest remnants with the new model (right panel of figure 5.27). Combining these results with the observations from the last paragraph (that multiple collisions between the same planets are uncommon), we can draw the following conclusion: the newly present second largest remnant tend to collide further, but with planets whose masses are in the 10 and 100 M_{\oplus} range.

The other collision parameters (mass ratio, velocity and angle) show similar distributions as for the previous cases and will not be discussed further here.

With the new collision model, mass accretion from collisions is not as straightforward as in the original version. Mass accretion is now computed as the mass difference between the target and the largest remnant for the first body and between the impactor and second largest remnant for the second body. In the case of hit-and-run events, we did

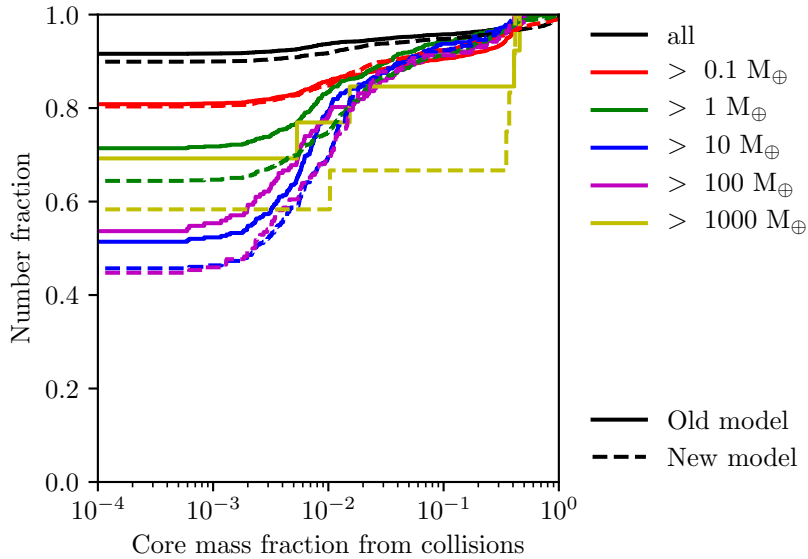


Figure 5.28: Cumulative distribution of the mass fraction that has been accreted from collision with other forming planets; for both the old and new collision models.

see that there is almost no mass transfer between the bodies. So even if they are quite numerous, they do not lead to accretion on the target. The same applies, to a lower extent, to collisions in the disruption regime. In the following results only mass difference is considered; however, one should not forget that even if masses do not change much, there can be material exchange resulting from a collision, which is not considered in the present analysis. The updated accretion per planet are shown in figure 5.28. Overall, we observe that the number of planets that accreted material from collisions with other massive bodies while the mass fraction remains similar. The most highest mass bin ($> 1000 M_{\oplus}$; in yellow on the figure) shows a strong increase of fraction of planets that accreted more than 10% of their mass from such collisions, to about 35%. We thus have more than one third of the very massive planets that accreted a significant fraction of their core from other forming planets while the remaining has almost no contribution from the other bodies.

A new possibility that arises from the new collision model is (solid) mass loss, in the erosion part of the disruption regime. This is not displayed in the figure; only about 4‰ of the planets are in a situation where the overall mass difference due to collisions is negative. Again, we encounter this situation for small planet masses.

The resulting core mass versus semi-major axis is shown in figure 5.29. The results are overall similar to the previous related population shown in this chapter (figure 5.20). The maximum core mass is now about $260 M_{\oplus}$, and we observe the same trend for the core mass as function of separation, without cut-off above 1 AU as in the population where the collision radius was assuming core's density (figure 5.19). We also observe a few cases of large core masses $m_c > 20 M_{\oplus}$ not dominated by gas. When comparing the total masses (figure 5.30), we observe that with the new collision model, there is a

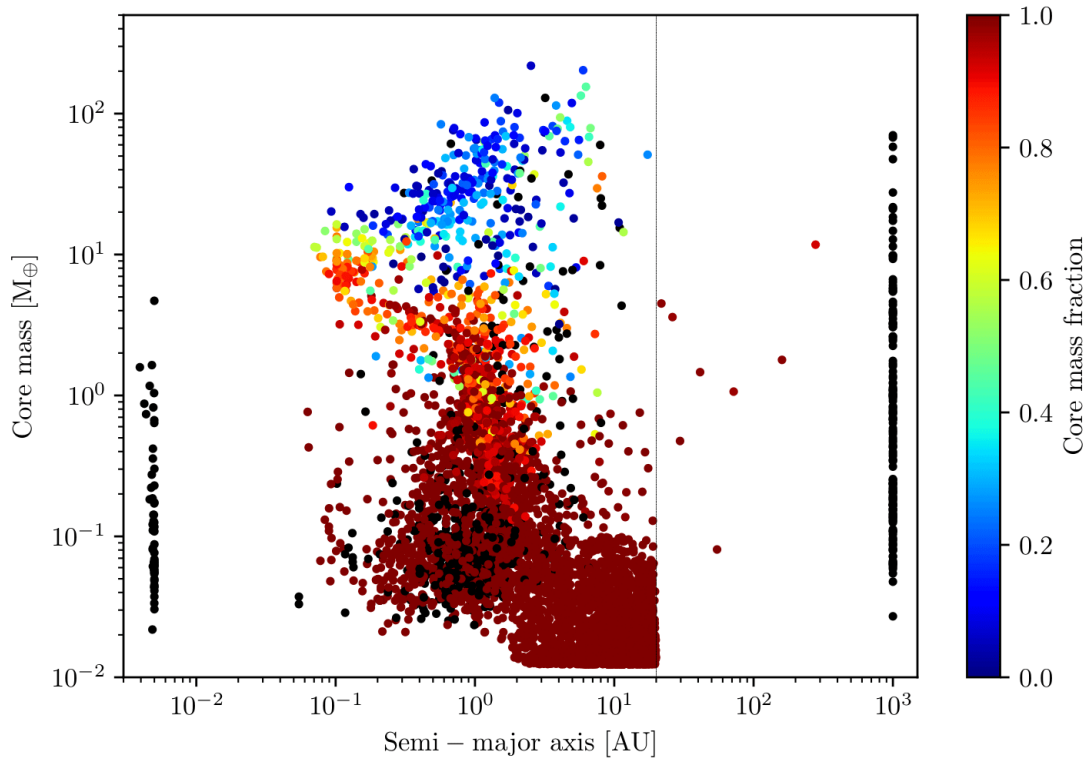


Figure 5.29: Same as figure 5.20, but the new collision model is being used.

reduction of the mass of the most massive planets. Also, there is no more jump between the few most massive planets and the remaining.

For the smaller mass planets, we however note some differences. We do observe some of them at large separation (more than 20 AU), which has not been the case for either of the two previous populations computed with the new formation model. Quite interestingly, less than the half of these planet suffered a collision, so the presence of those planets is not directly linked the new collision model.

The improvement of the collision model for impact between terrestrial planets leads to an increase of the number of collisions due to the second largest remnant suffering further collision events. The presence of the *hit-and-run* regime in the new model leads to a reduction of the mass accretion for such kind of collisions, but with only small effects at the population level, either in mass or location of these planets. Collisions between massive, terrestrial objects do not have a strong influence on the overall population of formed planets.

5.6 Other possible improvements

In the last section, the aim was to improve the collision model between planets without a significant envelope. This model handles a small majority of the collision events. The

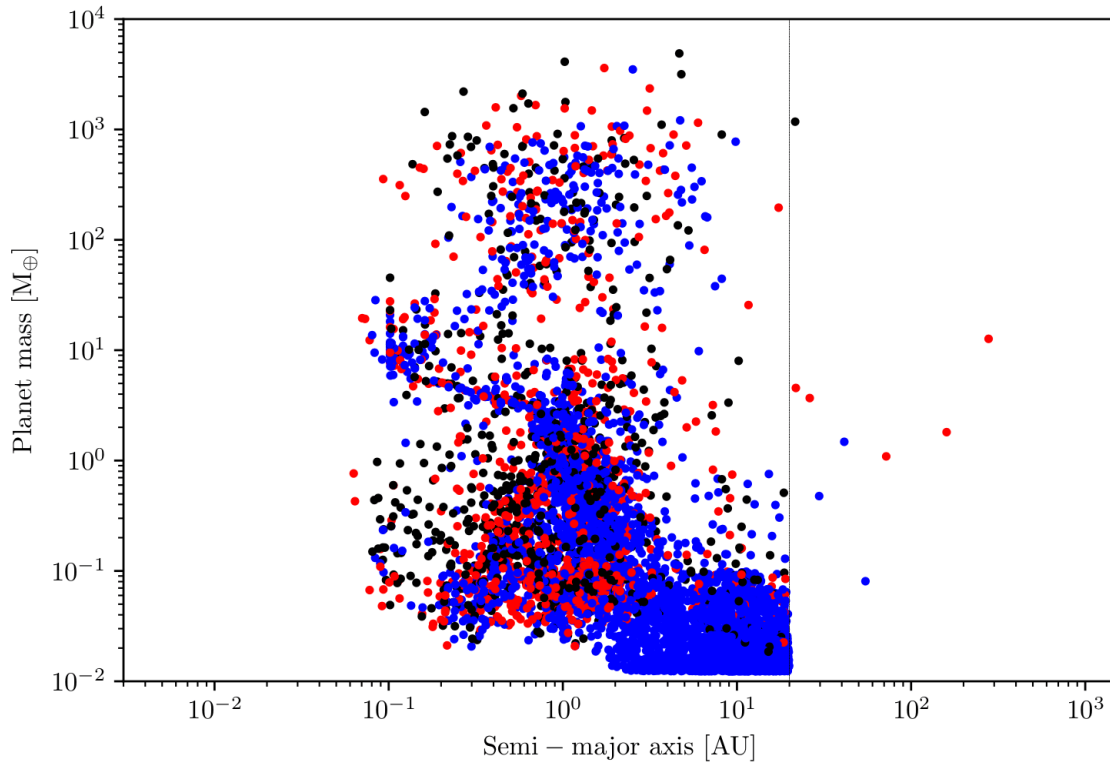


Figure 5.30: Mass-distance diagram for the comparison of two populations. *Black*: using old collision, *red*: with the new collision model, *blue*: planets that have the same characteristics in both populations.

other almost half still uses the original model, which could have a few enhancements. As a reminder, the original model works as follows: cores are merged, impactor’s envelope is always considered as lost and the fate of the target’s envelope depends on the impact energy: if the impact energy is greater than the gravitational binding, then the envelope is considered as lost and otherwise fully retained.

The effects of the episodic accretion of large bodies ($10^{-2} - 10^0 M_{\oplus}$) onto envelopes have been studied by Broeg and Benz (2012). They found that even for impact energies lower than the binding energy of the envelope, some part of the latter is stripped, although not as an entirely efficient process (i.e. not all the impact energy is used to counteract gravitational energy). For impact energies greater than the binding energy, the collision does not always lead to a full stripping of the envelope. The original collision model is not consistent with these results.

The loss of a part of the envelope can have important consequences on planet formation. For instance, this lead to a change of the fraction of solids if, for instance, the impact happens at the end of the disc so that the planet cannot accrete the same amount of gas it had previously. On the other hand, Broeg and Benz (2012) did also show that the episodic accretion of massive objects causes the removal of energy gained from the previously accreted gas due to envelope ejection. This effect subsequently enables faster

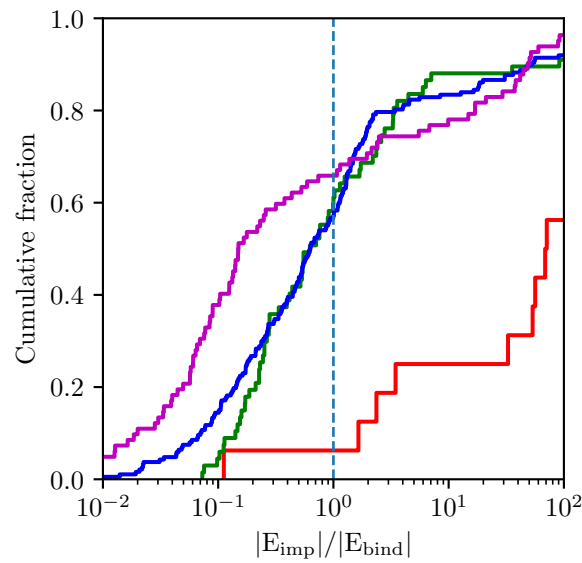


Figure 5.31: Ratio between impact energy and gravitational binding energy of the target's envelope. This value is used as criterion to determine whether it is ejected or not following the collision.

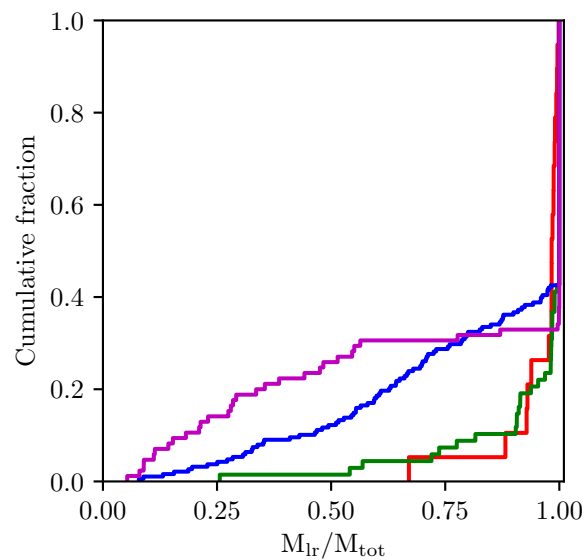


Figure 5.32: Ratio of largest remnant to total initial mass for collision events shown in figure 5.31.

accretion of gas.

For the collision model used in our formation model, the criterion for envelope ejection is shown in figure 5.31. It shows the population with the new collision model. Only the events that go through the old procedure are shown, hence the small amount of data available for the low masses. We see that the distributions show no special feature around $|E_{\text{imp}}|/|E_{\text{bind}}| \approx 1$, while mass of the largest remnant shown in figure 5.32 has a clear distinction between the case where the envelope is kept or not (the rapid increase just before $M_{\text{lr}}/M_{\text{tot}} = 1$; though not exactly at unity since the envelope of the impactor is always lost) and when it is stripped away (the remaining cases). Envelope non-ejection is almost always related to small values of γ (< 0.1) though the reciprocal is not true. The very different results that occur following a simple comparison between the impact and binding energy do not reflect what is obtained by Broeg and Benz (2012).

At the moment, the impact energy is disregarded when the envelope is not entirely stripped. This is not consistent with the accretion of planetesimals that contribute to the core's luminosity and Broeg and Benz (2012); the impact energy should then be added to the core and then released in the form of luminosity that will in turn affect the envelope structure. An implementation issue that arises is that there is no energy reservoir at the moment in the model; energy gained due to accretion and contraction is immediately radiated away.

5.7 Summary

In this chapter, we analysed collisions between planets in the context of planetary systems formation. The criterion to detect collisions as well as the model to process collisions between terrestrial planets (defined as when the mass of gas is lower than 1% of the total mass) have been improved. The following results have been obtained:

- The approach to calculate the eccentricity and inclination damping time scales affects the collision parameters, notably the impact velocity and angle. Using an approach consistent with results from hydrodynamical simulations (following (Cresswell and Nelson 2008)) leads to a distribution of impact angle closer to theoretical expectations and less collision events with impact velocity lower than the mutual escape velocity.
- The number of collision events is small compared to the number of planets, on average 1 per system with 10 embryos. The number of present planet at the end of the formation stage thus does not change much with the different methods to determine the radius for collision detection whereas the number of collisions increases by about 30%.
- Most of the planets that reach $1 M_{\oplus}$ did suffer a collision with another planet during the formation stages. Mass accretion from those events accounts for 1‰ to 30% of the solid component. This kind of collisions thus plays a minor role in the overall mass accretion.

- The outcome of collisions between terrestrial planets is now computed according to the scaling laws provided in Leinhardt and Stewart (2012) to better represent the physics of such events. Roughly half of the collisions happen in the "hit-and-run" regime where both remain almost undisrupted from the collision. The fraction of embryos that reach the end of the formation phase increases, mostly due to model not treating all events as mergers.
- Second largest remnants have a good probability to collide again, but with other objects in most cases.
- The modification of the collision model for terrestrial planets has a smaller effect on the population of giant planets than the modification of the radius for collision detection.
- The mass loss (in tertiary remnants or small bodies) is a small fraction of the pre-impact masses. For hit-and-run collisions, only a small fraction of events lead to mass transfer or loss.
- Orbital characteristics of the resulting bodies could be improved. In the case of an hit-and-run event, the orbit of the largest body remains unaltered while for the second a two bodies problem is assumed. Impactor slow down or deflection (e.g. Reufer 2011) are not taken into account.
- The collision model for planets with significant envelope has not been modified and it is not consistent with the results from Broeg and Benz (2012). The model could be enhanced by changing the binary switch that determines whether the envelope is ejected to account for those results.

Chapter 6

Modelling of collisions

This chapter presents the theoretical background and the numerical scheme used for the modelling of single collision events, which will be applied in the subsequent chapters. It starts with basic principles of fluid dynamics and thermodynamics that provide the constitutive equations. The applied numerical scheme is *Smoothed Particle Hydrodynamics* (SPH), a Lagrangian approach in which matter is divided into particles. Quantities are retrieved by interpolation on the neighbouring particles, thus avoiding the need of a grid. Smoothing, discretisation, and the representation of the governing equations will be discussed.

A part of this work has been dedicated to the addition of a model of solid forces, and its coupling the equation of state. This newly implemented model of solid stresses, will be used in chapter 8 to study Mars-scale giant collision, and the post-impact long-term evolution of the planets' interior. This method is further applied on a subset of simulations of new potential Moon-forming scenario (chapter 7).

The solid forces model is compared to laboratory experiments (section 6.5) in order to validate it. The problem of angular momentum conservation with this enhanced model is also addressed.

Density computation at material interfaces is a long-standing problem in SPH. A alternative approach will be investigated further in the last section of this chapter (6.7), along with a comparison with the standard variant of the SPH schemes.

6.1 Basic equations

In continuum mechanics, matter is treated as continuous and is evenly distributed in space. This is not true at the molecular level, but at the length scales considered here, it is a good approximation. The description of matter is made by macroscopic quantities. Fundamental principles such as the conservation of mass, momentum and energy are obeyed.

Two descriptions of the physical quantities are generally adopted. The Eulerian description use space as reference. In the following, time derivatives of quantities with respect to a fixed position will be noted using the partial derivative $\partial/\partial t$. The Lagrangian

description uses the matter itself as reference. Here the derivatives are calculated with respect the moving matter. They will be noted using the total derivative d/dt . The link between the two is obtained by

$$\frac{d}{dt} = \frac{\partial}{\partial t} + \mathbf{v} \cdot \nabla. \quad (6.1)$$

Mass conservation The continuity equation directly derives from mass conservation. It relates the temporal change of density with the divergence of the mass flux

$$\frac{\partial \rho}{\partial t} + \nabla \cdot \rho \mathbf{v} = 0. \quad (6.2)$$

In Lagrangian description, the equation reads as

$$\frac{d\rho}{dt} + \rho \nabla \cdot \mathbf{v} = 0 \quad (6.3)$$

due to the cancelation of the $\mathbf{v} \cdot \nabla \rho$ part of the divergence with the one from equation (6.1).

Momentum conservation leads to the equation of motion. The general one is given the *Navier-Stokes equation*. In the case of an inviscid flow, it reduces to the *Euler equation*

$$\frac{\partial \mathbf{v}}{\partial t} + (\mathbf{v} \cdot \nabla) \mathbf{v} = -\frac{\nabla p}{\rho} + \mathbf{g} \quad (6.4)$$

where the left hand part of the equation is actually the material derivative of the velocity (one can identify it with the right hand term of equation (6.1)), the first term of the right hand side corresponds to the pressure-gradient force and \mathbf{g} represent the external forces (e.g. gravity). This equation, together with the continuity equation have to be closed with a relation between p and ρ provided by the relevant equation of state (EoS). Leaving out the external force term and rewriting the equation to use material derivative gives

$$\frac{d\mathbf{v}}{dt} = -\frac{\nabla p}{\rho}. \quad (6.5)$$

For solid matter, forces are no longer always isotropic and the pressure term has to be generalised into a stress tensor. This is treated in more details in section 6.2.5 related to solid-state SPH.

Energy conservation In general, there are many contributions to the energy balance. However, the energy conservation related to the equation motion of a newtonian fluid (6.5) is quite simple as the only contribution is the work of the pressure force. We may thus start from the first principle of thermodynamics

$$dU = -pdV \quad \rightarrow \quad \frac{dU}{dt} = -p \frac{dV}{dt} \quad (6.6)$$

where the time variation of the volume can be reformulated in terms of density using

$$V = \frac{m}{\rho} \quad \rightarrow \quad \frac{dV}{dt} = -\frac{m}{\rho^2} \frac{d\rho}{dt} \quad (6.7)$$

assuming constant mass, and the time variation of density is computed with the continuity equation. Combining the two leads to

$$\frac{1}{m} \frac{dU}{dt} = -\frac{p}{\rho} \nabla \cdot \mathbf{v} \quad (6.8)$$

where the left hand term is the time variation of the specific internal energy $u = U/m$.

Another method to obtain an energy equation is to start with the conservation of total energy, $(e + u)$, where $e = 1/2 \cdot \mathbf{v}^2$ is the specific kinetic energy. The time variation of the specific kinetic energy is given by

$$\frac{de}{dt} = \frac{1}{2} \frac{d\mathbf{v}^2}{dt} = \frac{d\mathbf{v}}{dt} \cdot \mathbf{v} \quad (6.9)$$

so that by expanding $d(e + u)/dt = 0$ and replacing the expression of the kinetic energy by the above one obtains

$$\frac{du}{dt} = -\frac{d\mathbf{v}}{dt} \cdot \mathbf{v}. \quad (6.10)$$

Equation (6.8) is retrieved by replacing the $d\mathbf{v}/dt$ with equation (6.5).

6.2 SPH formalism

6.2.1 Smoothing

The idea of smoothing is that a spatial quantity, let it be called $B(\mathbf{r})$, can be approximated by performing a convolution between itself and a *kernel* function, usually called W

$$B'(\mathbf{r}) = \int B(\mathbf{r}') W(\mathbf{r}' - \mathbf{r}, h) d^3\mathbf{r}' \quad (6.11)$$

which provides the interpolation and where h is its characteristic spatial extend. The spatial derivatives of this quantity could be computed the same way. However, the advantage is that this integral can be transformed by integrating it by parts into

$$\nabla B'(\mathbf{r}) = \oint B(\mathbf{r}') W(\mathbf{r}' - \mathbf{r}, h) d\mathbf{S} - \int B(\mathbf{r}') \nabla_{\mathbf{r}} W(\mathbf{r}' - \mathbf{r}, h) d^3\mathbf{r}' \quad (6.12)$$

with the first term being applied on the surface of the integration volume. The subscript \mathbf{r} on the gradient of the last term indicates that the partial derivatives are to be taken with respect to \mathbf{r} . The sign of the whole term is changed by taking the gradient with reference to the spatial argument of the kernel. Also, if the surface term is neglected (see below), then the calculation of spatial derivatives simplifies to

$$\nabla B'(\mathbf{r}) = \int B(\mathbf{r}') \nabla W(\mathbf{r}' - \mathbf{r}, h) d^3\mathbf{r}'. \quad (6.13)$$

This is a strength of the smoothing scheme. The spatial derivatives of the quantities do not need to be known, rather they can be computed from the local variations of the quantity itself.

There are several constraints that hold on the kernel: first it must be normalised so that

$$\int W(\mathbf{r}', h) d^3\mathbf{r}' = 1. \quad (6.14)$$

A second condition is that it must be differentiable everywhere, so that interpolation of spatial derivatives shown above can also be performed. Furthermore, if the kernel fulfils the condition that it converges to a Dirac distribution when h tends toward zero, i.e.

$$\lim_{h \rightarrow 0} W(\mathbf{r}', h) = \delta(\mathbf{r}') \quad (6.15)$$

then it follows, by the properties of the Dirac distribution, that the interpolation converges to the initial quantity

$$\lim_{h \rightarrow 0} \int B(\mathbf{r}') W(\mathbf{r}' - \mathbf{r}, h) d^3\mathbf{r}' = B(\mathbf{r}). \quad (6.16)$$

There are also two usual property of the kernel: first it is isotropic, so that it only depends on the magnitude of the first argument. The kernel can then be given in the form $W(\mathbf{r}, h) = W(\|\mathbf{r}\|, h) = W(r, h)$. And the second property is to have compact support, where this support is given in terms of h : $W(r, h) = 0$ if $r > kh$. The latter condition is important for two reasons:

- In the case of numerical schemes as it allows a substantial performance increase when computing the different quantities, as the evaluation of the integral from equation (6.11) only has to be done over a specific volume rather than the whole space.
- The surface term of equation (6.12) is identically zero when the volume over which the integral is performed encompass the support of the kernel.

Cubic splines (Monaghan and Lattanzio 1985) are commonly used in SPH, where the 3D variant is given by

$$W(r, h) = \frac{1}{\pi h^3} \begin{cases} 1 - \frac{3}{2}v^2 + \frac{3}{4}v^3 & 0 \leq v < 1 \\ \frac{1}{4}(2 - v)^3 & 1 \leq v < 2 \\ 0 & 2 \leq v \end{cases} \quad v = \frac{r}{h} \quad (6.17)$$

and its gradient by

$$\nabla W(\mathbf{r}, h) = \frac{\mathbf{r}}{r} \frac{1}{\pi h^4} \begin{cases} -3v + \frac{9}{4}v^2 & 0 \leq v < 1 \\ -\frac{3}{4}(2 - v)^2 & 1 \leq v < 2 \\ 0 & 2 \leq v \end{cases} \quad (6.18)$$

Both vanish for $r \geq 2h$.

6.2.2 Particles

A continuum is not suitable for a numerical scheme as only a finite number of mathematical operations can be computed during a given period. Thus, a discretisation is done, and material is now represented by a given number of *particles*. As consequence, the integral (6.11) is replaced by a sum that iterate over the particles

$$B'(\mathbf{r}) = \sum_j B_j W(\mathbf{r} - \mathbf{r}_j, h) V_j \quad (6.19)$$

and where B_j is the value of the quantity of particle j and V_j its associated volume. The same applies for the gradient computation (equation (6.13)). Practically, this sum is only performed at a particle's location, but it is not a requirement, for instance when mapping quantities on a grid. For the following discussion, we assume that the sum is performed at the location of particle i , and the terms refers to that particle. The smoothing length get another meaning in combination with the compact support of the kernel: for each particle, only a subset of the other particles makes a contribution to the sum. They are commonly called *neighbours*, and the smoothing length defines their number. The optimal amount of neighbours is of the order of 50. To accommodate the huge variations of the particle density that arise in astrophysical problems, the smoothing length is variable both in time and space. Time variation will be discussed later. Spatial variation is achieved by giving an independent value to each particle, which is noted h_i . The SPH sum (6.19) needs to be modified accordingly. To retain conservation laws, it is desirable to have symmetrical terms, i.e. each particles pair should have to the same contribution to the sum of both particles, or in the case of the gradient, opposite. This implies that the smoothing length used to compute the kernel function must be the same. A way to achieve this is to consider the mean of the two smoothing lengths. Hence the following notation is introduced

$$h_{ij} = \frac{h_i + h_j}{2} \quad \mathbf{r}_{ij} = \mathbf{r}_i - \mathbf{r}_j \quad W_{ij} = W(\mathbf{r}_{ij}, h_{ij}) \quad \nabla W_{ij} = \frac{\partial W_{ij}}{\partial \mathbf{r}_i} \quad (6.20)$$

and equation (6.19) and the discrete version of equation (6.13) become

$$B'_i = \sum_j B_j W_{ij} V_j \quad \nabla B'_i = \sum_j B_j \nabla W_{ij} V_j. \quad (6.21)$$

A caveat of this modification is that, strictly speaking, h_i cannot be used to search for neighbours of the corresponding particle. For instance, if h_j is greater that the former, then the condition $r_{ij} < 2h_{ij}$ might not hold while $r_{ij} < 2h_i$ does. In this situation, particle i is a *neighbour* of particle j but not the reverse and the summation over the entire set is not symmetrical any more as the contribution of particle i is considered while performing SPH sums on particle j while the reverse is not true.

6.2.3 Hydrodynamics

In order to solve equation (6.19), the volume of the particles has to be retrieved. The standard SPH way is to assign a mass m_i to each particle and to compute its density. The

volume is then given by $V_i = m_i/\rho_i$. The advantage of this formulation is that solving the equation for the density with this volume prescription leads to a simplification

$$\rho_i = \sum_j m_j W_{ij} \quad (6.22)$$

which enables to compute other quantities without requiring other prior knowledge. It is also possible to use the continuity equation (6.3) to obtain the change rate of density.

$$\frac{d\rho_i}{dt} = -\rho_i(\nabla \cdot \mathbf{v})_i \quad (6.23)$$

In the latter case, density is treated as other integrated variables. Following (6.21), the velocity divergence would be computed with

$$(\nabla \cdot \mathbf{v})_i = \sum_j V_j (\mathbf{v}_j \cdot \nabla W_{ij}) \quad (6.24)$$

but the same problem as in the previous part is encountered: the terms are not symmetric. We thus follow the prescription of Monaghan (1992) and write the velocity divergence as

$$\nabla \cdot \mathbf{v} = \frac{1}{\rho} (\nabla \cdot (\rho \mathbf{v}) - \mathbf{v} \cdot \nabla \rho) \quad (6.25)$$

whose corresponding SPH formulation is

$$(\nabla \cdot \mathbf{v})_i = \frac{1}{\rho_i} \sum_j m_j (\mathbf{v}_{ij} \cdot \nabla W_{ij}). \quad (6.26)$$

There is no physical reason to prefer either of the two methods to compute density, it is purely a numerical problem. The continuity equation has the advantage that an absolute pressure can be given as initial condition, the SPH scheme then only computes its time variation whereas using the sum (6.22) leads to an absolute value of the density being re-computed at every step, thus it never remembers the previous state. Also, the sum makes an incorrect treatment of phase boundaries as for instance a part of sphere of radius $2h$ around particles close to these location are either empty or filled with other particle of a different material.

Momentum equation The SPH formulation of equation (6.5) is in principle easy to solve, but we again fall in the problem of symmetry. There are two ways to obtain a formulation which fulfils that condition: using the same trick as for the velocity divergence equation (6.26) or by deriving from Lagrangian mechanics. In either case, the resulting equation of motion reads as

$$\frac{d\mathbf{v}_i}{dt} = \sum_{j \neq i} m_j \left(\frac{p_i}{\rho_i^2} + \frac{p_j}{\rho_j^2} \right) \nabla W_{ij}. \quad (6.27)$$

The symmetry of the term with respect to the indices i and j ensures that momentum is conserved. One can also observe that the forces are central ($\nabla W_{ij} \parallel \mathbf{r}_{ij}$), and thus the equation of motion will conserve angular momentum.

Energy conservation In addition to the usual problem of symmetry, the SPH formulation of the energy equation (6.8) has to be consistent with the equation of motion in order to conserve the total energy of the system. The same procedure can be applied, re-writing the velocity divergence according to (Monaghan 1992) and taking the average between this one and the one derived using equation (6.26), that reads as

$$\frac{du_i}{dt} = \frac{1}{2} \sum_{j \neq i} m_j \left(\frac{p_i}{\rho_i^2} + \frac{p_j}{\rho_j^2} \right) \mathbf{v}_{ij} \cdot \nabla W_{ij}, \quad (6.28)$$

which is both symmetric with respect to the indices i and j and consistent with equation (6.27), i.e. equation (6.10) holds.

6.2.4 Artificial viscosity

Shock waves are irreversible process where kinetic energy is dissipated into thermal energy. The equation of motion derived above does not take this process into account. The SPH scheme would respond to the sharp changes by producing oscillation behind the shock front. An additional term is thus needed to model the effect of shocks. There are two main schemes to address to model shocks in SPH:

- Using a Riemann solver to address the Riemann problem. This is called Godunov SPH (Monaghan 1997).
- Adding an *artificial viscosity* that mimics the effects of shock waves. The idea is to smooth the transition and thus prevents the unphysical effects.

In our model, we use the second method, with the formulation of Monaghan (1992):

$$\Pi_{ij} = \begin{cases} \frac{-\alpha c_{ij} \mu_{ij} + \beta \mu_{ij}^2}{\rho_{ij}} & \text{if } \mathbf{r}_{ij} \cdot \mathbf{v}_{ij} < 0 \\ 0 & \text{else} \end{cases}, \quad \mu_{ij} = \frac{h_{ij} \mathbf{r}_{ij} \cdot \mathbf{v}_{ij}}{\mathbf{r}_{ij}^2 + 0.01 h_{ij}^2}. \quad (6.29)$$

where c_{ij} and ρ_{ij} are the averaged sound speed and density of the two particles i and j being computed as for h_{ij} using equation (6.20). The usual choice for the constants are $\alpha = 1$ and $\beta = 2$. The first term reproduces shear and bulk viscosities, while the second one is the *von Neumann* viscosity that is necessary to model high Mach number reached in shocks. The second term in the denominator of μ_{ij} is introduced to prevent singularities. The equation of motion is modified so that it now reads

$$\frac{d\mathbf{v}_i}{dt} = \sum_{j \neq i} m_j \left(\frac{p_i}{\rho_i^2} + \frac{p_j}{\rho_j^2} + \Pi_{ij} \right) \nabla W_{ij}. \quad (6.30)$$

The same observations as for the equation of motion can be made again, namely that both momentum and angular momentum are conserved due to symmetry and the forces being radial.

In order to retain energy conservation – equation (6.10) – the energy equation (6.28) has to be modified accordingly to

$$\frac{du_i}{dt} = \frac{1}{2} \sum_{j \neq i} m_j \left(\frac{p_i}{\rho_i^2} + \frac{p_j}{\rho_j^2} + \Pi_{ij} \right) \mathbf{v}_{ij} \cdot \nabla W_{ij}, \quad (6.31)$$

There are unfortunately some side-effects of the addition of this artificial viscosity, for instance it will also act on shear flows (Monaghan 1992).

6.2.5 Solid-state

The equations derived in the previous sections model a fluid material. For large objects, gravity is the dominant force and such treatment is sufficient. However, for smaller bodies this assumption no longer holds and solid forces must thus be included to provide physical results. An estimate about the size of bodies where solid might be neglected can be made on the following arguments. A first way is to infer it from the observation of solar system bodies: small objects, such as comets or small asteroids from the asteroid belt have irregular shape meaning that their internal strength is sufficient to counter act gravity whereas planets and big asteroids (e.g. 1 Ceres or 4 Vesta) have a spherical form indicating gravity is stronger. Second, for purpose of catastrophic disruption criterion the transition between the strength and gravity regime have been investigated (e.g. Benz and Asphaug 1999) and found to happen for sizes of ~ 1 km. Put together, one could argue that solid strength for objects bigger than a few hundred kilometres can be neglected. As we shall see, this limit is not sharp as discussed here and solid strength might still produce significant effect even on larger objects. The model described here to represent those solid forces is based on the one developed by Benz and Asphaug (1994, 1995). As this section will make an extensive use of tensors, the following convention will be in use: superscript Greek letter indicate the components of tensors and vectors whereas subscript Latin letter will denote SPH particles in the appropriate part.

As first step, we generalise equation (6.5) by replacing the pressure gradient with a stress tensor $\sigma^{\alpha\beta}$, which yield the modified equation of motion

$$\frac{\partial v^\alpha}{\partial t} = \frac{1}{\rho} \frac{\partial \sigma^{\alpha\beta}}{\partial x^\beta}. \quad (6.32)$$

This stress tensor can be decomposed in two parts: one being the mean stress normal to the surface (also called hydrostatic stress), from which the pressure is defined, and the second one being the deviatoric part of the same tensor. This allows us to write it as

$$\sigma^{\alpha\beta} = -p\delta^{\alpha\beta} + S^{\alpha\beta} \quad (6.33)$$

where p is the pressure, $\delta^{\alpha\beta}$ the Kronecker symbol and $S^{\alpha\beta}$ is said deviatoric stress tensor. One can see that in the case $S^{\alpha\beta} = 0$ the equation of motion reduces to the one for a fluid material. The value of the stress tensor shall now be computed. For that purpose, linear elasticity (Hooke's law) for an isotropic, continuous media is assumed. As we already

described the part for the hydrostatic stress tensor from the fluid dynamics parts, the following focuses on the deviatoric stress tensor. Hooke's law can be written as

$$S^{\alpha\beta} = 2\mu \left(\varepsilon^{\alpha\beta} - \frac{1}{3} \varepsilon^{\gamma\gamma} \delta^{\alpha\beta} \right) \quad (6.34)$$

with μ being the shear modulus of the material and $\varepsilon^{\alpha\beta}$ the strain tensor. The second term inside the parentheses makes the deviatoric stress tensor traceless. Its time derivative could in principle be simply written as

$$\dot{S}^{\alpha\beta} = 2\mu \left(\dot{\varepsilon}^{\alpha\beta} - \frac{1}{3} \dot{\varepsilon}^{\gamma\gamma} \delta^{\alpha\beta} \right) \quad (6.35)$$

but this formulation has the big disadvantage of being dependent on the choice of the reference frame. To avoid this, we use the Jaumann rate and write

$$\dot{S}^{\alpha\beta} = 2\mu \left(\dot{\varepsilon}^{\alpha\beta} - \frac{1}{3} \dot{\varepsilon}^{\gamma\gamma} \delta^{\alpha\beta} \right) + S^{\alpha\gamma} R^{\beta\gamma} + S^{\beta\gamma} R^{\alpha\gamma} \quad (6.36)$$

with $\dot{\varepsilon}^{\alpha\beta}$ and $R^{\alpha\beta}$ being the strain rate and rotation rate tensors respectively, which are defined as the symmetric and anti-symmetric parts of the velocity gradient

$$\dot{\varepsilon}^{\alpha\beta} = \frac{1}{2} (U^{\alpha\beta} + U^{\beta\alpha}) \quad (6.37)$$

$$R^{\alpha\beta} = \frac{1}{2} (U^{\alpha\beta} - U^{\beta\alpha}) \quad (6.38)$$

$$U^{\alpha\beta} = \frac{\partial v^\alpha}{\partial x^\beta} \quad (6.39)$$

The time derivative of the internal energy has also to be corrected so that the total energy is still conserved

$$\frac{\partial u}{\partial t} = \frac{1}{\rho} \sigma^{\alpha\beta} \dot{\varepsilon}^{\alpha\beta} = -\frac{p}{\rho} (\nabla \cdot \mathbf{v}) + \frac{1}{\rho} S^{\alpha\beta} \dot{\varepsilon}^{\alpha\beta} \quad (6.40)$$

For the SPH formulation of the above equations, the same procedure as for the fluid case is used. In standard SPH, the equations are the same as in Benz and Asphaug (1994) with (6.32), (6.39) and (6.40) written as

$$\frac{\partial v_i^\alpha}{\partial t} = \sum_{j \neq i} m_j \left(\frac{\sigma_i^{\alpha\beta}}{\rho_i^2} + \frac{\sigma_j^{\alpha\beta}}{\rho_j^2} \right) \frac{\partial W_{ij}}{\partial x_i^\beta} \quad (6.41)$$

$$U_i^{\alpha\beta} = \sum_{j \neq i} \frac{m_j}{\rho_j} v_{ij}^\alpha \frac{\partial W_{ij}}{\partial x_i^\beta} \quad (6.42)$$

$$\frac{\partial u_i}{\partial t} = -\frac{1}{2} \sum_{j \neq i} m_j \left(\frac{\sigma_i^{\alpha\beta}}{\rho_i^2} + \frac{\sigma_j^{\alpha\beta}}{\rho_j^2} \right) v_{ij}^\alpha \frac{\partial W_{ij}}{\partial x_i^\beta} \quad (6.43)$$

The Miscible SPH version (as defined in section 6.2.9) of those equations can be obtained in a similar way:

$$\frac{\partial v_i^\alpha}{\partial t} = \frac{1}{m_i} \sum_{j \neq i} \left(\frac{\sigma_i^{\alpha\beta}}{\delta_i^2} + \frac{\sigma_j^{\alpha\beta}}{\delta_j^2} \right) \frac{\partial W_{ij}}{\partial x_i^\beta} \quad (6.44)$$

$$U_i^{\alpha\beta} = \sum_{j \neq i} \frac{1}{\delta_j} v_{ij}^\alpha \frac{\partial W_{ij}}{\partial x_i^\beta} \quad (6.45)$$

$$\frac{\partial u_i}{\partial t} = -\frac{1}{2m_i} \sum_{j \neq i} \left(\frac{\sigma_i^{\alpha\beta}}{\delta_i^2} + \frac{\sigma_j^{\alpha\beta}}{\delta_j^2} \right) v_{ij}^\alpha \frac{\partial W_{ij}}{\partial x_i^\beta} \quad (6.46)$$

The equations so far describe a perfectly elastic material. In nature however, this is not the case and material experiences plastic deformation once they reach a certain stress level. Two models are used to reproduce this behaviour: first we follow Benz and Asphaug (1994) who uses the von Mises yield criterion. Its mathematical formulation is

$$J_2 = \frac{Y^2}{3} \quad (6.47)$$

where J_2 is the second invariant of the deviatoric stress tensor, and Y the yield strength of the material being considered. The former is defined as

$$J_2 = \frac{1}{2} S_{\alpha\beta} S_{\beta\alpha} = \frac{1}{2} S_{\alpha\beta} S_{\alpha\beta} \quad (6.48)$$

as the tensor is symmetric. In case this value gets higher than the right hand term of eq. (6.47), then the deviatoric stress tensor is reduced with

$$S_{\alpha\beta} \rightarrow S_{\alpha\beta} \frac{Y_0}{\sqrt{3J_2}} \quad (6.49)$$

so that the new stress tensor satisfies the criterion. We do not include crack growth due to tensile fracturing, but intend to model an entirely fractured (damaged) material. In the original model by Benz and Asphaug (1994), this falls back to the fluid case. We thus follow the approach used in Jutzi (2015) and apply the model by Collins et al. (2004) which used two yield strengths: one for intact material and one fully damaged one. They are defined respectively as follows:

$$Y_i = Y_0 + \frac{\mu_i p}{1 + \frac{\mu_i p}{Y - Y_0}} \quad (6.50)$$

$$Y_d = \mu_d p \quad (6.51)$$

where μ_i and μ_d are coefficient of friction for intact and damaged material, which we set as $\mu_i = 2$ and $\mu_d = 0.8$, and Y_0 is the yield strength at zero pressure (or cohesion). Y_i varies from Y_0 at zero pressure until Y for high values. We then compute the yield strength for the given damage with

$$Y \rightarrow Y_i(1 - D) + Y_d D \quad (6.52)$$

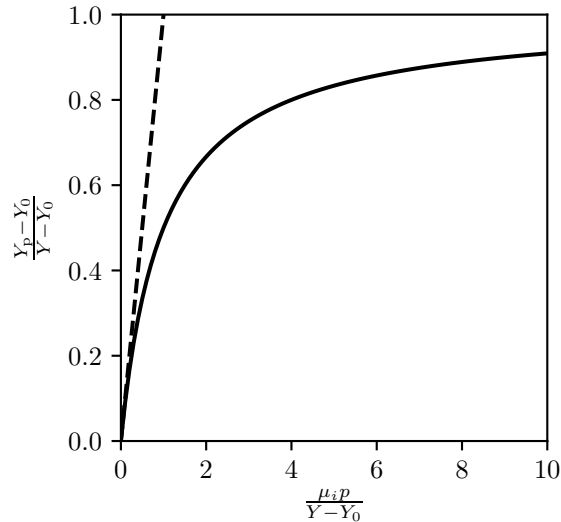


Figure 6.1: Yield strength versus pressure for the relation used in Collins et al. (2004) (solid line), and identity function for comparison (dashed line).

where D is the damage, which we set to unity. The expression reduces thus to $Y_d D$, but Y_i is still needed to serve as upper boundary for the yield strength at high pressure. The behaviour of this function is shown in fig. 6.1. The second modification is the computation of the stress tensor reduction, where the factor $\sqrt{3}$ is removed from eq. (6.49).

In addition, the temperature dependence of yield strength has to be taken into account. For instance, once the corresponding temperature is reached, material becomes molten, and thus cannot support shear stresses anymore. To avoid a discontinuity in the yield strength at the liquid-solid transition, Benz and Asphaug (1994) proposed to use a linear temperature dependence from maximum value at zero temperature until zero strength at melt temperature. Collins et al. (2004) used another expression that has the same boundary conditions, but keeps a higher strength at low temperature using the relation

$$Y \rightarrow Y \tanh \left(\xi \left(\frac{T_{\text{melt}}}{T} - 1 \right) \right) \quad (6.53)$$

with $\xi = 1.2$. The comparison of the two functions is shown in fig. 6.2.

One also has to determine the melt temperature. For the Tillotson equation of state, no temperature information is available, and the reduction of yield strength is based on the internal energy with the transition to fluid happening at a constant value u_{melt} . This simple approach is used in the model by Jutzi (2015). A more realistic approach to determine the melt temperature will be described in section 6.3.1.

6.2.6 Angular momentum conservation with solid strength

With the additional forces due to the solid strength model, angular momentum is not conserved. An example of such behaviour is shown in figure 6.3: the "non-corrected"

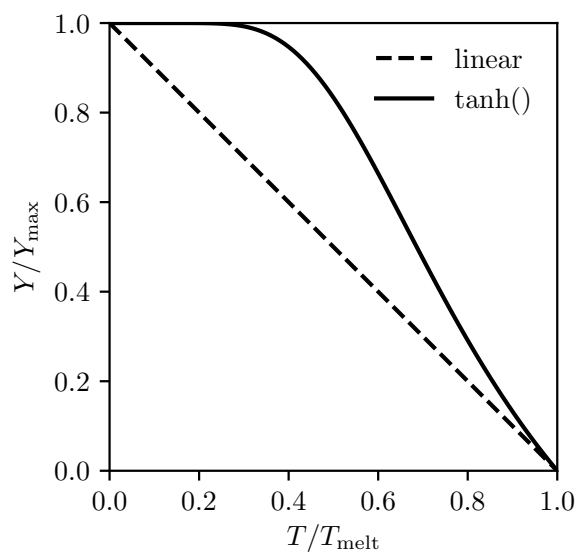


Figure 6.2: Comparison of two functions used to reduce the yield strength with temperature

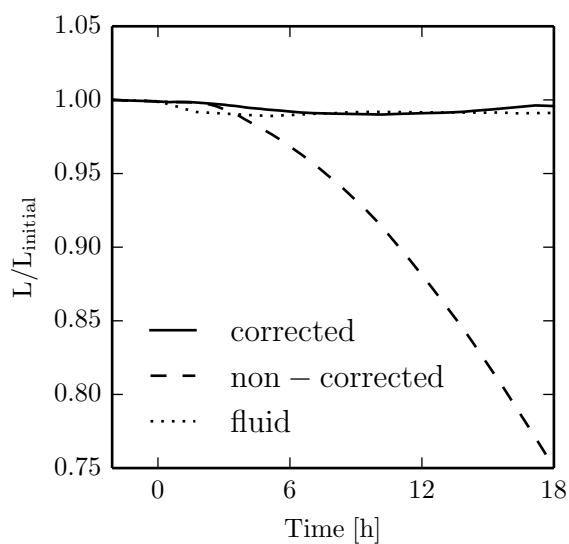


Figure 6.3: Angular momentum as function of time for three simulations of giant collisions on a Mars-like body. Same as figure 9 of the first paper presented in chapter 8.

(dashed line) case shows the behaviour with the solid forces models described in the last section, with the "fluid" case showing the results without the solid forces model. With the non-corrected solid forces model, angular momentum decrease as the solid body rotation takes places in the target following angular momentum transfer from the impactor. Therefore, there is no angular momentum loss during the initial stage, as there is no pre-impact rotation. Even though the body only rotates by about 180° during the simulation; the decrease is thus considerable (about 25%).

As suggested by Speith (2006), the reason for the slowdown is that the standard SPH formulation of equation (6.39) (equation (6.42)) is only zeroth order consistent. The solid body rotation is however linear in coordinates ($v \propto r$ in the rotation plane) and thus require a scheme that is also first order consistent. He proposed an expansion approach (called eSPH) to increase the consistency of the velocity gradient tensor, limited to the first order. He showed that the equation fulfilling this condition takes the form

$$\sum_{j \neq i} V_j v_{ij}^\alpha \frac{\partial W_{ij}}{\partial x_i^\gamma} C_i^{\alpha\gamma} = \delta^{\alpha\beta} \quad (6.54)$$

which means that the correction tensor C_i is the inverse of the tensor A_i (i.e. $C_i = A_i^{-1}$) which is written as

$$A_i^{\alpha\beta} = \sum_{j \neq i} V_j v_{ij}^\alpha \frac{\partial W_{ij}}{\partial x_i^\beta}. \quad (6.55)$$

The tensor C_i is now used to correct the computation of the velocity gradient tensor. The equation (6.42) is now written as

$$U_i^{\alpha\beta} = \sum_{j \neq i} \frac{m_j}{\rho_j} v_{ij}^\alpha \frac{\partial W_{ij}}{\partial x_i^\gamma} C_i^{\gamma\beta}. \quad (6.56)$$

For numerical reasons, if the determinant of the A_i tensor is lower than 10^{-20} in our unit system, then C_i is set to the identity. The angular momentum as function of time with the correction method is also shown on figure 6.3. We see that angular momentum is now conserved to the same precision as with purely-fluid SPH. The implementation of the scheme adds some complexity to the whole model; indeed the C_i tensor needs to be known before being able to compute any term of the velocity gradient tensor, which implies that the A_i tensor cannot be computed concurrently as the other SPH quantities.

6.2.7 Time and location dependent smoothing length

As stated in section 6.2.2, each particle has its own smoothing length, which gives the location dependence. Here we specify the time dependence. The basic idea is to maintain a stable number of neighbours, so that there are roughly $N_{\text{opt}} = 50$ particles within a sphere of radius h_i centred on the particle i . The particles' mass being fixed, their volume is inversely proportional to their density. And so, the volume of the sphere must follow the one of the particles, i.e.

$$h^3 \propto V \propto \frac{1}{\rho}. \quad (6.57)$$

From this follows the time variation of the smoothing length

$$\dot{h}_i = -\frac{h_i}{3\rho_i}\dot{\rho}_i = \frac{h_i}{3}(\nabla \cdot \mathbf{v})_i \quad (6.58)$$

where the last equality has been retrieved from equation (6.23). The velocity divergence is then computed using e.g. equation (6.26).

While the SPH sums are performed, the number of neighbours that make a contribution (i.e. $W_{ij} > 0$, that is $r_{ij} < 2h_{ij}$) is counted. In the case the number diverges significantly from the optimal value, the time variation is modified to bring it back closer to N_{opt} . This method is described in Reufer (2011). In short, it uses the maximum of the velocity divergence $\max_i(\nabla \cdot \mathbf{v})_i$ to add additional terms to equation (6.58) that predominate if the number of neighbours is lower than $\frac{2}{3}N_{\text{opt}}$ or higher than $\frac{5}{3}N_{\text{opt}}$.

For particles in locations where their number density is stable, the correction is not a problem, as the number of neighbours is roughly proportional to h_i^3 . However, when they are in regions where there are large fluctuations of the particles density, then the range for the smoothing length where the number of neighbours is between the limits is very narrow. This happens for instance in ejected material forming small clumps as well as in the case of isolated particles. It has been observed that the number of neighbours can change from zero to a few hundred for a very small change in the smoothing length. In such cases, the present scheme is never able to find a correct value for the smoothing length and constantly over corrects it in both directions, possibly leading to unstable simulations.

As noted by Monaghan (1992), the standard equations of SPH are not affected by a variable smoothing length.

6.2.8 Time integration

The conservation equations (with additional forces such as gravity), together with an equation of state (section 6.3) form a closed system of differential equations. These equations can be solved using the SPH technique as discussed above. An usual choice for the numerical scheme to perform the actual time integration is the predictor-corrector method (Press 2002) due to its simplicity and the low number of required evaluations of the derivatives per step (two). The first order scheme, for any integrated quantity B , reads as

$$B^{(1/2)} = B^{(0)} + \frac{1}{2} \left(3\dot{B}^{(0)} - \dot{B}^{(-1)} \right) \Delta t \quad (6.59)$$

$$B^{(1)} = B^{(0)} + \frac{1}{2} \left(\dot{B}^{(0)} + \dot{B}^{(1/2)} \right) \Delta t. \quad (6.60)$$

The first equation gives the predicted values and the second the corrected ones. At each step two computation of the derivative are required to obtain $\dot{B}^{(0)}$ and $\dot{B}^{(1/2)}$. $\dot{B}^{(0)}$ needs to be retained as it will be used as $\dot{B}^{(-1)}$ of the next step. An initialisation is required for the first step, which sets $\dot{B}^{(-1)} = \dot{B}^{(0)}$. The second order scheme is used for the time integration of positions and velocities. It is made from a chain of two first order schemes; the first for the velocity and the second for the position.

Different criteria are used to limit the time step. Hydrodynamical simulations must fulfil the Courant–Friedrichs–Lewy (or *CFL*) condition, which has the meaning that a wave should not propagate further than the spatial resolution during one time step. In the case of SPH, the spatial resolution is given by the spacing between particles, which is well represented by the smoothing length. Waves propagate at the sound speed, so the condition can be written as

$$\Delta t_i^{\text{CFL}} = C_{\text{CFL}} \frac{h_i}{c_{s,i}} \quad (6.61)$$

with $C_{\text{CFL}} = 0.4$ a constant. Another limit is set by the acceleration term which should not lead to a strong modification of the position within a step, so we define

$$\Delta t_i^{\text{A}} = C_{\text{A}} \sqrt{\frac{h_i}{|\mathbf{a}_i|}} \quad (6.62)$$

where $C_{\text{A}} = 0.25$ is another constant. Stability analysis also requires that the integrated variables do not change significantly during a step, so for any other integrated quantity B_i the limitation is set by

$$\Delta t_i^{\text{B}} = C_{\text{B}} \frac{B_i}{|\dot{B}_i|} \quad (6.63)$$

where the constants C_{B} are in the range 0.1 – 0.3. In the case of the stress tensor, this criterion is applied to each component separately. For most of the integrated variables, a minimum value B_{min} is enforced. This is particularly the case for the density (in the case the continuity equation is used) and smoothing length, as zero or negative values would break the whole scheme. For those variables, the time step condition is not enforced when $B_i < B_{\text{min}} (1 + C_{\text{B}})$ and $\dot{B}_i < 0$ they may reach the lower boundary during the following time step. There is no such requirements for the components of the stress tensor, so in order to avoid too small time steps, the numerator of equation (6.63) is modified to

$$B_i \rightarrow |B_i| + B_{\text{min}}. \quad (6.64)$$

The final time step is the minimum of all the individual values.

The predictor-corrector scheme requires a common time step for all particles. In the collision simulations performed in this thesis this is barely a problem, because the CFL criterion relates to the spatial resolution, hence the density. High density regions have a smaller smoothing length following relation (6.57), and are located within the bodies, which represent most of the particles. A multiple time approach would not lead to a significant advantage.

The problem regarding the correction of the smoothing length in the case of a non-uniform particle density discussed in the previous section also has a consequence on the time step. In the case the correction is strong, it will cause the time step to decrease drastically. Furthermore, the change will always be of the same magnitude ($\approx C_{\text{h}}$). It has been observed that in some circumstances, the time step becomes very small (a few orders of magnitude lower than the required from CFL condition) while the smoothing length oscillates between two extreme cases, one for which the number of neighbours is

small (a few particles) and one for which it is large (a few hundreds), without finding a solution where the number of neighbours is about the optimum. The point is that the correction does not work well with the predictor-corrector scheme. When it decreases due to the approach of the region where the number of neighbours is close to optimal, then the derivative suddenly drops, which is expected. However, the derivative of the previous time is still used to compute the prediction step; so even if the smoothing length's value leads to the expected number of neighbours then it need an additional time step to become stable again. During that particular time step, it has been observed that the smoothing length is shifted away from the optimal value due to feedback of the previous derivative.

A few modifications have been investigated to solve this issue. A possible work around is to only apply the time step criterion when the derivative is negative. Then, the number of neighbours can become large, but the increase of the smoothing length will not limit the value of the time step. This procedure is applied in most of the simulations performed in this work.

6.2.9 Density computation at interfaces

One of the major problems with standard SPH is that the density is not correctly computed at interfaces. These interfaces might occur at object surfaces, phase changes within a material, or when materials governed by different equations of state are in contact. In all cases, this relates to the presence of neighbours with a different density for a similar pressure and internal energy (or their absence in the case of the surface). In the case of density summation – equation (6.22) – this creates a group of particles where the density is averaged. Example of such behaviours are discussed in chapter 8. It is found that both methods to compute the density lead to artefacts close to the interfaces between the different materials and close to the surface.

There were quite a few attempts to solve this problem, some of them will be mentioned here. In the so-called *miscible SPH* (Ott and Schnetter 2003; Solenthaler and Pajarola 2008), the summation is weighted by the number density of particles rather than the usual mass density. This introduces a new quantity

$$\delta_i = \sum_j W_{ij}, \quad (6.65)$$

the smoothed volume, which is then related to the mass density with

$$\rho_i = m_i \delta_i. \quad (6.66)$$

The remaining equations for the fluid SPH are given in Reufer (2011) and in the relevant section above for the solid SPH part. As the smoothing now occurs using the volume, the new requirement is that all particles have the same volume initially. With the set up procedure used here this is already the case, but due to hydrostatic equilibrium the pressure (hence density) increases with depth, so even within a single phase of one material the masses will be slightly different. If the particles are moved around inside the bodies following a collision this might cause problems. Reufer (2011) showed

that this scheme reduces artefacts at the material transition (core-mantle boundary) after the set-up phase. We performed further test simulations using the miscible SPH scheme (presented in section 6.7) and identified a number of severe problems.

Saitoh and Makino (2013) developed another formulation of SPH where the interpolation is performed on the internal energy density (which is proportional to the pressure for an ideal gas equation of state) rather than mass density. The pressure has the advantage that it remains continuous at material interfaces; however, this is not the case at free surfaces. The method was later extended to arbitrary equations of state (Hosono et al. 2013) and has been applied for instance to a possible Moon-forming giant impact (Hosono et al. 2016).

Reinhardt and Stadel (2017) presented a method to correct the density of SPH particles at free surfaces. The fraction of empty volume in the sphere surrounding the particle is estimated and compensated accordingly. This method is complementary to the miscible SPH described above, as it applies only at interfaces, where the previous method would not solve the problem. The method is however too recent to have been incorporated in our SPH scheme.

6.3 Equation of state

The equations given in the previous parts require the pressure in order to be solved. A natural choice for SPH is to use an equation of state in the form of $p(\rho, u)$ as these two variables are already provided. A simple equation of state is the ideal gas, which is suitable for low density, high temperatures. To treat planetary interiors, which mostly involve solid and liquid phases, a more refined approach is needed.

A relatively simple equation of state was introduced by Tillotson (1962). Its advantage is to have the form $p(\rho, u)$, which makes it directly usable in SPH. On the other side, it only provides the pressure and sound speed; while this is sufficient to solve the differential equations, it can restrict further analysis. The phase space is divided into three regions: in the first region, the material is compressed or cold, in the second it is both expanded and hot and finally there is a region in between, but only for the expanded regime. The distinction between compressed and expanded state is made by comparing the density ρ to the standard zero-pressure density ρ_0 . In the expanded case (where $\rho < \rho_0$), there are two energy levels, the one of incipient vaporisation (E_{iv}) and the energy of complete vaporisation (E_{cv}), that serve as boundaries between the phases. A graphical representation is provided in figure 6.4. In the cold or compressed regime, the pressure is mainly driven by the bulk modulus and its first order correction. The compression ratio is given by

$$\eta = \rho/\rho_0 \qquad \mu = \eta - 1 \qquad (6.67)$$

and with the help of some parameters

$$k_3 = \frac{u}{E_0\eta^2} \qquad k_1 = \frac{1}{k_3 + 1} \qquad (6.68)$$

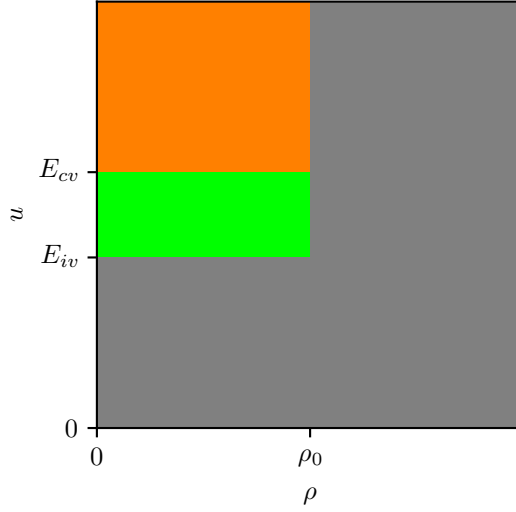


Figure 6.4: Schematic phase diagram for the Tillotson equation of state. The grey area is the cold or compressed regime, shown in orange is the the hot and expanded regime and in green for the intermediate one.

the pressure and sound speed have the following form:

$$p_c = (a + bk_1)\rho u + A\mu + B\mu^2 \quad (6.69)$$

$$c_{s,c}^2 = \frac{\partial p_c}{\partial \rho} = au + bu(3k_3 + 1)k_1^2 + \frac{p(a + bk_1^2)}{\rho} + \frac{A + 2B\mu}{\rho_0}. \quad (6.70)$$

The hot and expanded regime represent vaporised material. Here, the internal energy plays a more important role in the computation of the pressure. With the parameters

$$k_4 = 1/\eta \quad k_2 = k_4 - 1 \quad (6.71)$$

$$e_1 = e^{-\beta k_2} \quad e_2 = e^{-\alpha k_2^2}, \quad (6.72)$$

the pressure is now written as

$$p_e = a\rho u + (\rho b k_1 + A\mu e_1)e_2. \quad (6.73)$$

For the intermediate regime, a linear interpolation between p_c and p_e is performed to obtain the pressure. The same applies for the sound speed. For any regime, a minimal value of the sound speed is defined as

$$c_{s,\min}^2 = \frac{A}{4\rho_0}. \quad (6.74)$$

The equation of state depends thus on the following material parameters: ρ_0 the zero-pressure density, A the bulk modulus at ρ_0 , B its first order correction, also at ρ_0 , E_{iv} and E_{cv} , the energy limits for the regime transition, as well as a , b , α and β which are

non-dimensional parameters. As already mentioned, no other state variable is obtained directly from the equation of state. For representation purpose, and to get a physical meaning of the internal energy, the temperature is a useful quantity. The simple way to relate it with the quantities already present in the equation of state is to use the heat capacity and then write the temperature as

$$T = u/c_p \quad (6.75)$$

where c_p is the heat capacity at constant pressure. This formula doesn't consider phase transition and the respective latent heats, neither does Tillotson for solid-liquid transition. We could in principle handle the liquid-gas (or solid-gas) transition consistently as we can deduce the latent vaporisation heat by computing $(E_{cv} - E_{iw})$ and subtracting it from u in the case $\rho < \rho_0$.

An equation of state that handles better the condensed matter is called ANEOS (Thompson and Lauson 1972). At its root, is the minimisation of the Helmholtz free energy $F(\rho, T)$. Its input variables are thus the native ones of F , namely ρ and T . It can handle the different material phases and their transition. The routine also provides a value indicating in which phase (or mixture in case of phase transition) the material is. The transition between vapour and condensed phases is always included; the one between solid and liquid requires the latent heat of fusion (this part is important for the solid rheology; see below). The so-called *phase number* returned by ANEOS does not however make a distinction between liquid, gas and supercritical fluid. However, the equation of state provides the location of the critical point, which gives us a way to discriminate them with this simple algorithm: first if both pressure and temperature are above the critical values, then the material is in a supercritical state. If this is not the case, then the density is evaluated: if below the critical value, then it is in the gaseous form, otherwise it is liquid.

ANEOS has been improved by Melosh (2007) to better treat geological material, such as SiO_2 , that are used to represent the mantle of planets in astrophysical simulations. The modifications encompass the inclusion of molecular clusters in the vapour phase and correction of the potential in the solid phase. The original version of ANEOS was designed for metals, therefore some approximations were made, but they are only valid for these specific materials. For instance, in the vapour phase, all compounds were assumed to dissociate. For SiO_2 this approximation holds only for very high temperatures. Slightly above the boiling point, the gas phase is composed mainly of SiO and O_2 . The resulting modified version of the equation of state is called M-ANEOS. This modified treatment might still not well fit the real behaviour of silicates, as suggested by Kraus et al. (2012). They find a shock pressure to completely vaporise the material is about a factor two lower than what M-ANEOS predicts. They attribute this problem to both the lack of latent heat of melting and an incorrect heat capacity in the fluid region. Another consequence of the lack of the latent heat of melting is the impossibility to differentiate the solid and liquid phases (see hereafter). The modifications performed by Melosh (2007) are specifically made for silicates, and indeed the additional parameters are only provided for it. Consequently, the processing of the other materials (iron and water) is performed with the original ANEOS program.

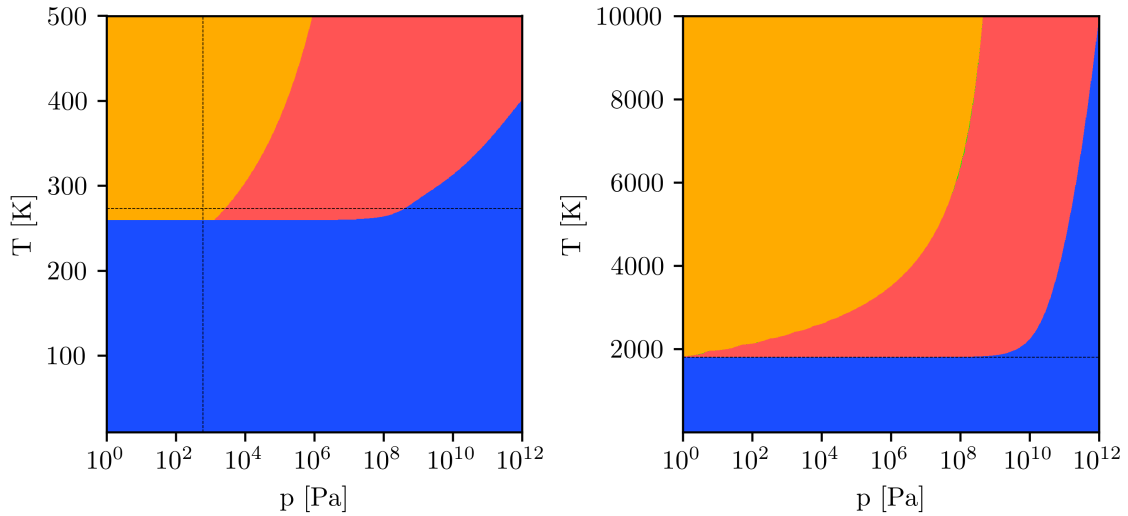


Figure 6.5: ANEOS phase diagram in the pressure-temperature space for water (left) and iron (right). The transition between the blue (solid) region and either orange (gas) or red (liquid) ones gives the melting temperature at a given pressure. The black dashed lines denote the location of the triple point taken from literature.

To obtain the equation with u rather than T as input variable, a root finding algorithm is used. Both the ANEOS routine and the root finding algorithm are computationally expensive. The results of ANEOS are thus tabulated during a preparation step. While performing the SPH simulation, the quantities are retrieved by interpolation in the said table. To encompass the huge density and energy contrast found during collision events, ANEOS is tabulated in the $(\log \rho, \log u)$ space, as well as $(\log \rho, \log S)$ for the isentropic relaxation phase prior to the collision simulation.

6.3.1 Coupling with solid model

As discussed in section 6.2.5, the melting temperature plays an important role for the solid rheology. For the Tillotson equation of state, only sparse information about phases is available, and the idea is to do the same thing for state transitions: use a constant value for the energy, which can in principle be related to the temperature using equation (6.75). ANEOS can handle the solid-liquid (or solid-gas) transition provided the latent heat is given for the material. This is the case for water and iron, but is missing for SiO_2 and dunite. For the two former materials, the melting curves as function of pressure are shown in figure 6.5. The algorithm to differentiate the liquid and gaseous phases is included, and permits to find on the plot where ANEOS finds the triple point. As comparison, the values from the literature are also given by the dashed black lines. For water, the melting temperature at low pressure is underestimated by about 15 K. One could also note that the liquid phase does not extend towards lower temperatures for pressures around 10 GPa. ANEOS was designed to be a rather general equation of state; it is therefore

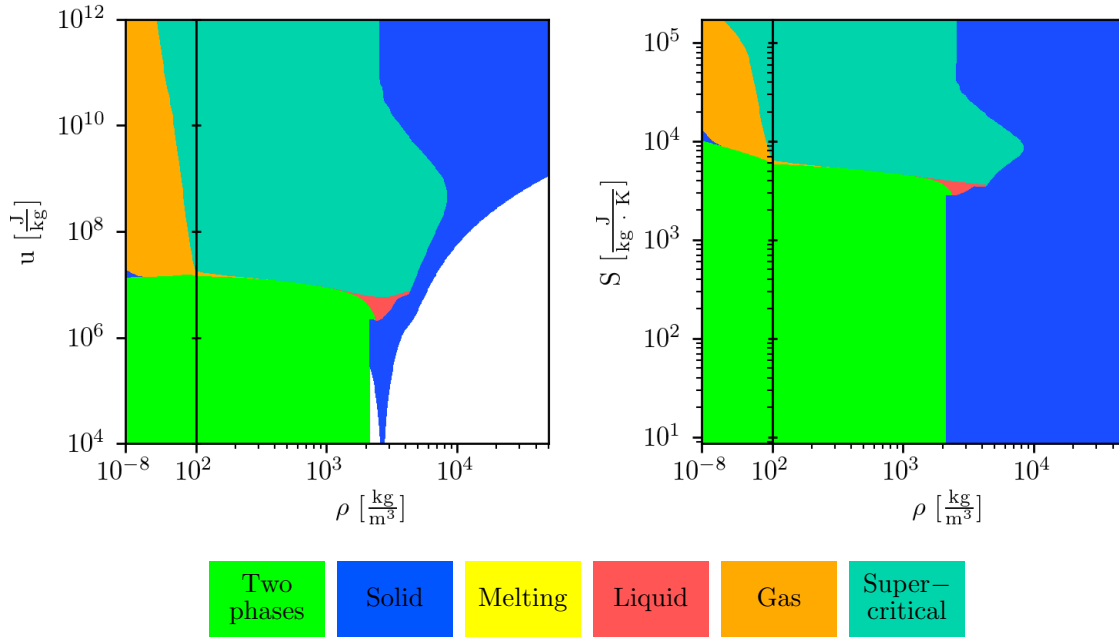


Figure 6.6: ANEOS phase plots of the tabulated SiO_2 results. The phase information shown here has been extended with the formula from Senft and Stewart (2009) to differentiate solid and fluid, and the algorithm to differentiate the fluid phases.

acceptable to not find such specific water features, including the lower density of water ice compared with liquid water. When ANEOS is capable to compute the solid-fluid transition itself, we will use it to determine the melting temperature at given pressure, for the solid rheology computation. The process itself is quite complicated; ANEOS uses (ρ, T) as input variables, so for each point hereafter, the equation $p(\rho, T) - p_{\text{target}} = 0$ has to be resolved by iteration, with the same principle as above to obtain $p(\rho, u)$. The next step is to find a rather small interval where the *phase number*—let us now call it k —is solid on one side and fluid on the other one. As k has the nice property of having greater values for the fluid phases than for the solid one, the same algorithm is used again to now solve the equation $k(p, T) - k_{\text{target}} = 0$. The root-finding algorithm is thus nested into itself, and the whole calculation is thus even more computationally expensive than to compute the general tables, and thus we will use a table again. Fortunately, our melting curve only depends on one single parameter, the pressure. For silicate, as no solid-fluid transition can be computed directly from the equation of state, we use the formula from Senft and Stewart (2009):

$$T_{\text{melt}, \text{SiO}_2} = \begin{cases} 2000 \text{ K} & p < 0.7 \text{ GPa} \\ 2000 \text{ K} + (p - 0.7) * 85.7 \text{ K/GPa} & \text{otherwise.} \end{cases} \quad (6.76)$$

The corresponding modified phase diagrams of the tabulated ANEOS results is provided in figure 6.6. For comparison, the original results from ANEOS can be found in the figure 3.1 of Emsenhuber (2013) (all phases but the phase shown in green denoting either solid-gas or liquid-gas mixture and the invalid region form a single region called *single*

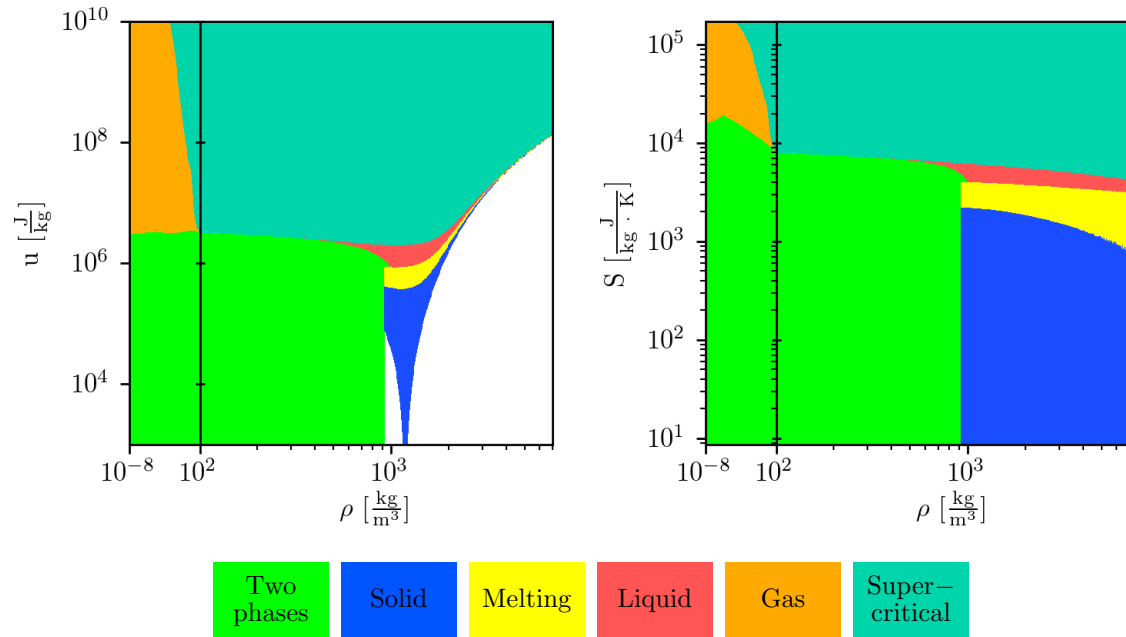


Figure 6.7: ANEOS phase plots of the tabulated water results. This is similar to the one in (Emsenhuber 2013), with the addition that the "fluid" phase is now split into "liquid", "gas" and "supercritical".

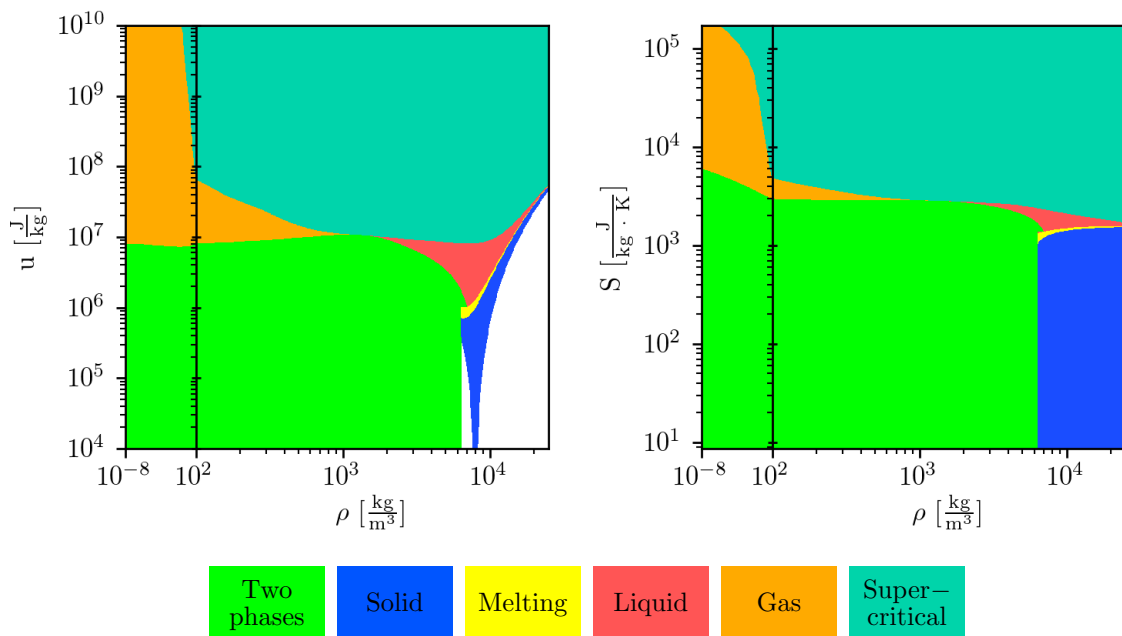


Figure 6.8: ANEOS phase plots of the tabulated iron results. This is similar to the one in (Emsenhuber 2013), with the addition that the "fluid" phase is now split into "liquid", "gas" and "supercritical".

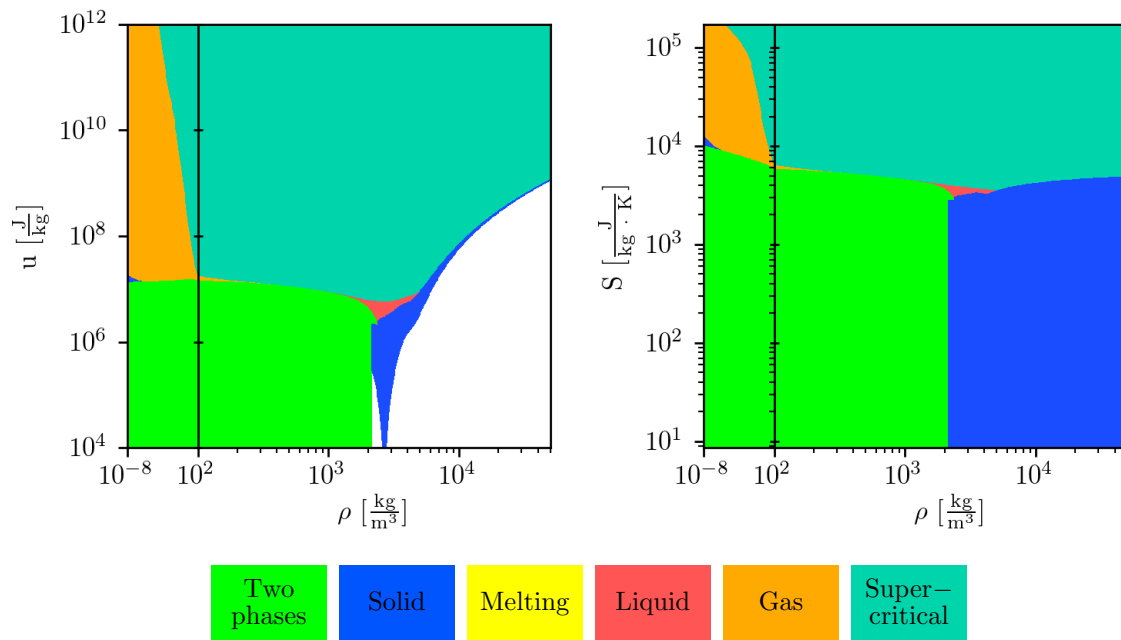


Figure 6.9: Same as figure 6.6, but using equation (6.77) for the melting temperature.

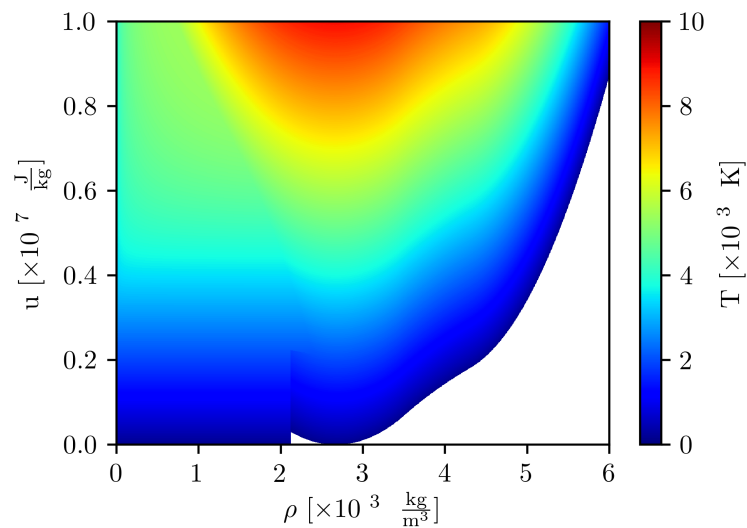


Figure 6.10: ANEOS temperature for SiO_2 as function of density and energy. The colour scale on the right is chosen so that it also gives the relationship between internal energy and temperature for the Tillotson EoS using the simple formula with $c_p = 1000$ J/K/kg.

phase). Equation (6.76) seems to overestimate the melting temperature for high pressures if we compare this phase plot to the ones for water (figure 6.7) and iron (figure 6.8). González-Cataldo et al. (2016) suggested the following relation for the SiO₂ melting temperature

$$T_{\text{melt, SiO}_2} = 1968.5 \text{ K} + 478.7 \text{ K} \left(\frac{p}{1 \text{ GPa}} \right)^{0.426} \quad (6.77)$$

which has a lower dependency on the pressure, and hence will reduce the melting temperature in the high-pressure range. The phase diagram is shown in figure 6.9; it can be observed that the melting curve resembles much more to the ones found by ANEOS for the other materials.

Another quantity which can be qualitatively interpreted from these plots is the temperature. For instance, the boundary of the invalid region is defined by $T = 0$, and the temperature gradient in normal to the boundary at that location. A simple formula to estimate the temperature was introduced for the Tillotson equation of state in equation (6.75), which uses a constant heat capacity and does not include the latent heat of vaporisation. We can now compare the result of this simple formula with the more sophisticated computations by ANEOS. This is shown in figure 6.10. Up to density of around 3000 kg/m³ and a specific energy of $3 \cdot 10^6$ J/kg, both match well. For higher specific energies or densities, the retrieved temperature is lower than in the Tillotson case.

6.4 Implementation

6.4.1 Tree

The placement of particles in space and the knowledge of their other neighbouring particles is an important problem when using SPH. This knowledge is necessary for the SPH scheme, as discussed in section 6.2.1, for a kernel which has a compact support, only neighbouring particle will make contribution to the SPH sums. To take advantage of this situation, an algorithm which is capable of quickly retrieving a list of neighbour particles within a pre-determined distance is needed. This ensures that only surrounding particles are iterated over, thus saving a considerable amount of resources compared to performing sum over the entire particles set.

A well-established method, which can be used for both this purpose as well as the computation of self-gravity was introduced by Barnes and Hut (1986). The idea behind is to create a tree which holds the spatial representation of the SPH particles. The base (or *root*) cell is a cube that encompasses the entire volume occupied by the particles. This cell is divided into 8 sub-cells that are half in length. Each cell may contain at most one particle; so, the tree is refined until two particles will lie in different cells. Its depth is variable and depends on the local number density of particles. Adjacent particles are found by going first up in the tree until the cell that encompasses the desired volume is found and then the iteration proceeds on the particles that are located within its volume.

In case the computation of self-gravity is desired, the same tree is used to compute the gravitational interactions. They are modelled either directly for close other particles, or using multipole approximation for more distant material. The procedure to compute

the acceleration due to gravity is as follows: for each particle, a complete tree walk is performed (down the tree starting with the root cell). At every encountered cell, the criterion that determines the use of the multipole approximation is evaluated. It reads as $s_c/|\mathbf{r}_p - \mathbf{r}_c| < \theta$ with s_c is the cell's spatial extend, which depend on its depth within the tree, \mathbf{r}_p the location of the particle whose acceleration is being computed, \mathbf{r}_c the centre of mass of the material located within the cell and $\theta = 0.7$ a constant. If the criterion is fulfilled, then the gravitational interaction is computed with the multipole approximation and the children are skipped. In the other case, the walk proceeds with the children of the said cell. This permits to lower the complexity of the calculation to $\mathcal{O}(N \log N)$ compared to the usual $\mathcal{O}(N^2)$ if the interactions are computed between all the particles, as it is the case for the N-body calculations of the planetary system formation model (see chapter 4).

Unlike for the SPH forces, the calculation of self-gravity using a tree does not guarantee conservation of linear and angular momentum.

6.4.2 Computer code

The computer code used in the work is based on SPHLATCHv2 by Reufer (2011), with correction and parallelisation of the equation of state that were performed in Emsenhuber (2013). SPHLATCHv2 changed the parallelisation paradigm from distributed to shared memory, while the first version of that code, SPHLATCHv1 added the tree algorithm. With the present work, the code has mainly been modified for the following purposes: the addition of solid strength along with its coupling to the ANEOS equation of state, and optimisations for high-resolution simulations.

Parallelisation is achieved with OpenMP¹, a shared memory scheme. All execution units work on the same memory. which greatly simplifies the code, with the requirement that all of them reside on the same machine. With the newest computers that have 48 and more CPU cores per machine, this is not a large drawback, except for extremely high resolution simulations.

The overall scheme of the SPH code is shown in figure 6.11. The left column shows the initial steps performed once at the beginning, and on the right, is the main loop that computes the time evolution of the SPH particles. The initialisation part mostly consists on the loading of ANEOS tabulated results into memory, when this equation of state is in use, and/or the reading of material parameters. The latter occurs on two conditions: the Tillotson equation of state is in use or the solid strength model is active. For the case where both ANEOS and solid strength model will be used, both operations will take place here. The reason is that the supplementary parameters needed for the solid model are kept in a text file together with the other parameters for the Tillotson equation of state. This allows to have a single format for those parameters, which is independent of the equation of state. In the case of ANEOS, the Tillotson-specific parameters are disregarded. A second ANEOS table is loaded when melting temperature is to be obtained self-consistently from the equation of state.

¹<http://www.openmp.org>

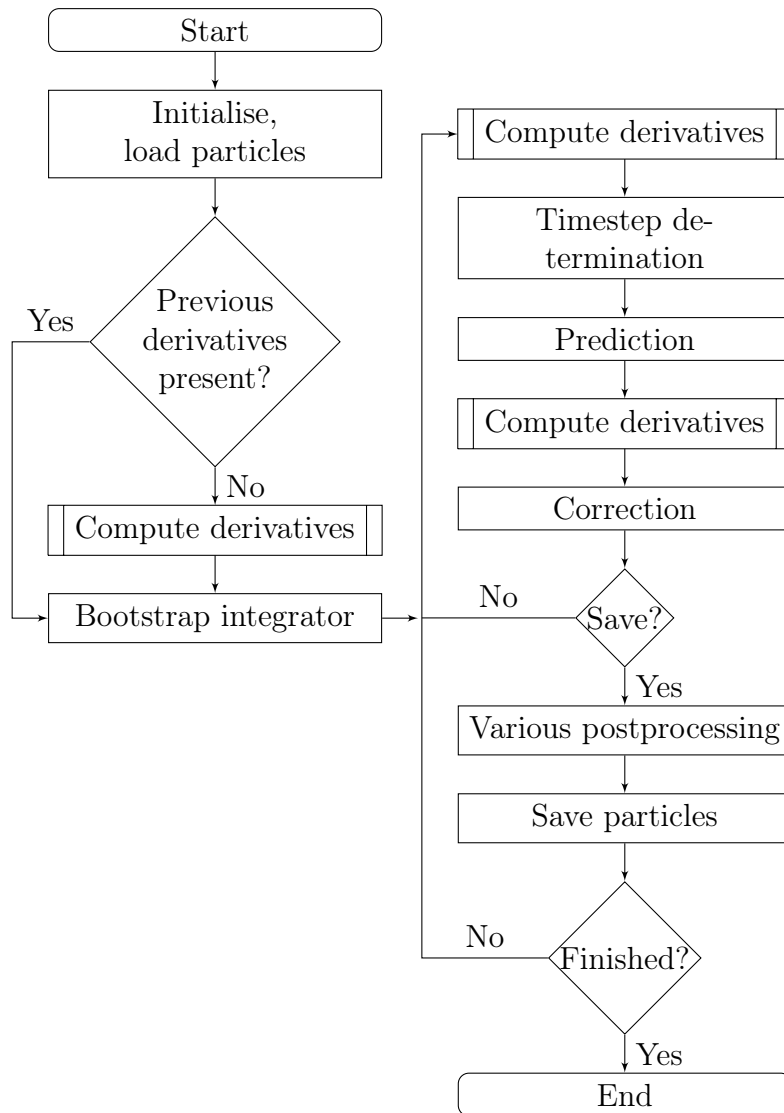


Figure 6.11: Algorithm of the SPH code. The left column represents the initialisation part, and the right one the main loop.

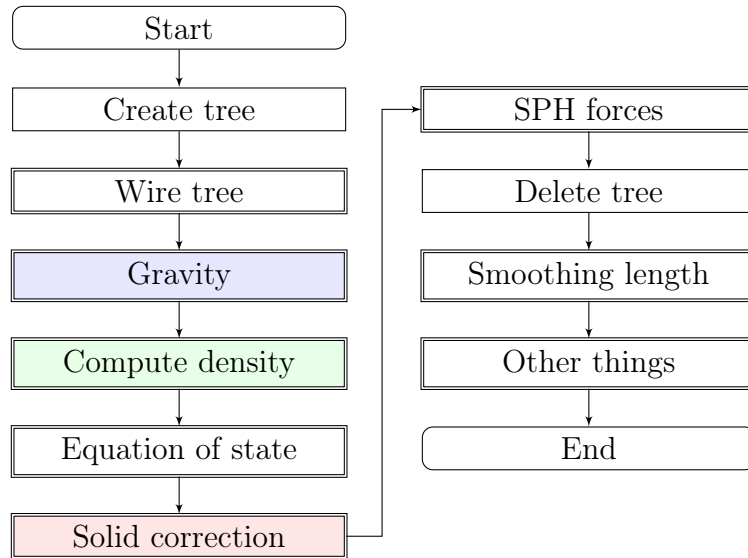


Figure 6.12: Algorithm of the derivation step. The steps that have support for parallel processing are shown with a double border.

It is also at this point that the SPH particles are loaded. This provides the initial state of the simulation. The data may come from either the setup procedure or a previous simulation. A good feature here is that the output of this SPH code can directly be used as input when restarting a simulation as well as for further analysis. The main difference between these two cases is what will happen next. When starting fresh from a setup procedure, not all previous derivatives are available. The predictor-corrector scheme however needs these derivatives and thus the routine that computes them is called once. The bootstrap is performed with these freshly computed derivatives. When restarting from a set of particles which has already been evolved by the main SPH code, the previous derivatives are readily available as they are now part of the output and thus they only need to be given to the integration algorithm. It would also be possible to not store the previous derivatives in output and use the same procedure as for when a *new* set of particles is used; however, by backing up the previous derivatives it is possible to obtain the exact same results as when the simulation is performed without interruption. This allows to verify that all quantities needed for the algorithm are indeed present in the output file and that there are no otherwise hidden variables that would produce a difference when restarting a simulation. There is a drawback, though: the output files are quite a bit larger than previously since for an integrated variable three values need to be saved: the present value, the present and previous derivatives. Once it becomes clear that a save point will never be used as a start point anymore (such as when the whole simulation is finished or a later one is available), the previous derivative and, for some quantities, the current derivative are no longer useful. The HDF5 file format does not permit the removal of data though. The easiest solution is then to copy only the useful part to a new file and then to overwrite the original file with the new one.

The upper right part of figure 6.11 shows the typical flow of the predictor-corrector scheme. The methodology used to compute the time derivatives (i.e. the "Compute derivatives" boxes) is shown in figure 6.12. The prediction and correction steps were described in section 6.2.8. Before being able to run the prediction step, the next time step needs to be known. It is therefore computed between the derivatives of the prediction step and the step itself. The scheme requires the same value of the time step for the correction part, so it is not re-computed at that point. This can sometime cause problem as it appeared that the values of the derivatives may significantly vary between the two steps (i.e. the differential equation is *stiff*). One possibility would be to introduce a rejection criterion for the correction step and if it is triggered then the whole step would restart with a reduced time increment.

The derivatives computation is the most resources consuming part of the code. The coloured boxes in figure 6.12 are optional, depending on whether the corresponding code features are enabled or not. For instance gravity is only computed when self-gravity is enabled, density when density summation is used, solid correction is for angular momentum conservation (see section 6.2.6) and smoothing length when this variable is integrated. The "Other things" box contains additional items which are not used in a standard collision simulation. These are for the set-up procedure and code tests. It contains for instance the following items: global acceleration, boundary conditions and damping term. The two former items are used for the "cliff collapse" test (see section 6.5) .

Furthermore, the code now catches various POSIX signals that are used to modify the work flow's behaviour. These signals are sent either by the operating system or other programs, such as the Sun Grid Engine when it manages the execution of simulations. This allows to carefully handle different situations such as the request for stopping execution. Without signal handling, one has either to wait until a save point is reached to interrupt the code without computational time loss or the program may be interrupted at any time, but the computation made since the previous save point are lost. With signal handling, the code detects its reception and performs the related action. Three cases have been foreseen:

- Save the particles and continue: particles are saved into a supplementary output, but the program continues otherwise as normal. This is mostly used for debugging when the current state of the simulation is needed.
- Save the particles and exit: the same as the previous one, but the code will exit just after the writing of the output.
- Exit after the next save: Nothing is performed immediately, but the program will exit after the next normal particle save.

Note that the various post-processing part is not performed when a save point outside of the normal schedule happens. The reason is that this part might be long to execute and thus the time limit between the reception of the signal and the actual end of the program could be above the limit, which results in loss of data. This signal handling coupled with the property that the results are identical after a stop and restart can be used for

different situations: for instance, it is very easy to move the simulation from one machine to another one. This can be even performed automatically by the Sun Grid Engine so that the computational cluster is used at best. There is also the case of machines which are only available for a short period, less than the expected duration of the simulation (for various reasons such as a planned maintenance) and that can still be used without fearing loss of time. Again, this goes in the direction of better resources usage.

6.4.3 Optimisations

Some optimisations were done on the tree code: removal of the cost property and cell retention. In Reufer (2011), a cost was assigned to each particle depending on the computing time that was needed for the whole cost zone. This cost would then be used during the creation of the next tree to have cost zones that are balanced in terms of computational difficulty. Each CPU thread would then get the same amount of cost zones to process. There are two issues with this scheme:

- The measured time to process a single cost zone does not depend only on the difficulty to process the particles but is also influenced by other events that occur on the CPU, such as input and smaller (system) tasks running on it. The number of cost zone cells varies from one tree instance to the other. The cost zone structure varies quite a lot from one step to the next following the small time variations during cost zone processing.
- Assignment of the cost to each single particle from the global time needed to compute a cost zone also involves a full tree walk. Even though the actual action performed on each particle is fast, each tree walk includes some overhead for the synchronisation and thus has a significant cost in terms of computation time.

So, in order to make the tree more stable and slightly faster, the cost property has been removed. Cost zones are now set so that each one has a comparable number of particles. The counter part is that the OpenMP schedule policy when iterating over the cost zone was changed to *runtime*. The cost zones are thus no longer restricted to a single thread, but rather distributed to the idle threads. This thus saves a complete tree walk by moving the responsibility of handling the different difficulty between particles to the OpenMP library. One could think that cost zones are not needed at all and could be removed in favour of handling each particle independently. However as Reufer (2011) showed, the cache mechanism of modern CPUs plays an important role. Handling nearby particles on the same CPU core can therefore increase quite a bit the overall code's performance.

The second improvement to the tree code is related to its creation and cleaning. In the original code, memory is allocated when building the tree for both cell and particle nodes, and then released when the tree is cleared. Only the root cell is kept across builds. These two steps (build and clear) are critical as they are performed on a single thread. On the other hand, the complexity of the tree creation phase is $\mathcal{O}(N \log N)$, the same as for the self-gravity algorithm, which indicates that the code does not scale well with an increase of the number of *threads* (parallel execution units). Various alternative methods

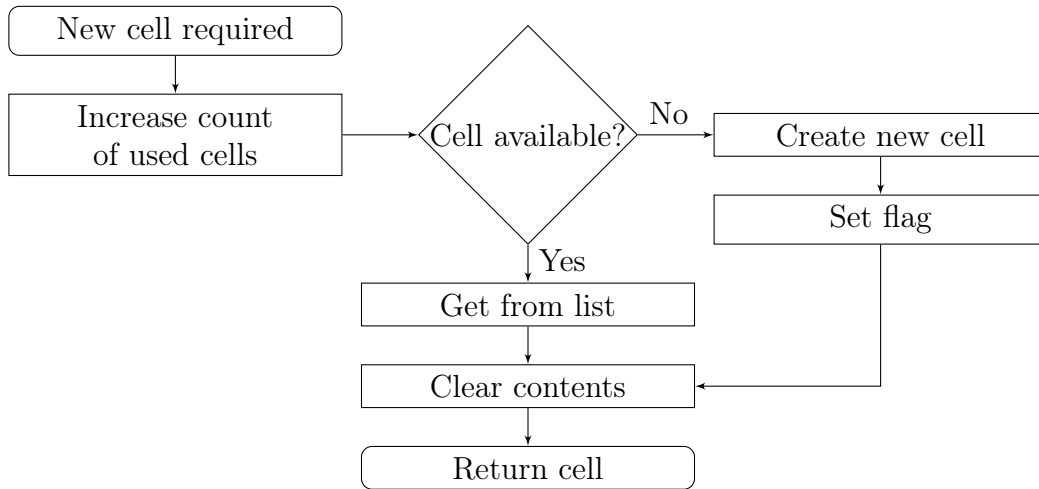


Figure 6.13: Algorithm to get a new cell node.

were attempted to make these parts perform better. The first idea was to perform the tree cleaning walk in parallel, the same way as for parallel computations. This was shown to have poorer performance than the original algorithm. A possible reason is that internally the C/C++ library needs to use locking to modify the allocation tables, and thus concurrently modifying it slows down the whole process. The next attempt was to try memory retention by the code itself. For particle nodes this is easy, as the node is kept attached to the corresponding particle during the whole program execution. It is only released at the end of the program or if the particle gets removed from the simulation (in the case of an escaping particle for instance). Pointers to the allocated cell and cost zone nodes are kept in tables so that they are not lost across builds. The aim is as follows: if all tree nodes are present in pointer arrays, then the tree clearing is unnecessary, as the only purpose of the involved tree walk is to release the memory. The only operation that remains is the state reset of the root cell, for the benefit of the next tree build. The new algorithm to obtain a cell node is shown in figure 6.13. The performance comparison shows that the build process is marginally slower whereas deletion is almost always very fast. The usual time requirement of the two processes is 60% for creation and 40% for deletion; so, the almost removal of the deletion step improves the overall time requirement of the serial parts of the code by roughly one third. The keeping of memory directly in the tree open new possibilities. The last performance improvement attempt is to perform the tree build in parallel. The tree is divided into *insertion regions*, which are independent from each other. A region has its own *root* cell, and a separate list of cell nodes. Each region is assigned to a specific thread, so that within a region the build process does not suffer to concurrency problems. Initially, it is not known in which region each particle belong. The list of particles is iterated over, and the region is determined by the location of the particle within the tree. The difficulty of this operation is that it occurs at the very beginning of the derivation step, and so it is not known where the particles are distributed across the tree. A simple strategy is to divide the tree at a fixed depth.

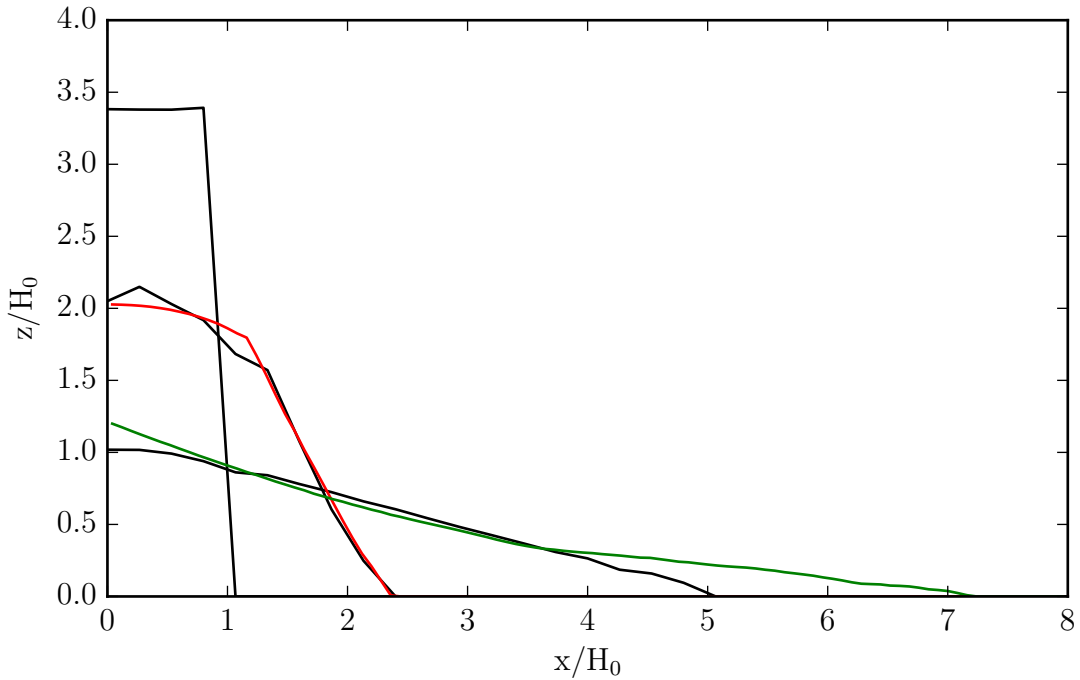


Figure 6.14: Profile of "cliff collapse" validation. Black lines show the simulated profiles at $t = 0$, $t = \tau$ and $t \rightarrow \infty$ as well as reference profiles from Jutzi (2015) at $t = \tau$ (red) and $t \rightarrow \infty$ (green).

However, in the general case of a collision simulation, the distribution of particles across space is very uneven. Indeed, the largest remnant usually contains the great majority of the particles and is concentrated in a small volume compared to whole set, especially when there is a large number of ejected particles. To split the insertion of particles from the largest remnant over several regions, then a certain depth of the tree is required, which is not quite practical. On the other hand, this simple strategy works rather well in particular cases such as when the bodies are being prepared. In this situation, a single object is evolved, so the tree is well centred and splits across different cells at the first level already. This feature is thus generally not enabled, as the advantage of working in parallel is almost non-existent due to the overhead required.

6.5 Verification of the solid model

The solid model described in section 6.2.5, coupled with the EoS model (section 6.3), has been newly implemented in the SPHLATCH code. Here we show a test of this model. For this purpose, the *cliff-collapse* test described in Jutzi (2015) is performed, i.e. the comparison between an SPH simulation and experimental results from Lajeunesse et al. (2005).

A few adaptations were performed to perform this test: self-gravity has been disabled and replaced by a constant acceleration in the z direction. To prevent the whole system from freely moving with the additional acceleration term, boundary conditions were introduced. The idea is as follows: when particles cross the defined boundaries, then their velocity and acceleration are forced to zero. These particles will thus build the walls which will prevent the other ones from crossing the boundaries. This will happen first at the bottom, but also on the sides, as the pressure from the above particles will induce a horizontal gradient. It is first required that a few particles cross the boundary, and so the number of remaining particles that are free to move is actually lower. Also, the energy equation has been left out, so the particles have a constant internal energy. This permits the pressure to depend only on the density. The friction coefficient has been changed to $\mu_d = \tan(20.9)$.

The design of the simulation is as follows: the volume has a square base of length $H_0 = 30$ km and height $z = 100$ km so that the size ratio between the height and base is $z/H_0 = 10/3$ in order to be comparable with the experimental results. The vertical acceleration is set to $g = -0.3$ m/s². The outcome of this problem has been shown to be scale-invariant; the important quantities are the length ratio z/H_0 and the characteristic time scale $\tau = \sqrt{H_0/g}$.

Particles are initially placed on a lattice, and the first step is to let the system evolve with all the wall present (bottom and four sides) and without the solid model to permit it to build a hydrostatic equilibrium. Then the boundary wall is removed and solid forces are enabled.

The resulting profiles are shown in figure 6.14. Overall, the profiles resulting from the simulations are consistent with experimental results. The discrepancy of the top part of the profile at $t = \tau$ might be related to the way the height of the cliff is computed from the SPH particles. For the final profile, we note that the areas are not the same for the experimental results as in the simulation. This might be linked to the fact that some of the SPH particles are needed to build the boundary conditions, so they seem to disappear from the simulation, but they are located outside of the boundary.

The results of simulations are consistent with experiments. The model is then able to reproduce the behaviour of granular material for our simulations.

6.6 Performing collision simulations

The preparation of an actual collision simulation involves multiple steps that will be discussed here. Here we assume that the collision will occur between two bodies, the most massive one being called the *target*, and the second one called the *impactor* (also sometimes referred as *projectile* in the literature). The first parts describe the different step required to obtain a single body at equilibrium and at rest. They must be performed for each object separately.

6.6.1 1D radial profile

The internal structure of self-gravitating objects is non-trivial. The basic idea is to first obtain a one dimensional, radial profile which is at hydrostatic equilibrium. The scheme from Benz (1991) is used, which is briefly described here. The initial conditions are provided by mass, density and either specific entropy or energy, which are constant for every material layer (in the case the body is differentiated). The structure is divided into Lagrangian cells of equal masses. The acceleration of each cell boundary is computed from the balance of gravity and the pressure gradient force, with the addition of a friction term to damp oscillations $\mathbf{a}|_{\text{fric}} = -\mathbf{v}/t_{\text{fric}}$ where t_{fric} is the friction time. Its value should be greater than the free-fall time $\tau_{\text{ff}} \sim 1/\sqrt{G\rho}$ to ensure that the motion of the cells to balance the forces is not too strongly reduced. The equation of state is the same as used in the SPH code. In the case of *ANEOS* the specific entropy is used as thermodynamic quantity rather than energy; this ensures an adiabatic profile. For *Tillotson*, the specific entropy is not accessible, so internal energy is used, with, however the energy equation left out in order to prevent heating caused by the artificial viscosity.

In the case of the *Tillotson* equation of state, an analytical profile could be obtained in principle as the analytical expressions are available. All of the bodies involved in the following studies are differentiated however, and the scheme would break in a such case. So for simplicity, we stick to the same scheme as for *ANEOS*.

For small bodies, up to ~ 10 km, the internal structure is simpler as the central pressure remains low. In this case the initial density can be deduced directly from the equation of state by deducing the density for which the $p = 0$ given the other thermodynamic quantity. This is usually a better initial guess than the reference density ρ_0 from the equation of state. The reason is that with the normal initial specific energy, the pressure obtained with $\rho = \rho_0$ is already significant and the scheme would not converge a proper profile. The ability to determine directly the correct density can be of a great help, as this allows to initially define the body by its radius rather than its mass.

6.6.2 SPH body

The next steps are to translate the obtained radial profile at equilibrium into a full 3D body consisting of SPH particles in the same state. An initial set of SPH particles is placed on an hexagonal close-packed (HCP) lattice with a characteristic length $l = 2/\sqrt[3]{kN_r}$ with $k = \pi/(3\sqrt{2})$ is the filling factor of the arrangement and N_r the desired number of SPH particles. The lattice is truncated to $r < 1$ to obtain a sphere. The actual number of particles N_a will slightly vary from the value requested initially. Each particle gets a volume $V = 4/3\pi/N_a$ and a smoothing length $h = 0.85l$ which gives them roughly 50 neighbours, except for the particles close to the surface.

The profile is then mapped onto the raw set of particles. The outer radius extracted from the profile and used to multiply all distances (position and smoothing length) by that value as well as the volume its cube. The various quantities from the profile are assigned to the particles depending on their radius, and their mass is set according to the density and volume.

At this point, there can be a few intermediate steps:

- In the case SPH with density summation is to be used, then a first SPH sum is performed in order to obtain the density consistently with the SPH scheme.
- When pre-impact rotation is desired, an initial velocity is set with $\mathbf{v}_r = \boldsymbol{\Omega} \times \mathbf{r}$. $\boldsymbol{\Omega}$ is chosen so that rotation happens in the same plane as the orbit and its magnitude $\Omega = 2\pi/t_r$, where t_r is the rotation period defined as positive if the rotation is prograde, i.e. the direction is the same as the relative motion of the objects in orbit prior to the impact and negative otherwise.

This initial SPH body is not exactly in equilibrium, so a final step is to let it evolve again. The SPH scheme used for this phase is different from the one that performs the collision simulation itself, and combines a few items from the 1D radial profile scheme: the same thermodynamic variable is used (i.e. entropy instead of energy for *ANEOS*), the energy equation is still normally left out and the damping term is added. The latter is modified in the presence of rotation to

$$\mathbf{a}|_{\text{fric}} = -\frac{\mathbf{v} - \mathbf{v}_r}{t_{\text{fric}}}. \quad (6.78)$$

The usual damping term would otherwise remove the rotation whereas this modified version forces the body to rotate with the correct frequency. This is also during this phase that the equatorial bulge forms.

6.6.3 Orbit setup

Once both objects are prepared, they need to be combined and their initial position and velocity set. An introduction to the different collision parameters has been given at the beginning of chapter 5. We will use the same variables here, but the purpose of this section is the opposite: we know the properties and want to determine the initial position and velocity that will produce the desired collision. A sketch of the quantities used in this section are shown in figure 6.15. Neglecting the deformation due to gravity that arises when the two bodies are close to each other, the impact takes place when the two bodies are separated with a distance which is equal to the sum of their respective radius:

$$r_{\text{coll}} = r_{\text{tar}} + r_{\text{imp}} \quad (6.79)$$

The impact velocity v_{coll} can be chosen arbitrary, but is usually set to a factor times the escape velocity, that is $v_{\text{coll}} = t \cdot v_{\text{esc}}$. Knowing v_{coll} , one can then compute the specific orbital energy

$$\epsilon = \frac{v_{\text{coll}}^2}{2} - \frac{\mu}{r_{\text{coll}}} \quad (6.80)$$

which take a strictly negative value if the orbit is closed, 0 if it is parabolic and strictly positive in case both objects are not gravitationally bound.

A second parameter is also needed to define the collision, either the impact angle β_{coll} or angular momentum $L_{\text{coll}} = h_{\text{coll}}m_r$, with h_{coll} the specific angular momentum and m_r

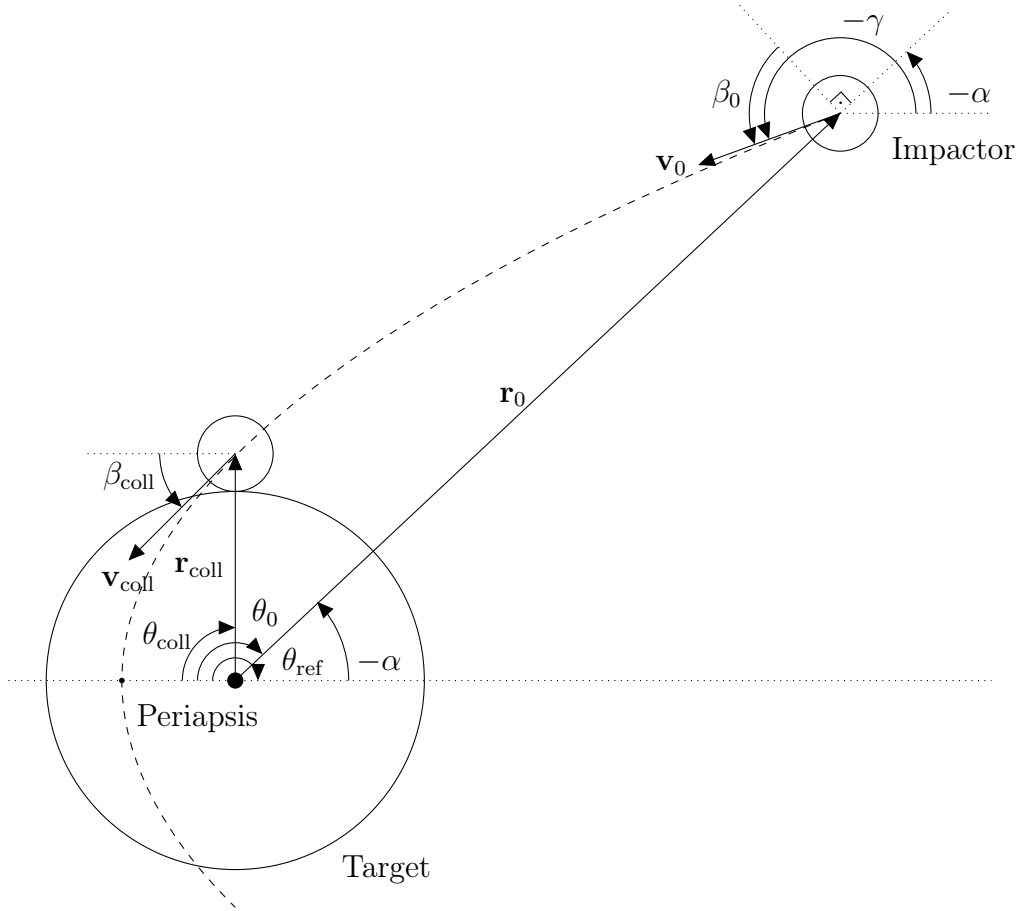


Figure 6.15: 2-Body problem. The case shown here is a parabolic orbit ($v_{coll} = v_{esc}$) with an impact angle of $\beta_{coll} = 45^\circ$. The principal axis goes to the right and the secondary towards the top.

the reduced mass. The specific angular momentum of a grazing collision, where both objects would barely interact can be computed with

$$h_{graz} = v_{coll} r_{coll} \tag{6.81}$$

the link between the two values is given with

$$\frac{h_{coll}}{h_{graz}} = \cos \beta_{coll} \tag{6.82}$$

These quantities allow to define the relative velocity and angle between the relative position and velocity at any distance. This initial distance can be freely chosen; in our scheme, we take a multiple of their relative distance at impact

$$r_0 = s \cdot r_{coll} \tag{6.83}$$

where s is between 3 and 5, so that both bodies still have time to be tidally deformed prior to impact. The velocity at that location is obtained by the conservation of orbital energy

$$v_0 = \sqrt{2 \left(\epsilon + \frac{\mu}{r_0} \right)} \quad (6.84)$$

In case of a bound orbit, it must still be checked that the argument of square root is positive, otherwise this means the given separation is unphysical for a such orbit. In addition to the magnitude of position and velocity, the angle between these two vectors also has to be computed. Following conservation of angular momentum, we obtain

$$\mathbf{r}_0 \cdot \mathbf{v}_0 = r_0 v_0 \cos \beta_0 = h_{\text{coll}} \quad (6.85)$$

This set of equations is sufficient to set up a collision with the desired properties, and either of these vectors can be aligned to a certain direction and the other one is set appropriately. If one wants to position the initial vectors so that alignment is for another moment of the orbit, then additional steps are required. The head-on case where $L_{\text{coll}} = 0$ breaks down in the following calculation; it will be treated later on. For the other cases, the specific angular momentum eq. (6.85) enables us to compute the semi-latus rectum and eccentricity

$$p = \frac{h_{\text{coll}}^2}{\mu} \quad (6.86)$$

$$e = \sqrt{1 + 2p\epsilon} \quad (6.87)$$

They allow to compute numerous other quantities, including the boundaries of the orbit, such as the periapsis

$$r_p = \frac{p}{1 + e} \quad (6.88)$$

and in the case of a closed orbit, the apoapsis

$$r_a = \frac{p}{1 - e} \quad (6.89)$$

which is also worth comparing against r_0 , as there is still a region where the velocity is non-zero, but is never reached during the orbit. The correspondence between the relative distance r and true anomaly f is obtained as follows

$$e \cos f = \frac{p}{r} - 1 \quad (6.90)$$

and in case the orbit is hyperbolic, one can take the limit for $r \rightarrow \infty$

$$f_\infty = \arccos \frac{-1}{e} \quad (6.91)$$

We now define a reference angle, which is the direction that will lie on the principal axis. We usually choose it as

$$f_{\text{ref}} = \begin{cases} f_\infty & e > 1 \\ \pi & e \leq 1 \end{cases} \quad (6.92)$$

and one notices that both branches yield the same value for the limiting case $e = 1$. We also need the true anomaly at initial separation, since objects are going to be placed at this location

$$f_0 = \arccos \frac{\frac{p}{r_0} - 1}{e} \quad (6.93)$$

The difference between them is then the angle between the principal axis at the initial relative distance. We also set the angle between the same axis and initial velocity, set so that objects are approaching each other. They are defined as:

$$\alpha = f_0 - f_{\text{ref}} \quad (6.94)$$

$$\gamma = f_0 - f_{\text{ref}} - \left(\frac{\pi}{2} + \beta_0 \right) \quad (6.95)$$

If α is negative, we reverse both angles so that initial position is always in the positive direction. This happens to be the case with our choice of reference angle as true anomaly is increasing along with relative distance, if we restrict it to be $0 \leq f \leq \pi$ such as when the function $\arccos x$ is used to retrieve f . For this reason, these angle shown in figure 6.15 have a minus sign.

We now set the initial position and velocity vectors

$$\mathbf{r}_0 = r_0 \begin{pmatrix} \cos \alpha \\ \sin \alpha \end{pmatrix} \quad (6.96)$$

$$\mathbf{v}_0 = v_0 \begin{pmatrix} \cos \gamma \\ \sin \gamma \end{pmatrix} \quad (6.97)$$

that we define in a two-dimensional plane. This plane is then matched with one of possible combination formed by two base vectors of the three-dimensional space. The two vectors \mathbf{r}_0 and \mathbf{v}_0 give the relative initial position and velocity respectively between the target and impactor. We then place the objects in space for the centre of mass to be located at origin and its velocity to be zero:

$$\mathbf{r}_{0,\text{tar}} = -\frac{m_{\text{tar}}}{m_{\text{tar}} + m_{\text{imp}}} \cdot \mathbf{r}_0 \quad (6.98)$$

$$\mathbf{v}_{0,\text{tar}} = -\frac{m_{\text{tar}}}{m_{\text{tar}} + m_{\text{imp}}} \cdot \mathbf{v}_0 \quad (6.99)$$

$$\mathbf{r}_{0,\text{imp}} = \frac{m_{\text{imp}}}{m_{\text{tar}} + m_{\text{imp}}} \cdot \mathbf{r}_0 \quad (6.100)$$

$$\mathbf{v}_{0,\text{imp}} = \frac{m_{\text{imp}}}{m_{\text{tar}} + m_{\text{imp}}} \cdot \mathbf{v}_0 \quad (6.101)$$

For convenience, the times are provided with respect to the initial contact between both objects rather than the beginning of the simulation itself. Is this therefore useful to know the theoretical time it will take the objects to travel from the initial to the contact location. For non head-on geometries ($L_{\text{coll}} > 0$), the following relation between true

anomaly and time exists (Beutler 2005):

$$t(f) = \sqrt{\frac{a^3}{\mu}} \begin{cases} \frac{e\sqrt{e^2-1}\sin f}{1+e\cos f} - 2\ln\left(\frac{\sqrt{e^2-1}+(e-1)\tan\frac{f}{2}}{\sqrt{e^2-1}-(e-1)\tan\frac{f}{2}}\right) & e > 1 \\ \frac{1}{2}\left(\tan\frac{f}{2} + \frac{1}{3}\tan^3\frac{f}{2}\right) & e = 1 \\ \frac{e\sqrt{1-e^2}\sin f}{1+e\cos f} + 2\arctan\left(\sqrt{\frac{1-e}{1+e}}\tan\frac{f}{2}\right) & e < 1 \end{cases} \quad (6.102)$$

with $t(f)$ the time relative to the last moment at periapsis and a being the semi-major axis given with

$$a = \frac{p}{e^2 - 1}. \quad (6.103)$$

The initial time is set to

$$t_0 = t(f_{\text{coll}}) - t(f_0) \quad (6.104)$$

with f_{coll} the true anomaly at impact also computed using (6.93).

In the head-on case, the various angles and anomalies are not defined. The motion is along one direction, so the related setup is fairly trivial: \mathbf{r}_0 and \mathbf{v}_0 are set along the principal axis, the equivalent of defining $\alpha = 0$ and $\gamma = \pi$ for use in equations (6.96) and (6.97). The time is now computed for a given separation with

$$t(r) = \begin{cases} \frac{rv(r)}{v_\infty^2} - \frac{\mu}{v_\infty^3} \ln(2v_\infty rv(r) + 2v_\infty^2 r + 2\mu) & \epsilon > 0 \\ \frac{1}{3}\sqrt{\frac{2r^3}{\mu}} & \epsilon = 0 \end{cases} \quad (6.105)$$

with $v(r)$ the velocity at the provided distance, computed by analogy to (6.84) and v_∞ the remaining velocity at infinity $v_\infty = \sqrt{2\epsilon}$. The bound case has no analytical solution. The initial time is now given by $t_0 = t(r_{\text{coll}}) - t(r_0)$.

6.6.4 Analysis

An output is saved every given physical time. This output data all information needed to re-start the simulation, if a longer integration time is required for instance.

All the desired results are not immediately available, and post-processing must be performed to obtain them. The scheme will be briefly presented here, as it has not been extensively modified since Reufer (2011). It is as follows:

- The different energies are computed: kinetic, thermal and potential. If the kinetic energy is too important relative to potential energy (the case for $v_{\text{coll}} \gg v_{\text{esc}}$), then the following procedure is skipped and left to be performed on a separate process to not slow down too much the main simulation.
- Gravitationally bound clumps are searched. Particles are sorted accorded to their potential energy and iterated over starting with the particle that has the lowest energy. The first particle is added to the initial clump and the remaining particles are checked whether they are gravitationally bound to it. In that case, the particle is added to the clump and the iteration is started again over the remaining unbound particles.

- For clumps that comprise at least 10% of the total mass present in the simulation, the status of particles within them are further investigated. The different categories in which the particles will be placed are as follows: *central body*, *re-impacting* and *disc*. To discriminate them, the procedure is to obtain a first guess of the position and size of the central body. A density limit is set to $3/4\rho_0$, the reference density of the material from the equation of state. Particles are again iterated over following their potential energy until 1% of them have a density lower than the limit. The centre of mass of those particle as well as the distance to the farthest particle give the initial guess. The second step is to properly determine the radius; a confidence value of 5% is set around the density limit, and the mean distance of particles that have a density within the confidence interval determines the radius. If there are not enough particles within the confidence interval, then its value is increased. Particles closer than the radius are marked as part of the central body; for the remaining ones, a 2-body problem is solved to determine their main orbital elements, namely the semi-major axis and eccentricity so that their periapsis can be determined. If the periapsis is below the surface of the central body, then the particle is marked as re-impacting, otherwise it assumed to be part of the disc.
- Escaping particles are removed. Following the discussion in section 6.2.7 about the problems caused by loose particles, unbound particles very far away from the main body potentially lead to issues and unstable simulations.

This scheme is normally performed at each save point in the main simulation program. It is also possible to perform it at a later stage, for instance when the kinetic energy is dominant, as discussed above. In the latter case however, the removal of escaping particles is not performed, as it requires to be done within the main simulation to have any effect.

The different aggregated quantities may be plotted versus the physical time of the simulation, which permits to test for their convergence.

6.7 Test of miscible SPH

The problem of density computation at material interfaces in standard SPH was discussed in section 6.2.9. It was stated there that *miscible* SPH is a possibility to solve it. Reufer (2011) showed that with this method, a body without artificial density fluctuations close to the material boundaries can be obtained after the preparation phase. In this section, we will investigate the *miscible* SPH further and apply it to collision simulations.

Applying the miscible SPH scheme with our usual set up procedure, produces puzzling results. An example is provided in figure 6.16, showing the result of a simulation of an ice-rich impactor on a Earth-like target. The simulation discussed here used similar initial conditions as in our study presented in chapter 7, for which the standard SPH method was used. It can be observed that in the miscible SPH case, particles of different materials tend to group themselves in the upper part of the mantle. This is in contrast with the standard SPH case where the material is more distributed. Furthermore, impactor's iron particles do not mix with target's core and form two large clumps at the core-mantle

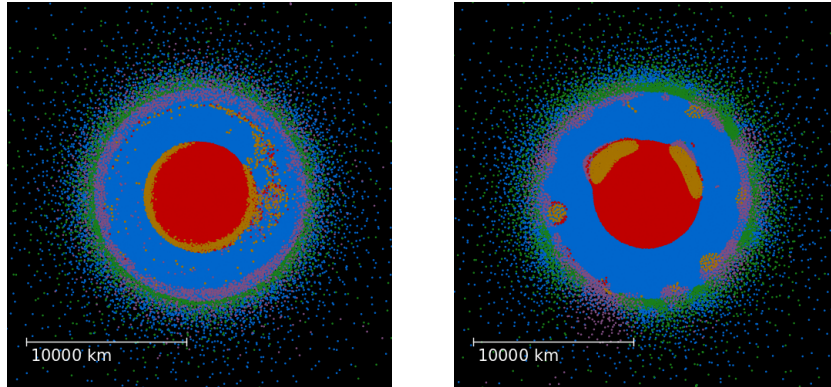


Figure 6.16: Comparison of results obtained for standard SPH (left) and miscible SPH (right) for a possible Moon-forming collision (case *ia08* of Reufer et al. 2012). Preparation has been performed according to the usual procedure. Each point is a SPH particle and the colour denotes its material and origin body; red: target's iron, yellow: impactor's iron, blue: target's silicates, purple: impactor's silicate and green: impactor's water.

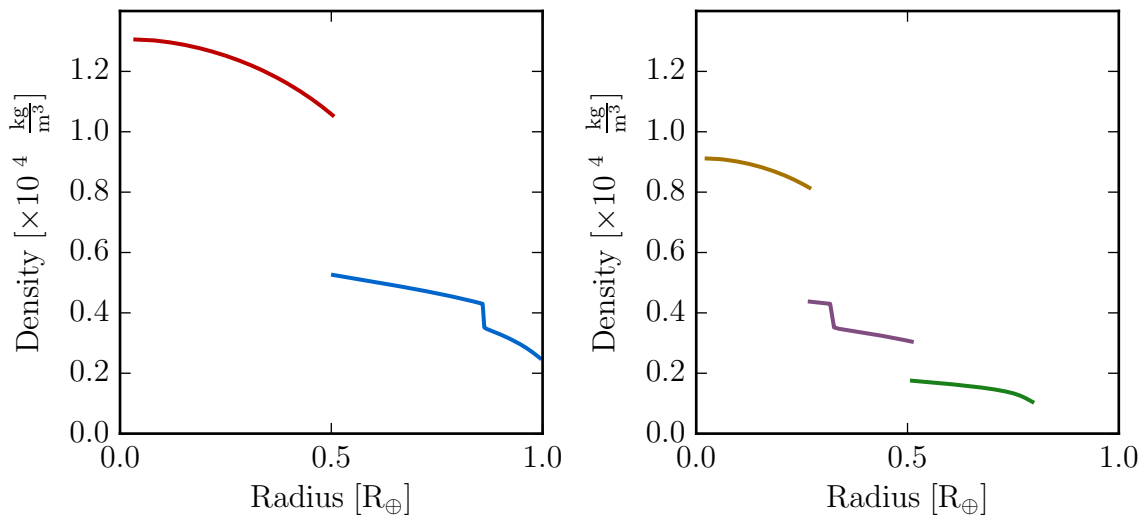


Figure 6.17: 1D radial density profiles of the target (left) and impactor (right). These are the same for both standard and miscible SPH as the distinction has not been made at this stage. Colours are the same as in figure 6.16.

boundary. The main problem is that in our case the masses of particles of the same material are different between the target and impactor. The initial number of particles has been chosen so that the average mass per particle is the same, but the problem is that the internal density profiles are rather different, and therefore the number density varies which leads to issues with the miscible SPH method. In this simulation half of the impactor's mass is water, which has a much lower reference density than silicate and iron. On the profile, the transition between silicate and water occurs at $r/r_{\text{imp}} \approx 0.64$ so that the volume ratio is $(r/r_{\text{imp}})^3 \approx 0.27$. So, if the average volume of iron and silicate particles is to be kept the same as in the target, then the number of particles in the impact has to be increased by a factor $0.5/0.27 \approx 1.9$. However, this solution is still not good though. As shown in figure 6.17, the density profiles of the two objects are not similar. There is a smaller density contrast between iron and silicate in the impactor compared to the target. This has two reasons: the impactor has a ice layer atop of the silicates while the target does not. Second the mass of the impactor ($0.2 M_{\oplus}$) is lower than the mass of the target ($0.9 M_{\oplus}$) and thus the pressures are not the same. For a constant number density, there is thus no possibility to obtain particles which have comparable mass in either object, because the mass of the particles scales with the density.

6.7.1 Alternative set up procedure

To circumvent the problem of the initial particle number density, another set up procedure has been investigated. The main difference with the original one is that the 1D radial phase has been left out. The SPH bodies are initially set out of hydrostatic equilibrium, with the initial density being the one used as reference in the equation of state. Furthermore, the number of particles is distributed according to the bodies' volume rather than mass. The idea behind is the following: since the initial density is the same in both bodies (for a given material), as the volume occupied by a single particle is almost equivalent (in our case the difference is on the order of 1‰), it follows that the particle mass is the same. Thus, there is no difference, again for a given material, on the origin body. Also, the distribution of particles between the bodies is considerably affected; the impactor now has 31% of the total for a mass share of 18%. This strong increase is due to the presence of water; had they both the same composition, they would have the number of particles proportional to their respective mass. The aim of this modified procedure is to avoid the spurious clumping observed on the right panel of figure 6.16, where most notably impactor's iron core (yellow) has a form close to a minimum contact surface with other materials.

The hydrostatic equilibrium is reached in the 3D phase. The mass density is now linked to the number density; the latter now varies with radius. This might seem contradictory with the initial assumption of miscible SPH (which requires a constant number density), but this is helpful when particles are re-distributed in the bodies following the collision, which is the case especially for the impactor. The comparison of results at the end of that phase between the different procedures are shown in figure 6.18 for the target and figure 6.19 for the impactor. The results of the new method described in this section are in the middle column of each figure. The obtained profiles follow quite well

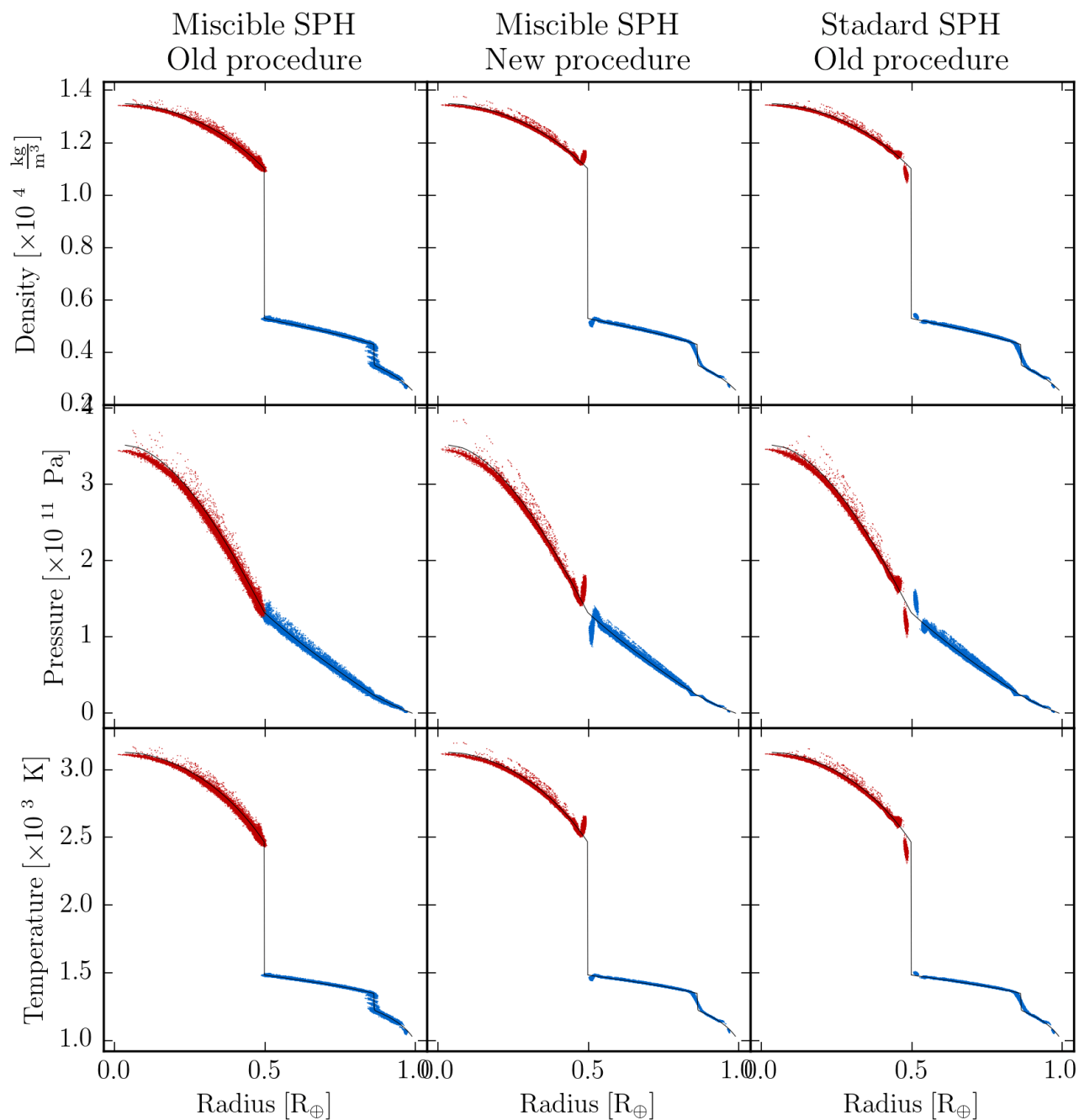


Figure 6.18: Radial profiles of the target SPH bodies with the different set up procedures. The thin black line gives the expected profile obtained from a 1D calculation.

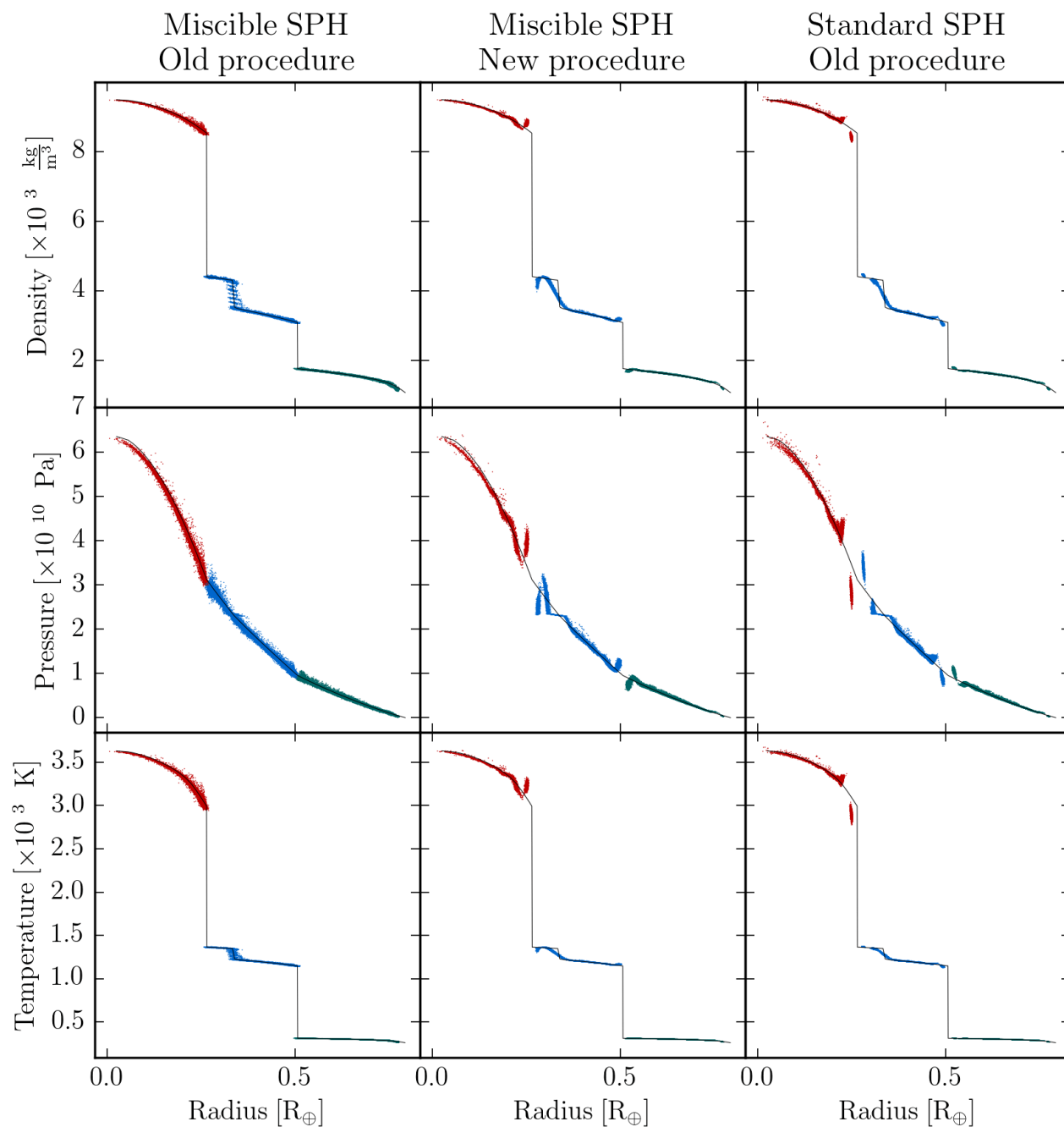


Figure 6.19: Radial profiles of the impactor SPH bodies with the different set up procedures. The thin black line gives the expected profile obtained from a 1D calculation.

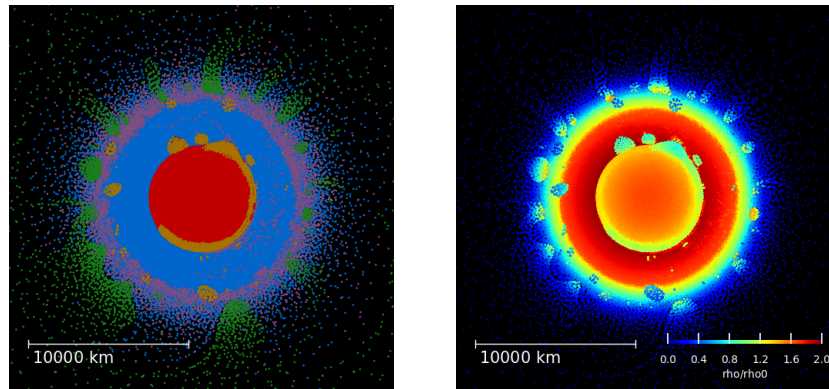


Figure 6.20: Similar collision has shown in figure 6.16, but for miscible SPH and using the new set up procedure. The right panel show the ratio between the computed density and the reference value from the equation of state.

the expectation. The phase transition in silicate is quite smooth compared to the 1D profile, and smoother than it would have been if the old procedure was employed. The behaviour at the material interfaces is quite different compared to the standard SPH, although the artefacts did not vanish. In the 1D profiles resulting from standard SPH simulations (right column of figures 6.18 and 6.19, also in figures 1 and 2 of the first article in chapter 8), there is a group of particles which is very disjoint from the remaining of the material, whose density is the average between the two materials due to the sharp density contrast. This is no longer the case here. We do not observe a separate group of particles at interfaces. The density is now slightly shifted away from the other material, which is the opposite of what happens with standard SPH.

The results with the new set up procedure are better than with the original, but not yet as satisfactory as with the standard SPH scheme in terms of mixing between materials. This is shown in figure 6.20. The large clumps of impactor iron have now vanished and that material now lies at the core-mantle boundary in a similar fashion as with standard SPH. However, there are still iron clumps inside the mantle, which relate more to the previous miscible SPH run rather than the standard method. Water particles however remain grouped in the planet's atmosphere, instead of mixing with silicate particles. There are then regions made exclusively of water and other of silicates. One of the reasons for the segregation between materials may be observed on the right panel of the figure 6.20. It shows the ratio between the computed density and the reference value from the equation of state, i.e. the initial value before hydrostatic equilibrium builds the density profile. It is thus closely related to the number density of particles in this region. The related density and temperature profiles are shown in figure 6.21. Impactor's iron shows the highest temperatures on average; it has thus a lower density than the remaining iron particles in order to preserve the pressure. On the other side, water shows possibly the lowest temperatures across the different materials, its density has thus to increase relative to its reference value. These different relative densities are observed in the right panel of figure 6.20. Due to the way density is computed with miscible SPH, this leads to an aggregation of particles of the same material. In contrast this is not the

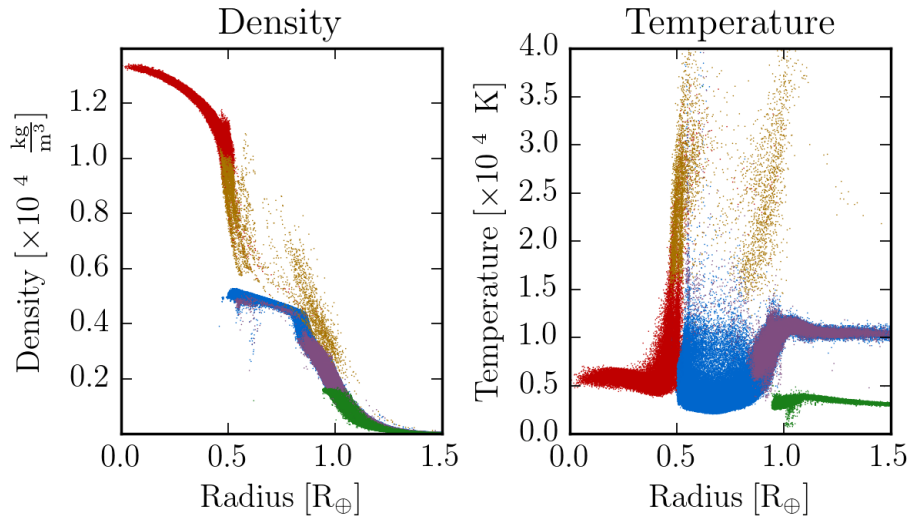


Figure 6.21: Density and temperature profile of the largest remnant at the end of simulation for the same case as in figure 6.20. Colours are the same as in the left panel of that figure.

case for standard SPH as that scheme tends to smooth the density, which is actually what is needed in order to obtain a similar pressure (figure 6.21, left panel). The particles thus mix well in that case.

The comparatively low temperature of water is not a characteristic resulting from using miscible SPH; the same is observed for standard SPH. This is neither a problem of the SPH scheme, as the specific internal energies are comparable between silicate and water in the outer part of the central body. Indeed, most of the internal energy at those location comes from the impact rather than from the pre-impact state. This can be deduced by observing that the temperatures from the initial bodies which are in the 1000 – 1500 K range (bottom panels of figure 6.18) whereas they are at the end of the simulation in the 10000 – 12000 K range (right panel of 6.21); almost an order of magnitude higher. The same applies to water, for which the temperature increases by a similar factor. The point is that water has a higher specific heat capacity than silicates and thus for a similar internal energy has a lower temperature (and in compensation a higher specific entropy).

The way pressure is computed is an important issue for the selection of the SPH scheme. In our case, the problem is that pressure is not only computed from density, but internal energy plays an equivalent role. If the latter was not the case, as in the original study by Solenthaler and Pajarola (2008), then miscible SPH would be an ideal candidate for solving the density problem at material interfaces. However, since pressure does not depend exclusively on density, scaling it by the reference value might not be the best choice. The conclusion may be different for cases where the energy increase is not so important, e.g. for smaller scales. Also the fact that water and silicate mix well in the atmosphere and disc following the impact event discussed here makes standard SPH a good candidate

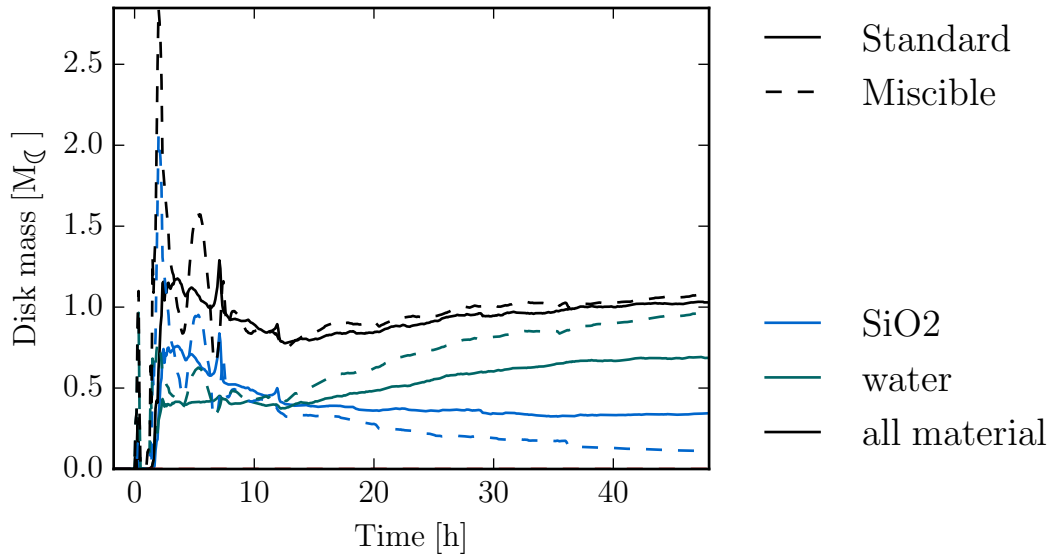


Figure 6.22: Comparison of disc mass versus time between the run with standard and miscible SPH.

for the Moon-forming simulations presented in chapter 7. Nevertheless, the investigations presented in this section suggest that the particle number should depend on the bodies volume rather than mass. This ensures that the average particle volume remains the same across the bodies, thus ensuring that the particle mass is similar for a given material. This should be considered in future simulations.

For reference, the disc masses obtained with the two SPH schemes are provided in figure 6.22. While the total mass remains mostly unchanged (slightly more than $1 M_{\text{moon}}$ in either case), the composition is quite different as the fraction of silicates is significantly lowered. This implies that the different behaviour of mixing may affect the composition of the disc.

Chapter 7

Application: Moon-forming giant impact

We did see in chapter 5 about the demographics of collisions in forming planetary systems that they frequent. If we base ourself on the population where there are initially 20 embryos per system (section 5.1.2), we observe on average four collision events for system that form at least one planet with the mass larger than the one of the Earth. Also a majority of such events happen between the "small" bodies; "small" in the sense of the formation process of giant planets, that is object with up to the mass of the Earth. One should not forget that the choice of the initial number of embryos is arbitrarily limited since the resulting population of giant planets are similar for higher initial embryos count. The discussion here is directed towards the low masses and such there can be multiple more objects within the mass range considered here (target mass $\sim 1 M_{\oplus}$; impactor mass $\sim 0.1 M_{\oplus}$). This kind of event is everything but unlikely in forming system. This is also found in studies on the formation of Solar System's terrestrial planets (e.g. Raymond et al. 2014).

In the manuscript presented in this chapter, we apply the collision simulation model shown in the previous chapter to one specific event, which could lead to the formation of our main natural satellite, the Moon.

Moon-Forming Giant Impacts with Icy Impactors

Alexandre Emsenhuber^{a,*}, Martin Jutzi^a, Willy Benz^a

^a*Physikalisches Institut & Center for Space and Habitability, Universität Bern, Sidlerstrasse 5, CH-3012 Bern, Switzerland*

Abstract

The Moon is believed to have formed from the debris generated by a giant impact. In the canonical impact scenario it is found that the Moon forms predominantly from impactor material. In contrast, the isotopic composition of the two objects match almost perfectly (Young et al., 2016, *Science* 351, 493-496). Various alternative scenarios were proposed to reconcile the impact model and observational constraints. In this work, we further explore the icy impactor scenario (Reufer et al., 2012, *Icarus* 221, 296-299). The influence of the thickness of the water ice layer on top of the impactor as well as the pre-impact spin of the proto-Earth are studied. The highest fraction of debris disc originating from the proto-Earth is found when the spin is anti-aligned to the impactor's trajectory (retrograde rotation). However, discs which are least as massive as the Moon are only found for prograde pre-impact rotation. We investigate one specific case that has both a sufficiently massive disc and a high similarity in material origin (of Earth mantle and Moon) for the influence of numerical resolution. The results in terms of disc mass and material origin are consistent within 15 %, while the iron content is more sensitive to a change of resolution. The effects of the initial temperature profile and the material rheology were also investigated for two specific cases. We find only relatively small differences in disc properties.

Keywords: Collisional physics, Satellites, formation, Moon

1. Introduction

The formation of the Moon through a giant impact (Hartmann and Davis, 1975) presently is the leading hypothesis. The first numerical simulations (Benz et al., 1986 and following papers of the series, Canup, 2004, 2008) were using a roughly Mars-sized impactor and an impact velocity of about escape velocity. This scenario was found to form a sufficiently massive circumterrestrial disc from which the Moon can later accrete. Most of the disc-forming material originates from the impactor, though. On the other hand, Earth and Moon are almost indistinguishable in various isotopic compositions, such as tungsten (Touboul

*Corresponding author

Email addresses: alexandre.emsenhuber@space.unibe.ch (Alexandre Emsenhuber), martin.jutzi@space.unibe.ch (Martin Jutzi), willy.benz@space.unibe.ch (Willy Benz)

et al., 2007) and oxygen (Wiechert et al., 2001). For the latter isotope, Herwartz et al. (2014) found a difference between Earth and Moon, but their results are contested (Young et al., 2016). There are two possibilities for this problem: either the impactor has almost the same isotopic composition as the proto-Earth or the resulting bodies have the same constituting materials.

Possible origins for the colliding bodies have been investigated. Mastrobuono-Battisti et al. (2015) found in their simulations that the majority of target-impactor pairs have more similar origin compared to neighbour planets, and thus compositional similarity could be a natural outcome of such impacts. However, Kaib and Cowan (2015) arrive at the opposite conclusion. They find a probability of less than $\sim 5\%$ for similar compositions when calibrating the results to reproduce the Earth-Mars difference.

Alternatively, impact scenarios that could lead to a disc with material mostly originating from the proto-Earth have been investigated, using different impact geometries, velocities, and impactor properties (e.g. iron-rich or ice-rich). However, the Earth-Moon system's angular momentum remains to be a constraint. Impact regimes were considered where part of the material and angular momentum escapes the system (Reufer et al., 2012), or where angular momentum is removed due to eviction resonance with the sun (Ćuk and Stewart, 2012). The latter allows for the exploration of high angular momentum impact scenarios (Ćuk and Stewart, 2012; Canup, 2012). Post-impact re-equilibration (Pahlevan and Stevenson, 2007) provides a further mechanism to reduce the isotopic differences. Lately, it was proposed (Rufu et al., 2017) that the Earth-Moon system could be the result of multiple collisions.

As a way to reduce the amount of impactor's silicate inside the disc, it has been suggested that the impactor had an outer layer consisting of volatile material (ice) (Reufer et al., 2012). This material would then be removed on longer term, and only refractories such as silicate and iron would remain to form the satellite. Hui et al. (2013) conclude that water content of the magma ocean was initially about 320 ppm and could have been up to 1.4 wt%. This implies that water was present early during the formation of the satellite, and thus could also have been provided by the impactor itself. The presence of a substantial amount of water in the impactor may not be reflected in the Moon, as it would accrete from very water-poor material (Hauri et al., 2015; Canup et al., 2015).

In this work, we study various impact scenarios involving icy impactors. We investigate the influence of the thickness of the water ice layer (section 3.1) and of pre-impact rotation of the proto-Earth (section 3.2). We also examine the dependence of the results on the resolution in one case (section 3.3), as well as the influence of material rheology and the initial temperature profile (section 3.4).

2. Numerical methods

The simulations are performed using the Smoothed Particles Hydrodynamics technique (see e.g. Monaghan, 1992, for a review). SPH is a lagrangian representation, where the material is divided into a fixed number of particles with given mass and type. This feature permits to track material, and thus to discriminate its origin. The code is similar to the one in Reufer et al. (2012). The equation of state is ANEOS (Thompson and Lauson, 1972)

for water and iron, and a modified version by Melosh (2007) called M-ANEOS for silicate to handle correctly molecular clusters in the vapor phase. The simulations involve around 500 000 particles; this total number of particles is distributed among the target (or proto-Earth) and the impactor (sometimes referred to as "Theia" in the literature) so that particles in both objects roughly have the same mass. Each body is set up using the following scheme: first a one dimensional radial profile is generated and evolved until hydrostatic equilibrium is reached. This profile is then mapped to a sphere consisting of SPH particles with identical volume. Their properties are assigned from the 1D profile. As particles have fixed volume, their mass is proportional to the local density. In the case of a rotating body, velocity is assigned to the particles at this point in order to obtain a rigid body rotation. The resulting body is also evolved in order to damp remaining velocities and in the case of a rotating body, to allow flattening to take place.

Each simulation is started when the bodies are at a distance of five times the sum of their radii. In case of the rotating targets, rotation and impact planes coincides to maximise the effects (Canup, 2008). The equatorial radius is used for the orbital setup. In such a case, initial angular momentum is computed as $\vec{L} = L_{\text{imp}}^{\vec{}} + L_{\text{rot}}^{\vec{}}$ where $L_{\text{imp}}^{\vec{}}$ is the contribution from the impactor's orbit around the proto-Earth and $L_{\text{rot}}^{\vec{}}$ is the angular momentum due to the self-rotation of the latter. As in our case these two vectors are aligned, this expression reduces to $L = L_{\text{imp}} \pm L_{\text{rot}}$ with a positive contribution of L_{rot} in case of prograde rotation and a negative one otherwise.

At regular periods, we compute the different outcomes of simulations, such as which particles are part of the debris disc from which the Moon can accrete. The scheme is the same as in previous work: in a first step we determine clumps of gravitationally bound particles and select the most massive one. We then search for the proto-Earth by walking through particles with increasing potential energy two times. The first iteration is limited by density going below the one at zero-pressure in order to guess the center of mass. In the second iteration the density limit is given a certain tolerance to determine the radius. All other bound particles have their orbit computed and are divided into two categories: particles that have their periapsis below the surface of the central body and thus will collide with it, and particles that are part of the disc.

We evolve simulations until they reach a steady state, but at least for a physical time of about 24 hours after the impact.

2.1. Analysis

To measure the difference in material origin, a factor indicating the origin of the proto-lunar disc has been introduced. First

$$f_T = (m_{\text{SiO}_2, \text{target}} / m_{\text{SiO}_2, \text{tot}})_{\text{disc}} \quad (1)$$

represents the fraction of silicate orbiting in the disc originating from the target (proto-Earth). The same factor can be calculated for the silicate present in the post-impact proto-Earth (part of the impactor is accreted onto the proto-Earth, thus it is not exactly one).

The ratio between these two factors then gives the compositional difference between the disc and the proto-Earth:

$$\delta f_T = \frac{(m_{\text{SiO}_2, \text{target}}/m_{\text{SiO}_2, \text{tot}})_{\text{disc}}}{(m_{\text{SiO}_2, \text{target}}/m_{\text{SiO}_2, \text{tot}})_{\text{proto-Earth}}} - 1 \quad (2)$$

which can take values of -1 when all the proto-lunar disc silicate's originate from the impactor to positive infinity. A value of 0 indicates that the same fraction of the material comes from the impactor in both the proto-lunar disc and the proto-Earth after the impact.

We also compute an estimate of the satellite mass that would form from the disc by using the scaling law derived by Kokubo et al. (2000):

$$M_{\text{sat}} \simeq 1.9 \frac{L_{\text{disc}}}{\sqrt{GM_{\text{earth}}a_R}} - 1.1M_{\text{disc}} - 1.9M_{\text{esc}} \quad (3)$$

where M_{sat} is the estimated mass of the satellite (the Moon mass), M_{disc} the mass of the disc, L_{disc} the angular momentum of the disc, M_{earth} the mass the earth, a_R the Roche radius of the Earth with $a_R = 2.9R_{\text{earth}}$ and R_{earth} the radius of the Earth, and finally M_{esc} the mass of material that escapes the system during the formation of the satellite, which is taken to be 0 in our work. This formula gives physical result only in the case where $0.6 < \frac{L_{\text{disc}}}{M_{\text{disc}}\sqrt{GM_{\text{earth}}a_R}} < 1.1$. Otherwise the mass of the satellite is either negative or greater than the mass of the disc from which it accretes. The estimate is computed twice, with and without taking the water component into account, as the Moon would accrete from water-ppor material (Hauri et al., 2015; Canup et al., 2015).

2.2. SPH with solid strength

All previous simulations of a Moon-forming impact were treating material as fluid. This is mainly due to the fact that gravity is the dominant force in such massive bodies. Furthermore due to the energy involved in these impacts, material gets molten. While we will use the same approximation for most of our runs, we include solid forces (material strength) to verify to correctness of this assumption for some of our runs. To model this, we adopt a similar model as the one described in Jutzi (2015): an elastic-perfectly plastic from Benz and Asphaug (1994) where we replace the yield strength computation with the model by Collins et al. (2004). For simplicity, we assume that the material is always entirely damaged (i.e. granular) and the Yield strength is proportional to the pressure. At high pressures, it is limited by the Yield strength of intact material. The details of this model are described in Emsenhuber et al. (2017).

As stated above, we use the (M-)ANEOS equations of state. We take advantage of its numerous output values in order to determine particles' state, if possible. For iron and water, ANEOS returns full information about the phase, so only the solid phase is considered for applying solid strength. The corresponding melting temperature is determined by finding the solid-liquid boundary at constant pressure. For silicate however, M-ANEOS returns only partial phase information. The information given is that the material is either mixed

liquid-vapour or single phase. The former is excluded from solid strength calculations, and for the latter the melting temperature is calculated as in Senft and Stewart (2009) with:

$$T_{\text{melt}} = \begin{cases} 2000 \text{ K} & p < 0.7 \text{ GPa} \\ 2000 \text{ K} + \\ (p - 0.7) * 85.7 \text{ K/GPa} & \text{otherwise} \end{cases} \quad (4)$$

where p is the particle's pressure. Using this melt temperature, we also limit the yield strength as in Collins et al. (2004):

$$Y \rightarrow Y \tanh \left(1.2 \left(\frac{T_{\text{melt}}}{T} - 1 \right) \right) \quad (5)$$

or $Y = 0$ if $T > T_{\text{melt}}$.

3. Results and discussion

In all simulations performed in this work, the proto-Earth starts with the same mass and composition: chondritic, differentiated body, of $0.9 M_{\text{E}}$ (Earth mass) with 30 wt% of iron core and 70 wt% silicate mantle. However, different types of impactors are used: chondritic, differentiated with $0.1 M_{\text{E}}$ (again 30 wt% of iron core and 70 wt% silicate mantle), with either zero, $0.05 M_{\text{E}}$ or $0.10 M_{\text{E}}$ water ice atop of it. The latter case has the same initial composition as the "icy" case from Reufer et al. (2012). We also consider a case with an impactor of $0.20 M_{\text{E}}$ water ice only. We perform several simulation sets, distinguished by the pre-impact rotation period of the proto-Earth. Five periods were selected: -6 h, -12 h, ∞ (no rotation), 12 h and 6 h. Negative rotation period means that the proto-Earth is rotating in the opposite direction as the one of the impactor when impacting the proto-Earth. The impact takes place in the same plane as the one in which the proto-Earth is rotating. A summary of the simulation set properties is shown in table 3. The disc content in silicate and iron along with δf_T plotted against impact velocity and angle is shown in figure 1 for a better overview of the results.

3.1. Water-ice layer thickness

We start by looking at the effects of a varying thickness of water ice layer on the impactor. As less silicates are present in the impactor's shell, this layer has the potential advantage to enhance the ratio of Earth's silicate material and thus make the disc more similar to the proto-Earth. The counterpart being that the total mass is decreased due to the absence of impactor silicates.

The purely icy impactor is an extreme case where δf_T takes value of zero by definition. The water ice layer, with its lower density changes the impactor's radius. For instance, for the ice only impactor, its radius is about 5600 km, just 12% smaller than the one of the target. Then, for the same impact angle, the initial angular momentum is higher and a lower proportion of the projectile will interact directly with the proto-Earth during the impact.

Results for the purely icy impactor are given in table 5. We see that such a scenario leads to a disc mass which is too small in all cases. The highest values for the disc's silicate content

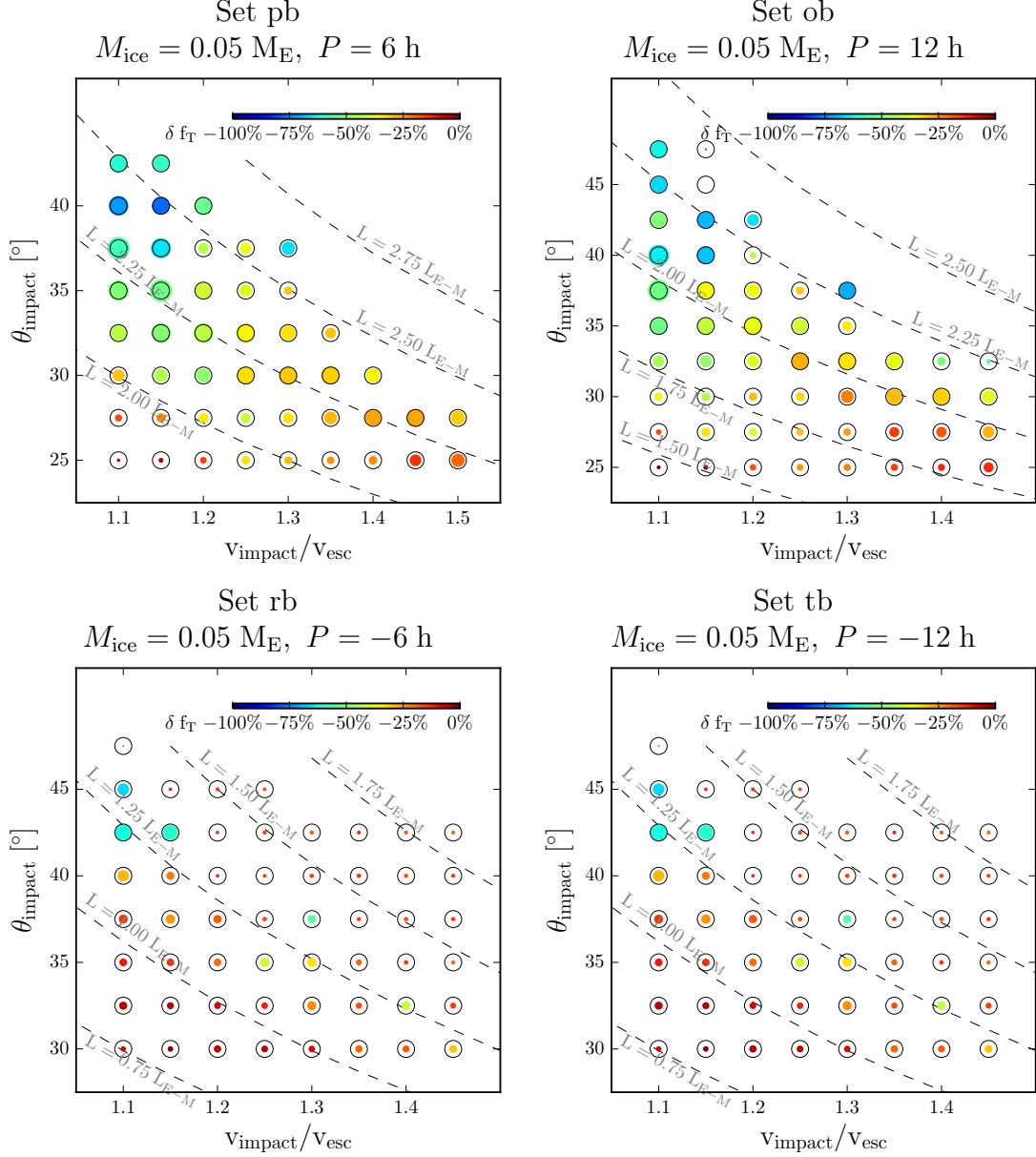


Figure 1: Disc content in silicate and iron, with δf_T as a function of impact velocity and angle for each simulation set. Each simulation is represented by one point; the disc mass in silicate and iron (that is not counting water) is proportional to the surface of the point, with the black circle showing one Moon mass. Colour represents the δf_T , going from -100% (dark blue, disc silicate coming only from the impactor) to 0% (dark red, same origin for both the proto-Earth and the disc). This variable can have a positive value, but this is never the case in our simulations.

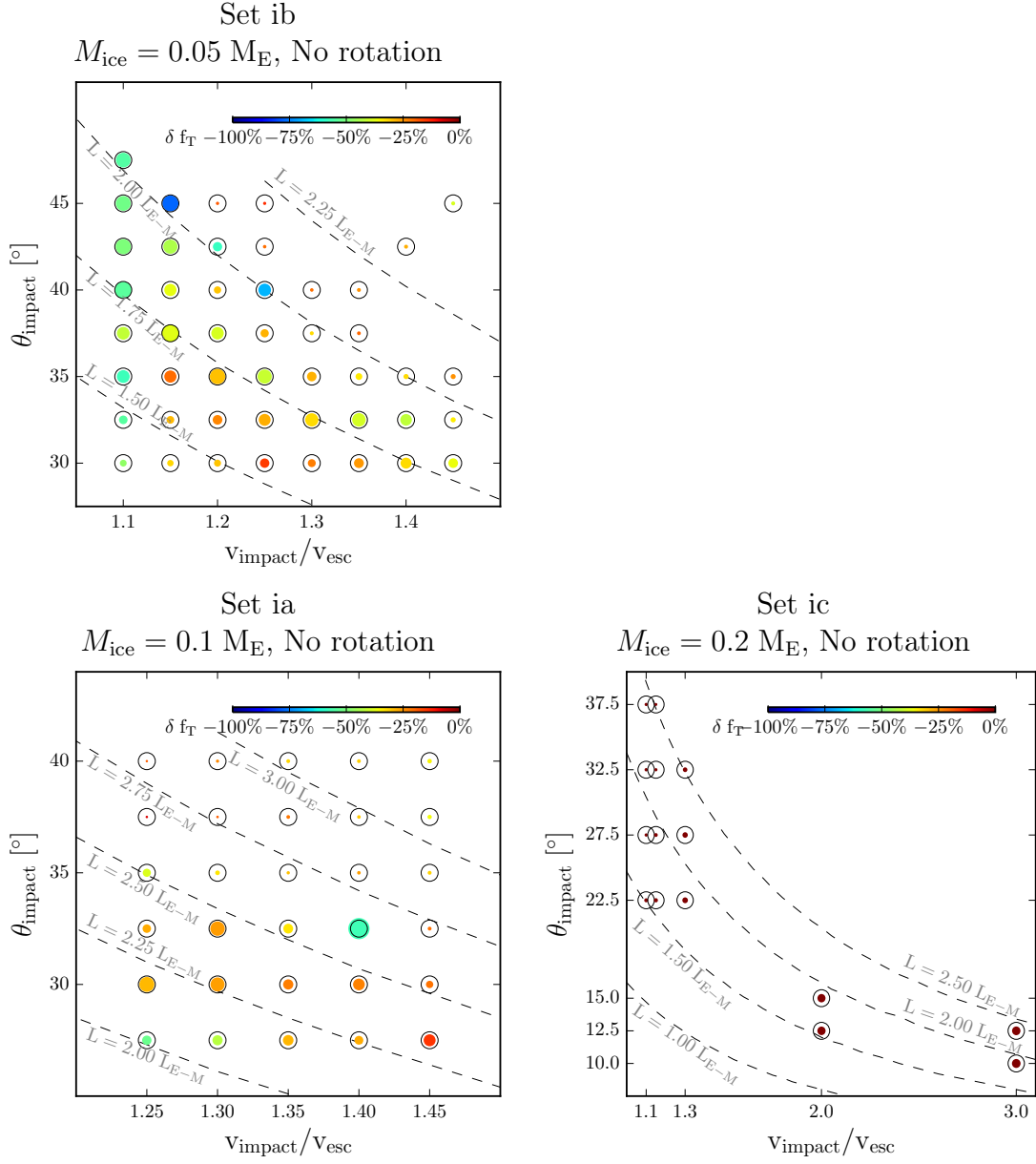


Figure 1: continued.

are $0.24 - 0.28 M_M$ from the cases with $v_{\text{imp}}/v_{\text{esc}} = 2.00$ or 3.00 . One can see that those runs yield a negative value for the satellite mass. This indicates that specific angular momentum is low ($L_{\text{disc}}/\sqrt{GM_{\text{disc}}a_R} \leq 0.22$), which can also be seen in the disc's angular momentum ($L_{\text{disc}} \leq 0.01 L_{E-M}$) and bound angular momentum ($0.14 L_{E-M} \leq L_{\text{bound}} \leq 0.30 L_{E-M}$). For the lower impact velocity cases, the value is lower than $0.12 M_M$. It can also be noted that no iron is present inside the disc in any of those simulations.

Cases with $v_{\text{imp}} = 1.10v_{\text{esc}}$ tend to retain a higher proportion of the impactor in orbit around the proto-Earth than the ones with $v_{\text{imp}} \geq 1.15v_{\text{esc}}$. This influences various outcomes, such as the disc content in water which is $4.37 M_M$ in run *ic01* and $0.09 M_M$ in run *ic02* ($v_{\text{imp}}/v_{\text{esc}} = 1.10$ and 1.15 respectively, both have $\theta_{\text{imp}} = 32.5^\circ$). Similarly, the bound angular momentum is higher (1.97 against $0.63 L_{E-M}$) and the mass escaping from the proto-Earth lower (1.37 against $9.55 M_M$). This difference is due to largest remnant of the impactor which is partly bound for the cases having $v_{\text{imp}} = 1.10v_{\text{esc}}$ whereas this is not the case for the other runs.

Such an impact will also lead to water being deposited onto the proto-Earth. In our cases, we have from 33 to 63 wt% of the impactor which finds itself on or close to the surface of the target. This value is extremely high compared the actual water amount on the Earth (lower than per-mil), and such type would then require water to evaporate.

In the *ia* set, half the impactor's mass consist of water ice. The results of these runs are provided in table 4. There is a single event that leads to a disc mass higher than the Moon's mass in silicates, but in this case, most of it comes from the impactor ($\delta f_T = -57\%$). Reufer et al. (2012) found a few other events with the same characteristics. In the simulations of set *ib*, in which the impactor has a water ice layer that is half in mass compared to set *ia* (results in table 8), there is also one single run with more than one Moon mass of silicates present in the disc; in this case the fraction provided by the proto-Earth $\delta f_T = -38\%$.

Generally, we find that a thick water ice layer on the impactor tends to generate discs with only small masses. Some silicates from the impactor are needed to obtain discs with enough mass to form the Moon. A moderately thick layer is thus a trade-off between compositional similarity and disc mass.

3.2. Pre-impact rotation

In this section, we investigate the effect of pre-impact rotation of the target on the disc properties. The composition of both target and impactor is kept constant. We will use the lowest ice thickness case from the previous section (set *ib*) as a base. The corresponding results are show in tables 6 to 10.

Oblique and low velocity impacts ($v_{\text{imp}}/v_{\text{esc}} \leq 1.15$) show similar result across all sets, that is an high compositional difference ($\delta f_T \leq -55\%$) together with disc masses up to $2.8 M_M$. Previous studies (Canup, 2004) found similar results using chondritic impactors. More head-on runs in the same velocity regime show low mass discs. The regime change happens at different angles across the sets, but is not completely related to initial angular momentum, as it happens around $1.3-2.0 L_{E-M}$ for most retrograde to most prograde initial spin.

The most noticeable effect of the pre-impact rotation is on the disc mass. Series *rb*, *tb* and *ib* (retrograde or no pre-impact rotation) have only a few cases where the disc’s silicate content is higher than one Moon mass, and all of them have $\delta f_T < -60\%$ (see below for more detailed explanation). On the other hand, prograde pre-impact rotation generally leads to an increase of the disc mass. In series *ob* and *pb* there are runs with more than one Moon mass and a relatively similar origin of silicates (δf_T closer to zero). In the *ob* set, these are runs *ob16* ($v_{\text{imp}}/v_{\text{esc}} = 1.15$, $\theta_{\text{imp}} = 37.5^\circ$) and *ob25* ($v_{\text{imp}}/v_{\text{esc}} = 1.20$, $\theta_{\text{imp}} = 35.0^\circ$). These two runs also have a similar angular momentum, $L = 2.05 L_{\text{E-M}}$ for the former and $L = 2.02 L_{\text{E-M}}$. The set *pb* contains more runs with such properties. We thus find that a situation with a velocity range $v_{\text{imp}}/v_{\text{esc}} = 1.25 - 1.35$ and impact angle $\theta_{\text{imp}} = 30 - 32.5^\circ$ are most likely to produce a disc with sufficient mass and target’s silicate. We note that Canup (2008) found that prograde rotation tended to reduce the disc mass, but this was for a fixed angular momentum. In our work, we base the comparison on a constant impact geometry and do not use the angular momentum constraint, following Āuk and Stewart (2012).

In the *pb* set, we also note that δf_T is increasing with increasing impact velocity: for $v_{\text{imp}}/v_{\text{esc}} = 1.20$, δf_T is around -40% and goes to -20% and -31% for the two cases at $v_{\text{imp}}/v_{\text{esc}} = 1.50$. Exceptions are low velocity and low impact angle cases, which lead to similar disc-planet compositions, but only very small disc masses. It can also be seen that the iron content increases along with impact velocity; run *pb44* is rejected due a too high iron content whereas run *pb38* has 4.5 wt% of iron, counting iron and silicate.

Simulations with counter-rotation generally lead to a more similar material origin. The majority of runs in the *rb* set have δf_T between -20% and -15% whereas for the *pb* set this is around -30% .

In summary, we find two competing effects: the most massive discs occur with prograde pre-impact rotation, while the lowest compositional differences result in cases with retrograde pre-impact rotation. The variation in composition between the different sets is lower than the one in disc mass. The simulations discussed above are located in the region where composition is most similar for prograde pre-impact rotation. We find that they are the ones that best matches both criteria.

Concerning the angular momentum, we see that the part escaping after the impact (the difference between L and L_{bound} columns of tables 4-10) is mainly governed by impact geometry, and little influenced by pre-impact rotation. The initial value however holds a contribution from the pre-impact spin of the target (a rotation period of 6 h lead to a contribution of about $0.63 L_{\text{E-M}}$). This explains why for both counter-rotating sets, there are only two runs (*tb55* and *tb57*) where the final bound angular momentum is higher than the one of the present-day Earth-Moon system. The situation is opposite for prograde pre-impact rotation where only 6 runs in the *ob* set and only one run in the *pb* set have an angular momentum which is lower than the present-day Earth-Moon system. Part of the angular momentum due to the initial rotation is transferred to the disc. Thus prograde pre-impact rotation helps to provide sufficient angular momentum to the disc a region where most of the impactor is also retained bound.

We note that the different sets don’t cover the same range of impact angles. The range was moved towards lower impact angles (more head-on) for prograde pre-impact rotation

sets in order to counter balance the angular momentum due to the initial target's spin. Therefore, simulations with both high velocity and angle having very low bound angular momentum were not studied.

Some cases show an high disc mass combined with a low δf_T and extreme value for the estimated satellite mass, ranging from negative to about twice the disc mass. They are located at the limit of the "hit-and-run" regime. In these cases, the remainings of the impactor form a clump which, as a whole, is not part of the circum-planetary disc. However some of its particles are nevertheless found as part of the disc due to the clump's spin. In the case this clump is escaping, these particles are seen as orbiting in the opposite direction compared the other disc particles, and will thus lower the aggregate disc's angular momentum. As consequence, the estimated disc mass will be low or even have a negative value. For instance, in run *rb55* the largest clump accounts for $0.73 M_M$ of the $0.89 M_M$ disc and has an orbit with $e \simeq 0.98$ and an orbital period of about 82 days. It is not feasible to simulate one complete orbit of that body, but it can be noted that the periapsis is at about half of the Roche limit, and thus could get disrupted on its next passage close to the proto-Earth. When these clumps are not taken into account, the satellite mass takes values 0.40 and $0.21 M_M$ with and without water respectively, and $\delta f_T = -17 \%$.

The disc's water content for the candidate cases varies between 24 wt% and 31 wt%, which is much higher than the upper limit of 1.4 wt% provided by Hui et al. (2013). However we only simulate the first couple of days after the impact whereas the lunar magma ocean forms after the coagulation of the debris and the formation of the Moon itself, which takes place in a time scale of hundred years after the impact (Salmon and Canup, 2012). During this period it is possible that due to the density contrast between water and silicate, the water contained first inside the disc and then in the proto-Moon is released and only a fraction is accreted in the final Moon.

We find that the water provided to the proto-Earth is only present in the uppermost part of the mantle (starting from $0.90 - 0.95 R_E$), with a mass fraction increasing along with radius, reaching values around 5 wt% at the surface. This mass fraction continues to increase in the ejecta until reaching a value of about one third.

3.3. Resolution

We investigated the dependence of the disc properties on the numerical resolution using run *pb38*. For this we performed two additional simulation where the code and initial conditions were kept equal, but for the number of particles which was either decreased or increased by a factor ten, leading to about 50 000 and 5 000 000 particles respectively. The high resolution run took four months to complete on a 64 CPUs machine.

A summary of the results is shown in table 1. The high resolution run was analysed two times, the only difference being which particles are forming the circumplanetary disc. The reason for this is the presence of a material clump, which as a whole is orbiting around the target. Due to its spin, not all of its constituting particles are not found to be part of the disc. The second last line in the table gives the result as when it is performed according to section 2 whereas for the last line all particles which are part of the clump orbiting are also deemed as part of the disc. The mass of the whole clump is $0.46 M_M$ composed of 85 wt%

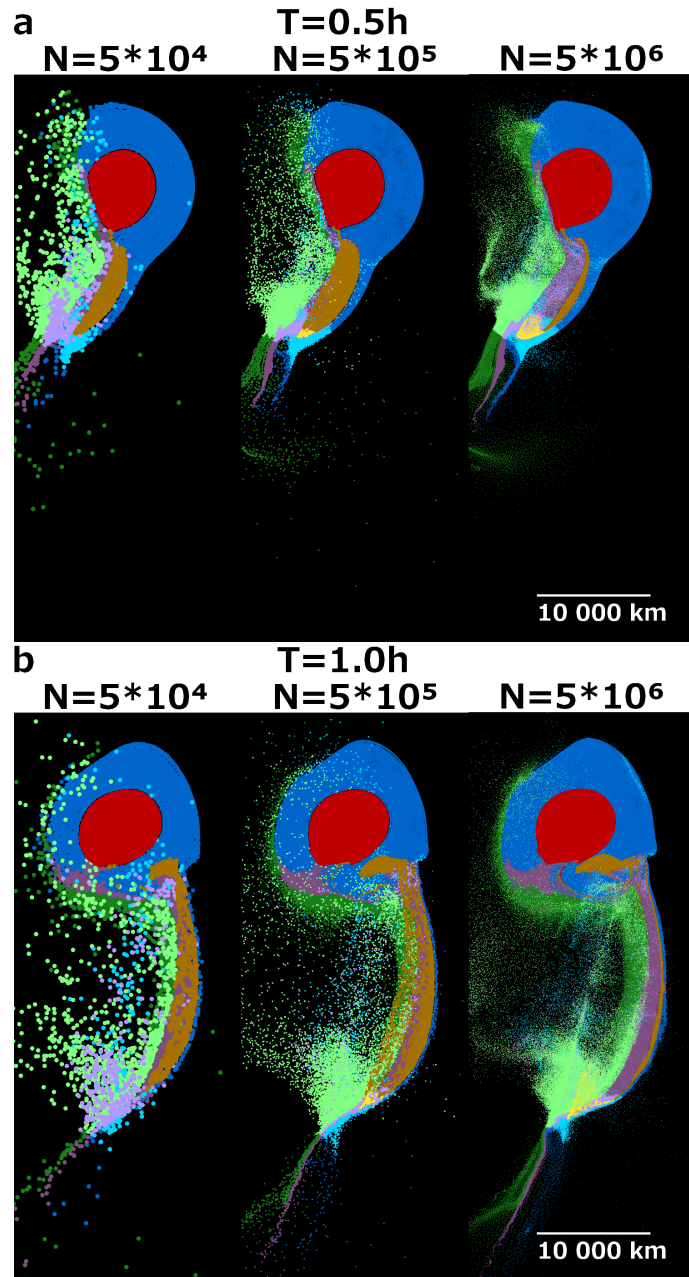


Figure 2: Comparison of three simulations with different resolutions using run *pb38*, at $t = 0.5$ h (panel a) and $t = 1$ h (panel b). In both panels, the left image shows the low resolution simulation (about 50 000 particles), centre image nominal one (about 500 000 particles) and right image the high resolution one (about 5 000 000 particles). Each point represents one SPH particle, with colour denoting its material and origin: red for target's iron, yellow for impactor's iron, green for impactor's water, blue for target's silicate and purple for impactor's silicate. Highlighted particles are the ones that will be part of the disc at the end of the simulations. Only a slice of 500 km in each direction from the impact plane is shown here, except for iron and highlighted particles which are all shown. Iron particles are plotted above all other particles.

N	M_S	M_{S^*}	δf_T	M_D [M_M]				L_D	L_{bound}
	[M_M]	[M_M]		SiO ₂	H ₂ O	Fe	tot.	[L_{E-M}]	[L_{E-M}]
50 000	1.24	0.90	-35%	1.02	0.52	0.00	1.54	0.26	1.48
500 000	1.40	1.10	-31%	1.09	0.37	0.06	1.52	0.28	1.52
5 000 000	1.32	1.06	-26%	0.86	0.28	0.08	1.23	0.24	1.54
5 000 000*	1.33	1.07	-25%	1.02	0.30	0.09	1.40	0.26	1.54

Table 1: Results for simulations with different resolutions. Each row gives the results for one simulation. In the last row, the algorithm used to find particles that are part of the circumplanetary disc was modified (see main text). The resolution is given in the first column. The other columns give the corresponding results: M_S and M_{S^*} are the estimated satellite mass using (3), with and without water respectively. δf_T is the compositional difference between the disc and the planet from (2). M_D is the mass of the different materials inside the disc and L_D the corresponding angular momentum. L_{bound} is the angular momentum of all bound material.

silicate, 11 wt% iron and 4 wt% water. It thus account for about one third of the whole disc. As in Canup et al. (2013), we find that simulations with high resolution form more massive clumps in the disc.

We see that δf_T value slightly increases with the resolution; also the presence of the clump in the high resolution run has a tiny effect. This effect results for an higher proportion of target’s material in the disc rather than a change of the planet’s composition. The disc’s content show a different pattern for each material: for silicate, it’s little affected by the resolution, if we take the whole clump as part of the disc in the high resolution run. The highest value is for the normal resolution run with 1.10 M_M and the two other cases have a value just greater than Moon’s mass. The two other materials show opposite trends. Water content decreases while iron content increases along with resolution. The iron content of the high resolution run would change its status from one of the most promising cases to rejection due to both the low content of silicate inside the disc, lower than the actual Moon mass, and high mass fraction of iron of about 8 wt% (taking into account only silicate and iron). However, we note that also the initial temperature profile affects the iron fraction (section 3.4).

The dependence of the amount of iron in the disc with the resolution is linked to its location inside the arm that forms after the impact. Figure 2 panel a shows the state of the three simulations at half an hour after impact and panel b at one hour, with material that will be part of the disc at the end being highlighted. Material further away from the highlighted zone of the arm will eventually escape the system whereas the one bellow will fall back to the proto-Earth. The location of the impactor’s iron is the same in all simulations until 0.5 h (panel a), and then starts to diverge where increasing resolution leads to a presence higher up within the arm. Thus no iron remains present in the part where most of the disc’s silicate is located in the low resolution run while for the normal and high resolution runs, there is an overlap (panel b). This overlap is bigger for the high resolution case, which explains the fact that an higher fraction is present inside the disc at then end of the simulation. One can also notice that there are water particles marked to be part of the disc along the whole arm.

Base	Rheology	Profile	M_S [M_M]	M_{S^*} [M_M]	δf_T	M_D [M_M]				L_D [L_{E-M}]	L_{bound} [L_{E-M}]
						SiO ₂	H ₂ O	Fe	tot.		
<i>pb38</i>	fluid	high	1.32	1.05	-29%	1.07	0.34	0.05	1.46	0.26	1.51
<i>pb38</i>	fluid	low	1.17	0.89	-31%	1.05	0.40	0.02	1.47	0.25	1.50
<i>pb38</i>	solid	high	0.99	0.75	-36%	0.83	0.35	0.05	1.23	0.21	1.47
<i>pb38</i>	solid	low	0.82	0.61	-23%	0.75	0.34	0.00	1.09	0.18	1.47
c. case	fluid	high	1.38	1.38	-61%	1.26	0.00	0.02	1.28	0.26	1.01
c. case	fluid	low	1.47	1.47	-60%	1.18	0.00	0.01	1.19	0.25	1.02
c. case	solid	high	1.33	1.33	-65%	1.31	0.00	0.01	1.31	0.21	0.98
c. case	solid	low	1.55	1.55	-75%	1.10	0.00	0.00	1.10	0.18	1.01

Table 2: Results for different rheologies and initial temperature profiles. One simulation is given in each line, and the three first columns give the model parameters. The first column indicates the case, the second the rheology and the third the temperature profile (*high* and *low* denote the relative mantle temperature). Remaining columns give the corresponding results and are the same as in table 1.

The ones on the lower part will fall inside the target along with the surrounding material in the next hours and then get ejected back from the body.

Constituting material of the clump present in the high resolution run comes from the most distant region of the arm forming after the impact. Few hours later, when this feature vanishes, multiple clumps are formed. The one in question here is formed by the agglomeration of several such clumps in a period spanning between 6 and 12 h after the impact. In the normal resolution case, the arm vanishes sooner, and no agglomeration occurs. However, calculating the orbit of the clump at the end of our simulation shows that it is on a very eccentric orbit ($e \simeq 0.87$), with a period of revolution around the proto-Earth of about three days and its periapsis is situated at about 1.3 times the proto-Earth’s radius or 0.4 times the Roche limit, which means it eventually will get disrupted by tidal forces. The fraction of the disc material which is part of a such clump depends on the resolution. As stated above, in the high resolution case it is about 33 wt%, compared to 18 wt% and 12 wt% for the middle and low resolution cases. The study of disc features is affected by the resolution of impact simulations. The eventual tidal disruption when approaching the periapsis might further alter disc properties, such as its mass or the distribution of clumps.

The different values reported here are consistent within 15 % except for material origin as well as disc content in water and iron. Values with the original analysis scheme for the high resolution show a bigger deviation. This is consistent with the results from Canup et al. (2013).

3.4. Solid strength and temperature profile

Here we perform investigations of the effect of using a solid rheology as described in section 2.2. Two simulations will be used as base: one which is comparable to the main case of Canup (2004) (same bodies but without water, $v_{\text{imp}} = v_{\text{esc}}$, $\theta_{\text{impact}} = 48^\circ$, hereafter referred as *canonical case*) and *pb38*, as in the previous section. We will use the same resolution as in the main part of this article. In addition, two different temperature profiles

were investigated: the first is the same as for the previous parts of this study where core and mantle have similar temperature (in the 3500 – 5500 K range for the proto-Earth and 2000 – 3500 K for the impactor). The second one is taken from Reufer et al. (2012), who used lower initial temperatures. The main reason for using different profiles is the strong dependence of yield strength on the temperature, and hence the solid strength. With the former profile, target’s silicate mantle has its upper part liquid as we have a temperature above 2000 K. At a depth of about 1000 km, it becomes solid again as the pressure term of eq. (4) dominates. For the latter profile, all bodies have a solid mantle along with a liquid core. With the combination of these three possibilities (base simulation, rheology and temperature profile), there are in total 8 runs performed, whose results are in table 2. The first result presented there (*pb38* with fluid rheology and high mantle temperature) has the same features as in the two previous sections; however the code had to be adapted in order to include solid rheology and this slightly affects results for fluid rheology. Hence the results are not identical, but the relative differences are within 10 %.

At the end of the simulations, the lower part of the mantle is always solid and the upper part liquid. The ratio of solid in silicates however varies: for the canonical case, we obtain 49 wt% and 73 wt% for the first (high initial mantle temperature) and second (low initial mantle temperature) profiles respectively and 36 wt% and 62 wt% in the *pb38* case. The lower values in *pb38* result from an higher energy being released by the impact as both the impactor is heavier (0.15 M_M compared to 0.10 M_M) and velocity higher ($v_{\text{imp}}/v_{\text{esc}} = 1.35$ versus 1.00).

The two *pb38* runs with fluid rheology have similar disc properties, such as the content in silicate (1.07 M_M and 1.05 M_M for the high and low temperature profiles respectively) and δf_T (–29 % versus –31 %). These differences are small and of the order of the numerical noise. The differences are larger in terms of the disc’s iron content, which is reduced by half (from 0.05 M_M to 0.02 M_M). Temperature profile shows a greater effect on solid rheology; δf_T changes by at least ten points each time and the disc’s silicate content by 5 %. We observe the same situation on the canonical case, with fluid rheology δf_T is almost the same (–61 % and –60 %) and the disc’s silicate content varies by 5 %. It is difficult to draw a conclusion on the iron content, as it is always quite low. When comparing the two runs with solid rheology we again note that these two values have a higher spread. The temperature profile is then more important when solid rheology is used. The rheology is also found to have an effect, as runs with solid strength show a disc mass which is about 25 % smaller than their fluid counterpart (and becomes lower than Moon’s mass). δf_T shows are more complicated behaviour, as for high mantle temperature it is lower with solid rheology (–36 % versus –29 %) whereas for low mantle temperature the opposite occurs (–23 % versus –31 %). As for the disc’s iron content, the values with solid rheology are 0.00 M_M and 0.05 M_M for the low and high mantle temperature profile, respectively. A modified temperature profile could potentially solve the issue regarding the disc’s iron content found in the high resolution simulation (previous section).

For the canonical case, the temperature profile makes only a small difference with fluid rheology. We don’t observe disc mass reduction using a solid rheology as for the *pb38* case, but the difference between the two profile is higher by a factor of more than two compared

to fluid rheology. A massive clump representing 46 wt% of the disc is present with low temperature profile and solid rheology run. 92 % of its constituting material comes from the impactor, which can explain the lower value of δf_T (-75 %) compared to the other cases. At the time the simulation ends, it did complete its first orbit around the proto-Earth but has not been disrupted during the closest approach. We also see a depletion of material in the inner part of the disc; the outer part remaining similar to the other runs. In the fluid case, the clump is formed as well; but has a lower periapsis; it gets disrupted after its first orbit. After the disruption, only half of its mass remains in the disc.

4. Conclusion

We performed several series of giant impact simulations in the context of the Moon formation using the SPH technique. Different parameters of the debris disc caused by the impact were computed, such as the mass of its constituent materials and its compositional similarity in silicate with the planet δf_T .

We studied the effect of a water-ice layer on the impactor with varying thickness. We find that a scenario of a pure water ice body of $0.2 M_E$ impacting a non-rotating proto-Earth ($0.9 M_E$) fails to put sufficient silicate material into orbit for impact velocities $v_{\text{imp}} = 1 - 3 v_{\text{esc}}$, and it also delivers too much water on the Earth. Such a scenario can thus almost certainly be ruled out. We also studied impactors with a chondritic composition inside (differentiated with 0.03 and $0.07 M_E$ of iron and silicate) with an ice layer on top with two different thickness. Our results show that these kind of impacts generally lead to only small disc masses (insufficient to form the Moon) in the case of non-rotating targets.

We used the impactor with the thinnest ice layer and studied the effect of pre-impact target rotation. Most massive discs (at least one Moon mass in silicates) are obtained when the proto-Earth has a (fast) prograde pre-impact rotation. However, δf_T is on average higher (closer to zero) for retrograde rotation, but as these cases lead to very low disc masses, they are not suitable for a successful Moon formation scenario. Therefore, a fast prograde pre-impact rotation, together with a relatively high impact velocity that produces discs at least as massive as our Moon from materials mostly originating from the proto-Earth, are the most promising cases found in this study. The following cases match these conditions and have $\delta f_T > -40$ %: *ob25* (with $M_{\text{disc,SiO}_2} = 1.17 M_M$, $\delta f_T = -36$ %), *pb27* ($1.26 M_M$, -35 %), *pb32* ($1.02 M_M$, -30 %), *pb38* ($1.09 M_M$, -31 %) and *pb44* ($1.03 M_M$, -27 %). The last case however produces a high fraction of iron ($0.08 M_M$).

We performed supplementary runs of the case *pb38* to determine if resolution, solid rheology and initial temperature profiles have an influence on the resulting disc properties. A higher proportion of disc material coming from the proto-Earth is observed in our highest resolution simulation, which can help to reconcile the giant impact scenario with isotopic measurements (e.g. Young et al., 2016). A resolution increase doesn't affect disc's silicates content but increases its iron content (in this specific case above the upper limit provided by experimental constraints (Hood et al., 1999)). Using a solid rheology leads to a disc mass reduction in silicate of about 25 %, independently of the temperature profiles, whereas the disc composition shows a dependency on the initial profiles in this case. By varying

initial temperature profiles we observed that iron almost disappeared from the disc with both rheologies and thus the issue of too much iron encountered in the high resolution simulation could be due to our choice of temperature profile. For impact conditions similar to the canonical scenario by Canup (2004) (no water, lower impact velocity and higher impact angle) we find that both the initial temperature profile and the rheology do have only small effect on the results. Solid rheology along with low mantle temperature leads to the formation of a massive clump inside the disc, which alters its composition towards more impactor material.

Overall, we find that these differences are generally lower or equal to 10 %, probably of the same order as potential numerical effects, with the exception of the mass reduction with solid rheology in the case of *pb38*. Our results suggest that a moderate resolution (500 000 particles) and using a fluid rheology are sufficient to study the global disc properties resulting from such Moon forming type of collisions. However, it is important to keep in mind that the mass of the disc may be slightly overestimated and the formation of clumps may not be fully resolved. Moreover, for simulations at smaller scales (e.g. giant impacts on Mars) and to study smaller disc masses, we expect that very high resolution as well as including a solid rheology are required (Emsenhuber et al, in prep).

In summary, the "icy impactor" Moon formation scenario studied here would require some specific conditions to match the observed properties of the Moon, and it remains to explain how the large amount of water would have been removed. However, also the other previously presented scenarios require specific conditions to work. There are still many parameters that remain unexplored. The study presented here, investigating a range of impactor properties, pre-impact rotation and resolution effects, can serve as a guideline for future explorations.

Acknowledgements

A.E. acknowledges the financial support of the Swiss National Science Foundation under grant 2000020_17246. This work has been carried out within the frame of the National Centre for Competence in Research PlanetS supported by the Swiss National Science Foundation. The authors acknowledge the financial support of the SNSF.

References

- W. Benz and E. Asphaug. Impact simulations with fracture. I - Method and tests. *Icarus*, 107:98, January 1994. doi: 10.1006/icar.1994.1009.
- W. Benz, W. L. Slattery, and A. G. W. Cameron. The origin of the moon and the single-impact hypothesis. I. *Icarus*, 66:515–535, June 1986. doi: 10.1016/0019-1035(86)90088-6.
- R. M. Canup. Simulations of a late lunar-forming impact. *Icarus*, 168:433–456, April 2004. doi: 10.1016/j.icarus.2003.09.028.
- R. M. Canup. Lunar-forming collisions with pre-impact rotation. *Icarus*, 196:518–538, August 2008. doi: 10.1016/j.icarus.2008.03.011.
- R. M. Canup. Forming a Moon with an Earth-like Composition via a Giant Impact. *Science*, 338:1052–, November 2012. doi: 10.1126/science.1226073.

- R. M. Canup, A. C. Barr, and D. A. Crawford. Lunar-forming impacts: High-resolution SPH and AMR-CTH simulations. *Icarus*, 222:200–219, January 2013. doi: 10.1016/j.icarus.2012.10.011.
- R. M. Canup, C. Visscher, J. Salmon, and B. Fegley, Jr. Lunar volatile depletion due to incomplete accretion within an impact-generated disk. *Nature Geoscience*, 8:918–921, December 2015. doi: 10.1038/ngeo2574.
- G. S. Collins, H. J. Melosh, and B. A. Ivanov. Modeling damage and deformation in impact simulations. *Meteoritics and Planetary Science*, 39:217–231, February 2004. doi: 10.1111/j.1945-5100.2004.tb00337.x.
- M. Čuk and S. T. Stewart. Making the Moon from a Fast-Spinning Earth: A Giant Impact Followed by Resonant Despinning. *Science*, 338:1047–, November 2012. doi: 10.1126/science.1225542.
- Alexandre Emsenhuber, Martin Jutzi, and Willy Benz. SPH calculations of Mars-scale collisions: the role of the Equation of State, material rheologies, and numerical effects. *Icarus*, 2017. doi: 10.1016/j.icarus.2017.09.017.
- W. K. Hartmann and D. R. Davis. Satellite-sized planetesimals and lunar origin. *Icarus*, 24:504–514, April 1975. doi: 10.1016/0019-1035(75)90070-6.
- E. H. Hauri, A. E. Saal, M. J. Rutherford, and J. A. Van Orman. Water in the Moon’s interior: Truth and consequences. *Earth and Planetary Science Letters*, 409:252–264, January 2015. doi: 10.1016/j.epsl.2014.10.053.
- Daniel Herwartz, Andreas Pack, Bjarne Friedrichs, and Addi Bischoff. Identification of the giant impactor Theia in lunar rocks. *Science*, 344:1146–1150, June 2014. doi: 10.1126/science.1251117.
- L. L. Hood, D. L. Mitchell, R. P. Lin, M. H. Acuna, and A. B. Binder. Initial measurements of the lunar induced magnetic dipole moment using Lunar Prospector Magnetometer data. *Geophysics Research Letters*, 26:2327–2330, 1999. doi: 10.1029/1999GL900487.
- Hejiu Hui, Anne H. Peslier, Youxue Zhang, and Clive R. Neal. Water in lunar anorthosites and evidence for a wet early moon. *Nature Geosci*, 6:177–180, March 2013. doi: 10.1038/ngeo1735.
- Martin Jutzi. SPH calculations of asteroid disruptions: The role of pressure dependent failure models. *Planetary and Space Science*, 107:3–9, March 2015. doi: 10.1016/j.pss.2014.09.012.
- N. A. Kaib and N. B. Cowan. The feeding zones of terrestrial planets and insights into Moon formation. *Icarus*, 252:161–174, May 2015. doi: 10.1016/j.icarus.2015.01.013.
- E. Kokubo, S. Ida, and J. Makino. Evolution of a Circumterrestrial Disk and Formation of a Single Moon. *Icarus*, 148:419–436, December 2000. doi: 10.1006/icar.2000.6496.
- A. Mastrobuono-Battisti, H. B. Perets, and S. N. Raymond. A primordial origin for the compositional similarity between the Earth and the Moon. *Nature*, 520:212–215, April 2015. doi: 10.1038/nature14333.
- H. J. Melosh. A hydrocode equation of state for SiO₂. *Meteoritics and Planetary Science*, 42:2079–2098, 2007. doi: 10.1111/j.1945-5100.2007.tb01009.x.
- J. J. Monaghan. Smoothed particle hydrodynamics. *Annual Review of Astron and Astrophys*, 30:543–574, 1992. doi: 10.1146/annurev.aa.30.090192.002551.
- K. Pahlevan and D. J. Stevenson. Equilibration in the aftermath of the lunar-forming giant impact. *Earth and Planetary Science Letters*, 262:438–449, October 2007. doi: 10.1016/j.epsl.2007.07.055.
- A. Reufer, M. M. Meier, W. Benz, and R. Wieler. A hit-and-run giant impact scenario. *Icarus*, 221:296–299, September 2012. doi: 10.1016/j.icarus.2012.07.021.
- Raluca Rufu, Oded Aharonson, and Hagai B. Perets. A multiple-impact origin for the Moon. *Nature Geoscience*, 10:89–94, February 2017. doi: 10.1038/ngeo2866.
- J. Salmon and R. M. Canup. Lunar Accretion from a Roche-interior Fluid Disk. *ApJ*, 760:83, November 2012. doi: 10.1088/0004-637X/760/1/83.
- L. E. Senft and S. T. Stewart. Dynamic fault weakening and the formation of large impact craters. *Earth and Planetary Science Letters*, 287:471–482, October 2009. doi: 10.1016/j.epsl.2009.08.033.
- S. L. Thompson and H. S. Lauson. Improvements in the CHART-D Radiation-hydrodynamic code III: Revised analytic equations of state. Technical Report SC-RR-71 0714, Sandia National Laboratories, 1972.
- M. Touboul, T. Kleine, B. Bourdon, H. Palme, and R. Wieler. Late formation and prolonged differentiation of the Moon inferred from W isotopes in lunar metals. *Nature*, 450:1206–1209, December 2007. doi: 10.1038/nature06428.

- U. Wiechert, A. N. Halliday, D.-C. Lee, G. A. Snyder, L. A. Taylor, and D. Rumble. Oxygen Isotopes and the Moon-Forming Giant Impact. *Science*, 294(5541):345–348, 2001. doi: 10.1126/science.1063037.
- E. D. Young, I. E. Kohl, P. H. Warren, D. C. Rubie, S. A. Jacobson, and A. Morbidelli. Oxygen isotopic evidence for vigorous mixing during the Moon-forming giant impact. *Science*, 351:493–496, January 2016. doi: 10.1126/science.aad0525.

Impactor mass [M_E]			Target rotation period [h]				
Iron	Silicate	Water	-6	-12	∞	12	6
0.03	0.07	0.05	rb	tb	ib	ob	pb
0.03	0.07	0.10			ia		
0.00	0.00	0.20			ic		

Table 3: Summary of simulation set properties, with rows denoting impactor composition and columns the rotation period of the target. Infinite rotation period means that the object is not rotating. Blank cells were not studied.

Run	v_{imp} [v_{esc}]	θ [$^\circ$]	L [$L_{\text{E-M}}$]	M_{S} [M_{M}]	M_{S^*} [M_{M}]	δf_T	M_D [M_{M}]				L_D [$L_{\text{E-M}}$]	L_{bound} [$L_{\text{E-M}}$]
							SiO ₂	H ₂ O	Fe	tot.		
ia01	1.30	30.0	2.27	1.07	0.65	-26%	0.69	0.55	0.00	1.24	0.22	1.13
ia02	1.35	30.0	2.36	0.47	0.29	-22%	0.36	0.31	0.00	0.68	0.11	0.98
ia03	1.30	32.5	2.44	1.64	1.00	-26%	0.72	0.60	0.00	1.32	0.28	1.05
ia04	1.35	32.5	2.53	0.61	0.37	-34%	0.33	0.25	0.00	0.58	0.11	0.90
ia05	1.30	35.0	2.61	0.38	0.08	-33%	0.07	0.20	0.00	0.27	0.06	0.70
ia06	1.35	35.0	2.71	-0.02	0.00	-29%	0.04	0.07	0.00	0.11	0.01	0.49
ia07	1.40	30.0	2.45	0.80	0.51	-23%	0.47	0.37	0.00	0.84	0.16	0.88
ia08	1.45	30.0	2.53	0.42	0.20	-21%	0.19	0.25	0.00	0.43	0.08	0.84
ia09	1.40	32.5	2.63	0.67	0.74	-57%	1.27	0.45	0.29	2.01	0.26	0.76
ia10	1.45	32.5	2.72	-0.02	0.00	-21%	0.05	0.07	0.00	0.12	0.01	0.48
ia11	1.40	35.0	2.81	-0.00	0.01	-26%	0.04	0.07	0.00	0.12	0.01	0.48
ia12	1.45	35.0	2.91	0.01	0.02	-31%	0.05	0.07	0.00	0.12	0.01	0.46
ia13	1.30	37.5	2.76	0.00	0.01	-20%	0.02	0.06	0.00	0.08	0.01	0.46
ia14	1.35	37.5	2.87	0.01	0.01	-22%	0.05	0.06	0.00	0.11	0.01	0.45
ia15	1.40	37.5	2.98	0.01	0.01	-30%	0.04	0.06	0.00	0.10	0.01	0.44
ia16	1.45	37.5	3.08	0.02	0.02	-36%	0.06	0.06	0.00	0.13	0.01	0.43
ia17	1.30	40.0	2.92	0.02	0.01	-24%	0.04	0.06	0.00	0.10	0.01	0.43
ia18	1.35	40.0	3.03	0.03	0.02	-32%	0.05	0.06	0.00	0.11	0.01	0.42
ia19	1.40	40.0	3.14	0.04	0.02	-31%	0.05	0.06	0.00	0.11	0.01	0.41
ia20	1.45	40.0	3.26	0.04	0.03	-35%	0.07	0.06	0.00	0.13	0.02	0.39
ia21	1.25	27.5	2.02	0.46	0.28	-52%	0.31	0.25	0.00	0.56	0.10	1.23
ia22	1.30	27.5	2.10	0.56	0.35	-43%	0.36	0.31	0.00	0.67	0.12	1.21
ia23	1.35	27.5	2.18	0.46	0.33	-28%	0.39	0.23	0.00	0.62	0.10	1.16
ia24	1.40	27.5	2.26	0.25	0.17	-27%	0.27	0.24	0.00	0.51	0.07	1.02
ia25	1.45	27.5	2.34	0.53	0.36	-15%	0.49	0.31	0.01	0.80	0.13	0.96
ia26	1.25	30.0	2.18	0.89	0.60	-29%	0.78	0.42	0.00	1.19	0.20	1.27
ia27	1.25	32.5	2.35	0.94	0.41	-27%	0.25	0.35	0.00	0.60	0.15	0.63
ia28	1.25	35.0	2.50	0.62	0.27	-39%	0.23	0.34	0.00	0.57	0.11	1.09
ia29	1.25	37.5	2.66	0.01	0.01	-8%	0.02	0.07	0.00	0.09	0.01	0.48
ia30	1.25	40.0	2.81	0.01	0.01	-19%	0.02	0.05	0.00	0.07	0.01	0.45

Table 4: Results for simulation set ia

Run	v_{imp} [v_{esc}]	θ [$^\circ$]	L [$L_{\text{E-M}}$]	M_{S} [M_{M}]	M_{S^*} [M_{M}]	δf_T	M_D [M_{M}]				L_D [$L_{\text{E-M}}$]	L_{bound} [$L_{\text{E-M}}$]
							SiO ₂	H ₂ O	Fe	tot.		
ic01	1.10	37.5	2.37	4.09	0.03	0%	0.04	4.37	0.00	4.40	0.81	1.74
ic02	1.15	37.5	2.41	0.02	0.02	0%	0.03	0.09	0.00	0.12	0.01	0.63
ic03	1.10	32.5	2.12	4.30	0.03	0%	0.04	3.14	0.00	3.18	0.71	1.62
ic04	1.15	32.5	2.22	0.06	0.02	0%	0.04	0.14	0.00	0.17	0.02	0.72
ic05	1.10	27.5	1.83	2.50	0.02	0%	0.04	1.78	0.00	1.82	0.41	1.31

ic06	1.15	27.5	1.91	0.11	0.02	0%	0.05	0.24	0.00	0.29	0.04	0.83
ic07	1.10	22.5	1.51	0.84	0.02	0%	0.06	0.82	0.00	0.88	0.16	1.05
ic08	1.15	22.5	1.58	0.44	0.01	0%	0.06	0.58	0.00	0.64	0.10	0.96
ic09	1.30	32.5	2.51	0.10	0.06	0%	0.08	0.18	0.00	0.25	0.03	0.66
ic10	1.30	27.5	2.16	0.16	0.08	0%	0.11	0.25	0.00	0.35	0.05	0.73
ic11	1.30	22.5	1.79	0.13	0.06	0%	0.12	0.24	0.00	0.35	0.05	0.74
ic12	2.00	15.0	1.86	-0.32	-0.19	0%	0.24	0.19	0.00	0.43	0.01	0.30
ic13	2.00	12.5	1.56	-0.39	-0.26	0%	0.25	0.22	0.00	0.48	0.01	0.26
ic14	3.00	12.5	2.33	-0.30	-0.19	0%	0.26	0.07	0.00	0.34	0.01	0.17
ic15	3.00	10.0	1.87	-0.31	-0.19	0%	0.28	0.07	0.00	0.35	0.01	0.14

Table 5: Results for simulation set ic

Run	v_{imp} [v_{esc}]	θ [$^\circ$]	L [$L_{\text{E-M}}$]	M_{S} [M_{M}]	M_{S^*} [M_{M}]	δf_T	M_D [M_{M}]				L_D [$L_{\text{E-M}}$]	L_{bound} [$L_{\text{E-M}}$]
							SiO ₂	H ₂ O	Fe	tot.		
rb01	1.30	30.0	0.99	0.10	0.10	-9%	0.14	0.04	0.00	0.19	0.03	0.41
rb02	1.35	30.0	1.10	0.18	0.15	-20%	0.19	0.08	0.00	0.28	0.04	0.41
rb03	1.30	32.5	1.20	0.46	0.34	-24%	0.29	0.13	0.01	0.42	0.08	0.50
rb04	1.35	32.5	1.06	0.09	0.08	-17%	0.13	0.04	0.00	0.18	0.03	0.40
rb05	1.30	35.0	1.17	0.31	0.24	-33%	0.28	0.12	0.02	0.42	0.07	0.42
rb06	1.35	35.0	1.31	0.09	0.06	-19%	0.12	0.06	0.00	0.18	0.03	0.22
rb07	1.40	30.0	1.13	0.09	0.09	-19%	0.15	0.04	0.02	0.21	0.03	0.37
rb08	1.45	30.0	1.19	0.17	0.15	-30%	0.18	0.06	0.03	0.27	0.04	0.36
rb09	1.40	32.5	1.26	0.27	0.21	-41%	0.24	0.09	0.02	0.36	0.06	0.33
rb10	1.45	32.5	1.33	0.08	0.06	-15%	0.13	0.06	0.00	0.19	0.03	0.24
rb11	1.40	35.0	1.39	0.01	0.01	-16%	0.07	0.03	0.00	0.10	0.01	0.12
rb12	1.45	35.0	1.46	0.01	0.00	-20%	0.06	0.03	0.00	0.10	0.01	0.08
rb13	1.30	37.5	1.36	-0.00	0.01	-55%	0.24	0.09	0.00	0.34	0.03	0.10
rb14	1.35	37.5	1.43	0.01	0.01	-15%	0.06	0.04	0.00	0.10	0.01	0.03
rb15	1.40	37.5	1.51	0.01	0.02	-18%	0.07	0.03	0.00	0.10	0.01	0.01
rb16	1.45	37.5	1.59	0.01	0.01	-14%	0.06	0.03	0.00	0.09	0.01	0.01
rb17	1.30	40.0	1.47	0.03	0.02	-15%	0.06	0.03	0.00	0.10	0.01	0.01
rb18	1.35	40.0	1.55	0.04	0.04	-14%	0.06	0.04	0.00	0.11	0.01	0.05
rb19	1.40	40.0	1.63	0.03	0.03	-16%	0.06	0.03	0.00	0.09	0.01	0.08
rb20	1.45	40.0	1.71	0.03	0.03	-15%	0.05	0.03	0.00	0.08	0.01	0.10
rb21	1.30	42.5	1.57	0.04	0.03	-19%	0.05	0.03	0.01	0.09	0.01	0.10
rb22	1.35	42.5	1.66	0.03	0.03	-14%	0.05	0.03	0.00	0.09	0.01	0.13
rb23	1.40	42.5	1.72	0.03	0.03	-17%	0.05	0.03	0.00	0.08	0.01	0.16
rb24	1.45	42.5	1.83	0.03	0.03	-20%	0.05	0.03	0.00	0.08	0.01	0.18
rb29	1.25	30.0	0.94	0.11	0.11	-5%	0.16	0.03	0.00	0.19	0.03	0.39
rb30	1.25	32.5	1.06	0.10	0.09	-12%	0.15	0.05	0.00	0.20	0.03	0.41
rb31	1.25	35.0	1.17	0.30	0.23	-40%	0.28	0.11	0.03	0.42	0.07	0.40
rb32	1.25	37.5	1.28	0.07	0.04	-17%	0.07	0.06	0.00	0.13	0.02	0.24

rb33	1.25	40.0	1.39	0.01	0.01	-15%	0.05	0.03	0.00	0.08	0.01	0.02
rb34	1.25	42.5	1.49	0.04	0.03	-16%	0.05	0.03	0.01	0.09	0.01	0.07
rb35	1.25	45.0	1.59	0.03	0.02	-17%	0.04	0.03	0.00	0.08	0.01	0.15
rb36	1.20	30.0	0.88	0.15	0.16	-5%	0.19	0.04	0.00	0.23	0.04	0.40
rb37	1.20	32.5	0.99	0.12	0.12	-9%	0.16	0.04	0.00	0.20	0.03	0.41
rb38	1.20	35.0	1.10	0.20	0.17	-21%	0.20	0.08	0.00	0.28	0.05	0.42
rb39	1.20	37.5	1.20	0.43	0.30	-19%	0.24	0.13	0.00	0.37	0.08	0.51
rb40	1.20	40.0	1.31	0.03	0.02	-13%	0.04	0.04	0.00	0.09	0.01	0.07
rb41	1.20	42.5	1.40	0.02	0.02	-15%	0.04	0.03	0.00	0.08	0.01	0.03
rb42	1.20	45.0	1.50	0.02	0.02	-14%	0.05	0.03	0.00	0.08	0.01	0.12
rb43	1.15	30.0	0.81	0.06	0.07	-2%	0.11	0.04	0.00	0.15	0.02	0.40
rb44	1.15	32.5	0.92	0.14	0.14	-5%	0.17	0.04	0.00	0.22	0.03	0.42
rb45	1.15	35.0	1.03	0.19	0.16	-13%	0.19	0.08	0.00	0.28	0.04	0.44
rb46	1.15	37.5	1.13	0.37	0.29	-25%	0.31	0.12	0.00	0.43	0.08	0.44
rb47	1.15	40.0	1.23	0.46	0.33	-22%	0.23	0.11	0.00	0.34	0.08	0.51
rb48	1.15	42.5	1.32	-1.18	-0.78	-60%	0.75	0.33	0.04	1.12	0.00	0.05
rb49	1.15	45.0	1.41	0.02	0.02	-12%	0.04	0.04	0.00	0.08	0.01	0.09
rb50	1.10	30.0	0.75	0.07	0.07	-8%	0.10	0.04	0.00	0.14	0.02	0.39
rb51	1.10	32.5	0.85	0.19	0.17	-5%	0.23	0.06	0.00	0.28	0.05	0.45
rb52	1.10	35.0	0.95	0.18	0.17	-11%	0.21	0.07	0.00	0.28	0.05	0.45
rb53	1.10	37.5	1.05	0.28	0.23	-14%	0.28	0.13	0.00	0.42	0.07	0.47
rb54	1.10	40.0	1.15	0.61	0.44	-28%	0.45	0.21	0.00	0.66	0.12	0.48
rb55	1.10	42.5	1.24	2.21	1.43	-62%	0.91	0.42	0.00	1.33	0.34	0.71
rb56	1.10	45.0	1.32	0.75	0.56	-66%	0.36	0.19	0.12	0.67	0.14	0.68
rb57	1.10	47.5	1.41	0.01	0.00	-17%	0.01	0.04	0.00	0.05	0.01	0.01

Table 6: Results for simulation set rb

Run	v_{imp} [v_{esc}]	θ [$^\circ$]	L [L_{E-M}]	M_S [M_M]	M_{S^*} [M_M]	δf_T	M_D [M_M]				L_D [L_{E-M}]	L_{bound} [L_{E-M}]
							SiO ₂	H ₂ O	Fe	tot.		
tb01	1.30	30.0	1.32	0.11	0.11	-13%	0.17	0.06	0.00	0.23	0.03	0.67
tb02	1.35	30.0	1.38	0.16	0.15	-19%	0.21	0.07	0.00	0.28	0.04	0.66
tb03	1.30	32.5	1.44	0.31	0.24	-21%	0.27	0.14	0.00	0.42	0.07	0.69
tb04	1.35	32.5	1.51	0.39	0.27	-27%	0.21	0.11	0.01	0.33	0.07	0.48
tb05	1.30	35.0	1.56	0.36	0.22	-25%	0.20	0.14	0.00	0.33	0.07	0.65
tb06	1.35	35.0	1.63	0.31	0.14	-38%	0.17	0.15	0.00	0.32	0.06	0.48
tb07	1.40	30.0	1.44	0.22	0.17	-26%	0.20	0.11	0.03	0.33	0.05	0.62
tb08	1.45	30.0	1.51	0.24	0.18	-24%	0.22	0.11	0.02	0.35	0.06	0.60
tb09	1.40	32.5	1.57	0.35	0.23	-26%	0.16	0.10	0.01	0.28	0.06	0.37
tb10	1.45	32.5	1.64	0.09	0.07	-23%	0.15	0.07	0.00	0.22	0.03	0.47
tb11	1.40	35.0	1.70	0.01	0.01	-25%	0.11	0.06	0.00	0.17	0.02	0.32
tb12	1.45	35.0	1.77	0.04	0.04	-22%	0.09	0.04	0.00	0.13	0.02	0.31
tb13	1.30	37.5	1.67	-0.01	0.03	-70%	0.57	0.16	0.13	0.86	0.08	0.30

tb14	1.35	37.5	1.75	0.04	0.04	-18%	0.07	0.04	0.00	0.11	0.02	0.26
tb15	1.40	37.5	1.82	0.04	0.04	-22%	0.07	0.04	0.00	0.11	0.01	0.24
tb16	1.45	37.5	1.90	0.05	0.04	-21%	0.07	0.04	0.00	0.12	0.02	0.22
tb17	1.30	40.0	1.78	0.04	0.03	-24%	0.06	0.05	0.00	0.11	0.01	0.21
tb18	1.35	40.0	1.86	0.05	0.04	-16%	0.06	0.04	0.00	0.11	0.01	0.19
tb19	1.40	40.0	1.94	0.04	0.04	-21%	0.05	0.03	0.00	0.09	0.01	0.16
tb20	1.45	40.0	2.02	0.05	0.04	-23%	0.06	0.03	0.01	0.10	0.01	0.15
tb21	1.30	42.5	1.89	0.04	0.03	-17%	0.05	0.04	0.00	0.09	0.01	0.15
tb22	1.35	42.5	1.97	0.04	0.03	-22%	0.05	0.04	0.01	0.09	0.01	0.13
tb23	1.40	42.5	2.06	0.04	0.03	-24%	0.05	0.04	0.00	0.09	0.01	0.11
tb24	1.45	42.5	2.14	0.04	0.03	-27%	0.05	0.03	0.00	0.09	0.01	0.09
tb29	1.25	30.0	1.26	0.18	0.17	-13%	0.27	0.06	0.00	0.33	0.05	0.69
tb30	1.25	32.5	1.37	0.24	0.20	-19%	0.24	0.11	0.00	0.35	0.06	0.72
tb31	1.25	35.0	1.49	0.88	0.69	-35%	0.35	0.13	0.00	0.48	0.13	0.47
tb32	1.25	37.5	1.60	0.54	0.35	-30%	0.21	0.15	0.00	0.36	0.09	0.69
tb33	1.25	40.0	1.70	0.07	0.07	-51%	0.20	0.12	0.00	0.33	0.04	0.27
tb34	1.25	42.5	1.80	0.04	0.02	-20%	0.05	0.04	0.00	0.10	0.01	0.18
tb35	1.25	45.0	1.90	0.03	0.03	-19%	0.04	0.04	0.00	0.08	0.01	0.11
tb36	1.20	30.0	1.19	0.17	0.16	-13%	0.21	0.07	0.00	0.29	0.04	0.72
tb37	1.20	32.5	1.31	0.21	0.19	-15%	0.24	0.08	0.00	0.32	0.05	0.74
tb38	1.20	35.0	1.41	0.42	0.32	-28%	0.41	0.19	0.00	0.60	0.10	0.75
tb39	1.20	37.5	1.52	0.62	0.43	-28%	0.40	0.20	0.00	0.60	0.12	0.74
tb40	1.20	40.0	1.62	0.41	0.28	-35%	0.16	0.10	0.00	0.26	0.06	0.73
tb41	1.20	42.5	1.72	0.01	0.01	-24%	0.08	0.08	0.00	0.17	0.02	0.22
tb42	1.20	45.0	1.81	0.03	0.02	-13%	0.04	0.04	0.00	0.08	0.01	0.14
tb43	1.15	30.0	1.13	0.14	0.13	-21%	0.15	0.06	0.00	0.21	0.03	0.71
tb44	1.15	32.5	1.24	0.22	0.19	-17%	0.24	0.09	0.00	0.33	0.05	0.77
tb45	1.15	35.0	1.34	0.28	0.23	-18%	0.29	0.12	0.00	0.41	0.07	0.78
tb46	1.15	37.5	1.44	0.84	0.62	-37%	0.68	0.32	0.01	1.00	0.18	0.78
tb47	1.15	40.0	1.54	0.68	0.45	-44%	0.39	0.23	0.00	0.61	0.13	0.77
tb48	1.15	42.5	1.64	1.30	0.77	-66%	0.49	0.23	0.03	0.74	0.19	0.87
tb49	1.15	45.0	1.73	0.14	0.07	-28%	0.08	0.12	0.00	0.19	0.03	0.20
tb50	1.10	30.0	1.07	0.12	0.10	-25%	0.12	0.07	0.00	0.19	0.03	0.72
tb51	1.10	32.5	1.17	0.13	0.11	-22%	0.14	0.07	0.00	0.21	0.03	0.78
tb52	1.10	35.0	1.27	0.14	0.11	-6%	0.15	0.10	0.00	0.25	0.04	0.78
tb53	1.10	37.5	1.37	0.44	0.34	-20%	0.47	0.24	0.00	0.71	0.11	0.82
tb54	1.10	40.0	1.46	0.88	0.64	-35%	0.59	0.30	0.00	0.89	0.17	0.78
tb55	1.10	42.5	1.55	4.05	2.63	-63%	1.47	0.81	0.00	2.29	0.60	1.12
tb56	1.10	45.0	1.64	1.14	0.71	-44%	0.57	0.40	0.03	1.00	0.21	0.95
tb57	1.10	47.5	1.72	1.71	1.28	-64%	0.88	0.42	0.03	1.33	0.29	1.05

Table 7: Results for simulation set tb

Run	v_{imp} [v_{esc}]	θ [$^\circ$]	L [$L_{\text{E-M}}$]	M_{S} [M_{M}]	M_{S^*} [M_{M}]	δf_T	M_D [M_{M}]				L_D [$L_{\text{E-M}}$]	L_{bound} [$L_{\text{E-M}}$]
							SiO ₂	H ₂ O	Fe	tot.		
ib01	1.30	30.0	1.62	0.21	0.15	-22%	0.22	0.14	0.00	0.36	0.05	0.89
ib02	1.35	30.0	1.68	0.34	0.25	-25%	0.34	0.19	0.00	0.53	0.08	0.88
ib03	1.30	32.5	1.74	0.68	0.51	-32%	0.56	0.26	0.05	0.87	0.15	0.95
ib04	1.35	32.5	1.81	0.99	0.76	-39%	0.55	0.26	0.08	0.90	0.18	0.86
ib05	1.30	35.0	1.86	0.61	0.39	-28%	0.31	0.21	0.00	0.53	0.11	0.89
ib06	1.35	35.0	1.93	0.42	0.21	-34%	0.16	0.15	0.00	0.31	0.07	0.70
ib07	1.40	30.0	1.74	0.43	0.34	-32%	0.34	0.16	0.08	0.58	0.10	0.90
ib08	1.45	30.0	1.81	0.38	0.26	-36%	0.28	0.17	0.04	0.49	0.08	0.82
ib09	1.40	32.5	1.87	0.89	0.69	-42%	0.37	0.19	0.10	0.66	0.14	0.72
ib10	1.45	32.5	1.94	0.11	0.06	-34%	0.09	0.08	0.00	0.17	0.03	0.53
ib11	1.40	35.0	2.00	0.06	0.04	-32%	0.09	0.06	0.00	0.15	0.02	0.40
ib12	1.45	35.0	2.07	0.05	0.05	-24%	0.08	0.06	0.00	0.14	0.02	0.48
ib13	1.30	37.5	1.97	0.04	0.03	-32%	0.05	0.06	0.00	0.11	0.01	0.46
ib14	1.35	37.5	2.05	0.03	0.02	-20%	0.05	0.04	0.00	0.09	0.01	0.47
ib17	1.30	40.0	2.08	0.02	0.02	-21%	0.04	0.04	0.00	0.08	0.01	0.44
ib18	1.35	40.0	2.16	0.03	0.03	-24%	0.05	0.04	0.00	0.09	0.01	0.42
ib23	1.40	42.5	2.35	0.04	0.03	-27%	0.05	0.03	0.00	0.09	0.01	0.37
ib28	1.45	45.0	2.55	0.04	0.03	-39%	0.05	0.03	0.00	0.09	0.01	0.32
ib29	1.25	30.0	1.56	0.27	0.24	-16%	0.31	0.10	0.00	0.41	0.07	1.01
ib30	1.25	32.5	1.67	0.45	0.36	-27%	0.49	0.22	0.01	0.71	0.11	1.00
ib31	1.25	35.0	1.79	0.93	0.69	-41%	0.60	0.26	0.09	0.96	0.18	0.96
ib32	1.25	37.5	1.89	0.47	0.29	-28%	0.23	0.17	0.00	0.40	0.08	0.98
ib33	1.25	40.0	2.00	0.02	0.09	-70%	0.52	0.20	0.04	0.75	0.08	0.54
ib34	1.25	42.5	2.10	0.03	0.02	-21%	0.04	0.04	0.00	0.09	0.01	0.42
ib35	1.25	45.0	2.20	0.03	0.02	-14%	0.03	0.04	0.00	0.07	0.01	0.37
ib36	1.20	30.0	1.49	0.16	0.14	-30%	0.17	0.08	0.00	0.25	0.04	1.01
ib37	1.20	32.5	1.61	0.37	0.29	-23%	0.32	0.15	0.00	0.47	0.08	1.06
ib38	1.20	35.0	1.71	0.90	0.70	-30%	0.79	0.33	0.03	1.14	0.20	1.05
ib39	1.20	37.5	1.82	0.94	0.65	-39%	0.54	0.26	0.00	0.80	0.17	1.02
ib40	1.20	40.0	1.92	0.33	0.22	-30%	0.18	0.13	0.00	0.31	0.06	1.02
ib41	1.20	42.5	2.02	-0.00	0.04	-58%	0.30	0.20	0.00	0.50	0.05	0.48
ib42	1.20	45.0	2.11	0.03	0.02	-19%	0.04	0.04	0.00	0.08	0.01	0.39
ib43	1.15	30.0	1.43	0.15	0.11	-32%	0.14	0.09	0.00	0.23	0.04	1.02
ib44	1.15	32.5	1.54	0.23	0.17	-29%	0.20	0.13	0.00	0.33	0.05	1.07
ib45	1.15	35.0	1.64	0.52	0.40	-21%	0.51	0.25	0.00	0.77	0.12	1.08
ib46	1.15	37.5	1.74	1.29	0.99	-38%	1.00	0.39	0.01	1.40	0.26	1.09
ib47	1.15	40.0	1.84	1.01	0.73	-37%	0.52	0.24	0.00	0.76	0.17	1.06
ib48	1.15	42.5	1.93	1.14	0.66	-44%	0.65	0.44	0.05	1.14	0.22	1.09
ib49	1.15	45.0	2.02	1.10	0.94	-78%	0.77	0.44	0.13	1.33	0.23	0.65
ib50	1.10	30.0	1.37	0.17	0.12	-47%	0.16	0.11	0.00	0.27	0.04	1.04

ib51	1.10	32.5	1.47	0.34	0.21	-55%	0.26	0.21	0.00	0.47	0.08	1.12
ib52	1.10	35.0	1.57	0.85	0.56	-58%	0.58	0.34	0.00	0.92	0.17	1.20
ib53	1.10	37.5	1.67	1.35	0.90	-42%	0.56	0.29	0.00	0.86	0.21	0.80
ib54	1.10	40.0	1.76	2.72	1.83	-54%	0.94	0.50	0.00	1.44	0.40	1.00
ib55	1.10	42.5	1.85	1.54	0.84	-50%	0.77	0.52	0.03	1.32	0.28	1.25
ib56	1.10	45.0	1.94	1.34	0.95	-51%	0.75	0.33	0.02	1.10	0.23	1.00
ib57	1.10	47.5	2.02	1.32	0.85	-55%	0.69	0.50	0.06	1.25	0.25	1.09

Table 8: Results for simulation set ib

Run	v_{imp} [v_{esc}]	θ [$^\circ$]	L [$L_{\text{E-M}}$]	M_{S} [M_{M}]	M_{S^*} [M_{M}]	δf_T	M_D [M_{M}]				L_D [$L_{\text{E-M}}$]	L_{bound} [$L_{\text{E-M}}$]
							SiO ₂	H ₂ O	Fe	tot.		
ob01	1.10	25.0	1.46	0.04	0.03	-0%	0.06	0.06	0.00	0.11	0.02	1.16
ob02	1.10	27.5	1.57	0.11	0.08	-16%	0.11	0.10	0.00	0.21	0.03	1.26
ob03	1.10	30.0	1.67	0.26	0.16	-34%	0.22	0.22	0.00	0.44	0.07	1.34
ob04	1.10	32.5	1.78	0.58	0.36	-45%	0.46	0.36	0.00	0.82	0.14	1.43
ob05	1.10	35.0	1.88	1.32	0.89	-52%	1.04	0.61	0.00	1.65	0.29	1.51
ob06	1.10	37.5	1.97	2.52	1.81	-51%	1.66	0.77	0.00	2.43	0.48	1.59
ob07	1.10	40.0	2.05	3.34	2.28	-64%	1.52	0.79	0.00	2.31	0.55	1.65
ob08	1.10	42.5	2.16	1.60	0.86	-50%	0.78	0.71	0.02	1.51	0.30	1.43
ob09	1.10	45.0	2.24	1.28	0.83	-66%	0.83	0.44	0.01	1.29	0.25	1.44
ob10	1.10	47.5	2.33	1.67	1.08	-64%	0.85	0.55	0.05	1.45	0.30	1.42
ob11	1.15	25.0	1.52	0.07	0.06	0%	0.08	0.05	0.00	0.14	0.02	1.18
ob12	1.15	27.5	1.63	0.52	0.27	-33%	0.28	0.29	0.00	0.57	0.10	0.88
ob13	1.15	30.0	1.74	0.34	0.23	-44%	0.27	0.20	0.00	0.48	0.08	1.35
ob14	1.15	32.5	1.84	0.73	0.46	-48%	0.50	0.39	0.00	0.89	0.16	1.43
ob15	1.15	35.0	1.95	1.67	1.02	-42%	0.90	0.71	0.00	1.61	0.32	1.32
ob16	1.15	37.5	2.05	1.67	1.18	-36%	1.05	0.57	0.01	1.63	0.32	1.27
ob17	1.15	40.0	2.15	3.09	2.08	-68%	1.13	0.66	0.00	1.80	0.47	1.33
ob18	1.15	42.5	2.24	1.81	1.30	-69%	1.00	0.44	0.02	1.46	0.31	1.44
ob19	1.15	45.0	2.33	0.11	0.02	-23%	0.00	0.05	0.00	0.05	0.02	0.08
ob20	1.15	47.5	2.42	0.04	0.01	-13%	0.02	0.07	0.00	0.09	0.01	0.61
ob21	1.20	25.0	1.57	0.12	0.11	-17%	0.14	0.06	0.00	0.20	0.03	1.19
ob22	1.20	27.5	1.68	0.25	0.20	-39%	0.24	0.11	0.00	0.34	0.06	1.27
ob23	1.20	30.0	1.80	0.26	0.18	-29%	0.23	0.17	0.00	0.40	0.06	1.31
ob24	1.20	32.5	1.91	0.79	0.45	-38%	0.50	0.49	0.00	0.99	0.17	1.28
ob25	1.20	35.0	2.02	1.46	1.12	-36%	1.19	0.45	0.02	1.66	0.30	1.37
ob26	1.20	37.5	2.12	1.14	0.83	-37%	0.60	0.28	0.00	0.88	0.19	1.30
ob27	1.20	40.0	2.23	0.34	0.20	-44%	0.16	0.16	0.00	0.32	0.06	1.20
ob28	1.20	42.5	2.32	-0.07	-0.04	-65%	0.49	0.28	0.00	0.78	0.07	0.66
ob29	1.25	25.0	1.62	0.15	0.14	-25%	0.17	0.06	0.00	0.23	0.04	1.19
ob30	1.25	27.5	1.74	0.20	0.16	-29%	0.20	0.09	0.00	0.29	0.05	1.25
ob31	1.25	30.0	1.86	0.35	0.24	-32%	0.27	0.19	0.00	0.45	0.08	1.30

ob32	1.25	32.5	1.98	0.98	0.76	-28%	0.95	0.36	0.01	1.32	0.22	1.32
ob33	1.25	35.0	2.09	1.14	0.86	-40%	0.68	0.30	0.04	1.02	0.21	1.23
ob34	1.25	37.5	2.20	0.43	0.26	-30%	0.22	0.16	0.00	0.38	0.08	1.24
ob35	1.30	25.0	1.67	0.15	0.15	-22%	0.18	0.05	0.00	0.23	0.04	1.17
ob36	1.30	27.5	1.80	0.18	0.16	-25%	0.19	0.08	0.00	0.27	0.04	1.22
ob37	1.30	30.0	1.92	0.58	0.45	-23%	0.56	0.24	0.00	0.80	0.13	1.29
ob38	1.30	32.5	2.05	1.24	0.95	-33%	0.92	0.39	0.04	1.34	0.25	1.15
ob39	1.30	35.0	2.16	0.70	0.46	-34%	0.34	0.24	0.00	0.58	0.12	1.14
ob40	1.30	37.5	2.28	-0.17	-0.13	-70%	0.80	0.24	0.16	1.19	0.10	0.75
ob41	1.35	25.0	1.73	0.13	0.13	-15%	0.18	0.05	0.00	0.23	0.03	1.15
ob42	1.35	27.5	1.86	0.34	0.30	-15%	0.36	0.10	0.00	0.46	0.07	1.23
ob43	1.35	30.0	1.99	0.74	0.58	-29%	0.74	0.29	0.04	1.07	0.17	1.22
ob44	1.35	32.5	2.11	1.12	0.84	-37%	0.62	0.30	0.09	1.01	0.20	1.07
ob45	1.40	25.0	1.78	0.12	0.12	-12%	0.18	0.06	0.00	0.23	0.03	1.16
ob46	1.40	27.5	1.92	0.32	0.28	-18%	0.39	0.13	0.00	0.52	0.08	1.18
ob47	1.40	30.0	2.05	0.94	0.73	-31%	0.73	0.25	0.10	1.08	0.19	1.16
ob48	1.40	32.5	2.18	0.26	0.21	-51%	0.26	0.13	0.02	0.41	0.06	0.79
ob49	1.45	25.0	1.83	0.29	0.28	-13%	0.35	0.06	0.00	0.41	0.07	1.16
ob50	1.45	27.5	1.97	0.47	0.36	-28%	0.46	0.19	0.01	0.66	0.11	1.15
ob51	1.45	30.0	2.11	0.85	0.66	-38%	0.48	0.19	0.11	0.77	0.15	1.11
ob52	1.45	32.5	2.25	0.29	0.11	-56%	0.08	0.10	0.00	0.18	0.04	0.19

Table 9: Results for simulation set ob

Run	v_{imp} [v_{esc}]	θ [$^\circ$]	L [$L_{\text{E-M}}$]	M_S [M_M]	M_{S^*} [M_M]	δf_T	M_D [M_M]				L_D [$L_{\text{E-M}}$]	L_{bound} [$L_{\text{E-M}}$]
							SiO ₂	H ₂ O	Fe	tot.		
pb01	1.10	25.0	1.79	0.06	0.02	-7%	0.04	0.10	0.00	0.15	0.02	1.49
pb02	1.10	27.5	1.90	0.19	0.09	-16%	0.18	0.23	0.00	0.41	0.06	1.59
pb03	1.10	30.0	2.00	0.53	0.32	-29%	0.48	0.38	0.00	0.86	0.14	1.68
pb04	1.10	32.5	2.11	1.00	0.65	-43%	0.85	0.54	0.01	1.40	0.23	1.75
pb05	1.10	35.0	2.21	1.84	1.28	-50%	1.47	0.78	0.00	2.25	0.40	1.80
pb06	1.10	37.5	2.30	3.04	2.11	-57%	1.71	0.91	0.01	2.62	0.55	1.91
pb07	1.10	40.0	2.40	3.47	2.41	-73%	1.35	0.69	0.00	2.04	0.53	1.97
pb08	1.10	42.5	2.49	1.68	1.05	-60%	1.08	0.56	0.04	1.68	0.33	1.83
pb09	1.15	25.0	1.84	0.08	0.05	-5%	0.08	0.08	0.00	0.17	0.02	1.52
pb10	1.15	27.5	1.96	0.29	0.19	-24%	0.29	0.24	0.00	0.53	0.08	1.61
pb11	1.15	30.0	2.07	0.71	0.48	-44%	0.62	0.38	0.00	1.00	0.17	1.70
pb12	1.15	32.5	2.18	1.55	1.09	-49%	1.36	0.67	0.00	2.03	0.35	1.77
pb13	1.15	35.0	2.28	2.70	1.96	-51%	1.74	0.75	0.00	2.49	0.50	1.84
pb14	1.15	37.5	2.38	2.99	2.05	-65%	1.40	0.76	0.00	2.16	0.50	1.91
pb15	1.15	40.0	2.48	2.84	1.92	-77%	1.07	0.53	0.00	1.60	0.43	1.98
pb16	1.15	42.5	2.57	1.28	0.84	-59%	0.88	0.48	0.02	1.38	0.26	1.59
pb17	1.20	25.0	1.90	0.16	0.12	-16%	0.16	0.12	0.00	0.28	0.04	1.54

pb18	1.20	27.5	2.02	0.41	0.31	-34%	0.35	0.21	0.00	0.56	0.09	1.63
pb19	1.20	30.0	2.13	0.87	0.59	-48%	0.71	0.43	0.00	1.15	0.19	1.69
pb20	1.20	32.5	2.24	2.16	1.50	-43%	1.38	0.78	0.01	2.17	0.41	1.67
pb21	1.20	35.0	2.35	1.39	0.99	-40%	0.88	0.47	0.00	1.35	0.26	1.62
pb22	1.20	37.5	2.46	0.84	0.52	-43%	0.40	0.29	0.00	0.70	0.15	1.64
pb23	1.20	40.0	2.56	1.84	1.24	-53%	1.03	0.57	0.02	1.62	0.33	1.58
pb24	1.25	25.0	1.95	0.26	0.22	-33%	0.25	0.10	0.00	0.35	0.06	1.54
pb25	1.25	27.5	2.07	0.39	0.29	-41%	0.35	0.21	0.00	0.56	0.09	1.60
pb26	1.25	30.0	2.19	0.91	0.70	-33%	0.98	0.38	0.01	1.36	0.22	1.61
pb27	1.25	32.5	2.31	1.62	1.23	-35%	1.26	0.50	0.01	1.77	0.32	1.60
pb28	1.25	35.0	2.42	1.02	0.71	-38%	0.53	0.29	0.00	0.81	0.17	1.59
pb29	1.25	37.5	2.53	0.59	0.37	-36%	0.44	0.30	0.01	0.75	0.13	1.47
pb30	1.30	25.0	2.00	0.23	0.20	-29%	0.23	0.09	0.00	0.32	0.05	1.51
pb31	1.30	27.5	2.13	0.42	0.31	-33%	0.40	0.23	0.00	0.63	0.10	1.56
pb32	1.30	30.0	2.26	1.14	0.90	-30%	1.06	0.39	0.03	1.48	0.25	1.56
pb33	1.30	32.5	2.38	1.21	0.91	-33%	0.75	0.32	0.00	1.07	0.22	1.54
pb34	1.30	35.0	2.50	0.52	0.31	-30%	0.25	0.22	0.00	0.47	0.09	1.46
pb35	1.30	37.5	2.61	-0.27	-0.25	-65%	0.61	0.24	0.02	0.87	0.06	0.87
pb36	1.35	25.0	2.06	0.21	0.18	-25%	0.21	0.10	0.00	0.31	0.05	1.49
pb37	1.35	27.5	2.19	0.59	0.47	-29%	0.57	0.27	0.00	0.84	0.14	1.53
pb38	1.35	30.0	2.32	1.40	1.10	-31%	1.09	0.37	0.06	1.52	0.28	1.52
pb39	1.35	32.5	2.44	0.65	0.45	-29%	0.40	0.21	0.00	0.61	0.12	1.48
pb40	1.40	25.0	2.11	0.27	0.23	-24%	0.26	0.13	0.00	0.38	0.06	1.49
pb41	1.40	27.5	2.25	0.84	0.69	-27%	0.84	0.28	0.02	1.15	0.19	1.49
pb42	1.40	30.0	2.38	1.04	0.79	-35%	0.62	0.25	0.09	0.95	0.19	1.41
pb43	1.45	25.0	2.16	0.48	0.43	-14%	0.47	0.12	0.00	0.59	0.10	1.48
pb44	1.45	27.5	2.30	1.21	0.96	-27%	1.01	0.33	0.08	1.41	0.25	1.44
pb45	1.50	25.0	2.22	0.54	0.47	-20%	0.61	0.18	0.00	0.79	0.12	1.41
pb46	1.50	27.5	2.36	0.86	0.67	-31%	0.58	0.20	0.10	0.88	0.16	1.35

Table 10: Results for simulation set pb

Chapter 8

Application: Mars-scale collisions

This series of two papers aims at providing the bases for a study of the long term effects of giant impacts on planetary interiors. Here we propose a new method to couple SPH modelling of the collision phase, where velocities are high and shocks occur, followed by a thermochemical model for the long term evolution of the internal structure of the planet. The objects are a differentiated, 1000 km radius impactor colliding with a Mars-like target (radius ≈ 3400 km) at mutual escape velocity. This scenario is a candidate to explain the martian surface dichotomy (Wilhelms and Squyres 1984; Marinova et al. 2008).

The first paper discusses the different possibilities of the SPH technique (the inclusion of solid rheology, the equation of state – ANEOS or Tillotson –, the numerical method to compute the density as well as the impact geometry) and their implications onto the results immediately after the collision. We in particular find that solid plays a role at least as important as the equation of state for material and temperature distribution, even at this scale. At the end of the SPH phase, results are first transferred from its Lagrangian description into an Cartesian grid by means of SPH interpolation.

The second paper treats of the transfer between the two models and the formation of crust on longer time scales (~ 0.5 Myr).

SPH calculations of Mars-scale collisions: the role of the Equation of State, material rheologies, and numerical effects

Alexandre Emsenhuber^{a,*}, Martin Jutzi^a, Willy Benz^a

^a*Physikalisches Institut & Center for Space and Habitability, Universität Bern, Gesellschaftsstrasse 6, CH-3012 Bern, Switzerland*

Abstract

We model large-scale (≈ 2000 km) impacts on a Mars-like planet using a Smoothed Particle Hydrodynamics code. The effects of material strength and of using different Equations of State on the post-impact material and temperature distributions are investigated. The properties of the ejected material in terms of escaping and disc mass are analysed as well. We also study potential numerical effects in the context of density discontinuities and rigid body rotation. We find that in the large-scale collision regime considered here (with impact velocities of 4 km/s), the effect of material strength is substantial for the post-impact distribution of the temperature and the impactor material, while the influence of the Equation of State is more subtle and present only at very high temperatures.

Keywords: Terrestrial planets, impact processes, interiors

1. Introduction

Giant impacts occurring at the end stages of planet formation define the properties of the final planets and moons. Examples include Mercury's anomalously thin silicate mantle (Benz et al., 1988, 2007; Asphaug and Reufer, 2014), the origin of the Earth's Moon (Hartmann and Davis, 1975; Cameron and Ward, 1976; Canup and Asphaug, 2001; Canup, 2004, 2012; Ćuk and Stewart, 2012; Reufer et al., 2012) or the formation of the Pluto-Charon system (Canup, 2005, 2011). Smaller, but still planet-scale collisions were proposed for the formation of the martian dichotomy (Wilhelms and Squyres, 1984; Frey and Schultz, 1988; Andrews-Hanna et al., 2008; Nimmo et al., 2008; Marinova et al., 2008, 2011). Numerical simulations of such giant impact scenarios are performed using shock physics codes, which are often based on the smoothed particle hydrodynamics (SPH) method. In such simulations of planet-scale collisions it is typically assumed that material strength is negligible due to large overburden pressures caused by self-gravitation. However, it was found in previous studies (e.g. Jutzi, 2015) that for collisions at 100 km to 1000 km scale, the effect of material strength can still be

*Corresponding author

Email addresses: alexandre.emsenhuber@space.unibe.ch (Alexandre Emsenhuber), martin.jutzi@space.unibe.ch (Martin Jutzi), willy.benz@space.unibe.ch (Willy Benz)

very important. The impactor size range for which the assumption of purely hydrodynamic behaviour is justified has not yet been studied systematically. Other uncertainties in giant impact simulations are related to the Equation of State (EoS) models. Often used EoS are the simple Tillotson (Tillotson, 1962) EoS (e.g. Marinova et al., 2008, 2011) or the more sophisticated (M-)ANEOS (Thompson and Lauson, 1972; Melosh, 2007). Last but not least, there are potential numerical issues that have to be added to the uncertainties. Concerning the SPH method, known numerical issues are related to surface and contact discontinuities (e.g. Hosono et al., 2013; Reinhardt and Stadel, 2017) or rotational instabilities in rigid body rotations (e.g. Speith, 2006).

In this study, we focus on large-scale (≈ 2000 km) impacts on a Mars-like planet. The conditions studied here are chosen to be quite general, but at the same time they also cover a range of possible dichotomy forming events (Marinova et al., 2008). We want to assess the relative importance of the effects mentioned above (i.e., material strength; choice of EoS; numerical issues) in collision simulations of such scale. This knowledge is important in order to be able to make an educated choice of the material models and numerical methods, and to know their limitations.

Collisions are modelled using an updated SPH code (Reufer et al., 2012), which includes self-gravity, a newly implemented strength model (following Jutzi, 2015) and various EoS (Tillotson and M-ANEOS). We investigate the effects of the above mentioned material properties (namely material strength and the EoS models) on the outcome of the collisions for different impact geometries. We focus on the material and temperature distributions in the final planet but also analyse the properties of the ejected material (orbiting and unbound). Finally, potential numerical effects are studied as well. We investigate the known SPH issue in the case of rigid body rotation. We also consider different schemes to compute the density, in order to investigate potential numerical issues at discontinuities (such as the free surface and the core-mantle boundary).

A subset of the SPH calculations presented here is coupled with thermochemical simulations of planetary interiors in a companion paper (Golabek et al., 2017). The effects of the different models on the long-term evolution (over a time period of about 0.5 Myr) and the crust formation will be discussed there.

In section 2 we describe our modeling approach and discuss in detail the implemented strength model and its coupling with the EoS models. The initial conditions (target and projectile properties and impact geometry) are detailed in section 3. In section 4, we present the results of our simulations using different material models and numerical schemes, followed by a discussion and conclusions in section 5.

2. Modelling approach

We use a smoothed particle hydrodynamics (SPH) code (e.g. Benz and Asphaug, 1994; Reufer et al., 2012; Jutzi, 2015) to model the impact event. The code used here is based on the SPHLATCH code developed by Reufer et al. (2012). It includes a newly implemented pressure and temperature dependent shear strength model, as described below, which is appropriate for the large scale collisions considered here. To study smaller scale collisions

	ANEOS		Tillotson	
	iron	silicate	iron	olivine
G [GPa]	76	44.4	76	72
σ_M [GPa]	0.68	3.5	0.68	3.5
u_m [J/kg]	-	-	$9.2 \cdot 10^5$	$3.4 \cdot 10^6$
T_m [K]	-	-	920	3400

Table 1: Material parameters for the solid rheology model. G is the shear modulus. σ_M is the von Mises plastic limit. Melting temperature T_m is computed from u_m using equation (11).

in geological materials, we use a different code, which also includes a tensile fracture and a porosity model (see Jutzi, 2015, for details).

SPH uses a Lagrangian representation where material is divided into particles. Quantities are interpolated (‘smoothed’) by summing over surrounding particles (called neighbours) according to

$$B(\vec{x}) = \sum_i B_i W(\vec{x} - \vec{x}_i, h_i) V_i \quad (1)$$

where B_i represents the quantity (field variable) to be interpolated, and \vec{x}_i , h_i and V_i are the position, smoothing length, and volume of particle i , respectively. $W(\vec{x}, h)$ is a smoothing kernel, which has the propriety to vanish if $\|\vec{x}\| > 2h$, so that the hydrodynamic variables (pressure, density, stress tensor) are integrated over a local group of neighbouring particles. In our simulations, we use a 3D cubic spline kernel (Monaghan and Lattanzio, 1985).

This interpolation scheme is used in SPH to solve the relevant differential equations. In standard SPH, the density is computed by direct summation (equation 1). We refer to this method as *density summation* through this article. Alternatively, it can be computed by using the changing rate of density, which is given by the continuity equation:

$$\frac{D\rho}{Dt} + \rho \frac{\partial v_x}{\partial x} + \rho \frac{\partial v_y}{\partial y} + \rho \frac{\partial v_z}{\partial z} = 0 \quad (2)$$

where D/Dt stands for the substantive time derivative. We call it *density integration*. A similar equation gives the time derivative of the smoothing length:

$$\frac{Dh}{Dt} + h \frac{\partial v_x}{\partial x} + h \frac{\partial v_y}{\partial y} + h \frac{\partial v_z}{\partial z} = 0 \quad (3)$$

Thus the smoothing length grows in sparse regions and shrinks in dense regions, so that the number of neighbours within $2h$ is ≈ 50 .

Body accelerations are the result of the pressure gradient, and for this we use the pressure as computed from an equation of state (EoS) (see below), which is a function $P(\rho, u)$ of density ρ (see equation 2) and internal energy u . For solid materials the pressure gradient is generalised into a stress tensor (Benz and Asphaug, 1994) with the resulting equation of motion given by:

$$\frac{Dv_a}{Dt} = \frac{1}{\rho} \frac{\partial \tau_{ab}}{\partial x_b} \quad (4)$$

The stress tensor is defined as

$$\tau_{ab} = -P\delta_{ab} + \sigma_{ab} \quad (5)$$

where P is the pressure, δ_{ab} is the Kronecker symbol and σ_{ab} is the traceless deviatoric stress tensor. The time evolution of σ_{ab} is computed adopting Hooke's law as in Benz and Asphaug (1994, 1995). In the limit of zero deviatoric stress this reduces to the familiar pressure-gradient acceleration. Energy conservation now reads

$$\frac{Du}{Dt} = \frac{1}{\rho} \tau_{\alpha\beta} \dot{\epsilon}_{\alpha\beta} \quad (6)$$

with $\dot{\epsilon}_{\alpha\beta}$ being the strain rate tensor.

In standard SPH, the computation of the strain and rotation rate tensors fails to conserve angular momentum in rigid body rotations. Following the approach by Speith (2006), we use a correction tensor in the computation of the velocity derivatives, which allows conservation of angular momentum at the cost of an additional computation step.

Equations (4) and (5) describe an entirely elastic material. To model plastic behaviour we use a Drucker-Prager-like yield criterion (e.g. Collins et al., 2004; Jutzi, 2015). The model has one yield strength σ_i , corresponding to intact material, and another σ_d corresponding to completely fragmented material:

$$\sigma_i = C + \frac{\mu_i P}{1 + \mu_i P / (\sigma_M - C)} \quad (7)$$

$$\sigma_d = \mu_d P \quad (8)$$

where C is the cohesion (yield strength as zero pressure), σ_M is the von Mises plastic limit, and μ_i and μ_d are the coefficients of friction for intact and completely damaged material, respectively. We set them as $\mu_i = 2$ and $\mu_d = 0.8$ as in Collins et al. (2004). Note that σ_d is limited to $\sigma_d < \sigma_i$ at high pressures. For the large-scale collisions considered here cohesion and tensile strength are negligible due to the large gravity-induced lithostatic stress (see e.g. Jutzi et al., 2015). We therefore set $C = 0$. However, shear strength (limited by σ_M) is still important and cannot be neglected, as we shall see below.

The yield strength of intact material is a function of temperature. To take this into account, we adopt the same relation as in Collins et al. (2004):

$$\sigma \rightarrow \sigma \tanh \left(\xi \left(\frac{T_m}{T} - 1 \right) \right) \quad (9)$$

where ξ is a material constant which we set to $\xi = 1.2$, T is the temperature and T_m is the corresponding liquidus temperature (see below). If $T > T_m$ the material is molten and we set $\sigma = 0$. Finally, if the measure of the stress state, the second invariant of the deviatoric stress tensor

$$\sigma_{II} = \sqrt{\frac{1}{2} \sigma_{ab} \sigma_{ab}} \quad (10)$$

exceeds σ , the components of the deviatoric stress tensor are reduced by a factor σ / σ_{II} . The parameters for the solid rheology model are provided in table 1.

Name	Description	Value
ρ_0	Reference density	7850 kg/m ³
T_0	Reference temperature	0
p_0	Pressure at the reference point	0
B_0	Bulk modulus at the reference point	$1.45 \cdot 10^{11}$ Pa
T_{Debye}	Reference Debye temperature	464 K
γ_{max}	Limiting value of the Gruneisen coefficient	2/3
E_{sep}	Zero temperature separation energy	$2 \cdot 10^8$ J/kg
T_{melt}	Melting temperature	1809 K
H_f	Heat of fusion	$2.471 \cdot 10^5$ J/kg
$\rho_{\text{liq}}/\rho_{\text{solid}}$	Ratio of liquid to solid density at melt point	0.955

Table 2: Material parameters for iron with ANEOS equation of state. Other parameters are set to zero.

To complete the set of equations, an equation of state providing a relation between pressure, temperature and density is needed. We use either Tillotson (Tillotson, 1962) or (M-)ANEOS (Thompson and Lauson, 1972; Melosh, 2007). The Tillotson equation of state provides both the pressure P and the speed of sound as output, but it does not give the temperature directly, so as an approximation we use the internal energy as a proxy for temperature by dividing by the heat capacity

$$T = u/c_p \quad (11)$$

In this case equation (9) is modified to use u and u_m instead of T and T_m respectively, and u_m is treated as a material constant independent of pressure. Iron parameters are from Tillotson (1962) (also in Melosh, 1989) and the ones for olivine from Marinova et al. (2008).

For a more physical computation of temperature, and to handle phase transitions in a more thermodynamically consistent way than is done with Tillotson EoS, we use ANEOS (Thompson and Lauson, 1972) for iron with the parameters provided in table 2, and M-ANEOS (Melosh, 2007) for silicates. These equations of state provide numerous output variables including the temperature and phase information (e.g. melt and vapor fraction). Depending on the parameters used in the equation of state, this phase information can be given in different ways. For iron, it can be used to infer the melting temperature at a given pressure. However, this is not the case for silicates, for which we apply the same procedure as used in Senft and Stewart (2009) to obtain the melting temperature at a given pressure.

It is important to point out that neither the Tillotson nor the ANEOS equation of state include the latent heat of melting and therefore, temperatures above the melt temperature are overestimated.

Shocks occur when the impact speed (or particle velocity) exceeds the sound speed in the medium. If not treated properly, this can lead to particle interpenetration and other non-physical effects. We use a standard artificial viscosity term (Monaghan, 1992) that deposits internal energy and momentum behind the shock in a manner that is consistent with the Hugoniot shock relations (c.f. Melosh, 1989) but spread out over several smoothing lengths.

In addition to the body force accelerations given by equation (4), we also compute the accelerations due to self-gravity, using a tree-code method (Barnes and Hut, 1986).

The set of equations described above provides the time dependence of the physical quantities, which are then integrated using a prediction-correction scheme (Press, 2002). For a more detailed description of the method see e.g. Jutzi et al. (2015).

3. Initial conditions

3.1. Setup

We perform a series of SPH collision models, where we use a Mars-mass target body ($r = 3400$ km) and an impactor with 1000 km radius. We use different EoS (ANEOS or Tillotson), material rheologies (solid or fluid) and numerical schemes (density summation or integration), in order to study the effects on the collision outcome and to assess their relative importance. For each combination, we use two impact angles: 0° (head-on) or 45° (oblique), which gives a total of 16 simulations. The mutual escape velocity (Asphaug, 2010) defines the impact speed. As a nominal case, we define the simulation with ANEOS, solid rheology, integrated density and oblique impact angle.

The target and impactor both start with a Mars-like internal structure with an iron core radius half of the body radius, while SiO₂ comprises the bodies' mantles. The use of SiO₂ to represent Mars' basaltic mantle is a simplified but reasonable assumption, given available equation of state information. Note also that the crust of the target is not resolved at these large scales and is not explicitly included in the model. For simulations using Tillotson EoS, each layer is initially isothermal; iron core temperature is fixed to $T_{\text{Fe}} = 1800$ K and mantle to $T_{\text{Si}} = 1500$ K. For the simulations with ANEOS, an isentropic profile is used for which core's central temperature is 1800 K and for the silicate at the core-mantle boundary it is 1500 K. The choice of these values is explained in Golabek et al. (2017).

We begin by setting up self-gravitating, hydrostatically-equilibrated planets, starting with one-dimensional (1D) spherically symmetric bodies modelled using a Lagrangian hydrocode (Benz, 1991) with the same EoS as in the SPH model. This structure is divided in 1 000 cells (100 for the impactor) of equal mass. Cell boundaries according to the force balance between self-gravity and pressure (including a damping term). This profile is evolved until hydrostatic equilibrium is reached so that radial velocities are small (less than 1% of the escape velocity). Afterwards we transfer the 1D radial profile onto SPH particles that are placed onto a 3D lattice. Parameters of each particle are copied from the profile according to the radius. As particles are equally spaced on the lattice, variation of density is taken into account by adjusting the particle mass. The spherical SPH bodies are then also evolved in an initialising step to reach a hydrostatic equilibrium and negligible radial velocities. Thus the SPH simulations start with two relaxed differentiated spherical planets approaching from several radii away; they get tidally deformed prior to the impact.

The SPH simulations are performed with a resolution of about one million particles for the target. The number of particles for the impactor is scaled according to the mass ratio between the two objects, so that particle spacing h is approximately constant, for the

greatest numerical accuracy during the collision. The corresponding smoothing length is then approximately 60 km for both bodies.

3.2. Initial radial profiles

Initial radial profiles of density, pressure and temperature are shown in figures 1 and 2 for the impactor and target respectively. For the cases with the Tillotson EoS, the internal energy is being evolved during the equilibration phase, hence the spread in temperature. The comparison with a case where this value is kept fixed is discussed later in section 4.3.3. The 1D profiles for the two different approaches to compute the density (density sum and density integration) are identical as the distinction only happens during the SPH phase itself.

There is a noticeable difference in the density between the cases with a different EoS: iron has higher density with ANEOS and the opposite happens for silicate. The density contrast at the core-mantle boundary is thus higher when using ANEOS. Since the objects have the same mass in the two cases, their radius is affected by this density variation and we obtain about 3440 km using ANEOS and 3290 km using Tillotson, which makes a relative difference of the radii around 4 %. It is known that standard SPH has problems handling sharp density changes, at boundaries between materials and at the surface. We see artificial numerical effects at these locations. With density summation, particles beyond the boundary enter in the SPH sum (equation 1) and thus smooth the discontinuity. Particles in this region then have a slightly different density. At the surface, the effect is due to the lack of close-by particles (see Reinhardt and Stadel, 2017 for an improved scheme). The density variation is reflected in pressure and temperature. Although in the case of density integration there is no such summation involved to compute the density, there are still some artificial effects (oscillations) at the boundaries. More sophisticated ways to deal with discontinuous boundaries in SPH have been developed recently (e.g. Hosono et al., 2013) and shall be implemented in our code for future studies.

However, as we shall see below, the amplitude of the unphysical 'noise' in the initial profiles is small enough not to affect significantly the outcome of the collision simulations.

4. Results

4.1. Nominal case

We show a time series of the nominal case along with the corresponding fluid case in figure 3. Shown are the post-impact material and temperature distributions. The simulations start roughly two hours before the first snapshot. Due to the angular momentum transferred to the target by the impact, the target begins to rotate after a few hours, hence the impact location is shifted by $\sim 180^\circ$ between the two last snapshots. One can note the impactor's tidal deformation before the impact mainly in the fluid case. The effect of the material rheology leads to significant differences in terms of the post-impact material and temperature distribution. Another notable difference is the degree of the impact induced target oscillation, which is much stronger in the fluid case (see snapshots at 3 and 4 h).

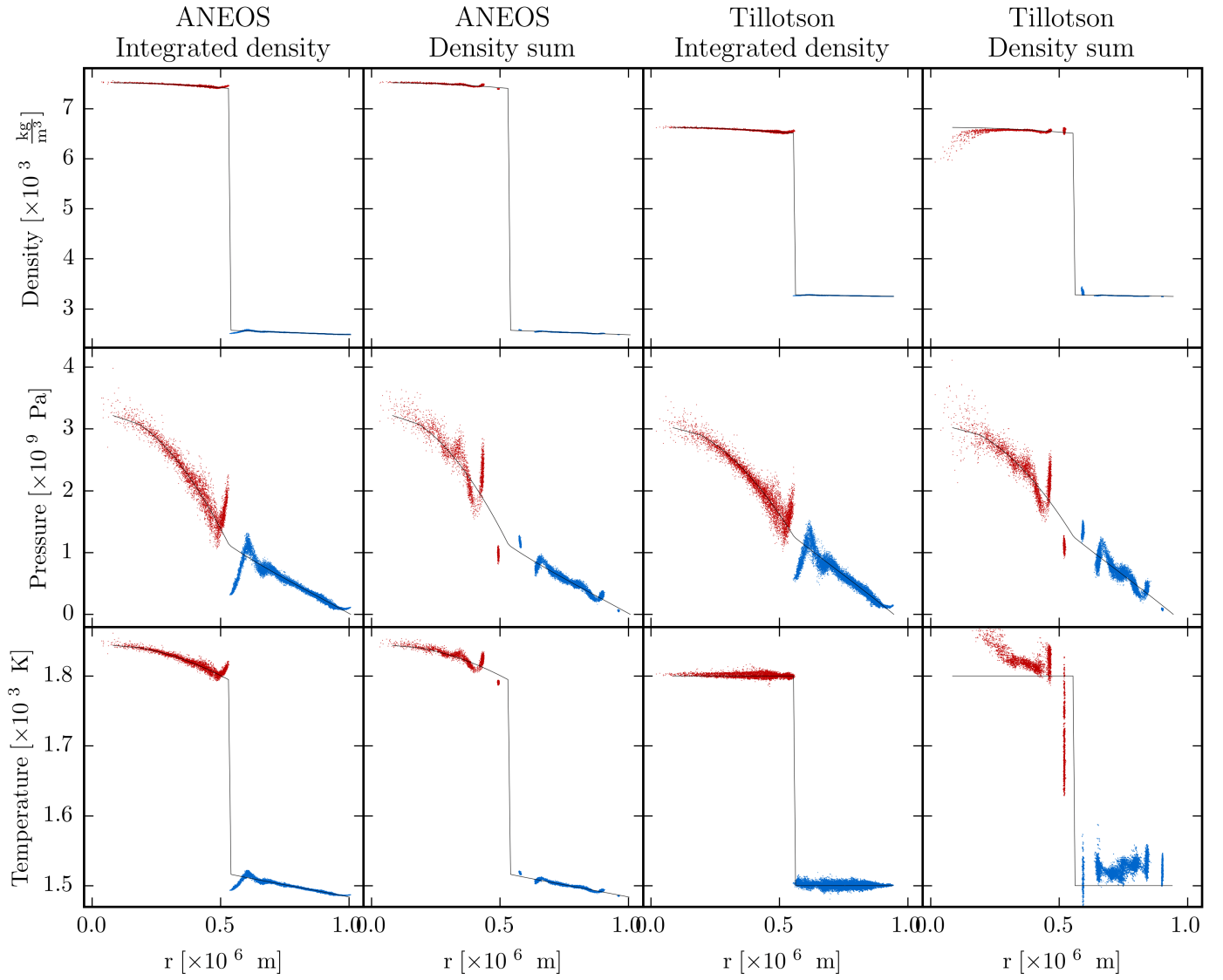


Figure 1: Initial profiles of the different impactors used in this study. The 1D profile is depicted by the black line. Each point is one SPH particle and its color represents the material: red for iron and blue for silicate.

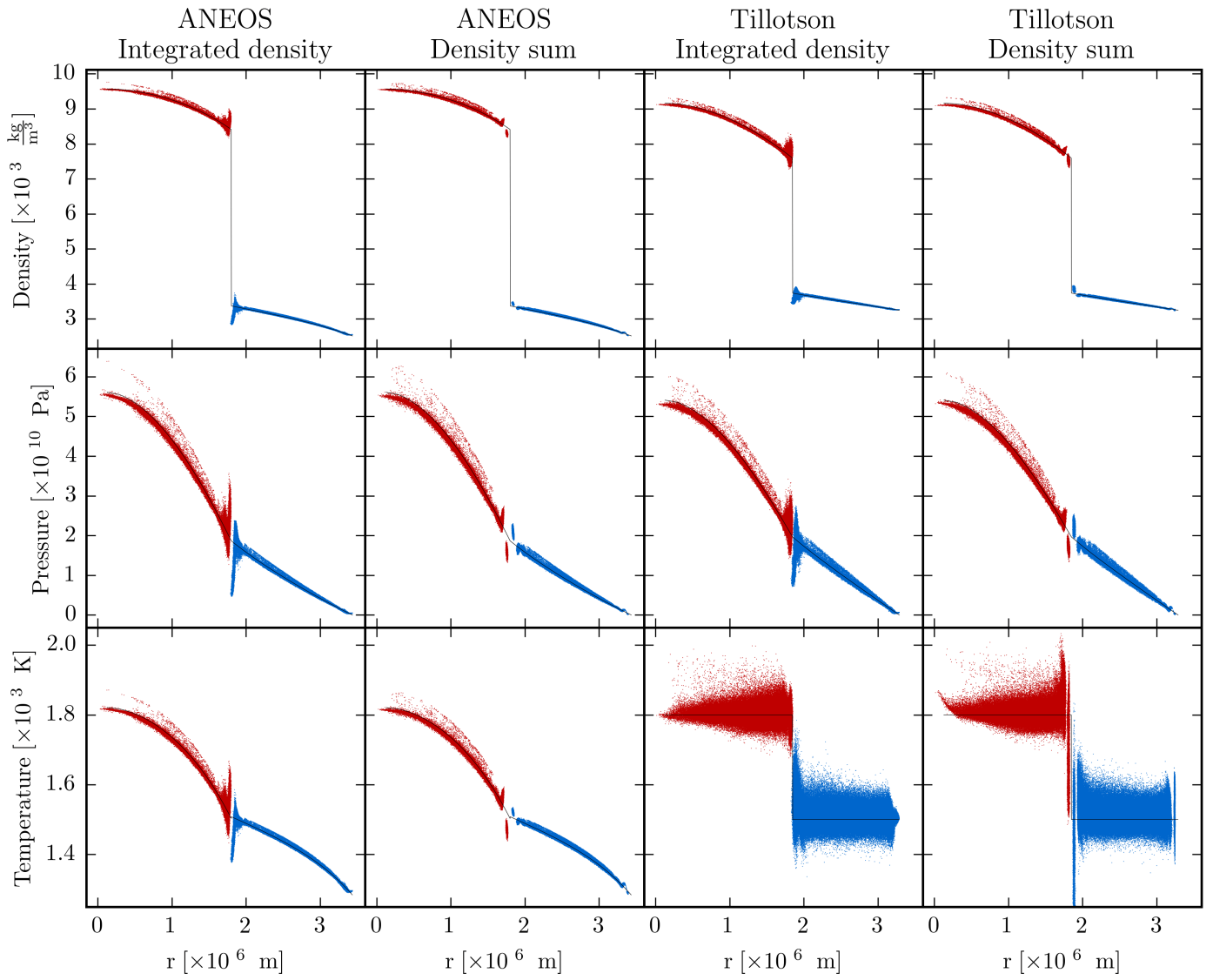
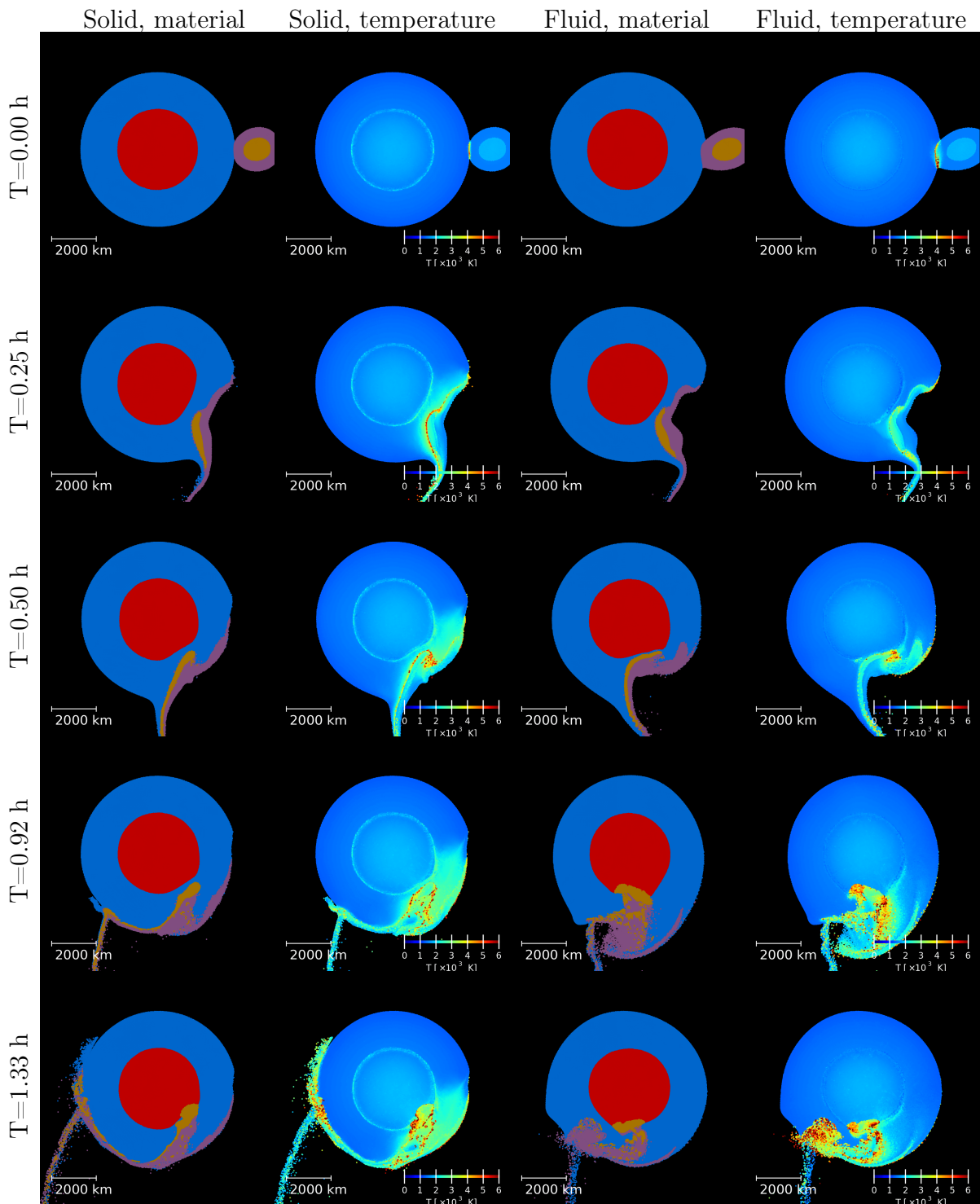


Figure 2: Initial profiles of the different targets used in this study.



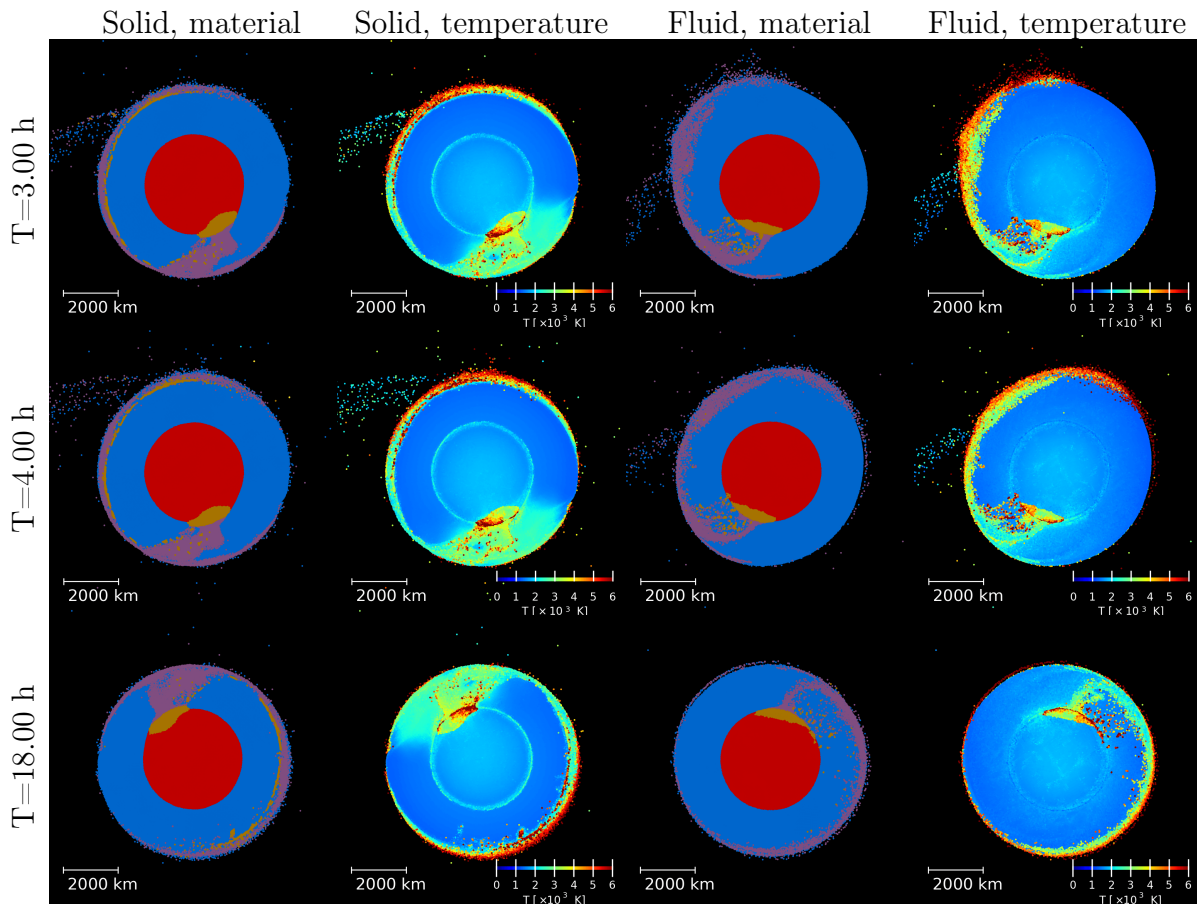


Figure 3: Time series showing material distribution for the nominal case (45° , ANEOS, solid, integrated density; two left columns) and the corresponding fluid case (two right columns). Impactor's trajectory is clockwise. This is a slice of 1000 km depth inside the impact plane. Plots are centered on the center of mass of the main body. On material plots, colour represents the type and origin: blue is target's mantle, purple impactor's mantle, red target's core and yellow impactor's core.

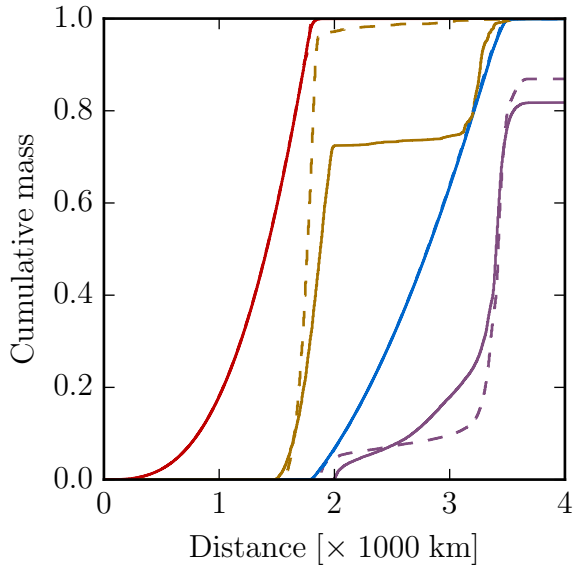


Figure 4: Cumulative mass distribution at the end of the simulation as function of radius. Colour represents material type and origin: red is target’s core, yellow impactor’s core, blue target’s mantle and purple impactor’s mantle, as for material plots in figure 3. Solid lines depict the run with solid rheology and dashed lines are for fluid rheology.

The heat generated by the impact is spread out over a broader region with solid rheology compared to the fluid one. Already at $t = 0.25$ h the higher temperature zone extend to several hundreds of kilometres away from the contact zone and expands until covering a wide region at the end of our simulations. With fluid rheology only the contact zone has high temperature material at the beginning and towards the end only impactor material retains these high temperatures. Note that the annulus of warm material (~ 3000 K) that forms at the target’s core-mantle boundary with solid rheology is not due to the impact but is an artificial feature caused by the set up routine. The small remaining velocities (on the order of 10 m/s) at the beginning of the impact simulation, when forces are enabled and the damping term removed are sufficient to create instabilities that lead to internal energy increase due to the artificial viscosity.

At early times, the impactor does not penetrate as deep inside the target with solid rheology as in the fluid case (see snapshots at 0.50 h and 0.92 h).

To get a better overview of the location where impactor material is deposited inside the target at the end of the simulation, we show a cumulative mass plot against radius in figure 4. The curves are normalised by the total mass of each material.

Note that some of the impactor’s silicate material is still orbiting around the body or has been ejected. This accounts for 13 wt% and 18 wt% for the fluid and solid rheologies respectively. In both cases, about one sixth of this material is still bound whereas the remaining is on an escaping orbit.

There are significant differences for impactor’s material distribution between the two

rheologies. 27 wt% of impactor’s core remains inside the mantle with solid rheology whereas this value falls to 3 wt% for fluid rheology. The remaining lies at the target’s core-mantle boundary. The impactor’s silicate shows a different behaviour. For fluid rheology, there is a small part close to the core-mantle boundary, some inside the target’s mantle and the majority close to the surface. For solid rheology, there is one half distributed inside the mantle and the other half close to the surface.

4.2. Comparison of EoS and material rheologies

The results from our series of 16 simulations, using different material rheologies, EoS and numerical schemes are shown in figure 5 for oblique cases and in figure 6 for head-on ones. The differences between density integration and summation will be discussed in section 4.3.2. Temperature and energy distributions for four of these cases (oblique impacts; density integration) are provided in figure 7. Note that our nominal case and its fluid counterpart that were discussed in the previous section are shown again in the first row of figure 5 (ANEOS; integrated density) and with the black lines on figure 7.

At first look, we note that the differences (concerning material and temperature distribution) discussed in the previous section between the runs with rheologies are also present in the simulations using different EoS and numerical techniques (density computation). The more pronounced temperature increase around the impact zone with solid rheology is noticeable on figure 7 between 2000 and 3000 K; it is about 10 – 20 wt% for ANEOS and a bit less for Tillotson.

The differences between the runs with different EoS are more subtle. For instance, using the Tillotson EoS, the impactor’s particles close to the surface have higher temperatures. This effect appears both in figures 5 and 6 as well as in 7. In figure 7, the curves for the two EoS diverge above about 4000 K, whereas the energy distribution remains similar. ANEOS includes the latent heat of vaporisation which our simple conversion formula (eq. 11) for Tillotson neglects. Hence the high temperatures are overestimated with Tillotson. It should be noted that for silicate, neither EoS takes the latent heat of melting into account. One can also see in figure 7 that the behaviour at low temperature depends on the initial profile, and that almost all mantle gets a small temperature increase (of the order of hundred kelvins).

When looking at head-on cases, again the same general features appear. Hot surface material is now located directly above the impact location. The fluid cases however show some specific results. The impact itself produces surface waves that propagate and are focused at the antipode. At this location, these waves lead to some spallation of mantle material, which gets heated when falling back. We thus see an increase in temperature at the antipode; here there are some notable differences between the Tillotson and the ANEOS cases.

Comparing the influence of both effect, we find that rheology plays an important role for both material and heat distribution, even at this scale. The EoS, despite changing the radius of the bodies by $\sim 4\%$, has little influence on these effects. Compared to Tillotson, the more sophisticated temperature computation by ANEOS, which includes the latent heat of vaporisation, leads to differences only at relatively high temperatures (above 4000 – 5000 K).

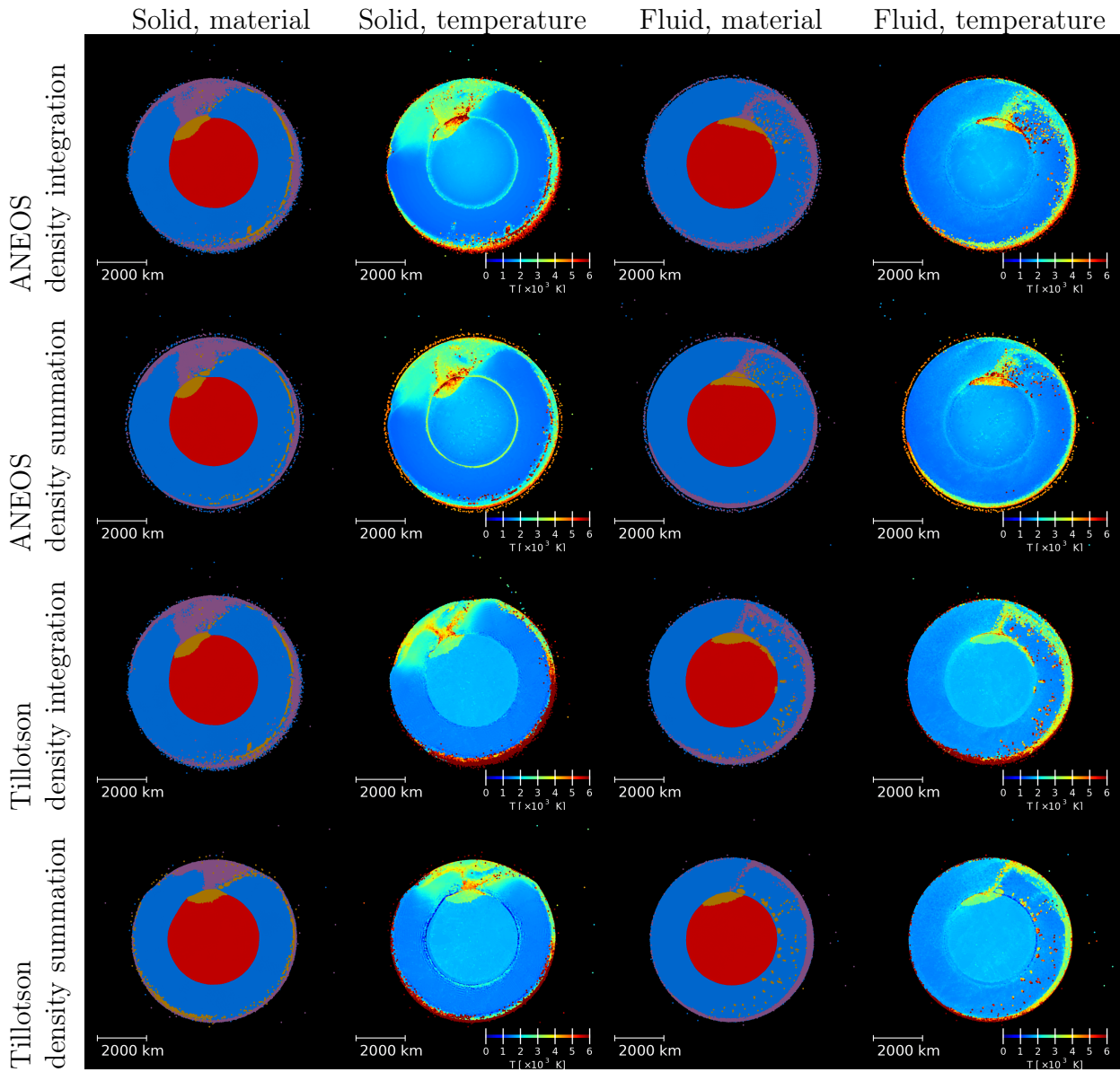


Figure 5: Material and temperature plots for the oblique impact cases at the end of the simulations. The top line is the same as the final one of figure 3.

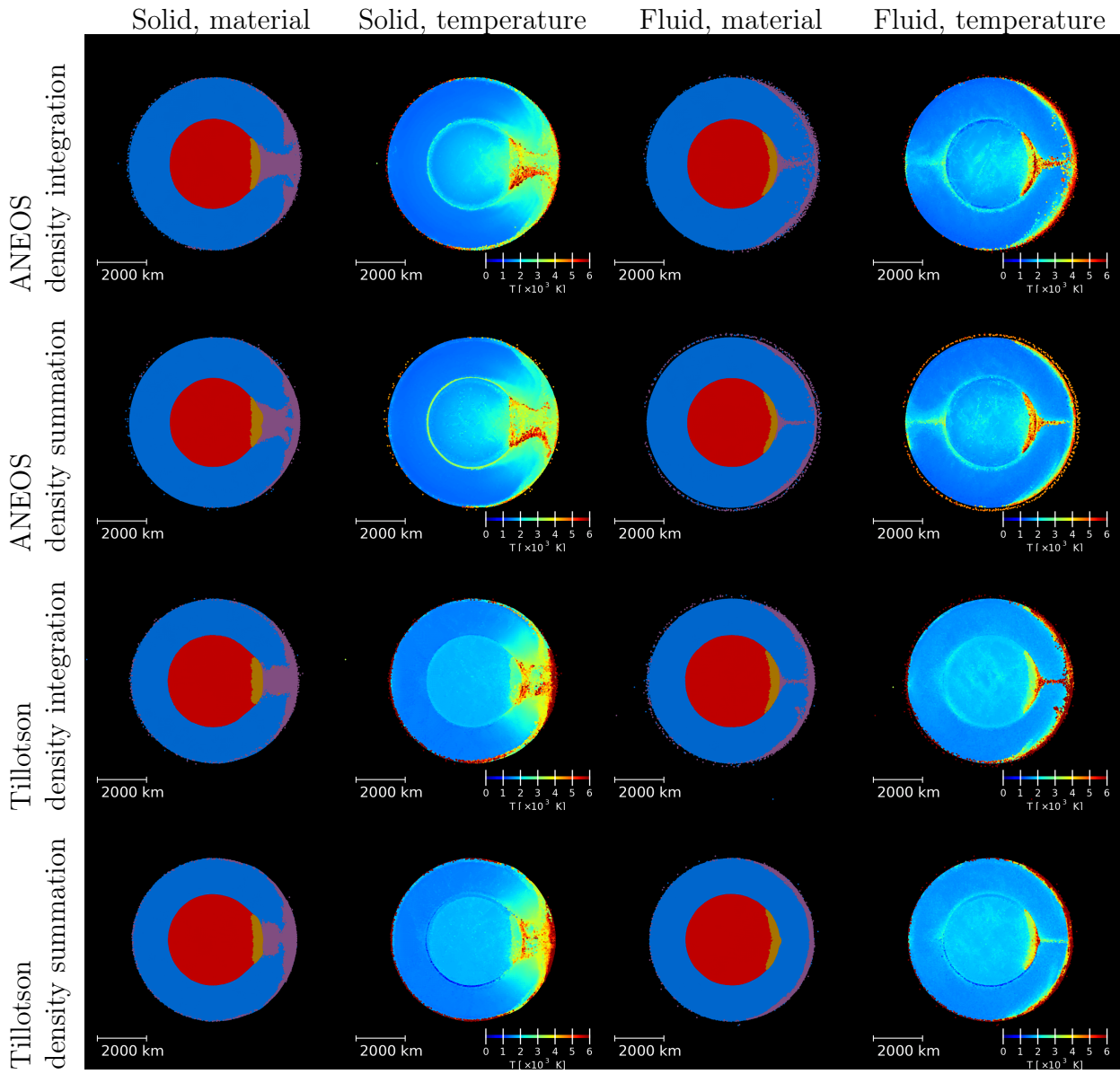


Figure 6: Same as figure 5, but for the corresponding head-on cases. Initial contact happens on the right side.

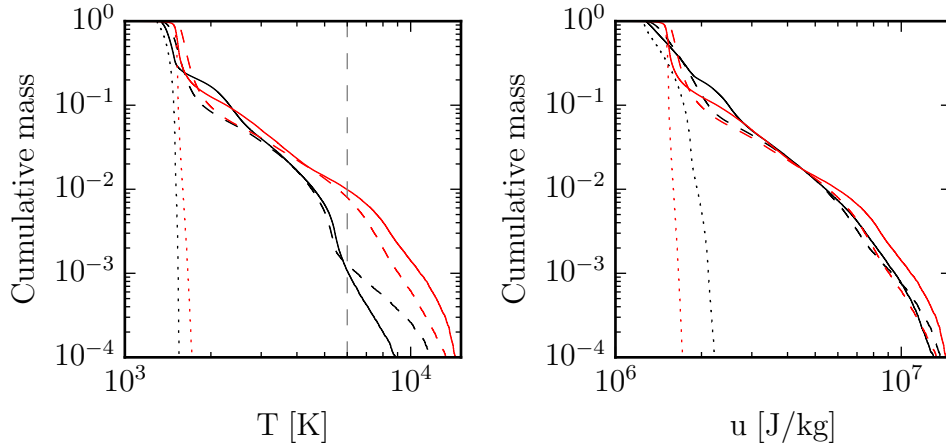


Figure 7: Cumulative mass fraction of the mantle with temperature (left panel) or specific internal energy (right panel) greater than a given value. Black lines denote ANEOS whereas red is for Tillotson. Solid lines are for solid rheology, dashed lines for fluid rheology and the dotted lines show the initial target profile. Only density integration with oblique geometry is considered. The dashed grey line on the temperature plot shows the upper bound of the colour scale on figures 3, 5 and 6.

4.3. Numerical effects

4.3.1. Rotational instability

In figure 8 we show the effect of applying the correction tensor in the computation of the stress tensor to avoid rotational instability effects in the case of a solid rheology (e.g. Speith, 2006). As it can be seen, the post-impact material and temperature distributions are very similar in the cases with and without correction tensor, except for the temperature artefact due to the set up routine at the core-mantle boundary. We note that the amplitude of the artificial temperature increase at the boundary is much smaller in the simulation with the correction tensor (about ~ 1000 K increase) than in the one without (about ~ 5000 K increase). Furthermore, the longer term target rotation is slower in the case without correction tensor, because the angular momentum is not conserved.

The angular momentum is plotted as a function of time in figure 9 for the two cases. We also include the corresponding fluid case for comparison. For the solid rheology with correction and the fluid rheology, the variation of angular momentum over the whole simulations (about 20 h) is lower than 1 % whereas for the solid rheology without correction, angular momentum is reduced by almost 25 %. The decrease starting a few hours after time impact reflects the slow down of the rigid body rotation which is not treated correctly without the correction tensor. Ejected material is not subject to this problem as it does not encounter solid forces. The rotation rate decrease implies that target's position is not the same during late stages of simulations. At 18 hours after impact, the target rotated around 20 degrees less than in the case where angular momentum is conserved (figure 8). Here, the target rotates about 100° between the merging of both cores at two hours after the impact and the end at 18 hours.

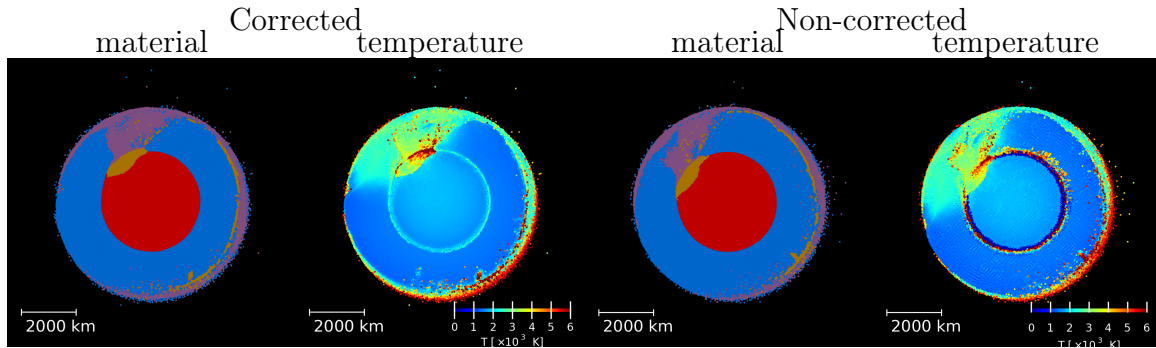


Figure 8: End result comparison for case with angular conservation (two left panels) and without (two right panels). Colours for material plots are the same as in figure 3.

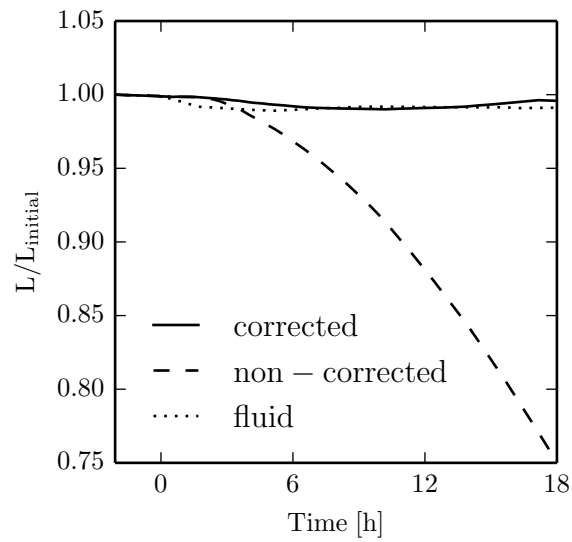


Figure 9: Angular momentum as function of time for the two cases shown above (45° , ANEOS, solid, integrated density), with/without correction tensor and the corresponding fluid case for comparison.

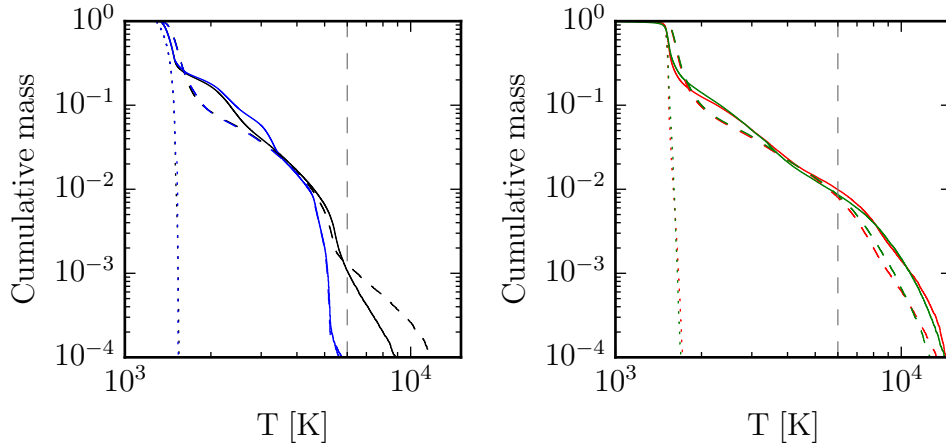


Figure 10: Cumulative mass fraction of mantle with temperature greater than a given value. Same as left panel of figure 7, but comparing density computation instead. Left panel is for ANEOS, where blue lines are now density summation. Right panel is Tillotson with green lines for density summation.

These results confirm that standard SPH does not handle well problems which involve rigid body rotation (Speith, 2006) and point out the importance of applying the correction tensor to deal with such cases, in particular for situations where the rotation timescale is comparable to the simulated time.

4.3.2. Density computation (summation vs. integration)

As discussed in section 2, we test two different methods to compute the densities of the SPH particles. We use *density integration* for our nominal cases.

Major differences arise at the boundaries between materials or at the surface where steep density gradients are located. For density summation, a group of particles separates in all quantities shown in radial profiles (figures 1 and 2). These groups contain particles closer than $2h$ from the boundary and where the adjacent material enters in the SPH sum (or where there is a lack of neighbouring particles when close to the surface). Their density is shifted towards the one beyond the boundary. For integrated density, as no such sum is involved, particles close to the boundary do not separate from the remaining. However, there are still some oscillations close to the discontinuity.

Despite the issues mentioned above, which result in different initial density profiles (at the boundaries), the results at end of the simulations do not show any major differences between the two schemes (figures 5 and 6). However, there are some subtle effects. For instance, we observe a different behaviour of hot surface particles which were ejected during the early stage of impact and reaccreted later on. With ANEOS and density summation, they form a layer separated from the planet's surface. In the other cases, this feature is less pronounced and not present at all in the cases with density integration. In the ANEOS case, the different densities of the surface particles also affect the temperature (figure 10, left panel) although the energy distribution remains essentially identical. As surface particle

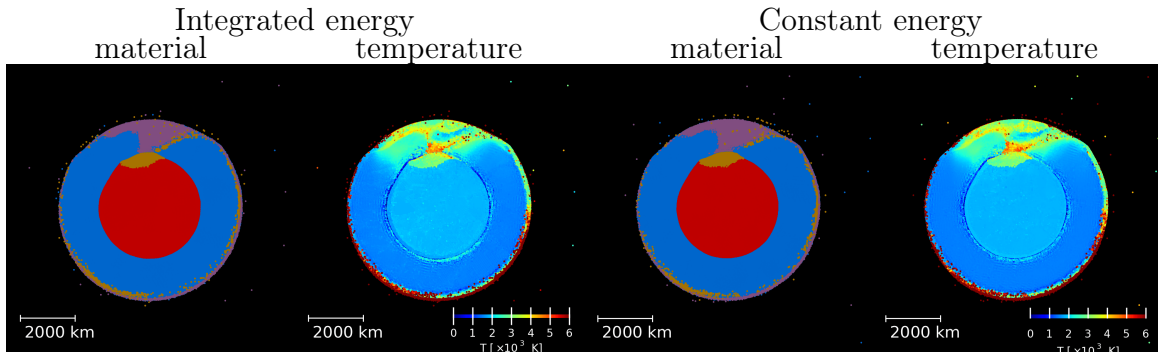


Figure 11: End result comparison for case with evolved internal energy during setup phase (two left panels) and constant (two right panels). Colours for material plots are the same as in figure 3.

density is lower in the density summation case than for density integration, ANEOS does not find them in the same phase: mixed liquid-vapour for the former and liquid in the latter. Density summation simulations exhibit lower temperature since part of the internal energy is used for the phase transition rather than temperature increase. This explains the absence of material with temperature above 6000 K with ANEOS density summation on the figure. The second small bump located between 2000 and 3000 K in the case with solid rheology and density summation (solid blue line on figure 10) is due to the core-mantle boundary. As phase transition does not influence the temperature in the case with Tillotson EoS, we don't see this feature on the right panel of figure 10.

We note that the differences between the numerical schemes discussed above result from differences at small scales, representing only a small fraction of the total mass involved in the simulation. Even at the relatively high resolution (one million SPH particles) used in the simulations performed here, some of these small-scale features are under-resolved. This is certainly the case for the layer of reaccreted material discussed above. Also the peak pressures and temperatures produced in the initial stages of the collision may not be fully resolved.

With the resolution used in the simulations presented here, the numerical scheme with density integration appears to be the better choice as it leads to a better defined surface. It is clear, however, that a more consistent treatment of the boundaries, as well as very high resolution simulations, are required to obtain more accurate physical properties at such small scales.

4.3.3. Effect of the initial energy profile (constant energy vs. integrated energy)

Bodies computed using the Tillotson EoS were evolved during set up phase with the internal energy allowed to vary. This leads to a spread in temperature for those bodies shown in figures 1 and 2 as well as the density decrease close to the centre for the impactor computed using density summation.

For test purposes, a second series of bodies was generated with internal energy kept

EoS	Rheology	Density	Period [Sidereal day]
ANEOS	Solid	Integrated	1.22
	Solid	Summed	1.19
	Fluid	Integrated	1.11
	Fluid	Summed	1.14
Tillotson	Solid	Integrated	1.18
	Solid	Summed	0.95
	Fluid	Integrated	1.13
	Fluid	Summed	1.13

Table 3: Impact-induced rotation periods for oblique geometry runs

constant. For the latter case we don't observe a density decrease close to body centres.

We don't observe any notable difference between the results from the two different setup schemes. A comparison is shown in figure 11. The main differences are located at the core-mantle boundary where the effect of the set up method discussed here and the instability with solid rheology explained in section 4.1 overlap. This effect is small compared with all the previously discussed parameters.

4.4. Rotation period

The rotation periods resulting from the oblique impacts considered in this study, calculated by applying a correction tensor to the angular momentum, are presented in table 3. They are comparable to Mars' present rotation period. All fluid rheology runs have a very similar rotation periods (1.11 – 1.14 Martian sidereal days). The solid rheology usually leads to a slightly slower rotation, except for the case with Tillotson EoS and density summation which does not follow this trend and is rotating faster.

4.5. Ejecta, disc mass and escaping material

We provide in table 4 components of non-accreted material. The amount of unbound material ("Escaping" column) remains almost constant from several hours after impact onward. At the end of the simulations, it represents the biggest component of the ejecta. We find that runs with fluid rheology lead to roughly 30% less escaping mass than the runs with solid rheology. This is visible in figure 4 as the impactor's mantle (purple lines) is less present in the planet with solid rheology. The impactor penetrate less deeply inside the target during the initial phase for the latter case. As consequence, there is a slight increase in the amount of material not directly accreted by the planet, which is reflected in the escaping mass.

The amount of material which is still bound but not (yet) reaccreted is lower than the amount of escaping material by 6 hours after impact. It decreases as material fall back onto the planet and eventually reaches a value about three times lower at the end. For a further analysis of that part, the reader is referred to Golabek et al. (2017).

EoS	Rheology	Density	Ejecta [M_{Mars}]	Disc [M_{Mars}]	Escaping [M_{Mars}]
ANEOS	Solid	Integrated	$1.4 \cdot 10^{-3}$	$2.2 \cdot 10^{-5}$	$2.7 \cdot 10^{-3}$
	Solid	Summed	$1.3 \cdot 10^{-3}$	$2.2 \cdot 10^{-4}$	$2.5 \cdot 10^{-3}$
	Fluid	Integrated	$1.3 \cdot 10^{-3}$	0	$2.0 \cdot 10^{-3}$
	Fluid	Summed	$1.4 \cdot 10^{-3}$	$2.1 \cdot 10^{-4}$	$1.9 \cdot 10^{-3}$
Tillotson	Solid	Integrated	$1.6 \cdot 10^{-3}$	$5.6 \cdot 10^{-5}$	$2.8 \cdot 10^{-3}$
	Solid	Summed	$1.5 \cdot 10^{-3}$	$1.8 \cdot 10^{-4}$	$2.6 \cdot 10^{-3}$
	Fluid	Integrated	$1.2 \cdot 10^{-3}$	0	$2.0 \cdot 10^{-3}$
	Fluid	Summed	$1.3 \cdot 10^{-3}$	$1.0 \cdot 10^{-4}$	$1.8 \cdot 10^{-3}$

Table 4: Non accreted masses for oblique geometry runs. *Ejecta* column gives the amount of bound ejecta, computed at 6 hours after impact. *Disc* is the amount of material that remains orbiting around the simulations’ end (18 hours after impact) and *Escaping* represents the unbound material, also at simulations’ end.

Also shown in table 4 are the disc’s masses. These values fluctuate and tend to increase with time. Particles composing the disc come from a small subset of the bound ejecta. We find large variations of the disc mass, depending mostly on the numerical scheme. However, the discs masses are very small (a few $10^{-4} M_{\text{Mars}}$ at most) and are under-resolved (they contain between 138 and 332 SPH particles for density summation and up to 74 for density integration). Much higher resolution would be required to obtain meaningful results in terms of the properties of such small discs. We note that recent studies of the impact-formation of the Martian moons (Citron et al., 2015; Canup and Salmon, 2016), which considered comparable disc masses, used similar or lower resolution and did not include material strength.

5. Discussion and Conclusions

In this paper, we model large-scale (≈ 2000 km) impacts on a Mars-like planet using an updated SPH code (Reufer et al., 2012), which includes self-gravity, a newly implemented strength model (Jutzi, 2015) and various EoS (Tillotson and M-ANEOS). A subset of these simulations is used as initial conditions in a thermochemical code to study the long-term interior evolution of Mars (Golabek et al., 2017). Here, we investigate the effects of material strength and of using different EoS. Some potential numerical effects (in the context of discontinuities) which may result from the different ways to compute the density in SPH are studied as well. Finally, an advanced SPH scheme to avoid rotational instability in rigid body rotation (Speith, 2006) is applied and tested in the regime of large-scale collisions.

We find that in the collision regime considered here (with impact velocities of 4 km/s), the Tillotson and ANEOS equations of state lead to post-impact temperature distributions which are quite similar in the temperature range below ~ 4000 K with only subtle differences. This indicates that the Tillotson EoS works reasonably well in this regime (where vaporisation

is not significant) and the simple estimation of the temperature from the specific energy by using a constant heat capacity $T = u/c_p$ is justified.

On the other hand, our results strongly suggest that the effect of material strength is substantial even for the large-scale collisions considered here. When strength is taken into account, the post-impact distributions of the impactor material and temperature are very different. For instance, in this case, the heat generated by the impact is spread out over a much broader region of mantle material localised around the impact point. We expect this finding to be generally important for collisions in this regime. We note that previous SPH simulations at this scale (e.g. Marinova et al., 2008; Canup, 2005; Citron et al., 2015; Canup and Salmon, 2016) did not include material strength. Our results also suggested that Pluto-Charon type collisions (e.g. Canup, 2005) might well be in a regime where material strength is not negligible.

The different density computation schemes used here do not show large differences in the final global outcome of the simulations. However, we observe some differences at small scales, and a more consistent treatment of density discontinuities (e.g. Hosono et al., 2013) is needed. Our study confirms that the known issue of standard SPH in the case of rigid body rotation is solved by using an appropriate correction tensor which increases the SPH consistency (Speith, 2006).

In conclusion, our results show that in the modelling of collisions at scales of ≈ 2000 km, it is essential to use a material strength model. The details of the EOS are less important in this regime. Finally, an improved treatment of boundaries as well as a very high resolution are required to obtain accurate physical properties at small scales.

Acknowledgements

We thank Gregor J. Golabek and Taras V. Gerya for helpful discussion in the study's design, and anonymous referee for suggestions that improved this paper. A.E. acknowledges the financial support of the Swiss National Science Foundation under grant 200020_17246. This work has been carried out within the frame of the National Centre for Competence in Research PlanetS supported by the Swiss National Science Foundation. The authors acknowledge the financial support of the SNSF.

- J. C. Andrews-Hanna, M. T. Zuber, and W. B. Banerdt. The Borealis basin and the origin of the martian crustal dichotomy. *Nature*, 453:1212–1215, June 2008. doi: 10.1038/nature07011.
- E. Asphaug. Similar-sized collisions and the diversity of planets. *Chemie der Erde / Geochemistry*, 70: 199–219, 2010. doi: 10.1016/j.chemer.2010.01.004.
- E. I. Asphaug and A. Reufer. Making an Iron Planet: The Case for Repeated Hit and Run Collisions. *AGU Fall Meeting Abstracts*, page A3, December 2014.
- J. Barnes and P. Hut. A hierarchical $O(N \log N)$ force-calculation algorithm. *Nature*, 324:446–449, December 1986. doi: 10.1038/324446a0.
- W. Benz. An introduction to computation methods in hydrodynamics. In C. B. de Loore, editor, *Late stages of stellar evolution, computational methods in astrophysical hydrodynamics*, volume 373, pages 258–312. Springer, 1991. ISBN 0387536205.
- W. Benz and E. Asphaug. Impact simulations with fracture. I - Method and tests. *Icarus*, 107:98, January 1994. doi: 10.1006/icar.1994.1009.

- W. Benz and E. Asphaug. Simulations of brittle solids using smooth particle hydrodynamics. *Comput. Phys. Commun.*, 1-2:253–265, 1995. doi: 10.1016/0010-4655(94)00176-3.
- W. Benz, W. L. Slattery, and A. G. W. Cameron. Collisional stripping of Mercury’s mantle. *Icarus*, 74: 516–528, June 1988. doi: 10.1016/0019-1035(88)90118-2.
- W. Benz, A. Anic, J. Horner, and J. A. Whitby. The Origin of Mercury. *Space Sci. Rev.*, 132:189–202, October 2007. doi: 10.1007/s11214-007-9284-1.
- A. G. W. Cameron and W. R. Ward. The Origin of the Moon. In *Lunar and Planetary Science Conference*, volume 7 of *Lunar and Planetary Science Conference*, page 120, March 1976.
- R. M. Canup. Simulations of a late lunar-forming impact. *Icarus*, 168:433–456, April 2004. doi: 10.1016/j.icarus.2003.09.028.
- R. M. Canup. A Giant Impact Origin of Pluto-Charon. *Science*, 307:546–550, January 2005. doi: 10.1126/science.1106818.
- R. M. Canup. On a Giant Impact Origin of Charon, Nix, and Hydra. *Astron. J.*, 141:35, February 2011. doi: 10.1088/0004-6256/141/2/35.
- R. M. Canup. Forming a Moon with an Earth-like Composition via a Giant Impact. *Science*, 338:1052–, November 2012. doi: 10.1126/science.1226073.
- R. M. Canup and E. Asphaug. Origin of the Moon in a giant impact near the end of the Earth’s formation. *Nature*, 412:708–712, August 2001.
- R. M. Canup and J. Salmon. On an Origin of Phobos-Deimos by Giant Impact. In *Lunar and Planetary Science Conference*, volume 47 of *Lunar and Planetary Science Conference*, page 2598, March 2016.
- R. I. Citron, H. Genda, and S. Ida. Formation of Phobos and Deimos via a giant impact. *Icarus*, 252: 334–338, May 2015. arXiv:1503.05623. doi: 10.1016/j.icarus.2015.02.011.
- G. S. Collins, H. J. Melosh, and B. A. Ivanov. Modeling damage and deformation in impact simulations. *Meteorit. Planet. Sci.*, 39:217–231, February 2004. doi: 10.1111/j.1945-5100.2004.tb00337.x.
- M. Čuk and S. T. Stewart. Making the Moon from a Fast-Spinning Earth: A Giant Impact Followed by Resonant Despinning. *Science*, 338:1047–, November 2012. doi: 10.1126/science.1225542.
- H. Frey and R. A. Schultz. Large impact basins and the mega-impact origin for the crustal dichotomy on Mars. *Geophys. Res. Lett.*, 15:229–232, March 1988. doi: 10.1029/GL015i003p00229.
- Gregor J. Golabek, Martin Jutzi, Alexandre Emsenhuber, Taras V. Gerya, and Erik I. Asphaug. Coupling SPH and thermochemical models of planets: Methodology and example of a Mars-sized body. *Icarus*, 2017.
- W. K. Hartmann and D. R. Davis. Satellite-sized planetesimals and lunar origin. *Icarus*, 24:504–514, April 1975. doi: 10.1016/0019-1035(75)90070-6.
- N. Hosono, T. R. Saitoh, and J. Makino. Density-Independent Smoothed Particle Hydrodynamics for a Non-Ideal Equation of State. *Publ. Astron. Soc. Jpn*, 65:108, October 2013. arXiv:1307.0916. doi: 10.1093/pasj/65.5.108.
- Martin Jutzi. SPH calculations of asteroid disruptions: The role of pressure dependent failure models. *Planet. Space Sci.*, 107:3–9, March 2015. arXiv:1502.01860. doi: 10.1016/j.pss.2014.09.012.
- Martin Jutzi, K. Holsapple, K. Wünneman, and Patrick Michel. Modeling Asteroid Collisions and Impact Processes. In Patrick Michel, Francesca E. DeMeo, and William F. Bottke Jr., editors, *Asteroids IV*, page 679. The University of Arizona Press, 2015. arXiv:1502.01844.
- M. M. Marinova, O. Aharonson, and E. Asphaug. Mega-impact formation of the Mars hemispheric dichotomy. *Nature*, 453:1216–1219, June 2008. doi: 10.1038/nature07070.
- M. M. Marinova, O. Aharonson, and E. Asphaug. Geophysical consequences of planetary-scale impacts into a Mars-like planet. *Icarus*, 211:960–985, February 2011. doi: 10.1016/j.icarus.2010.10.032.
- H. J. Melosh. *Impact cratering: A geologic process*. Oxford University Press, 1989.
- H. J. Melosh. A hydrocode equation of state for SiO₂. *Meteorit. Planet. Sci.*, 42:2079–2098, 2007. doi: 10.1111/j.1945-5100.2007.tb01009.x.
- J. J. Monaghan. Smoothed particle hydrodynamics. *Annu. Rev. Astron. Astrophys.*, 30:543–574, 1992. doi: 10.1146/annurev.aa.30.090192.002551.
- J. J. Monaghan and J. C. Lattanzio. A refined particle method for astrophysical problems. *Astron. Astro-*

- phys.*, 149:135–143, August 1985.
- F. Nimmo, S. D. Hart, D. G. Korycansky, and C. B. Agnor. Implications of an impact origin for the martian hemispheric dichotomy. *Nature*, 453:1220–1223, June 2008. doi: 10.1038/nature07025.
- William H. Press. *Numerical recipes in C++ : the art of scientific computing*. Cambridge University Press, 2002. ISBN: 0-521-75033-4.
- C. Reinhardt and J. Stadel. Numerical aspects of giant impact simulations. *Mon. Not. R. Astron. Soc.*, 467: 4252–4263, June 2017. arXiv:1701.08296. doi: 10.1093/mnras/stx322.
- A. Reufer, M. M. M. Meier, W. Benz, and R. Wieler. A hit-and-run giant impact scenario. *Icarus*, 221: 296–299, September 2012. arXiv:1207.5224. doi: 10.1016/j.icarus.2012.07.021.
- L. E. Senft and S. T. Stewart. Dynamic fault weakening and the formation of large impact craters. *Earth Planet. Sci. Lett.*, 287:471–482, October 2009. doi: 10.1016/j.epsl.2009.08.033.
- Roland Speith. Improvements of the numerical method Smoothed Particle Hydrodynamics. Habilitationsschrift, 2006.
- S. L. Thompson and H. S. Lauson. Improvements in the CHART-D Radiation-hydrodynamic code III: Revised analytic equations of state. Technical Report SC-RR-71 0714, Sandia National Laboratories, 1972.
- J. H. Tillotson. Metallic Equations of State for Hypervelocity Impact. Technical Report GA-3216, General Atomic, July 1962.
- D. E. Wilhelms and S. W. Squyres. The martian hemispheric dichotomy may be due to a giant impact. *Nature*, 309:138–140, May 1984. doi: 10.1038/309138a0.

Coupling SPH and thermochemical models of planets: Methodology and example of a Mars-sized body

G.J. Golabek^{1,2,*}, A. Emsenhuber³, M. Jutzi³, E.I. Asphaug^{4,5} & T.V. Gerya²

¹ Bayerisches Geoinstitut, University of Bayreuth, Universitätsstrasse 30, 95440 Bayreuth, Germany.

² ETH Zurich, Institute of Geophysics, Sonneggstrasse 5, 8092 Zürich, Switzerland.

³ University of Bern, Physics Institute, Space Research and Planetary Sciences, Center for Space and Habitability, Gesellschaftsstrasse 6, 3012 Bern, Switzerland.

⁴ Arizona State University, School of Earth and Space Exploration, PO Box 876004, Tempe, AZ 85287, USA.

⁵ University of Arizona, Lunar and Planetary Laboratory, 1269 E. University Blvd, Tucson, AZ 85721, USA.

* Corresponding author. G.J. Golabek (gregor.golabek@uni-bayreuth.de)

Accepted for publication in *Icarus*.

Abstract

Giant impacts have been suggested to explain various characteristics of terrestrial planets and their moons. However, so far in most models only the immediate effects of the collisions have been considered, while the long-term interior evolution of the impacted planets was not studied. Here we present a new approach, combining 3-D shock physics collision calculations with 3-D thermochemical interior evolution models.

We apply the combined methods to a demonstration example of a giant impact on a Mars-sized body, using typical collisional parameters from previous studies. While the material parameters (equation of state, rheology model) used in the impact simulations can have some effect on the long-term evolution, we find that the impact angle is the most crucial parameter for the resulting spatial distribution of the newly formed crust. The results indicate that a dichotomous crustal pattern can form after a head-on collision, while this is not the case when considering a more likely grazing collision. Our results underline that end-to-end 3-D calculations of the entire process are required to study in the future the effects of large-scale impacts on the evolution of planetary interiors.

1. Introduction

Towards the end of terrestrial planetary accretion, giant impacts are inevitable [Wetherill, 1985; Melosh, 1990; Canup & Asphaug, 2001]. It has been suggested that they can explain various characteristics of the terrestrial planets like Mercury's anomalously thin silicate mantle [Benz *et al.*, 1988, 2007; Asphaug and Reufer, 2014], the retrograde spin of Venus [Alemi and Stevenson, 2006], the origin of the Earth's Moon [Hartmann and Davis, 1975; Cameron and Ward, 1976; Canup and Asphaug, 2001; Canup, 2004, 2012; Čuk and Stewart, 2012; Reufer *et al.*, 2012] and the formation of the martian dichotomy [Wilhelms and Squyres, 1984; Frey and Schultz, 1988; Andrews-Hanna *et al.*, 2008; Nimmo *et al.*, 2008; Marinova *et al.*, 2008, 2011]. For the case of Mars, numerical model results suggest that the northern lowlands of Mars could correspond to a giant impact basin formed after primordial crust formation. However in these models only the impact process and its immediate aftermath are considered, while the longer-term evolution featuring post-collision crust formation is not studied.

Thermochemical codes consider the physical evolution of the planetary interior, and are better suited than impact models to study the long-term evolution of planetary interiors following a major collision. For the case of the martian dichotomy these endogenic models [e.g., Weinstein, 1995], suggest a degree-1 mantle upwelling underneath the southern highlands [Zhong and Zuber, 2001; Roberts and Zhong, 2006; Zhong, 2009; Keller and Tackley, 2009; Šrámek and Zhong, 2010, 2012]. These models rely on a high Rayleigh number and a particular viscosity profile to form a low degree convective planform within the geological constraints for Mars dichotomy formation. Also for the case of the martian dichotomy formation, a hybrid exogenic-endogenic approach was suggested [Reese and Solomatov, 2006, 2010; Reese *et al.*, 2010; Golabek *et al.*, 2011], proposing an impact-induced regional magma ocean and subsequent superplume in the southern hemisphere.

These thermochemical simulations usually rely on highly simplified impact models, for instance a uniform or localized deposition of energy or matter representative of the collision [e.g. Wilhelms and Squyres, 1984]. Although a simplified approach might be suitable for the limited case of a head-on impact, it is well established that impacts at 45 degrees are most likely [Gilbert, 1893; Shoemaker, 1962]. This is true for cratering and for giant impacts, however for cratering, the infinite target means that impact angle does not matter very much. No matter what the angle, the projectile can not find its way beyond the target, and there is no abrupt transition to 'grazing' behavior until impact angles of around 75 degrees from vertical [Melosh, 1989]. However for giant impacts and other similar-sized collisions [Asphaug, 2010], even a close-to-head-on impact (less than 20 degrees) can allow for lopsided evolution of material. Thus, the combined effects of gravity, angular momentum, and linear downrange momentum require 3-D models.

Thus to better understand the influence of giant impacts on the early evolution of terrestrial planets, methodological improvements are necessary, ideally using the advantages of both methods to overcome the current model limitations. In a recent study, results of 2-D axisymmetric impact calculations were used as input in thermochemical evolution models [Rolf *et al.*, 2017]. We present here a new approach using the results of 3-D large-scale collision models performed with a shock physics code to be used as initial conditions in a thermochemical code and present demonstration calculations.

In section 2 we introduce the methods used by both codes, one for giant impacts and one for the thermochemical evolution. In section 3 we describe the model scenario of our demonstration calculation, which we use to test the coupled method. In section 4 we discuss the effect of parameters like the equation of state, the rheology and the transfer time on the post-impact crust formation. The two final sections are devoted to discussion and outlook.

2. Methodology

2.1 SPH code

We use a smoothed particle hydrodynamics (SPH) code [Benz and Asphaug, 1994; Reufer *et al.* 2012; Jutzi *et al.*, 2013] to model the collision. This code is based on the SPHLATCH code developed by Reufer *et al.* [2012] and includes self-gravity, a newly implemented strength model and various equations of state (EoS). The details of the strength and EoS models are described in Emsenhuber *et al.*, *in press*. Here we only give a short summary of the basic method.

SPH uses a Lagrangian representation where material is divided into particles. Quantities are interpolated (‘smoothed’) over a certain length by summing over surrounding particles (called neighbours) using a kernel function

$$B(\vec{x}) = \sum_i B_i W(\vec{x} - \vec{x}_i, h_i) \quad (1)$$

where \vec{x}_i , h_i and V_i are the position, smoothing length, and volume of particle i , respectively. B_i represents the quantity (field variable) to be interpolated and $W(\vec{x}, h)$ is the kernel. This interpolation scheme is used in SPH to solve the relevant differential equations [see Emsenhuber *et al.*, *in press*]. SPH is an adaptive resolution technique, thus large volumes of space can be modelled economically. Indeed ‘space’ has no particles and costs no resolution. The method is therefore quite popular in three-dimensional (3-D) planetary collisional studies [e.g. Jutzi *et al.*, 2015], and includes good equations of state and treatments of shock and self-gravity. But being a 2nd order method limited to the Courant timescale (that is, the sound-crossing time of a particle smoothing length), it is not suited to model the longer-term post-impact evolution.

Body accelerations are the result of the pressure gradient, and for this SPH uses the pressure as computed from an equation of state (EoS; see below) which is a function $P(\rho, u)$ of density ρ and internal energy u . For solid materials the pressure gradient is generalized into a stress tensor [Benz and Asphaug, 1994]. We use a Drucker-Prager-like yield criterion [Collins *et al.*, 2004, Jutzi, 2015] with yield strength σ_i of intact material, which is a

function of temperature [Collins *et al.*, 2004]. A more sophisticated model for geological materials, which includes also a tensile fracture and a porosity model, and its application in SPH (using a different code) is described in Jutzi [2015]; for problems at the global-scale of a Mars-sized body these aspects can be ignored.

As for the EoS we use either Tillotson [Tillotson, 1962] or ANEOS [Thompson and Lauson, 1972; Melosh, 2007]. The Tillotson equation of state provides both the pressure P and the speed of sound v_s as output, but it does not give the temperature T , so as an approximation we use the internal energy u as a proxy for temperature by dividing by the heat capacity c_p . However it should be noted that eq. (2) does not take into account that heat capacity is temperature-dependent.

$$T = u/c_p \quad (2)$$

For a more physical computation of temperature, and to allow for phase transitions, which do not occur in the Tillotson EoS, we use ANEOS [Thompson and Lauson, 1972] for iron and M-ANEOS [Melosh, 2007] for silicates. These equations of state provide numerous output variables including the temperature and phase information (e.g. melt and vapor fraction). Depending on the parameters used in the equation of state, this phase information can be given in different ways. For iron, it can be used to infer the melting temperature at a given pressure. However, this is not the case for silicates, for which we apply the same procedure as used in [Senft and Stewart, 2009] to obtain the melting temperature at a given pressure.

Numerous tests have been made comparing SPH with other codes in the area of impact contact and compression and the early stages of dynamical evolution. Canup *et al.* [2013] find that SPH and CTH (a popular grid-based shock physics hydrocode) both give similar answers for the amount of mass and momentum ejected into a protolunar disk for a Moon-forming giant impact scenario, although varying in detailed aspects such as clumping. Pierazzo *et al.* [2008] make comparisons and find overall agreement for the early impact ejection phase of large-scale impact cratering calculations.

2.2 I3ELVIS code

The study of giant impacts over the past 30 years has depended on hydrocode methods such as SPH, whose methods are generally familiar to the planetary science community. Global thermochemical methods are required to study the post-collision evolution of a planetary object after a giant impact, so we describe that methodology in more detail.

We consider 3-D creeping flow using the Boussinesq approximation, in which both thermal and chemical buoyancy forces are included. For this purpose we performed 3-D simulations using the code I3ELVIS by applying the 'spherical-Cartesian' methodology [see also Gerya and Yuen, 2007]. The methodology combines finite differences on a fully staggered rectangular Eulerian grid with a Lagrangian marker-in-cell technique for solving the momentum, continuity and temperature equations. In order to model a planetary body on a Cartesian grid, the code calculates self-consistently the gravitational field for a self-gravitating planetary body.

In detail, the gravitational potential can be described using the Poisson equation

$$\frac{\partial^2 \phi}{\partial x^2} + \frac{\partial^2 \phi}{\partial y^2} + \frac{\partial^2 \phi}{\partial z^2} = 4\pi G\rho \quad (3)$$

where ϕ is the gravitational potential and G is the gravitational constant. Knowing the gravitational potential, the components of the gravity vector can be computed as follows:

$$g_x = -\frac{\partial \phi}{\partial x}; g_y = -\frac{\partial \phi}{\partial y}; g_z = -\frac{\partial \phi}{\partial z} \quad (4)$$

We assume the Boussinesq approximation in 3-D geometry:

$$\frac{\partial v_x}{\partial x} + \frac{\partial v_y}{\partial y} + \frac{\partial v_z}{\partial z} = 0 \quad (5)$$

where v_x , v_y and v_z are the x , y and z component of the velocity vector, respectively. The local density ρ depends explicitly on temperature T , pressure P , composition c and melt fraction ϕ .

The density of iron and both solid and molten silicates varies with P - T conditions according to the relation:

$$\rho = \rho_0 [1 - \alpha(T - T_0)] \cdot [1 + \beta(P - P_0)] \quad (6)$$

where ρ_0 is the density of the distinct material at $T_0 = 298.15$ K and $P_0 = 10^5$ Pa, α is the thermal expansion coefficient and β is the compressibility coefficient.

For partially molten silicates we take additionally into account that the density will vary with the melt fraction ϕ as follows [see *Burg and Gerya, 2005*]:

$$\rho_{eff} = \rho_{Si-sol} - \phi [\rho_{Si-sol} - \rho_{Si-liq}] \quad (7)$$

where ρ_{Si-sol} and ρ_{Si-liq} are the pressure and temperature-dependent densities of the solid silicates and liquid silicates, respectively.

For this purpose we use a batch-melting model assuming a peridotite composition. Pressure-dependent parameterizations for both the solidus and liquidus temperatures, T_{sol} and T_{liq} of peridotite are applied [Herzberg et al. 2000; Trønnes and Frost, 2002; Wade and Wood 2005]:

$$T_{sol} [\text{K}] = 1416.2 + 58.3 P [\text{GPa}] + 52.3 P^2 [\text{GPa}] - 16.3 P^3 [\text{GPa}] + 2.3 P^4 [\text{GPa}] - 0.2 P^5 [\text{GPa}] + 8 \cdot 10^{-3} P^6 [\text{GPa}] - 2 \cdot 10^{-4} P^7 [\text{GPa}] + 2 \cdot 10^{-6} P^8 [\text{GPa}] \quad (8)$$

$$T_{liq} [\text{K}] = 1973 + 28.57 P [\text{GPa}] \quad (9)$$

For $T \leq T_{sol}$, the silicate melt fraction ϕ is zero, for $T \geq T_{liq}$, it is equal to 1. In the intermediate temperature range $T_{sol} < T < T_{liq}$, the melt fraction is assumed to increase linearly with temperature according to the following relation [Burg and Gerya, 2005]:

$$\phi = \frac{T - T_{sol}}{T_{liq} - T_{sol}} \quad (10)$$

Both consumption and release of latent heat due to melting and freezing of silicates are taken into account.

The 3-D Stokes equations for creeping flow take the form:

$$\frac{\partial \sigma_{xx}}{\partial x} + \frac{\partial \sigma_{xy}}{\partial y} + \frac{\partial \sigma_{xz}}{\partial z} - \frac{\partial P}{\partial x} = -g_x \rho \quad (11)$$

$$\frac{\partial \sigma_{yx}}{\partial x} + \frac{\partial \sigma_{yy}}{\partial y} + \frac{\partial \sigma_{yz}}{\partial z} - \frac{\partial P}{\partial y} = -g_y \rho \quad (12)$$

$$\frac{\partial \sigma_{zx}}{\partial x} + \frac{\partial \sigma_{zy}}{\partial y} + \frac{\partial \sigma_{zz}}{\partial z} - \frac{\partial P}{\partial z} = -g_z \rho \quad (13)$$

where σ_{ij} represents the components of the deviatoric stress tensor and P is the total pressure, which includes both dynamic and lithostatic components.

We have adopted a Lagrangian frame in which the energy conservation equation takes the following form [Gerya and Yuen, 2003, 2007]:

$$\rho c_p \left(\frac{DT}{Dt} \right) = -\frac{\partial q_x}{\partial x} - \frac{\partial q_y}{\partial y} - \frac{\partial q_z}{\partial z} + H_r + H_s + H_L \quad (14)$$

where D/Dt is the substantive time derivative, H_r is the radiogenic heating term, H_s is the shear heating term, H_L is the latent heating term and q_i is a heat flux component.

The shear heating term is given by

$$H_s = \sigma_{xx}\dot{\epsilon}_{xx} + \sigma_{yy}\dot{\epsilon}_{yy} + \sigma_{zz}\dot{\epsilon}_{zz} + 2\sigma_{xy}\dot{\epsilon}_{xy} + 2\sigma_{xz}\dot{\epsilon}_{xz} + 2\sigma_{yz}\dot{\epsilon}_{yz} \quad (15)$$

where $\dot{\epsilon}_{ij}$ are the components of the strain-rate tensor defined as

$$\dot{\epsilon}_{ij} = \frac{1}{2} \left(\frac{\partial v_i}{\partial x_j} + \frac{\partial v_j}{\partial x_i} \right) \quad (16)$$

The heat flux q_i is defined as

$$q_x = -k \frac{\partial T}{\partial x}, q_y = -k \frac{\partial T}{\partial y}, q_z = -k \frac{\partial T}{\partial z} \quad (17)$$

where k is the thermal conductivity.

We employ a viscous constitutive relationship between stress and strain-rate with η representing the effective viscosity:

$$\sigma_{ij} = 2\eta\dot{\epsilon}_{ij} \quad (18)$$

We use for solid silicates a viscosity η , which depends on temperature T , pressure P and strain rate $\dot{\epsilon}$ defined in terms of deformation invariants [Ranalli, 1995] as:

$$\eta_{eff} = A^{1/n} \exp\left(\frac{E_a + PV_a}{nRT}\right) \dot{\epsilon}_{II}^{(1-n)/n} \quad (19)$$

where $\dot{\epsilon}_{II} = \sqrt{\frac{1}{2}\dot{\epsilon}_{ij}\dot{\epsilon}_{ij}}$ is the second invariant of the strain-rate tensor and A , E_a and n are the pre-exponential parameter, the activation energy and the power law coefficient, respectively. R is the gas constant and V_a is the activation volume.

For solid silicates, this ductile rheology is combined with a brittle rheology to yield an effective viscoplastic rheology. For this purpose the Mohr-Coulomb [e.g., Ranalli, 1995] and Peierls [e.g., Kameyama et al., 1999] yield criteria are simultaneously implemented by limiting the creep viscosity as follows:

$$\eta_{eff} \leq \frac{C + Pf}{2\dot{\epsilon}_{II}} \quad (20)$$

and for $C + Pf \geq \sigma_p$

$$\eta_{eff} \leq \frac{\sigma_p}{2\dot{\epsilon}_{II}} \quad (21)$$

where C is the cohesion, f is the internal friction coefficient and σ_p is the Peierls stress limit.

The presence of a melt fraction $\varphi > 0.1$ has for silicate material an additional influence on the effective viscosity as given here [Pinkerton and Stevenson, 1992]

$$\eta_{eff} = \eta_{Si-liq} \exp\left\{ \left[2.5 + \left(\frac{1-\varphi}{\varphi} \right)^{0.48} \right] (1-\varphi) \right\} \quad (22)$$

where η_{Si-liq} is the viscosity of molten silicates, which we assume to be a constant.

2.2.1 Effective thermal conductivity of largely molten silicates:

Within a narrow silicate melt fraction range, the silicate behaviour undergoes a transition from a solid-like material to a low viscosity crystal suspension [see *Costa et al., 2009; Solomatov, 2015*]. Thus, the viscosity of largely molten silicates is $\eta_{\text{Si-liq}} \sim 10^{-4}\text{-}10^2$ Pa s [Rubie et al., 2003; Liebske et al., 2005; Bottinga and Weill, 1972]. Hence, due to the low viscosity, both the Rayleigh Ra and the Nusselt number Nu will be high and cooling will be a very efficient process.

Due to numerical restrictions, the lower cut-off viscosity in the numerical model is $\eta_{\text{num}} = 10^{18}$ Pa s, many orders of magnitude higher than realistic viscosities for largely molten silicates. It was suggested that the heat flux from a magma ocean [e.g. *Solomatov, 2015*] can be described using the so-called soft turbulence model [Kraichnan, 1962; Siggia, 1994]. In this model the expected convective heat flux q is given as:

$$q = 0.089 \frac{k(T-T_{\text{surf}})}{L} Ra^{1/3} \quad (23)$$

where the Rayleigh number Ra is defined as

$$Ra = \frac{\alpha g(T-T_{\text{surf}})\rho_{\text{eff}}^2 c_p D^3}{k\eta_{\text{Si-liq}}} \quad (24)$$

T_{surf} is the surface temperature and D is the depth of the magma ocean.

Depending on the actual silicate melt viscosity in the numerical model η_{num} , one can estimate an increased effective thermal conductivity k_{eff} by using the theoretically expected heat flux from a low viscosity magma ocean q from eq. (23). This effective thermal conductivity can simulate the heat flux of a medium with a realistic magma ocean viscosity [Zahnle et al., 1988; Tackley et al., 2001; Hevey and Sanders, 2006; Golabek et al., 2011, 2014], despite our numerical limitations. Combining eq. (23) and (24) this can be done using the following expression for the effective thermal conductivity k_{eff} :

$$k_{\text{eff}} = \left(\frac{q}{0.089}\right)^{\frac{3}{2}} \frac{1}{(T-T_{\text{surf}})^2 \rho_{\text{eff}}} \left(\frac{\alpha g c_p}{\eta_{\text{num}}}\right)^{-\frac{1}{2}} \quad (25)$$

2.2.2 Crust formation

Partial melting of the mantle, melt extraction and percolation toward the bottom of the forming basaltic crust is implemented in a simplified manner. According to our model, mafic magma added to the crust is balanced by melt production and extraction in the mantle. However, melt percolation is not modelled directly and is considered to be nearly instantaneous. The standard (i.e. without melt extraction) volumetric degree of mantle melting φ changes with pressure and temperature according to the linear batch melting model (see eq. 10). Lagrangian markers track the amount of melt extracted during the evolution of each numerical experiment. The total amount of melt, φ_{tot} for every marker takes into account the amount of previously extracted melt and is calculated as

$$\varphi_{\text{tot}} = \varphi - \sum_N \varphi_{\text{ext}} \quad (26)$$

where $\sum_N \varphi_{\text{ext}}$ is the total melt fraction extracted during the previous N extraction episodes. The rock is considered to be non-molten (refractory) when the extracted melt fraction is larger than the current one (i.e. when $\sum_N \varphi_{\text{ext}} > \varphi$). Since the extracted melt fraction propagates much faster than the rocks deform [Condomines et al., 1988], melts produced at depth are moved towards the surface and added to the bottom of

the forming crust. In order to ensure melt volume conservation and account for mantle compaction and subsidence in response to the melt extraction, melt addition to the bottom of the crust is performed at every time step by converting the shallowest markers of mantle into crustal markers. The local volume of these new crustal markers matches the local volume of extracted melt computed for the time step. Basaltic melts are assumed to be only extracted from relatively shallow (≤ 300 km depth) mantle regions with low degree of melting ($\varphi \leq 0.2$). This corresponds roughly to the pyroxene fraction of a fertile mantle, being the main component in the basaltic to andesitic composition of crustal material [McKenzie and Bickle, 1988]. For simplicity, we do not take partitioning of heat producing elements into the crustal material into account.

3. Model setup

We now apply the combined methods to the example of a giant impact on a Mars-sized body, using typical collisional parameters from previous studies. We perform a series of 8 SPH collision models, using a Mars-mass target body ($R = 3436$ km) and an impactor with 1000 km radius made of silicates and iron, with no initial crust on both bodies. The collision occurs at 5 Myr after CAI formation, within the constraints for the last giant impact onto a smaller planetary embryo [Nimmo & Kleine, 2007; Mezger et al. 2013; Morishima et al. 2013]. For each combination of physical properties (solid and fluid rheologies with either Tillotson or ANEOS EoS) we test different impact angles of 0° (head-on collision) and 45° (grazing collision), as defined in [Asphaug, 2010]. For details see Table 1. We use in all our models a collision at mutual escape velocity [Asphaug, 2010]. With a value $\sim 3 \cdot 10^{-3}$ for the ratio of kinetic impactor energy over gravitational binding energy, this model setup is expected to cause significant post-impact melting [Reese and Solomatov, 2006], resulting in significant crust formation following the giant impact. The simulations used here are a subset of the suite of calculations performed in [Emsenhuber et al., in press].

The target and impactor both start with a Mars-like internal structure with an iron core radius half of the body radius. For simulations using Tillotson EoS, we start with an isothermal mantle with an initial temperature close to the surface solidus temperature of peridotite ($T_{Si} = 1500$ K) [Reese and Solomatov, 2010]. The core temperature is initially set for both objects to a constant value of $T_{Fe} = 1800$ K, which ensures that at the pressure conditions at the center of the target body the assumed eutectic Fe-FeS is molten [Chudinkovich and Boehler, 2007]. For the simulations with ANEOS, an isentropic profile is used for which the temperature at the center of the core is 1800 K and 1500 K for the silicate at the core-mantle boundary.

We begin setting up self-gravitating, hydrostatically-equilibrated planetary objects, starting with one dimensional (1-D) spherically symmetric bodies modelled using a Lagrangian hydrocode [Benz, 1991], with the same EoS model as for SPH. This profile is evolved by computing the force balance between self-gravity and pressure (including a damping term), until hydrostatic equilibrium is reached so that radial velocities are small (less than 1% of the escape velocity). Afterwards we transfer the 1-D radial profile onto SPH particles that are placed onto a 3-D lattice. Parameters of each particle are copied from the 1-D profile according to the radius. As particles are equally spaced on the lattice, variation of density is taken into account by adjusting the particle mass. The spherical SPH bodies are then also evolved in a last initializing step to reach hydrostatic equilibrium and negligible radial velocities. Thus the SPH simulations start with two relaxed, differentiated

spherical planetary objects. To model the collision they start at an initial distance of several radii, so that during the approach they begin to deform tidally prior to the collision, which has an effect on the collision outcome.

The SPH simulations are performed with a resolution of about one million particles for the target. The number of particles for the impactor is scaled according to the mass ratio between the two planetary objects, so that particle spacing h is approximately constant, for the greatest numerical accuracy during the collision. The corresponding smoothing length is then approximately 60 km for both bodies. For more details of the SPH calculations see *Emsenhuber et al., in press*.

The results from SPH are transferred to I3ELVIS at earliest after the collision when (i) the seismic shock waves in the target body have decayed and (ii) after the bulk of ejecta material has either fallen back to the surface of the target body or has escaped (see section 4.1.2). For most cases the transfer time is 18 hours after the collision, several times the self-gravity timescale. To study the sensitivity of the post-collision model evolution to the transfer time, we performed for the reference case (ANEOS EoS, grazing collision) additional thermochemical calculations starting at 8 and 12 hours after the collision (see also Table 1).

The temperature and composition results are interpolated (using the SPH Kernel function as in eq. (1)) onto a Eulerian equally spaced grid of $(10,000 \text{ km})^3$ size centered on the middle of the post-impact target body. The resulting grid spacing is 20 km, which corresponds to a grid resolution of 501^3 . The computational domain is filled with $5.24 \cdot 10^8$ randomly distributed Lagrangian markers. The informations are then transferred from these nodal points to the markers using a bilinear interpolation scheme described in detail elsewhere [*Gerya and Yuen, 2003, 2007*]. To avoid unrealistic silicate melt densities, we introduce in the I3ELVIS models a lower density cut-off at 2500 kg/m^3 .

The I3ELVIS model requires some cleanup of the SPH input. Thus material at a distance of more than 3700 km from the planetary center is considered to be remnant ejecta material and is therefore deleted. The rest of the box is filled with sticky air material of nearly zero density, constant viscosity ($\eta_{\text{sa}} = 10^{18} \text{ Pa s}$) and constant temperature of $T_{\text{sa}} = 220 \text{ K}$. This layer represents an infinite reservoir to absorb heat released from the planetary body [*Golabek et al., 2014; Tkalcic et al., 2013*] and ensures a free surface of the planetary body [*Schmeling et al., 2008; Crameri et al., 2012*].

For numerical reasons, the viscosity range is limited to six orders of magnitude. The silicate viscosity is cut off at lower and upper limits of 10^{18} and 10^{24} Pa s , whereas the iron viscosity is kept constant at 10^{18} Pa s . A similar value for the maximum silicate viscosity ($10^{24} - 10^{28} \text{ Pa s}$) was suggested before [*Karato and Murthy, 1997*]. It should be noted that the iron viscosity in the model ($\eta_{\text{Fe}} = 10^{18} \text{ Pa s}$) is, for numerical reasons, many orders of magnitude higher than its physical value, which is expected to range from 10^{-2} Pa s (in the liquid state) [*Rubie et al., 2015*] up to 10^{12} Pa s in the solid state under high temperature and pressure conditions [*Yunker and Van Orman, 2007*].

For all models, we consider time-dependent radioactive heating by both short- (^{26}Al , ^{60}Fe) and long-lived (^{40}K , ^{235}U , ^{238}U , ^{232}Th) radiogenic isotopes. In the early solar system, ^{26}Al is by far the dominant radioactive energy

source and the initial $^{26}\text{Al}/^{27}\text{Al}$ is taken as $5.85 \cdot 10^{-5}$ [Thrane *et al.*, 2006], this value representing an upper limit for the abundance of ^{26}Al [see Jacobsen *et al.*, 2008].

We use a wet olivine rheology [Ranalli, 1995]. This is reasonable as olivine represents the majority of the martian mantle composition and is weaker relative to pyroxenes, thus controlling mantle deformation [Mackwell, 1991]. The Peierls stress limit σ_P employed for wet olivine rheology [Katayama and Karato, 2008] is 2.9 GPa. As suggested for a Mars-like mantle composition, we apply a density crossover between solid and molten silicates at 600 km depth [Suzuki *et al.*, 1998]. For all other physical parameters employed see Table 2.

4. Results

4.1 SPH results

In this section, we briefly summarize the results of the SPH impact simulations. A detailed description of the full set of simulations, as well as a discussion of other physical and numerical effects is given in Emsenhuber *et al.* (*in press*).

4.1.1 Material and temperature distribution resulting from the SPH simulations

A snapshot of the grazing impact simulations at the time of the first contact of the impactor with the target is shown in figure 1 for the two different material rheologies. We note that with fluid rheology, the impactor is tidally deformed prior to the collision in a more pronounced way than with solid rheology. Qualitative differences in the collision outcome due to the equation of state and the rheology can be seen in figure 2, which shows for the two cases the material and temperature distributions (at $t = 18$ h after the impact) resulting from the impact. There are two main effects of using solid rheology observable in the final results: the impactor's material location and the heat distribution around the impact zone.

Considering material location, about 25 wt% of impactor's core remains in the upper part of the target's mantle under solid rheology whereas for fluid rheology this is insignificant. Also the distribution of the mantle of the impactor within the target is quite different. For solid rheology, about half of the impactor's mantle ends up in the interior while the remaining impactor mantle material is close to the surface. In contrast, with fluid rheology, about 10 wt% of the impactor's mantle lies close to the core-mantle boundary, very little across the rest of the target's mantle, and the majority is located close to the surface. Assuming solid rheology the heat distribution is focussed around the impact zone; in contrast, mostly the impactor material gets heated in models assuming a fluid rheology and the temperature distribution is less localised. This results in initially less silicate melt being present in all fluid rheology cases than in cases assuming a solid rheology.

The differences due to the different equations of state are more subtle. Material with high internal energy has a lower temperature with ANEOS compared to Tillotson. While ANEOS includes the latent heat of vaporisation, we compute the temperature from the specific energies in the runs with the Tillotson EoS using eq. (2) that does not take this into account. However, this affects only a small fraction of material, which is located close to the surface. This issue is discussed in more detail in Emsenhuber *et al.*, *in press*. In future simulations with

much higher surface resolution the effect may be significant.

4.1.2 Re-impacting ejecta

At the standard transfer time ($t = 18$ h) at which we switch from the SPH impact simulations to the interior evolution code I3ELVIS, there is still some ejecta material in orbit, which will potentially get accreted onto the target body later on. We use the following procedure to compute the amount of ejecta remaining to re-impact the Mars-sized target body as a function of time: For each SPH particle it is checked whether it is (1) bound to the target body, (2) on a crossing orbit and (3) outside a sphere with a radius of 3700 km around the center of mass of the target body. Figure 3 shows that within ~ 18 hours after the collision the remaining ejecta mass in orbit drops to values below $<10^{-3} M_{\text{Mars}}$.

To estimate the potential thermal effect of this remaining ejecta on the global evolution, we can calculate its thickness when distributed into a global surface layer of average thickness d by

$$d = \sqrt[3]{\frac{3(M+m)}{4\pi\bar{\rho}}} - R \quad (27)$$

where M is the mass of the target planet, m is the mass of the ejecta layer and $\bar{\rho}$ is the average density of the planet and R its average radius without the ejecta blanket. For simplicity we assume that the remaining orbiting ejecta and the planet have the same average density. However it should be kept in mind that local effects of falling ejecta not considered here may be important.

Using the characteristic diffusion time scale $t \sim d^2/\kappa$, where κ is the thermal diffusivity, we can estimate the minimum cooling timescale of this remaining ejecta material (see Figure 4). For remaining ejecta masses $<10^{-3}M_{\text{Mars}}$ the characteristic diffusion timescale becomes very short compared to the crust formation timescale (see section 4.2), therefore we expect that the disregarded ejecta mass will not affect the evolution of the post-impact planet significantly.

4.2 I3ELVIS results

As described in section 3, for each impact simulation (see table 1) the SPH output is transferred into the I3ELVIS code used to study the post-impact interior evolution. In these longer-term calculations, the crust formation is computed by the procedure outlined in section 2.2.2. The resulting crustal distributions at $t \sim 5 \cdot 10^5$ yr after the collision are displayed in Figures 5-7. Since the early post-collision evolution involves the sinking of iron diapirs through the target's mantle, additional mantle melting occurs due to the release of potential energy. For the head-on collisions the bulk of the sinking iron is concentrated in one iron diapir, as a result most of the heat release occurs in the impact region. For the grazing collisions the post-impact iron distribution is more complex and various-sized iron diapirs are initially distributed throughout a larger portion of the target mantle (see Figure 2). Due to the power law rheology the sinking velocity of the iron diapirs is faster than in a Newtonian medium [e.g. Weinberg & Podladchikov, 1994]. Thus merging of the iron diapirs with the target's core occurs in all calculations on a timescale of $\sim 10^4$ yrs. Due to the shear heating related to the sinking of the iron diapirs hot wakes form [Zieth and Spohn, 2007], evolving on the longer-term into thermal plumes. Due to the cooling of the silicate melt a basaltic crust forms, however delamination from the

bottom occurs repeatedly. This delaminating crust sinks towards the core-mantle boundary and limits the crustal thickness. To determine the time-dependent total volume and distribution of crust, we consider only stable crustal material, meaning that disconnected crustal drips are disregarded. While we observe differences in the time evolution and the final volume of stable crust, all models show that the amount of stable crustal volume stabilizes after several hundred thousand years of evolution (see Figure 8). However, we observe a factor of two difference in the volume of stable crustal material for the different calculations, especially when considering the grazing collisions using Tillotson EoS with different rheologies.

Figure 5 shows the cumulative distribution of the crustal thickness for the head-on and grazing impacts at $\sim 5 \cdot 10^5$ yr after the collision, respectively. A comparison of the results for the two different EoS is shown as well. In Figures 6 and 7, the corresponding crustal thickness maps are displayed, showing the spatial distribution for each case. Overall, the main differences in the spatial crustal pattern result from the impact angle. This effect can be clearly seen in the crustal thickness maps, which for head-on impacts show very different patterns than for grazing impacts. In all cases considered, head-on impacts result in a hemispherical crustal dichotomy (see Figure 6). On the other hand the crustal pattern resulting from the grazing impacts is less consistent (see Figure 7).

As above, the differences between the runs with fluid and with solid rheology are generally more pronounced in the cases using Tillotson EoS (see Figure 5). These variations appear to mostly emerge from the different distributions of hot material just after the collision. As mentioned above a larger fraction of the silicates is molten in simulations with solid SPH rheology (coll02; see table 1), preferentially resulting in the formation of more crust in the long-term. However, the results for fluid rheology (coll08; see table 1) show at 300-1000 km depth the presence of hotter (~ 300 K) and more abundant (>5 times larger volume) impactor-derived melt in the mantle than in cases assuming a solid SPH rheology. For simulation coll02 this allows for fast cooling of the near surface layers and the crust tends to remain stable since no extended regions of still largely molten, thus low viscosity material, are present beneath the crust that would favour its destabilization. On the other hand, in simulation coll08 these regions of very hot silicate material are present for an extended time. Due to the presence of this low viscosity material beneath the newly formed crust the growth of crustal Rayleigh-Taylor instabilities is favoured. This is because the instability growth rate depends on the viscosity of the underlying material [Turcotte & Schubert, 2014]. This causes more crustal dripping events in simulation coll08 and more crustal material sinks into the mantle (see Figure 9). Comparing the two simulation outcomes it can be observed that only $\sim 34\%$ of the crustal material is stable at the end of simulation coll08 compared to $\sim 56\%$ for simulation coll02.

For our nominal case (coll04; see table 1), we performed additional longer-term evolution simulations using different SPH-I3ELVIS transfer times. Figure 10 shows the corresponding crustal thickness distributions. These look relatively similar for the three cases (transfer time of 8 h, 12 h, 18 h) investigated, indicating that as expected the timing of the data transfer does not have a major effect on the crustal distribution.

Although this paper is only about the demonstration of the methodology, it is interesting to compare our results to the observed crustal volumes on a planet like Mars. At $\sim 5 \cdot 10^5$ yr after the collision the volume of stable crust lies between $1.23 \cdot 10^{18} \text{ m}^3$ and $2.39 \cdot 10^{18} \text{ m}^3$, this corresponds to 17-34 % of the present-day volume of

the martian crust [Taylor & McLennan, 2009]. Data indicate that at the end of the simulations 10-15% of the mantle material is partially molten and buoyant. This is related to the presence of hot plumes formed from the wakes left by the sinking iron diapirs. However most of the material in the shallow mantle is already highly depleted, therefore future crust formation is limited. Despite this some additional crust formation related to plumes can be expected to occur on the longer-term.

5. Discussion

The presented numerical models employing SPH and thermochemical simulations performed in series show that while the total volume of crust formed after a collision is comparable for both head-on and grazing collisions, the spatial crustal distribution is strongly affected by the impact angle. While we observe variations in the distribution and total crustal volume, the present results show that for both EoS and both SPH rheologies employed the resulting post-collision crust displays a crustal dichotomy, when considering a head-on collision, while this is not the case for all models assuming the more likely grazing collision.

Focussing on the outcome of the calculations based on SPH models with the more realistic solid rheology, the influence of the EoS on both the total volume and the spatial distribution of crustal material is more limited. The results also show that the rheology employed in the SPH models does have a significant influence on the immediate post-impact internal heat distribution and amount of silicate melt, but for the long-term crust formation process it is only a second-order effect. We note that its influence is more pronounced in the Tillotson cases. This might be related to the simplified treatment of silicate melting employed in models employing the Tillotson EoS. As discussed this can have an effect on the volume of stable crust since the presence of very hot material during the crust formation stage favours crustal dripping events.

5.1 Possible future improvements

As mentioned above, some partial melt is still present at the end of the presented simulations. To study how much additional crust can be formed afterwards and whether all of the post-collision crust will be stable on the long-term additional calculations will be necessary in the future. A possible approach would be the transfer of the I3ELVIS results into the code StagYY [Tackley, 2008] suited to model the long-term evolution of terrestrial planets as done previously in 2-D geometry in Golabek *et al.* [2011]. Also it would be useful to study the effect of the impact angle on crust formation in more detail and determine where the transition between a dichotomous crust as observed for all head-on models and the more complex crustal pattern found for grazing collisions occurs in the parameter space. Also due to numerical limitations we have to use a lower cut-off for viscosity of all materials at 10^{18} Pa s. This limits the possibility of the post-collision magma ocean to spread due to isostatic relaxation [Reese and Solomatov, 2006]. A possible approach would require a reduced effective thermal conductivity, so magma ocean cooling would be extended, allowing for a longer spreading time. Additionally, a more realistic initial temperature profile with an increasing temperature with depth would allow for more efficient spreading since the viscosity of the deeper mantle would be reduced, thus isostatic relaxation could occur on a shorter timescale. Clearly these features have to be investigated in the future in more detail.

6. Conclusions

The present demonstration calculations suggest that the coupled SPH-thermochemical approach in 3-D geometry, although computationally expensive, can help in the future to obtain a more realistic post-collision evolution of planetary interiors as these models are able to capture both the collision process, the following magma ocean cooling, crust formation and solid-state deformation processes in detail. Our results indicate that significant amounts of crustal material taking a dichotomous crustal pattern can form after a head-on collision, while this is not the case when considering a more likely grazing collision. This coupled approach can be applied to various planetary bodies to improve our understanding of their early evolution.

Acknowledgements

We thank two anonymous reviewers for detailed comments that helped to improve the manuscript considerably. Helpful discussions with Francis Nimmo and Don Korycansky on giant impacts are appreciated. A.E. acknowledges the financial support of the Swiss National Science Foundation under grant 200020_17246. This work has been carried out within the frame of the National Centre for Competence in Research PlanetS supported by the Swiss National Science Foundation.

References

- Alemi, A., Stevenson, D.J., 2006. Why Venus has No Moon, American Astronomical Society, DPS meeting #38, #07.03; *Bulletin of the American Astronomical Society*, 38, 491.
- Andrews-Hanna, J.C., Zuber, M.T., Banerdt, W.B., 2008. The Borealis basin and the origin of the martian crustal dichotomy. *Nature* 453, 1212-1215.
- Asphaug, E., 2010. Similar-sized collisions and the diversity of planets. *Chem. Erde - Geochemistry* 70, 199-219.
- Asphaug, E. & Reufer, A., 2014. Mercury and other iron-rich planetary bodies as relics of inefficient accretion. *Nature Geosci.* 7, 564-568.
- Benz, W., 1991. An Introduction to Computation Methods in Hydrodynamics. In: Loore, C.B. de, (Ed.), *Lecture Notes in Physics* 373, Late stages of stellar evolution, computational methods in astrophysical hydrodynamics. Springer, pp. 258-312.
- Benz, W., Cameron, A.G.W., Slattery, W.L., 1988. Collisional Stripping of Mercury's Mantle. *Icarus* 74, 516-528.
- Benz, W., Asphaug, E., 1994. Impact simulations with fracture. I - Method and tests. *Icarus* 107, 98-116.
- Benz, W., Anic, A., Horner, J., Whitby, J.A., 2007. The Origin of Mercury. *Space Sci. Rev.* 132, 189-202.
- Bottinga, Y., Weill, D.F., 1972. The viscosity of magmatic silicate liquids: A model for calculation. *Am. J. Sci.* 272, 438-475.
- Burg, J.-P., Gerya, T.V., 2005. The role of viscous heating in Barrovian metamorphism of collisional orogens: Thermomechanical models and application to the Lepontine Dome in the Central Alps. *J. Metamorp. Geol.* 23, 75-95.
- Cameron, A.G.W., Ward, W.R., 1976. The origin of the Moon. *Lunar Sci.* 7, 120-122.
- Canup, R.M., Asphaug, E., 2001. Origin of the Moon in a giant impact near the end of the Earth's formation. *Nature*, 412, 708-712.
- Canup, R.M., 2004. Simulations of a late lunar-forming impact. *Icarus* 168, 433-456.
- Canup, R.M., 2012. Forming a Moon with an Earth-like Composition via a Giant Impact. *Science* 338, 1052-1055.
- Canup, R.M., Barr, A.C., Crawford, D.A. 2013. Lunar-forming impacts: High-resolution SPH and AMR-CTH simulations. *Icarus* 222, 200-219.
- Collins, G.S., Melosh, H.J., Ivanov, B.A., 2004. Modeling damage and deformation in impact simulations. *Meteor. Planet. Sci.* 39, 217-231.
- Condomines, M., Hemond, C., Allègre, C.J., 1988. U-Th-Ra Radioactive Disequilibria and Magmatic Processes. *Earth Planet. Sci. Lett.* 90, 243-262.
- Ćuk, M., Stewart, S.T., 2012. Making the Moon from a Fast-Spinning Earth: A Giant Impact Followed by Resonant Despinning. *Science* 338, 1047-1052, 2012.
- Chudinovskikh, L., Boehler, R., 2007. Eutectic melting in the system Fe-S to 44 GPa. *Earth Planet. Sci. Lett.* 257, 97-103.
- Costa, A., Caricchi, L., Bagdassarov, N., 2009. A model for the rheology of particle-bearing suspensions and partially molten rocks. *Geochem. Geophys. Geosyst.* 10, Q03010.

Cramer, F., Schmeling, H., Golabek, G.J., Duretz, T., Orendt, R., Buiter, S.J.H., May, D.A., Kaus, B.J.P., Gerya T.V., Tackley, P.J., 2012. A comparison of numerical surface topography calculations in geodynamic modelling: an evaluation of the 'sticky air' method. *Geophys. J. Int.* 189, 38-54.

Emsenhuber, E., Jutzi, M., Benz, W., SPH calculations of Mars-scale collisions: The role of the equation of state, material rheologies, and numerical effects. *Icarus*, in press.

Escartín, J., Hirth, G., Evans, B., 2001. Strength of slightly serpentinized peridotites: Implications for the tectonics of oceanic lithosphere. *Geology* 29, 1023-1026.

Frey, H., Schultz, R.A., 1988. Large impact basins and the mega-impact origin for the crustal dichotomy on Mars. *Geophys. Res. Lett.* 15, 229-232.

Gerya, T.V., Yuen, D.A., 2003. Characteristics-based marker-in-cell method with conservative finite-differences schemes for modeling geological flows with strongly variable transport properties. *Phys. Earth Planet. Int.* 140, 293-318.

Gerya, T.V., Yuen, D.A., 2007. Robust characteristics method for modelling multiphase visco-elasto-plastic thermo-mechanical problems. *Phys. Earth Planet. Int.* 163, 83-105.

Gilbert, G.K., 1893. The Moon's face, a study of the origin of its features. *Bull. Philos. Soc. Wash. (DC)* 12, 241-292.

Golabek, G.J., Keller, T., Gerya, T.V., Zhu, G., Tackley, P. J., Connolly, J.A.D., 2011. Origin of the martian dichotomy and Tharsis from a giant impact causing massive magmatism. *Icarus* 215, 346-357.

Golabek, G.J., Bourdon, B., Gerya, T.V., 2014. Numerical models of the thermomechanical evolution of planetesimals: Application to the acapulcoite-lodranite parent body. *Meteorit. Planet. Sci.* 49, 1083-1099.

Hartmann, W. K., Davis, D. R., 1975. Satellite-sized planetesimals and lunar origin. *Icarus* 24, 504-515.

Hevey, P.J., Sanders, I.S., 2006. A model for planetesimal meltdown by ^{26}Al and its implications for meteorite parent bodies, *Meteorit. Planet. Sci.* 41, 95-106.

Herzberg, C., Raterron, P., Zhang, J., 2000. New experimental observations on the anhydrous solidus for peridotite KLB-1. *Geochem. Geophys. Geosyst.* 1, 2000GC000089.

Jacobsen, B., Yin, Q.-Z., Moynier, F., Amelin, Y., Krot, A.N., Nagashima, K., Hutcheon, I.D., Palme, H., 2008. ^{26}Al - ^{26}Mg and ^{207}Pb - ^{206}Pb systematics of Allende CAIs: Canonical solar initial $^{26}\text{Al}/^{27}\text{Al}$ ratio reinstated. *Earth Planet. Sci. Lett.* 272, 353-364.

Jutzi, M., Asphaug, E., Gillet, P., Barrat, J.-A., Benz, W., 2013. The structure of the asteroid 4 Vesta as revealed by models of planet-scale collisions. *Nature* 494, 207-210.

Jutzi, M., 2015. SPH calculations of asteroid disruptions: The role of pressure dependent failure models. *Planet. Space Sci.* 107, 3-9.

Jutzi, M., Holsapple, K.A., Wünnemann, K., Michel, P., 2015. Modeling asteroid collisions and impact processes. In *Asteroids IV* (P. Michel, F. DeMeo, and W. F. Bottke, eds.), Univ. of Arizona, Tucson, pp. 679-700.

Kameyama, M., Yuen, D.A., Karato, S.-i., 1999. Thermal-mechanical effects of low-temperature plasticity (the Peierls mechanism) on the deformation of a viscoelastic shear zone, *Earth Planet. Sci. Lett.* 168, 159-172.

Karato, S.-i., Murthy, V.R., 1997. Core formation and chemical equilibrium in the Earth I. Physical considerations. *Phys. Earth Planet. Int.* 100, 61-79.

Katayama, I., Karato, S.-i., 2008. Low-temperature, high-stress deformation of olivine under water-saturated conditions. *Phys. Earth Planet. Int.* 168, 125-133.

- Keller, T., Tackley, P.J., 2009. Towards self-consistent modelling of the martian dichotomy: The influence of one-ridge convection on crustal thickness distribution. *Icarus* 202, 429-443.
- Kraichnan R.H., 1962. Turbulent thermal convection at arbitrary Prandtl number. *Phys. Fluids* 5, 1374-1389.
- Liebske, C., Schmickler, B., Terasaki, H., Poe, B.T., Suzuki, A., Funakoshi, K.-I., Ando, R., Rubie, D.C., 2005. Viscosity of peridotite liquid up to 13 GPa: Implications for magma ocean viscosities. *Earth Planet. Sci. Lett.* 240, 589-604.
- Lodders, K., Fegley, B., 1998. *The Planetary Scientist's Companion*. Oxford Univ. Press, New York, 371pp.
- Mackwell, S.J., 1991. High-temperature rheology of enstatite: Implications for creep in the mantle. *Geophys. Res. Lett.* 18, 2027-2030.
- Marinova, M.M., Aharonson, O., Asphaug, E., 2008. Mega-impact formation of the Mars hemispheric dichotomy. *Nature* 453, 1216-1219.
- Marinova, M.M., Aharonson, O., Asphaug, E., 2011. Geophysical consequences of planetary scale impacts into a Mars-like planet. *Icarus* 211, 960-985.
- Melosh, H.J., 1989. *Impact Cratering: A Geologic Process*. Monographs on Geology and Geophysics. 11.
- Melosh, H.J., 1990. Giant impacts and the thermal state of the early Earth. In: *Origin of the Earth*, edited by H. E. Newsom & J. H. Jones, Oxford Univ. Press, 69-83.
- Melosh, H.J., 2007. A hydrocode equation of state for SiO₂. *Meteor. Planet. Sci.* 42, 2079-2098.
- McKenzie, D., Bickle, M.J., 1988. The volume and composition of melt generated by extension of the lithosphere. *J. Petr.* 29, 625-679.
- Mezger, K., Debaille, V., Kleine, T., 2013. Core Formation and Mantle Differentiation on Mars. *Space Science Rev.* 174, 27-48.
- Morishima, R., Golabek, G.J. and Samuel, H., 2013. N-body simulations of oligarchic growth of Mars: Implications for Hf-W chronology. *Earth Planet. Sci. Lett.* 366, 6-16.
- Nimmo, F., Kleine, T., 2007. How rapidly did Mars accrete? Uncertainties in the Hf-W timing of core formation. *Icarus* 191, 497-504.
- Nimmo, F., Hart, S.D., Korycansky, D.G., Agnor, C.B., 2008. Implications of an impact origin for the martian hemispheric dichotomy. *Nature* 453, 1220-1223.
- Pinkerton, H., Stevenson, R.J., 1992. Methods of determining the rheological properties of magmas at subliquidus temperatures. *J. Volcan. Geotherm. Res.* 53, 47-66.
- Ranalli, G., 1995. *Rheology of the Earth*, second ed., Chapman & Hall, London, UK, 436pp.
- Reese, C.C., Solomatov, V.S., 2006. Fluid Dynamics of local martian magma oceans. *Icarus* 184, 102-120.
- Reese, C.C., Solomatov, V.S., 2010. Early martian dynamo generation due to giant impacts. *Icarus* 207, 82-97.
- Reese, C.C., Orth, C.P., Solomatov, V.S., 2010. Impact origin for the martian crustal dichotomy: Half-emptied or half-filled? *J. Geophys. Res.* 115, E05004.
- Reufer, A., Meier, M.M.M., Benz, W. & Wieler, R., 2012. A hit-and-run Giant Impact scenario. *Icarus* 221, 296-299.
- Roberts, J.H., Zhong, S., 2006. Degree-1 convection in the Martian mantle and the origin of the hemispheric dichotomy. *J. Geophys. Res.* 111, E06013.
- Rolf, T., Zhu, M.-H., Wünnemann, K., Werner, S.C., 2017. The role of impact bombardment history in lunar evolution. *Icarus* 286, 138-152.
- Rubie, D., Melosh, H.J., Reid, J.E., Liebske, C., Richter, K., 2003. Mechanisms of metal-silicate equilibration

in the terrestrial magma ocean. *Earth Planet. Sci. Lett.* 205, 239-255.

Rubie, D.C., Nimmo, F., Melosh, H.J., 2015. Formation of the Earth's core. In *Treatise on Geophysics*, 2nd ed., Volume 9: Evolution of the Earth. Stevenson D. J. (ed.), Amsterdam: Elsevier B.V. pp. 43-79.

Schmeling, H., Babeyko, A.Y., Enns, A., Faccenna, C., Funiciello, F., Gerya, T.V., Golabek, G.J., Grigull, S., Kaus, B.J.P., Morra, G., Schmalholz, S.M., van Hunen, J., 2008. A benchmark comparison of spontaneous subduction models - Towards a free surface. *Phys. Earth Planet. Int.* 171, 198-223.

Shoemaker, E.M., 1962. Interpretation of lunar craters. In: Kopal, Z. (Ed.), *Physics and Astronomy of the Moon*. Academic Press, New York, pp. 283-359.

Siggia, E.D., 1994. High Rayleigh number convection. *Annu. Rev. Fluid Mech.* 26, 137-168.

Solomatov, V.S., 2015. Magma oceans and primordial mantle differentiation. In: Stevenson, D.J. (Ed.), *Treatise on Geophysics*, 2nd ed., Evolution of the Earth, vol. 9., Elsevier B.V., Amsterdam, Netherlands, pp. 81-104.

Senft, L.E., Stewart, S.T., 2009. Dynamic fault weakening and the formation of large impact craters. *Earth Planet. Sci. Lett.* 287, 471-482.

Šrámek, O., Zhong, S., 2010. Long-wavelength stagnant-lid convection with hemispheric variation in lithospheric thickness: link between Martian crustal dichotomy and Tharsis? *J. Geophys. Res.* 115, E09010.

Šrámek, O., Zhong, S., 2012. Martian crustal dichotomy and Tharsis formation by partial melting coupled to early plume migration. *J. Geophys. Res.* 117, E01005.

Stolper, E., Hager, B.H., Walker, D., Hays, J.F., 1981. Melt segregation from partially molten source regions - The importance of melt density and source region size. *J. Geophys. Res.* 86, 6261-6271.

Suzuki, A., Ohtani, E., Kato, T., 1998. Density and thermal expansion of a peridotite melt at high pressure. *Phys. Earth Planet. Int.* 107, 53-61.

Tackley, P.J., Schubert, G., Glatzmaier, G.A., Schenk, P., Ratcliff, J.T., 2001. Three-dimensional simulations of mantle convection in Io. *Icarus* 149, 79-93.

Tackley, P.J., 2008. Modelling compressible mantle convection with large viscosity contrasts in a three-dimensional spherical shell using the yin-yang grid. *Phys. Earth Planet. Int.* 171, 7-18.

Taylor, S.R., McLennan, S.M., 2009. *Planetary Crusts: Their Composition, Origin and Evolution*. Cambridge Univ. Press, Cambridge, UK, 404pp.

Thompson, S.L., Lauson, H.S., 1972. Improvements in the CHART-D Radiation-hydrodynamic code III: Revised analytic equations of state. *Technical report SC-RR-71 0714*.

Thrane, K., Bizzarro, M., Baker, J.A., 2006. Extremely brief formation interval for refractory inclusions and uniform distribution of ^{26}Al in the early Solar System. *Astrophys. J.* 646, L159-L162.

Tillotson, J.H., 1962. *Metallic Equations of State for Hypervelocity Impact. GA-3216, General Atomic, San Diego, CA*.

Tkalcec, B.J., Golabek, G.J., Brenker, F.E., 2013. Solid-state plastic deformation in the dynamic interior of a differentiated asteroid. *Nat. Geosci.* 6, 93-97.

Trønnes, R.G., Frost, D.J., 2002. Peridotite melting and mineral-melt partitioning of major and minor elements at 22–24.5 GPa. *Earth Planet. Sci. Lett.* 197, 117-131.

Turcotte D. L., Schubert G., 2014. *Geodynamics*, 3rd ed. New York: Cambridge University Press. 636 pp.

Wade, J., Wood, B.J., 2005. Core formation and the oxidation state of the Earth. *Earth Planet. Sci. Lett.* 236, 78-95.

- Weinberg, R.F., Podladchikov, Y., 1994. Diapiric ascent of magmas through power law crust and mantle. *J. Geophys. Res.* 99, 9543-9559.
- Weinstein, S.A., 1995. The effects of a deep mantle endothermic phase change on the structure of thermal convection in silicate planets. *J. Geophys. Res.* 100, 11719-11728.
- Wetherill, G.W., 1985. Occurrence of giant impacts during the growth of the terrestrial planets. *Science* 228, 877-879.
- Wilhelms, D.E., Squyres, S.W., 1984. The martian dichotomy may be due to a giant impact. *Nature* 309, 138-140.
- Yunker, M.L., Van Orman, J.A., 2007. Interdiffusion of solid iron and nickel at high pressure, *Earth Planet. Sci. Lett.* 254, 203-213.
- Zahnle, K.J., Kasting, J.F., Pollack, J.B., 1988. Evolution of a steam atmosphere during Earth's accretion. *Icarus* 74, 62-97.
- Ziethel, R., Spohn, T., 2007. Two-dimensional stokes flow around a heated cylinder: A possible application for diapirs in the mantle. *J. Geophys. Res.* 112, B09403.
- Zhong, S., 2009. Migration of Tharsis volcanism on Mars caused by differential rotation of the lithosphere. *Nat. Geosci.* 2, 19-23.
- Zhong, S., Zuber, M.T., 2001. Degree-1 mantle convection and the crustal dichotomy on Mars. *Earth Planet. Sci. Lett.* 189, 75-84.

Figures

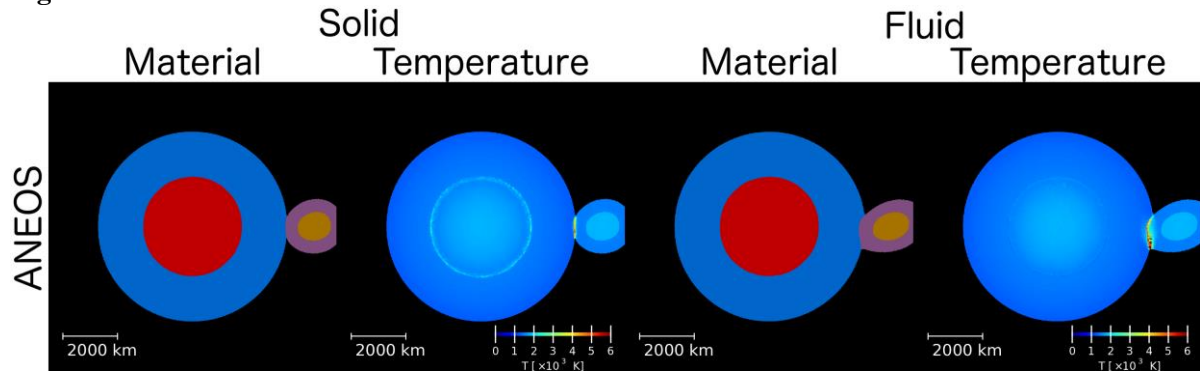


Figure 1: Grazing impact simulations at $t = 0$ s. The impactor's trajectory is clockwise. Shown is a slice at 1000 km depth inside the impact plane. Plots are centered on the center of mass of the target body. Only simulations using ANEOS are shown here; models using Tillotson show almost no difference at this stage. Temperature distributions for solid and fluid rheologies according to captions. Colors for material distribution are as follows: blue for target mantle, purple for impactor mantle, red for target core and orange for impactor core.

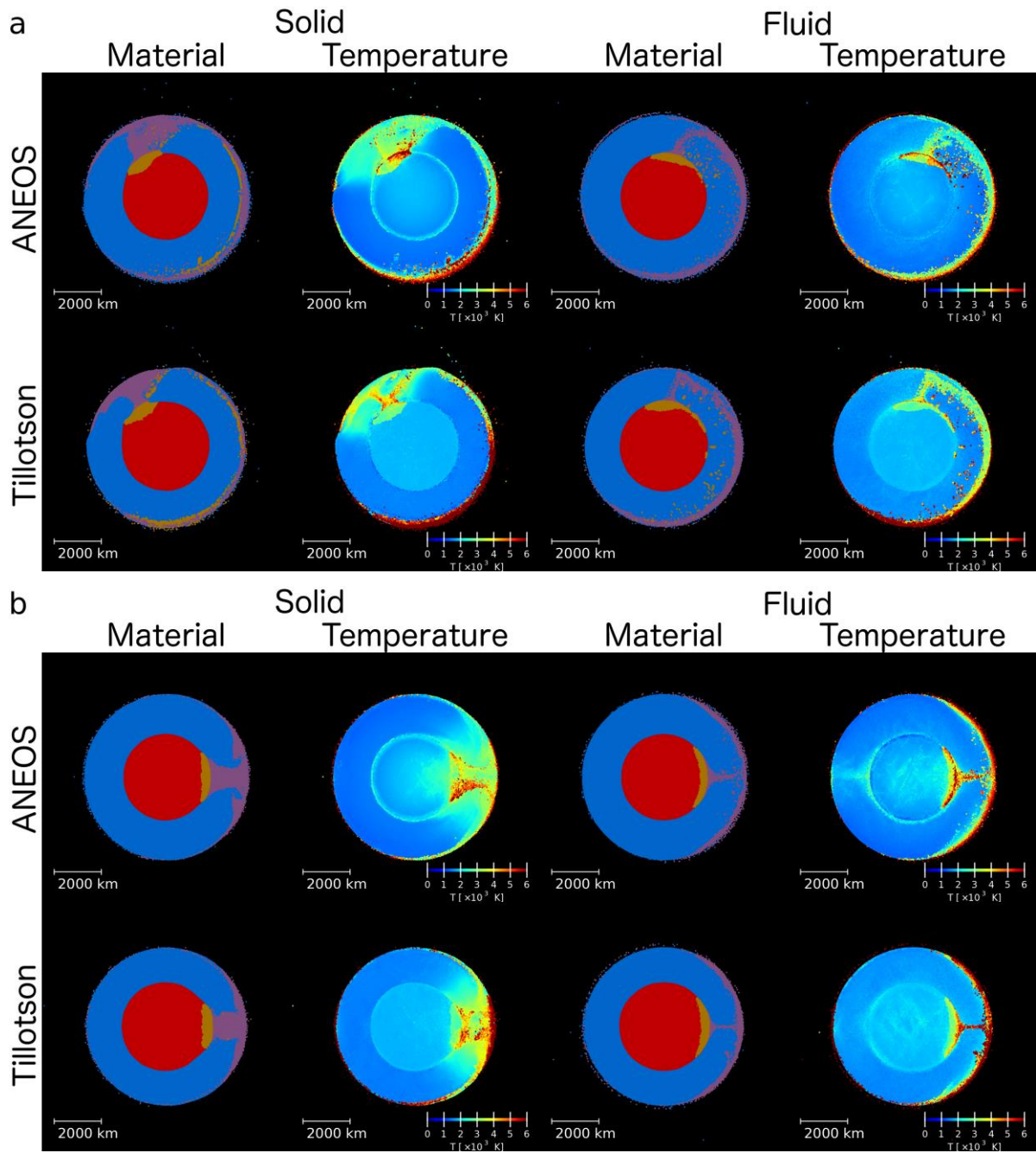


Figure 2: Material and temperature distributions resulting from the (a) grazing collision simulations and (b) head-on collisions, at $t = 18$ hours after the impact. Colors for material distribution as given in Figure 1. Note that due to the grazing impacts, the targets have rotated clockwise by ~ 270 degrees.

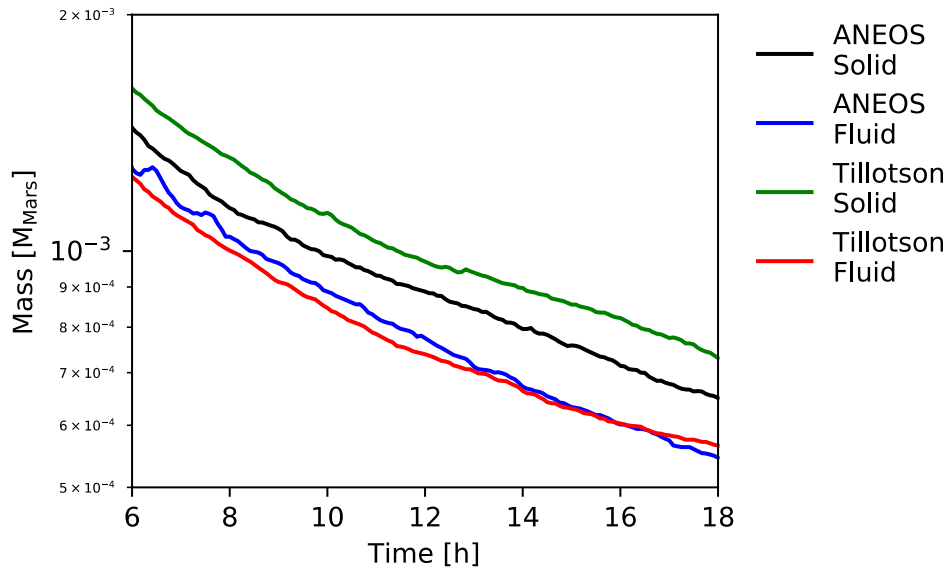


Figure 3: Remaining ejecta in orbit as a function of time for the grazing cases shown in Figure 2a.

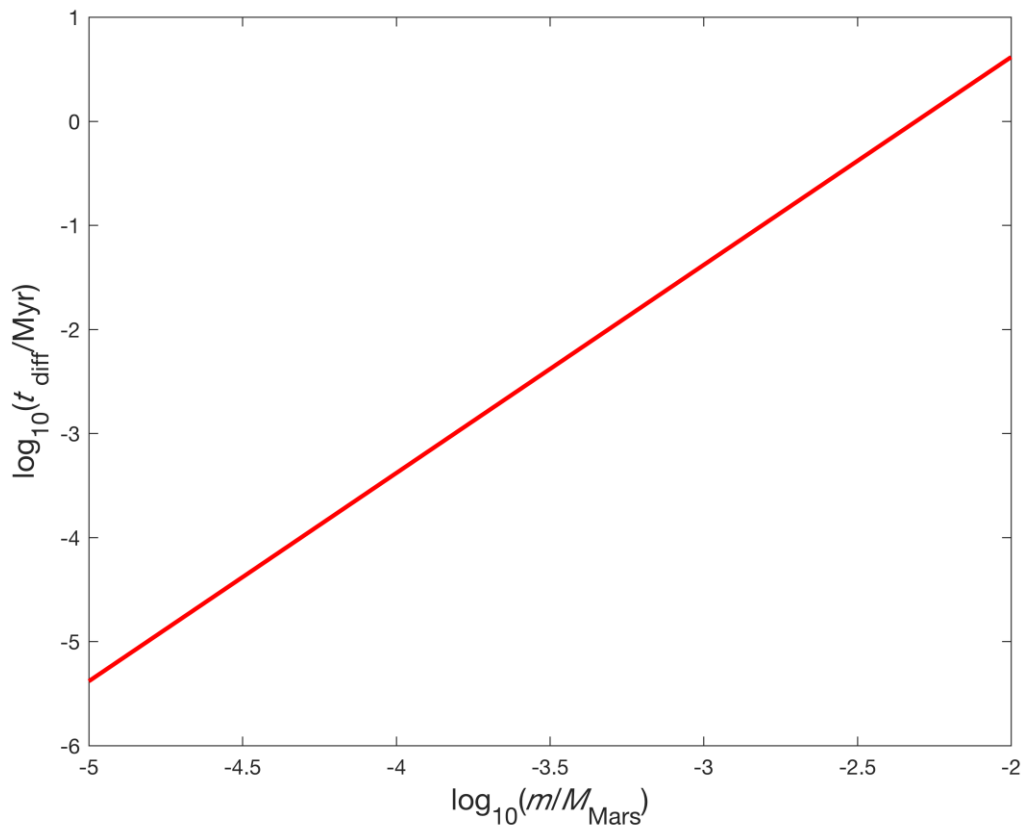


Figure 4: Characteristic cooling timescale for the disregarded ejecta material when spread out into a global surface layer.

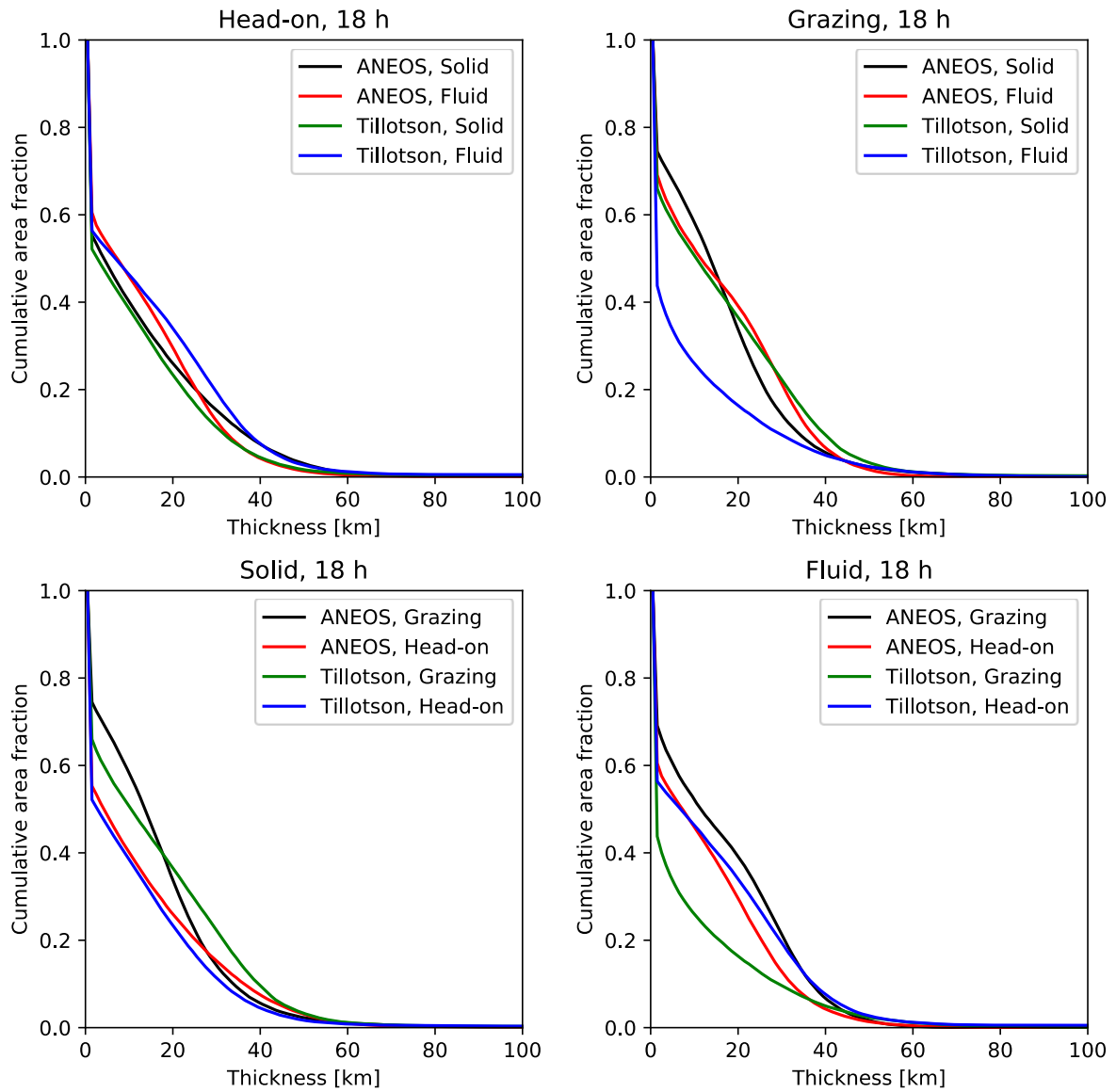


Figure 5: Cumulative crustal thickness distributions at $\sim 5 \cdot 10^5$ yr after the collision for different impact angle (upper row) and different rheology used in the SPH simulation (lower row). The curves show for each case the fraction of the surface area that has an underlying crust of a thickness larger than the value given on the x-axis.

Head-on collision

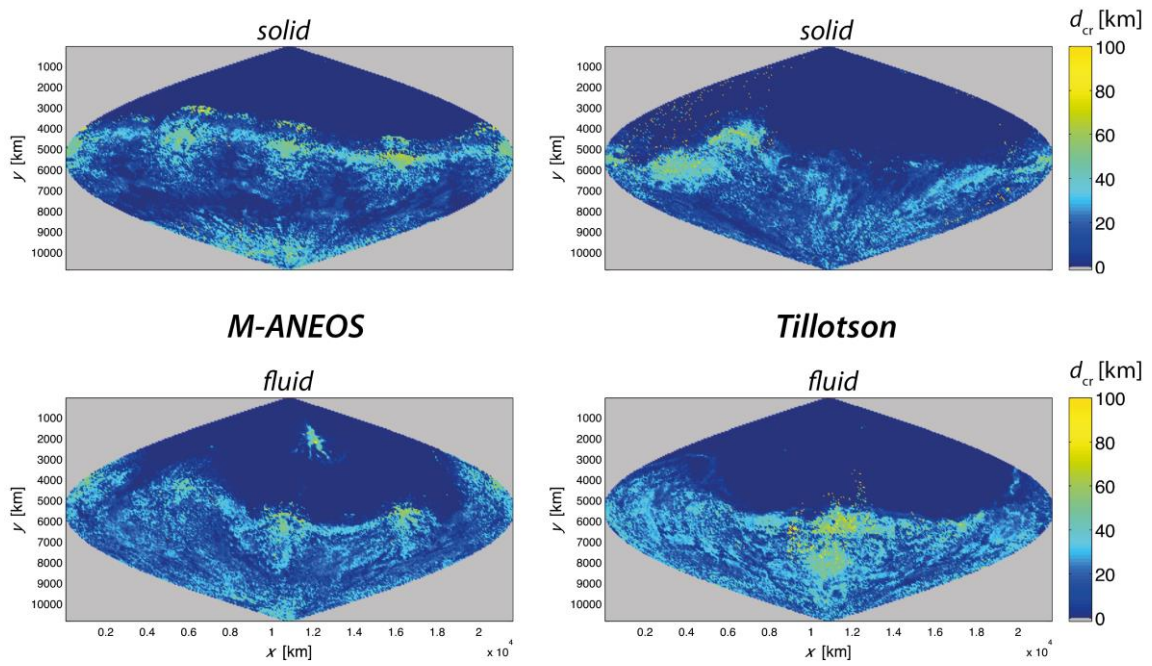


Figure 6: Maps of crustal thickness distribution at $\sim 5 \cdot 10^5$ yr after the collision resulting from head-on collisions using the Mercator equal-area projection.

Grazing collision

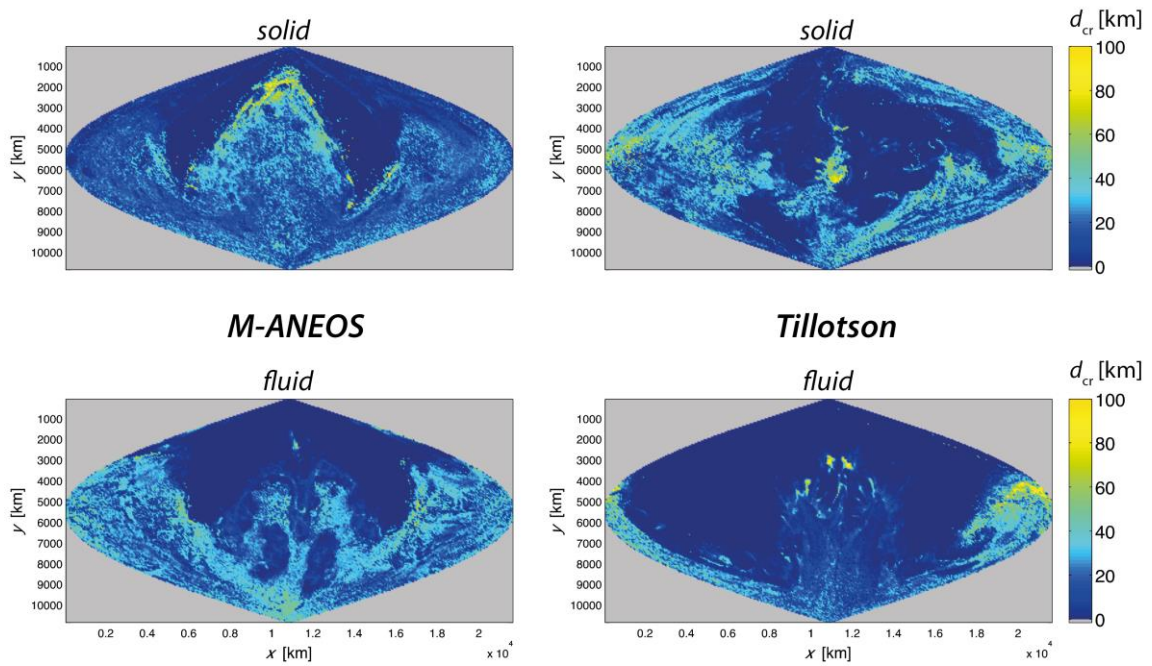


Figure 7: Maps of crustal thickness distribution at $\sim 5 \cdot 10^5$ yr after the collision resulting from grazing collisions using the Mercator equal-area projection.

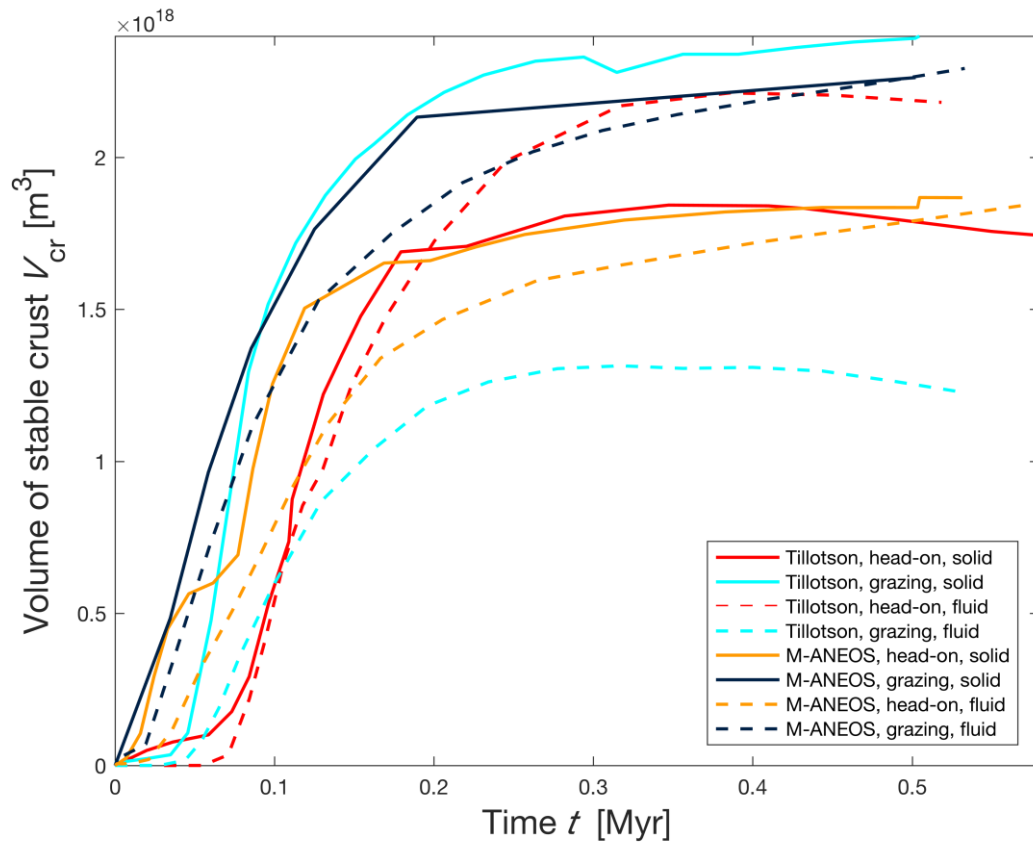


Figure 8: Time evolution of the volume of stable crust (disconnected crustal drips are disregarded).

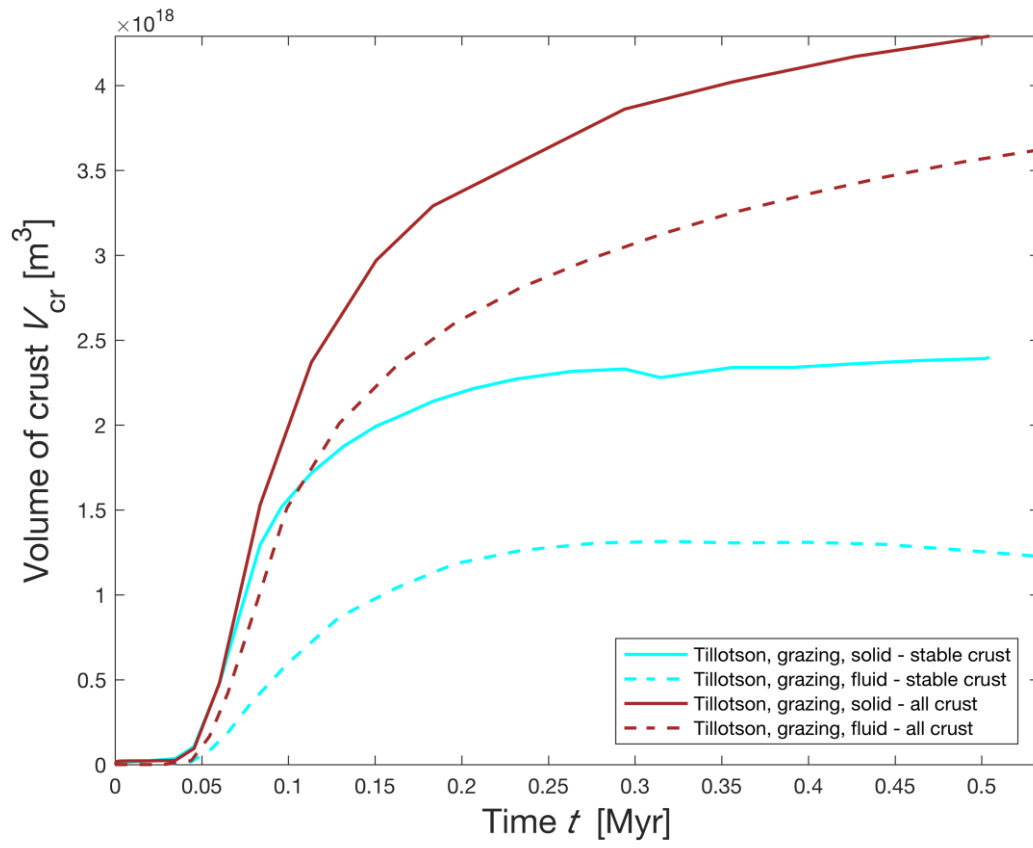


Figure 9: Time evolution of the volume of stable crust (cyan coloured lines) and total volume of crust (auburn coloured lines) for the two extreme cases (coll02, coll08) from Figure 8.

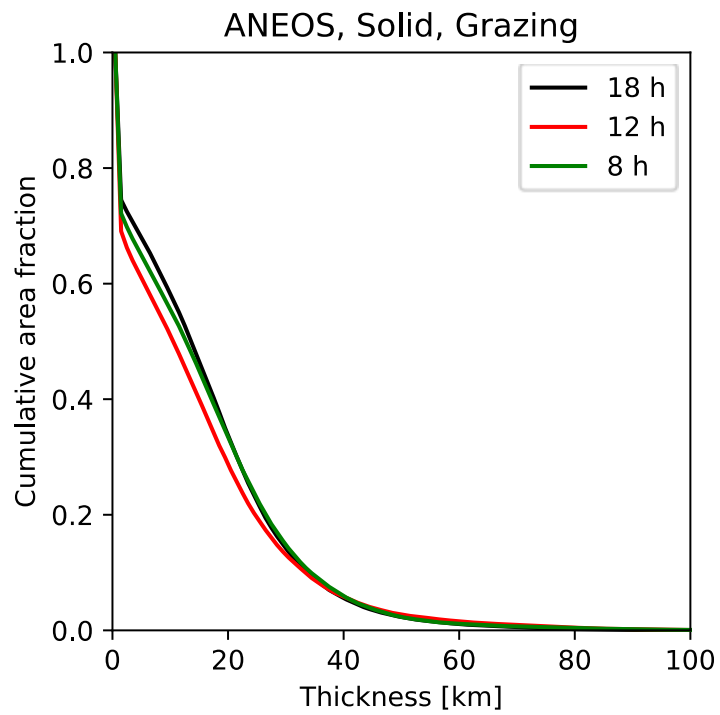


Figure 10: Cumulative crustal thickness distributions at $\sim 5 \cdot 10^5$ yr after the collision for the nominal case using different SPH-I3ELVIS transfer times.

Tables

Table 1: List of numerical models

<i>Model name</i>	<i>Impact angle [degrees]</i>	<i>EoS</i>	<i>Transfer time SPH-I3ELVIS [h]</i>	<i>SPH rheology</i>
coll01	0	Tillotson	18	solid
coll02	45	Tillotson	18	solid
coll03	0	M-ANEOS	18	solid
coll04	45	M-ANEOS	18	solid
coll05	45	M-ANEOS	8	solid
coll06	45	M-ANEOS	12	solid
coll07	0	Tillotson	18	fluid
coll08	45	Tillotson	18	fluid
coll09	0	M-ANEOS	18	fluid
coll10	45	M-ANEOS	18	fluid

Table 2: Physical parameters used in I3ELVIS

Parameter	Symbol	Value	Units	Reference
Density of uncompressed silicate melt	$\rho_{\text{Si-liq}}$	2900	kg/m ³	(1,2)
Density of uncompressed solid silicates	$\rho_{\text{Si-sol}}$	3500	kg/m ³	(1)
Temperature of space (sticky air)	T_{sa}	220	K	(3)
Activation energy	E_{a}	470	kJ/mol	(4)
Activation volume	V_{a}	$8 \cdot 10^{-6}$	m ³ /mol	(5)
Dislocation creep onset stress	σ_0	$3 \cdot 10^7$	Pa	(6)
Power law exponent	n	4		(4)
Cohesion	C	10^8	Pa	(5)
Internal friction coefficient of solid silicates	f	0.3		(7)
Latent heat of silicate melting	L_{Si}	400	kJ/kg	(6)
Silicate melt fraction at rheological transition	φ_{crit}	0.4		(8,9)
Heat capacity of silicates	c_{p}	1000	J/(kg K)	(6)
Thermal expansivity of solid silicates	$\alpha_{\text{Si-sol}}$	$3 \cdot 10^{-5}$	1/K	(2)
Thermal expansivity of molten silicates	$\alpha_{\text{Si-liq}}$	$6 \cdot 10^{-5}$	1/K	(2)
Thermal conductivity of solid silicates	k	3	W/(m K)	(6)
Thermal conductivity of molten silicates	k_{eff}	$\leq 10^6$	W/(m K)	(10)

References: (1) Stolper et al. (1981), (2) Suzuki et al. (1998), (3) Lodders & Fegley (1998), (4) Ranalli (1995), (5) Golabek et al. (2011), (6) Turcotte & Schubert (2014), (7) Escartín et al. (2001), (8) Solomatov (2015), (9) Costa et al. (2009), (10) Golabek et al. (2014)

Appendix A

Equations for the disc's vertical structure

This appendix shows the methodology to compute the gas disc's vertical structure in the planetary formation model used in this thesis. These equations are not directly solved, but instead are used to build pre-determined values of the quantities that depend on both the location r and the local gas surface density Σ_g .

We follow the prescription from Papaloizou and Terquem (1999) and take into account the vertical energy transport. The viscous dissipation due to radial shearing of disc produces energy, which need to be transported away, in the direction of the disc's surface where it can be radiated away. The energy production rate is

$$\frac{\partial L}{\partial z} = \frac{9}{4} \rho \nu \Omega_k^2 \quad (\text{A.1})$$

where L is the energy flux, otherwise referred as the luminosity and ν the kinematic viscosity. The energy flux induces a temperature gradient in the disc. We assume that energy transport is always radiative and thus write

$$L = -\frac{16}{3} \frac{\pi \sigma T^3}{\kappa \rho} \frac{\partial T}{\partial z} \quad (\text{A.2})$$

where T is the gas temperature, κ the opacity and σ the Stefan-Boltzmann constant. This gives a full set of equation to be solved together given an equation of state for $\rho(p, T)$ and opacities $\kappa(\rho, T)$. The sound speed is given by the ideal gas equation

$$c_s^2 = \gamma \frac{k_b T}{\mu m_H} \quad (\text{A.3})$$

where γ is the adiabatic index ($\gamma = c_p/c_v$), k_b the Boltzmann constant, μ the mean molecular weight and m_H the proton's mass. The last missing elements are the boundary conditions. The surface of the disc is set at $z = H$ and the boundary conditions are derived from the integration of the differential equations themselves, but assuming an isothermal case as well as a constant opacity. The pressure at the surface is obtained by

rewriting equation (2.1) keeping in mind that $\partial\tau/\partial\rho = \kappa$

$$p_s = \frac{\Omega_k^2 H \tau_s}{\kappa_s} \quad (\text{A.4})$$

with τ_s the optical depth of the surface. Then we have a couple of equations giving the energy flux

$$L_s = \frac{3}{8\pi} \dot{M}_* \Omega_k^2 \quad (\text{A.5})$$

$$L_0 = 0 \quad (\text{A.6})$$

where \dot{M}_* is the steady state radial gas flow; see equation (2.9). The latter comes from symmetry across the mid-plane. The surface temperature is also linked to the energy flux with

$$2\sigma (T_s^4 - T_b^4) - \frac{9}{8} \frac{\nu \Omega_k^2}{\kappa_s} - L_s = 0. \quad (\text{A.7})$$

The surface temperature may also appear in ν depending on how it is computed; this is for instance the case with the value chosen below, through the sound speed. T_b is the background temperature, which we take to be 10 K as in molecular clouds (Dobbs et al. 2014). The surface temperature found using this boundary condition is only due to the local energy production. The central star also emits energy, which changes the equilibrium temperature on the disc surface. A straightforward correction to the above temperature is to use the irradiation temperature from Hueso and Guillot (2005)

$$T_{s,\text{irr}}^4 = T_s^4 + T_{\text{irr}}^4 \quad ; \quad T_{\text{irr}}^4 = T_\star^4 \left(\frac{2}{3\pi} \left(\frac{R_\star}{r} \right)^3 + \frac{1}{2} \left(\frac{R_\star}{r} \right)^2 \frac{H}{r} \left(\frac{\partial \ln H}{\partial \ln r} - 1 \right) \right) \quad (\text{A.8})$$

with T_\star and R_\star the surface temperature and radius of the central star. The first term in the parenthesis is for a flat disc, the second one is due to the flaring. The effect of stellar irradiation on planet populations was studied in Fouchet et al. (2012).

Bibliography

- Yann Alibert, Christoph Mordasini, and Willy Benz. Migration and giant planet formation. *Astron. Astrophys.*, 417:L25–L28, April 2004. arXiv:astro-ph/0403574. doi:10.1051/0004-6361:20040053.
- Yann Alibert, Christoph Mordasini, Willy Benz, and Christophe Winisdoerffer. Models of giant planet formation with migration and disc evolution. *Astron. Astrophys.*, 434:343–353, April 2005. arXiv:astro-ph/0412444. doi:10.1051/0004-6361:20042032.
- Yann Alibert, Frédéric Carron, Andrea Fortier, Samuel Pfyffer, Willy Benz, Christoph Mordasini, and David Swoboda. Theoretical models of planetary system formation: mass vs. semi-major axis. *Astron. Astrophys.*, 558:A109, October 2013. arXiv:1307.4864. doi:10.1051/0004-6361/201321690.
- Sean M. Andrews and Jonathan P. Williams. Circumstellar Dust Disks in Taurus-Auriga: The Submillimeter Perspective. *Astrophys. J.*, 631:1134–1160, October 2005. arXiv:astro-ph/0506187. doi:10.1086/432712.
- Sean M. Andrews and Jonathan P. Williams. A Submillimeter View of Circumstellar Dust Disks in ρ Ophiuchi. *Astrophys. J.*, 671:1800–1812, December 2007. arXiv:0708.4185. doi:10.1086/522885.
- Sean M. Andrews, David J. Wilner, A. M. Hughes, Chunhua Qi, and Cornelis P. Dullemond. Protoplanetary Disk Structures in Ophiuchus. II. Extension to Fainter Sources. *Astrophys. J.*, 723:1241–1254, November 2010. arXiv:1007.5070. doi:10.1088/0004-637X/723/2/1241.
- Philip J. Armitage. *Astrophysics of Planet Formation*. Cambridge University Press, December 2009. ISBN 978-0-511-69136-2.
- Erik Asphaug. Similar-sized collisions and the diversity of planets. *Chemie der Erde / Geochemistry*, 70:199–219, 2010. doi:10.1016/j.chemer.2010.01.004.
- Erik Asphaug and Andreas Reufer. Mercury and other iron-rich planetary bodies as relics of inefficient accretion. *Nat. Geosci.*, 7:564–568, August 2014. doi:10.1038/ngeo2189.
- Erik Asphaug, Craig B. Agnor, and Quentin Williams. Hit-and-run planetary collisions. *Nature*, 439:155–160, January 2006. doi:10.1038/nature04311.

- Josh Barnes and Piet Hut. A hierarchical $O(N \log N)$ force-calculation algorithm. *Nature*, 324:446–449, December 1986. doi:10.1038/324446a0.
- Willy Benz. An introduction to computation methods in hydrodynamics. In C. B. de Loore, editor, *Late stages of stellar evolution, computational methods in astrophysical hydrodynamics*, volume 373, pages 258–312. Springer, 1991. ISBN 0387536205.
- Willy Benz and Erik Asphaug. Impact simulations with fracture. I - Method and tests. *Icarus*, 107:98, January 1994. doi:10.1006/icar.1994.1009.
- Willy Benz and Erik Asphaug. Simulations of brittle solids using smooth particle hydrodynamics. *Comput. Phys. Commun.*, 1-2:253–265, 1995. doi:10.1016/0010-4655(94)00176-3.
- Willy Benz and Erik Asphaug. Catastrophic Disruptions Revisited. *Icarus*, 142:5–20, November 1999. arXiv:astro-ph/9907117. doi:10.1006/icar.1999.6204.
- Willy Benz, Augustin Anic, J. Horner, and James A. Whitby. The Origin of Mercury. *Space Sci. Rev.*, 132:189–202, October 2007. doi:10.1007/s11214-007-9284-1.
- Willy Benz, Shigeru Ida, Yann Alibert, Douglas Lin, and Christoph Mordasini. Planet Population Synthesis. In Henrik Beuther, Ralf S. Klessen, Cornelis P. Dullemond, and Thomas Henning, editors, *Protostars and Planets VI*, pages 691–713. University of Arizona Press, 2014. arXiv:1402.7086. doi:10.2458/azu_uapress_9780816531240-ch030.
- Gerhard Beutler. *Methods of celestial mechanics. Vol. I: Physical, mathematical, and numerical principles*. Springer, 2005. ISBN 3-540-40749-9.
- Bertram Bitsch, Michiel Lambrechts, and Anders Johansen. The growth of planets by pebble accretion in evolving protoplanetary discs. *Astron. Astrophys.*, 582:A112, October 2015. arXiv:1507.05209. doi:10.1051/0004-6361/201526463.
- Peter Bodenheimer and James B. Pollack. Calculations of the accretion and evolution of giant planets The effects of solid cores. *Icarus*, 67:391–408, September 1986. doi:10.1016/0019-1035(86)90122-3.
- Alan P. Boss. Rapid Formation of Outer Giant Planets by Disk Instability. *Astrophys. J.*, 599:577–581, December 2003. doi:10.1086/379163.
- Christopher H. Broeg and Willy Benz. Giant planet formation: episodic impacts versus gradual core growth. *Astron. Astrophys.*, 538:A90, February 2012. arXiv:1112.0498. doi:10.1051/0004-6361/201117038.
- Robin M. Canup. A Giant Impact Origin of Pluto-Charon. *Science*, 307:546–550, January 2005. doi:10.1126/science.1106818.
- Frédéric Carron. *Formation of multi-planetary systems*. PhD thesis, Universität Bern, February 2013.

- John E. Chambers. A hybrid symplectic integrator that permits close encounters between massive bodies. *Mon. Not. R. Astron. Soc.*, 304:793–799, April 1999. doi:10.1046/j.1365-8711.1999.02379.x.
- Robert I. Citron, Hidenori Genda, and Shigeru Ida. Formation of Phobos and Deimos via a giant impact. *Icarus*, 252:334–338, May 2015. arXiv:1503.05623. doi:10.1016/j.icarus.2015.02.011.
- Gareth S. Collins, H. Jay Melosh, and Boris A. Ivanov. Modeling damage and deformation in impact simulations. *Meteorit. Planet. Sci.*, 39:217–231, February 2004. doi:10.1111/j.1945-5100.2004.tb00337.x.
- P. Cresswell and Richard P. Nelson. Three-dimensional simulations of multiple protoplanets embedded in a protostellar disc. *Astron. Astrophys.*, 482:677–690, May 2008. arXiv:0811.4322. doi:10.1051/0004-6361:20079178.
- Aurélien Crida, Alessandro Morbidelli, and Frédéric Masset. On the width and shape of gaps in protoplanetary disks. *Icarus*, 181:587–604, April 2006. arXiv:astro-ph/0511082. doi:10.1016/j.icarus.2005.10.007.
- Nicolas Dauphas. The isotopic nature of the Earth’s accreting material through time. *Nature*, 541:521–524, January 2017. doi:10.1038/nature20830.
- Donald R. Davis, Daniel D. Durda, Francesco Marzari, Adriano Campo Bagatin, and Ricardo Gil-Hutton. Collisional Evolution of Small-Body Populations. In W. F. Bottke, Jr., A. Cellino, P. Paolicchi, and R. P. Binzel, editors, *Asteroids III*, pages 545–558. University of Arizona Press, March 2002.
- Kai-Martin Dittkrist, Christoph Mordasini, Hubert Klahr, Yann Alibert, and Thomas Henning. Impacts of planet migration models on planetary populations. Effects of saturation, cooling and stellar irradiation. *Astron. Astrophys.*, 567:A121, July 2014. arXiv:1402.5969. doi:10.1051/0004-6361/201322506.
- Clare L. Dobbs, Mark R. Krumholz, Javier Ballesteros-Paredes, Alberto D. Bolatto, Yasuno Fukui, Mark Heyer, Mordecai-M. Mac Low, Eve C. Ostriker, and Enrique Vázquez-Semadeni. Formation of Molecular Clouds and Global Conditions for Star Formation. In Henrik Beuther, Ralf S. Klessen, Cornelis P. Dullemond, and Thomas Henning, editors, *Protostars and Planets VI*, pages 3–26. University of Arizona Press, 2014. arXiv:1312.3223. doi:10.2458/azu_uapress_9780816531240-ch001.
- Carsten Dominik, Jürgen Blum, Jeffrey N. Cuzzi, and Gerhard Wurm. Growth of Dust as the Initial Step Toward Planet Formation. In Bo Reipurth, David Jewitt, and Klaus Keil, editors, *Protostars and Planets V*, page 783–800. University of Arizona Press, April 2007. arXiv:astro-ph/0602617.
- Cornelis P. Dullemond and Carsten Dominik. Dust coagulation in protoplanetary disks: A rapid depletion of small grains. *Astron. Astrophys.*, 434:971–986, May 2005. arXiv:astro-ph/0412117. doi:10.1051/0004-6361:20042080.

- Christoph Dürmann and Wilhelm Kley. Migration of massive planets in accreting disks. *Astron. Astrophys.*, 574:A52, February 2015. arXiv:1411.3190. doi:10.1051/0004-6361/201424837.
- Alexandre Emsenhuber. *Giant Impact*. Master thesis, Universität Bern, 2013.
- D. C. Fabrycky, J. J. Lissauer, D. Ragozzine, J. F. Rowe, J. H. Steffen, E. Agol, T. Barclay, N. Batalha, W. Borucki, D. R. Ciardi, E. B. Ford, T. N. Gautier, J. C. Geary, M. J. Holman, J. M. Jenkins, J. Li, R. C. Morehead, R. L. Morris, A. Shporer, J. C. Smith, M. Still, and J. Van Cleve. Architecture of Kepler’s Multi-transiting Systems. II. New Investigations with Twice as Many Candidates. *Astrophys. J.*, 790:146, August 2014. arXiv:1202.6328. doi:10.1088/0004-637X/790/2/146.
- J. A. Fernandez and W.-H. Ip. Some dynamical aspects of the accretion of Uranus and Neptune - The exchange of orbital angular momentum with planetesimals. *Icarus*, 58: 109–120, April 1984. doi:10.1016/0019-1035(84)90101-5.
- Martyn J. Fogg and Richard P. Nelson. The effect of type I migration on the formation of terrestrial planets in hot-Jupiter systems. *Astron. Astrophys.*, 472:1003–1015, September 2007. arXiv:0707.2674. doi:10.1051/0004-6361:20077950.
- Andrea Fortier, Yann Alibert, Frédéric Carron, Willy Benz, and Kai-Martin Dittkrist. Planet formation models: the interplay with the planetesimal disc. *Astron. Astrophys.*, 549:A44, January 2013. arXiv:1210.4009. doi:10.1051/0004-6361/201220241.
- Laure Fouchet, Yann Alibert, Christoph Mordasini, and Willy Benz. Effects of disk irradiation on planet population synthesis. *Astron. Astrophys.*, 540:A107, April 2012. doi:10.1051/0004-6361/201117617.
- François Fressin, Guillermo Torres, David Charbonneau, Stephen T. Bryson, Jessie Christiansen, Courtney D. Dressing, Jon M. Jenkins, Lucianne M. Walkowicz, and Natalie M. Batalha. The False Positive Rate of Kepler and the Occurrence of Planets. *Astrophys. J.*, 766:81, April 2013. arXiv:1301.0842. doi:10.1088/0004-637X/766/2/81.
- Peter Goldreich and Scott Tremaine. Disk-satellite interactions. *Astrophys. J.*, 241:425–441, October 1980. doi:10.1086/158356.
- Felipe González-Cataldo, Sergio Davis, and Gonzalo Gutiérrez. Melting curve of SiO₂ at multimegabar pressures: implications for gas giants and super-Earths. *Scientific Reports*, 6:26537, May 2016. doi:10.1038/srep26537.
- Carsten Güttler, Jürgen Blum, Andras Zsom, Chris W. Ormel, and Cornelis P. Dullemond. The outcome of protoplanetary dust growth: pebbles, boulders, or planetesimals?. I. Mapping the zoo of laboratory collision experiments. *Astron. Astrophys.*, 513:A56, April 2010. arXiv:0910.4251. doi:10.1051/0004-6361/200912852.
- William K. Hartmann and Donald R. Davis. Satellite-sized planetesimals and lunar origin. *Icarus*, 24:504–514, April 1975. doi:10.1016/0019-1035(75)90070-6.

- Yasuhiro Hasegawa and Shigeru Ida. Do Giant Planets Survive Type II Migration? *Astrophys. J.*, 774:146, September 2013. arXiv:1307.4811. doi:10.1088/0004-637X/774/2/146.
- Chushiro Hayashi. Structure of the Solar Nebula, Growth and Decay of Magnetic Fields and Effects of Magnetic and Turbulent Viscosities on the Nebula. *Progress of Theoretical Physics Supplement*, 70:35–53, 1981. doi:10.1143/PTPS.70.35.
- Daniel Herwartz, Andreas Pack, Bjarne Friedrichs, and Addi Bischoff. Identification of the giant impactor Theia in lunar rocks. *Science*, 344:1146–1150, June 2014. doi:10.1126/science.1251117.
- Natsuki Hosono, Takayuki R. Saitoh, and Junichiro Makino. Density-Independent Smoothed Particle Hydrodynamics for a Non-Ideal Equation of State. *Publ. Astron. Soc. Jpn*, 65:108, October 2013. arXiv:1307.0916. doi:10.1093/pasj/65.5.108.
- Natsuki Hosono, Takayuki R. Saitoh, Junichiro Makino, Hidenori Genda, and Shigeru Ida. The giant impact simulations with density independent smoothed particle hydrodynamics. *Icarus*, 271:131–157, June 2016. arXiv:1602.00843. doi:10.1016/j.icarus.2016.01.036.
- Kevin R. Housen and Keith A. Holsapple. On the fragmentation of asteroids and planetary satellites. *Icarus*, 84:226–253, March 1990. doi:10.1016/0019-1035(90)90168-9.
- Ricardo Hueso and Tristan Guillot. Evolution of protoplanetary disks: constraints from DM Tauri and GM Aurigae. *Astron. Astrophys.*, 442:703–725, November 2005. arXiv:astro-ph/0506496. doi:10.1051/0004-6361:20041905.
- Shigeru Ida and Douglas N. C. Lin. Toward a Deterministic Model of Planetary Formation. I. A Desert in the Mass and Semimajor Axis Distributions of Extrasolar Planets. *Astrophys. J.*, 604:388–413, March 2004. arXiv:astro-ph/0312144. doi:10.1086/381724.
- Shigeru Ida and Junichiro Makino. Scattering of planetesimals by a protoplanet - Slowing down of runaway growth. *Icarus*, 106:210, November 1993. doi:10.1006/icar.1993.1167.
- Satoshi Inaba, Hidekazu Tanaka, Kiyoshi Nakazawa, George W. Wetherill, and Eiichiro Kokubo. High-Accuracy Statistical Simulation of Planetary Accretion: II. Comparison with N-Body Simulation. *Icarus*, 149:235–250, January 2001. doi:10.1006/icar.2000.6533.
- Martin Jutzi. SPH calculations of asteroid disruptions: The role of pressure dependent failure models. *Planet. Space Sci.*, 107:3–9, March 2015. arXiv:1502.01860. doi:10.1016/j.pss.2014.09.012.
- Akimasa Kataoka, Hidekazu Tanaka, Satoshi Okuzumi, and Koji Wada. Fluffy dust forms icy planetesimals by static compression. *Astron. Astrophys.*, 557:L4, September 2013. arXiv:1307.7984. doi:10.1051/0004-6361/201322151.

- Eiichiro Kokubo and Shigeru Ida. Oligarchic Growth of Protoplanets. *Icarus*, 131:171–178, January 1998. doi:10.1006/icar.1997.5840.
- Eiichiro Kokubo and Shigeru Ida. Formation of Protoplanet Systems and Diversity of Planetary Systems. *Astrophys. J.*, 581:666–680, December 2002. doi:10.1086/344105.
- Stephan König, Carsten Münker, Simon Hohl, Holger Paulick, A. R. Barth, Markus Lagos, Jörg Pfänder, and Anette Büchl. The Earth’s tungsten budget during mantle melting and crust formation. *Geochim. Cosmochim. Acta*, 75:2119–2136, April 2011. doi:10.1016/j.gca.2011.01.031.
- Richard G. Kraus, Sarah T. Stewart, D. C. Swift, C. A. Bolme, R. F. Smith, S. Hamel, B. D. Hammel, D. K. Spaulding, D. G. Hicks, J. H. Eggert, and G. W. Collins. Shock vaporization of silica and the thermodynamics of planetary impact events. *J. Geophys. Res. (Planets)*, 117:E09009, September 2012. doi:10.1029/2012JE004082.
- A.-M. Lagrange, D. Gratadour, G. Chauvin, T. Fusco, D. Ehrenreich, D. Mouillet, G. Rousset, D. Rouan, F. Allard, É. Gendron, J. Charton, L. Mugnier, P. Rabou, J. Montri, and F. Lacombe. A probable giant planet imaged in the β Pictoris disk. VLT/NaCo deep L'-band imaging. *Astron. Astrophys.*, 493:L21–L25, January 2009. arXiv:0811.3583. doi:10.1051/0004-6361:200811325.
- E. Lajeunesse, J. B. Monnier, and G. M. Homsy. Granular slumping on a horizontal surface. *Phys. Fluids*, 17(10):103302, 2005. doi:10.1063/1.2087687.
- Man Hoi Lee and Stanton J. Peale. Dynamics and Origin of the 2:1 Orbital Resonances of the GJ 876 Planets. *Astrophys. J.*, 567:596–609, March 2002. doi:10.1086/338504.
- Zoë M. Leinhardt and Sarah T. Stewart. Full numerical simulations of catastrophic small body collisions. *Icarus*, 199:542–559, February 2009. arXiv:0811.0175. doi:10.1016/j.icarus.2008.09.013.
- Zoë M. Leinhardt and Sarah T. Stewart. Collisions between Gravity-dominated Bodies. I. Outcome Regimes and Scaling Laws. *Astrophys. J.*, 745:79, January 2012. arXiv:1106.6084. doi:10.1088/0004-637X/745/1/79.
- Min Li and Lin Xiao. Lifetimes and Accretion Rates of Protoplanetary Disks. *Astrophys. J.*, 820:36, March 2016. doi:10.3847/0004-637X/820/1/36.
- Douglas N. C. Lin and John Papaloizou. Tidal torques on accretion discs in binary systems with extreme mass ratios. *Mon. Not. R. Astron. Soc.*, 186:799–812, March 1979. doi:10.1093/mnras/186.4.799.
- Douglas N. C. Lin and John Papaloizou. On the tidal interaction between protoplanets and the primordial solar nebula. II - Self-consistent nonlinear interaction. *Astrophys. J.*, 307:395–409, August 1986a. doi:10.1086/164426.

- Douglas N. C. Lin and John Papaloizou. On the tidal interaction between protoplanets and the protoplanetary disk. III - Orbital migration of protoplanets. *Astrophys. J.*, 309:846–857, October 1986b. doi:10.1086/164653.
- Jack J. Lissauer. Planet formation. *Annu. Rev. Astron. Astrophys.*, 31:129–174, 1993. doi:10.1146/annurev.aa.31.090193.001021.
- Jack J. Lissauer, Olenka Hubickyj, Gennaro D’Angelo, and Peter Bodenheimer. Models of Jupiter’s growth incorporating thermal and hydrodynamic constraints. *Icarus*, 199:338–350, February 2009. arXiv:0810.5186. doi:10.1016/j.icarus.2008.10.004.
- Stephen H. Lubow and Gennaro D’Angelo. Gas Flow across Gaps in Protoplanetary Disks. *Astrophys. J.*, 641:526–533, April 2006. arXiv:astro-ph/0512292. doi:10.1086/500356.
- Donald Lynden-Bell and Jim E. Pringle. The evolution of viscous discs and the origin of the nebular variables. *Mon. Not. R. Astron. Soc.*, 168:603–637, September 1974. doi:10.1093/mnras/168.3.603.
- Eric E. Mamajek. Initial Conditions of Planet Formation: Lifetimes of Primordial Disks. In T. Usuda, M. Tamura, and M. Ishii, editors, *American Institute of Physics Conference Series*, volume 1158 of *American Institute of Physics Conference Series*, pages 3–10, August 2009. arXiv:0906.5011. doi:10.1063/1.3215910.
- Margarita M. Marinova, Oded Aharonson, and Erik Asphaug. Mega-impact formation of the Mars hemispheric dichotomy. *Nature*, 453:1216–1219, June 2008. doi:10.1038/nature07070.
- Michel Mayor and Didier Queloz. A Jupiter-mass companion to a solar-type star. *Nature*, 378:355–359, November 1995. doi:10.1038/378355a0.
- Héloïse Meheut, Zakaria Meliani, Peggy Varniere, and Willy Benz. Dust-trapping Rossby vortices in protoplanetary disks. *Astron. Astrophys.*, 545:A134, September 2012. arXiv:1208.4947. doi:10.1051/0004-6361/201219794.
- H. J. Melosh. A hydrocode equation of state for SiO₂. *Meteorit. Planet. Sci.*, 42:2079–2098, 2007. doi:10.1111/j.1945-5100.2007.tb01009.x.
- David A. Minton and Harold F. Levison. Planetesimal-driven migration of terrestrial planet embryos. *Icarus*, 232:118–132, April 2014. doi:10.1016/j.icarus.2014.01.001.
- Hiroshi Mizuno. Formation of the Giant Planets. *Progress of Theoretical Physics*, 64:544–557, August 1980. doi:10.1143/PTP.64.544.
- Paul Mollière and Christoph Mordasini. Deuterium burning in objects forming via the core accretion scenario. Brown dwarfs or planets? *Astron. Astrophys.*, 547:A105, November 2012. arXiv:1210.0538. doi:10.1051/0004-6361/201219844.

- Joe J. Monaghan. Smoothed particle hydrodynamics. *Annu. Rev. Astron. Astrophys.*, 30:543–574, 1992. doi:10.1146/annurev.aa.30.090192.002551.
- Joe J. Monaghan. SPH and Riemann Solvers. *J. Comput. Phys.*, 136:298–307, 1997.
- Joe J. Monaghan and John C. Lattanzio. A refined particle method for astrophysical problems. *Astron. Astrophys.*, 149:135–143, August 1985.
- Christoph Mordasini, Yann Alibert, and Willy Benz. Extrasolar planet population synthesis. I. Method, formation tracks, and mass-distance distribution. *Astron. Astrophys.*, 501:1139–1160, July 2009. arXiv:0904.2524. doi:10.1051/0004-6361/200810301.
- Christoph Mordasini, Yann Alibert, H. Klahr, and Thomas Henning. Characterization of exoplanets from their formation. I. Models of combined planet formation and evolution. *Astron. Astrophys.*, 547:A111, November 2012. arXiv:1206.6103. doi:10.1051/0004-6361/201118457.
- Christoph Andrea Mordasini. *Planetesimal Impacts into Protoplanetary Atmospheres*. Master thesis, Universität Bern, 2004.
- F. Ott and E. Schnetter. A modified SPH approach for fluids with large density differences. *ArXiv Physics e-prints*, March 2003. arXiv:physics/0303112.
- Sijme-J. Paardekooper, Clément Baruteau, Aurélien Crida, and Wilhelm Kley. A torque formula for non-isothermal type I planetary migration - I. Unsaturated horseshoe drag. *Mon. Not. R. Astron. Soc.*, 401:1950–1964, January 2010. arXiv:0909.4552. doi:10.1111/j.1365-2966.2009.15782.x.
- Kaveh Pahlevan and David J. Stevenson. Equilibration in the aftermath of the lunar-forming giant impact. *Earth Planet. Sci. Lett.*, 262:438–449, October 2007. arXiv:1012.5323. doi:10.1016/j.epsl.2007.07.055.
- John C. B. Papaloizou and John D. Larwood. On the orbital evolution and growth of protoplanets embedded in a gaseous disc. *Mon. Not. R. Astron. Soc.*, 315:823–833, July 2000. arXiv:astro-ph/9911431. doi:10.1046/j.1365-8711.2000.03466.x.
- John C. B. Papaloizou and Caroline Terquem. Critical Protoplanetary Core Masses in Protoplanetary Disks and the Formation of Short-Period Giant Planets. *Astrophys. J.*, 521:823–838, August 1999. arXiv:astro-ph/9903310. doi:10.1086/307581.
- Samuel Pfyffer. *On the long term evolution of planetary systems*. PhD thesis, Universität Bern, September 2015.
- James B. Pollack, Olenka Hubickyj, Peter Bodenheimer, Jack J. Lissauer, Morris Podolak, and Yuval Greenzweig. Formation of the Giant Planets by Concurrent Accretion of Solids and Gas. *Icarus*, 124:62–85, November 1996. doi:10.1006/icar.1996.0190.
- William H. Press. *Numerical recipes in C++ : the art of scientific computing*. Cambridge University Press, 2002. ISBN: 0-521-75033-4.

- Roman R. Rafikov. Fast Accretion of Small Planetesimals by Protoplanetary Cores. *Astron. J.*, 128:1348–1363, September 2004. arXiv:astro-ph/0311440. doi:10.1086/423216.
- Sean N. Raymond, Eiichiro Kokubo, Alessandro Morbidelli, Ryuji Morishima, and Kevin J. Walsh. Terrestrial Planet Formation at Home and Abroad. In Henrik Beuther, Ralf S. Klessen, Cornelis P. Dullemond, and Thomas Henning, editors, *Protostars and Planets VI*, pages 595–618. University of Arizona Press, 2014. arXiv:1312.1689. doi:10.2458/azu_uapress_9780816531240-ch026.
- Christian Reinhardt and Joachim Stadel. Numerical aspects of giant impact simulations. *Mon. Not. R. Astron. Soc.*, 467:4252–4263, June 2017. arXiv:1701.08296. doi:10.1093/mnras/stx322.
- Andreas Reufer. *Collisions in planetary systems*. PhD thesis, Universität Bern, September 2011.
- Andreas Reufer, Matthias M. M. Meier, Willy Benz, and Rainer Wieler. A hit-and-run giant impact scenario. *Icarus*, 221:296–299, September 2012. arXiv:1207.5224. doi:10.1016/j.icarus.2012.07.021.
- Pascal Rosenblatt, Sebastien Charnoz, Kevin M. Dunseath, Mariko Terao-Dunseath, Antony Trinh, Ryuki Hyodo, Hidenori Genda, and Stéven Toupin. Accretion of Phobos and Deimos in an extended debris disc stirred by transient moons. *Nat. Geosci.*, 9: 581–583, August 2016. doi:10.1038/ngeo2742.
- Takayuki R. Saitoh and Junichiro Makino. A Density-independent Formulation of Smoothed Particle Hydrodynamics. *Astrophys. J.*, 768:44, May 2013. arXiv:1202.4277. doi:10.1088/0004-637X/768/1/44.
- D. Saumon, Gilles Chabrier, and H. M. van Horn. An Equation of State for low-mass Stars and Giant Planets. *Astrophys. J. Suppl. Ser.*, 99:713–741, August 1995. doi:10.1016/0010-4655(94)00176-3.
- Laurel E. Senft and Sarah T. Stewart. Dynamic fault weakening and the formation of large impact craters. *Earth Planet. Sci. Lett.*, 287:471–482, October 2009. doi:10.1016/j.epsl.2009.08.033.
- N. I. Shakura and R. A. Sunyaev. Black holes in binary systems. Observational appearance. *Astron. Astrophys.*, 24:337–355, 1973.
- Eugene M. Shoemaker. Interpretation of lunar craters. In Zdeněk Kopal, editor, *Physics and Astronomy of the Moon*, pages 283–359. Academic Press, 1962.
- B. Solenthaler and R. Pajarola. Density Contrast SPH Interfaces. In M Gross and D James, editors, *Eurographics/ ACM SIGGRAPH Symposium on Computer Animation*, 2008.

- Roland Speith. *Improvements of the numerical method Smoothed Particle Hydrodynamics*. Habilitationsschrift, Fakultät für Mathematik und Physik der Eberhard-Karls-Universität Tübingen, 2006.
- Sarah T. Stewart and Zoë M. Leinhardt. Velocity-Dependent Catastrophic Disruption Criteria for Planetesimals. *Astrophys. J. Lett.*, 691:L133–L137, February 2009. doi:10.1088/0004-637X/691/2/L133.
- David Swoboda. *Extrasolar multi-planetary system population synthesis*. PhD thesis, Universität Bern, in prep.
- Yasuhiko Takagi, Hitoshi Mizutani, and Shin-Ichi Kawakami. Impact fragmentation experiments of basalts and pyrophyllites. *Icarus*, 59:462–477, September 1984. doi:10.1016/0019-1035(84)90114-3.
- Hidekazu Tanaka and William R. Ward. Three-dimensional Interaction between a Planet and an Isothermal Gaseous Disk. II. Eccentricity Waves and Bending Waves. *Astrophys. J.*, 602:388–395, February 2004. doi:10.1086/380992.
- S. L. Thompson and H. S. Lauson. Improvements in the CHART-D Radiation-hydrodynamic code III: Revised analytic equations of state. Technical Report SC-RR-71 0714, Sandia National Laboratories, 1972.
- J. H. Tillotson. Metallic Equations of State for Hypervelocity Impact. Technical Report GA-3216, General Atomic, July 1962.
- Kleomenis Tsiganis, Rodney Gomes, Alessandro Morbidelli, and Hal F. Levison. Origin of the orbital architecture of the giant planets of the Solar System. *Nature*, 435:459–461, May 2005. doi:10.1038/nature03539.
- Diana Valencia, Masahiro Ikoma, Tristan Guillot, and Nadine Nettelmann. Composition and fate of short-period super-Earth. *Astron. Astrophys.*, 516:A20, 2010. arXiv:0907.3067. doi:10.1051/0004-6361/200912839.
- Julia Elisa Venturini. *Planet formation and characterisation including envelope enrichment*. PhD thesis, Universität Bern, May 2016.
- Kevin J. Walsh, Alessandro Morbidelli, Sean N. Raymond, David P. O’Brien, and Avi M. Mandell. A low mass for Mars from Jupiter’s early gas-driven migration. *Nature*, 475:206–209, July 2011. arXiv:1201.5177. doi:10.1038/nature10201.
- William R. Ward. Protoplanet Migration by Nebula Tides. *Icarus*, 126:261–281, April 1997. doi:10.1006/icar.1996.5647.
- Uwe Wiechert, Alex N. Halliday, Der-Chuen Lee, Gregory A. Snyder, Lawrence A. Taylor, and Douglas Rumble. Oxygen Isotopes and the Moon-Forming Giant Impact. *Science*, 294(5541):345–348, 2001. doi:10.1126/science.1063037.

Don E. Wilhelms and Steven W. Squyres. The martian hemispheric dichotomy may be due to a giant impact. *Nature*, 309:138–140, May 1984. doi:10.1038/309138a0.

Edward D. Young, Issaku E. Kohl, Paul H. Warren, David C. Rubie, Seth A. Jacobson, and Alessandro Morbidelli. Oxygen isotopic evidence for vigorous mixing during the Moon-forming giant impact. *Science*, 351:493–496, January 2016. doi:10.1126/science.aad0525.

A. Zindler and S. B. Jacobsen. Isotopic Equilibration of Earth’s Mantle and the Moon Subsequent to the Giant Impact? In *Lunar and Planetary Science Conference*, volume 40 of *Lunar and Planetary Science Conference*, page 2542, March 2009.

Acknowledgements

First, I want to thank my thesis advisor, Prof. Willy Benz. It has been a real pleasure to learn from his extensive and broad knowledge of various fields of astrophysics. He allowed me to join an excellent work environment here in the Space Research and Planetary Science department of the University of Bern. He gave me good advices, coming back to basic physics when necessary instead of struggling with technical problems. Also he had a critical view on my work, which, I hope, greatly improved it.

Many thanks go to Professors Christoph Mordasini and Yann Alibert, whose have been very supportive while working with the planet formation model. Their extensive knowledge about planet formation has been a great treasure to me.

I want to also thank Martin Jutzi for the time he spent discussing the issues of collision modelling. Moreover, he permitted me to join the great collaboration with Gregor Golabek, Taras Gerya and other persons from the ETH Zürich for the simulation of long term effects of collisions on planetary interiors. It has been a great opportunity to meet with people from the geophysics community and to learn quite a bit from them.

I will not forget the remaining of the TAPS group (Theoretical Astrophysics and Planetary Science) of the University of Bern for the fruitful scientific discussion and the memorable otherwise not-so-scientific talks that we have had. They also remained understanding when I was bothering them with technical details about our computational cluster Who-Should-Not-Be-Named. Among them, David Swoboda, with whom I collaborated and fought the internals of *planete*, trying to understand why planets were migrating outward.

It has been a pleasure to collaborate with the people from the University of Zürich, especially Christian Reinhardt and Joachim Stadel. Their different point of view on SPH have been particularly enlightening. I also thank Prof. Ben Moore, who kindly accepted to be the external referee for this thesis.

Finally, my family has also provided a great moral support. They were present in the difficult times, and cheering me up when necessary. Many thanks for your patience during these years!

I wish to acknowledge the financial support of the Swiss National Science Foundation which permitted me to carry the work presented in this thesis.

Declaration of consent

on the basis of Article 28 para. 2 of the RSL05 phil.-nat.

Name/First Name: Emsenhuber, Alexandre

Matriculation Number: 07-503-568

Study program: Physics

Bachelor

Master

Dissertation

Title of the thesis: Collisions during planetary systems formation

Supervisor: Prof. Dr. Willy Benz

I declare herewith that this thesis is my own work and that I have not used any sources other than those stated. I have indicated the adoption of quotations as well as thoughts taken from other authors as such in the thesis. I am aware that the Senate pursuant to Article 36 para. 1 lit. r of the University Act of 5 September, 1996 is authorised to revoke the title awarded on the basis of this thesis. I allow herewith inspection in this thesis.

Bern, the 13th of October 2017

Place/Date

Signature

Curriculum vitae

Name: Alexandre Emsenhuber
Date of birth: 10.11.1988
Address: rue des Bourguillards 8
CH-2072 St-Blaise
ORCID: 0000-0002-8811-1914

Education

1994-1999 Primary school at St-Blaise
1999-2004 Secondary school at St-Blaise and Marin
2004-2007 Lycée Denis-de-Rougemont at Neuchâtel

Academic record

2007-2011 Bachelor in physics at the University of Neuchâtel
2011-2013 Master of science with specialisation in experimental physics
at the University of Bern
2012-2013 Master thesis *Giant Impact*
2013-2017 Ph.D. candidate at the University of Bern

Publications

- **Alexandre Emsenhuber**, Martin Jutzi and Willy Benz. SPH calculations of Mars-scale collisions: The role of the equation of state, material rheologies, and numerical effects. *Icarus*, in press. arXiv:1710.03245. doi:10.1016/j.icarus.2017.09.017.
- Gregor J. Golabek, **Alexandre Emsenhuber**, Martin Jutzi, Erik I. Asphaug and Taras V. Gerya. Coupling SPH and thermochemical models of planets: Methodology and example of a Mars-sized body. *Icarus*, in press. arXiv:1710.03250. doi:10.1016/j.icarus.2017.10.003.